



**HAL**  
open science

# Analyse du comportement en écoulement à la paroi de polymères dans des conditions de mélangeur interne

Prashanth Thirunavukkarasu

► **To cite this version:**

Prashanth Thirunavukkarasu. Analyse du comportement en écoulement à la paroi de polymères dans des conditions de mélangeur interne. Mechanics of materials [physics.class-ph]. Université Paris sciences et lettres, 2021. English. NNT : 2021UPSLM070 . tel-03771834

**HAL Id: tel-03771834**

**<https://pastel.hal.science/tel-03771834>**

Submitted on 7 Sep 2022

**HAL** is a multi-disciplinary open access archive for the deposit and dissemination of scientific research documents, whether they are published or not. The documents may come from teaching and research institutions in France or abroad, or from public or private research centers.

L'archive ouverte pluridisciplinaire **HAL**, est destinée au dépôt et à la diffusion de documents scientifiques de niveau recherche, publiés ou non, émanant des établissements d'enseignement et de recherche français ou étrangers, des laboratoires publics ou privés.



**THÈSE DE DOCTORAT**  
**DE L'UNIVERSITÉ PSL**

Préparée à MINES ParisTech

**Analysis of the interfacial flow behavior of polymers  
along the walls of an internal mixer**

**Analyse du comportement en écoulement à la paroi de  
polymères dans des conditions de mélangeur interne**

Soutenue par

**Prashanth  
THIRUNAVUKKARASU**

Le 31 mars 2021

Ecole doctorale n° 364

**Sciences Fondamentales et  
Appliquées**

Spécialité

**Mécanique Numérique et  
Matériaux**

Composition du jury :

<b>Pr Ulrich GIESE</b> Leibniz University of Hannover	<i>Rapporteur</i>
<b>Pr Jean-Charles MAJESTÉ</b> Université Jean Monnet	<i>Rapporteur</i>
<b>Dr Céline COHEN</b> Université Nice-Sophia Antipolis	<i>Examineur</i>
<b>Pr Rémi DETERRE</b> Université de Nantes	<i>Président</i>
<b>Dr Pascal TREMBLAY</b> Michelin – MFP	<i>Examineur</i>
<b>Dr Édith PEUVREL-DISDIER</b> MINES ParisTech – CEMEF	<i>Examineur</i>
<b>Pr Rudy VALETTE</b> MINES ParisTech – CEMEF	<i>Examineur</i>

**MINES ParisTech**  
**Centre de Mise en Forme des Matériaux (CEMEF)**  
CNRS UMR 7635  
1 rue Claude Daunesse, CS 10207, 06904 Sophia Antipolis Cedex, France  
<http://cemef.mines-paristech.fr>

---

## Acknowledgements

I would like to share my gratitude to Michelin for funding this thesis and providing me with the opportunity to work on this subject. I wish to express my special thanks to Pascal Tremblay, Bruno Dratz and Jean-Marc Gonet for their dedication and interest on this work. Thanks to Guillaume Foyart and Kévin Queffelec for helping me with the experiments and sharing their expertise with me.

This work could only be achieved due to the contributions of my academic supervisors, Édith Peuvrel-Disdier and Rudy Valette. Their guidance and supportive collaboration are the main reasons for completing this work and I am indebted to them. I would also like to thank Bruno Vergnes, Romain Castellani and Franck Pigeonneau from CEMEF for the scientific discussions and their participation in this project.

My sincere thanks to Ulrich Giese, Jean-Charles Majesté, Céline Cohen and Rémi Deterre, for agreeing to be part of the jury and reviewing my work. I would also like to acknowledge Céline Cohen and Jean-Charles Majesté for sharing their knowledge and helping me during this work.

A large part of this work is dedicated to the conception, experimentation and analysis of the prototype mixer. This could only be possible thanks to the efforts of the MEA team from CEMEF, especially Francis Fournier and Arnaud Pignolet. I am grateful for their contribution and that of the other members of the MEA team, Christelle Combeaud, Marc Bouyssou, Eric Brotons and Guillaume Corvec. My warm thanks to Gilbert Fiorucci and Thierry Colin for helping me to find solutions for the various experiments and for helping me when the machines broke down. I also acknowledge Nikhil Tembhornikar from ICI-SPIN, Christophe Pradille, Gabriel Monge and for their assistance during this work.

I am also thankful to the works of Alexandre Vigier during his internship in CEMEF who showed great autonomy and dedication. Supervising your internship was one of the easiest tasks of this PhD.

My heartfelt thanks to my friends, officemates, colleagues and staff from CEMEF for making my time in CEMEF a pleasant experience: Ayoub Aalilija, Shitij Arora, Christophe Berto, Séverine Boyer, Coraline Chartier, Patrick Coels, Émilie Forestier, Feng Gao, Jordi Girones, Fabien Goldspiegel, Marie-Françoise Guenegan, Jean-Marc Haudin, Nagasai Meghana Rani Kauta, Clément Laügt, Isabelle Liotta, Florence Morecamp, Saoussen Ouhiba, Arvind Parakulam-Ramaswamy, Aakash Patil, Corentin Perderiset, Chau Thuy Pham, Juhi Sharma, Diego Uribe, Marie-Anne Vidal, Loan Vo and Fangxin Zou. Not to forget Max, Phillipe and Renato from CRHEA.

இறுதியாக, இந்த வேலை என் குடும்பம், நெருங்கிய நண்பர்கள் மற்றும் மில்லிக்கு (PSL) அர்ப்பணிக்கப்பட்ட உள்ளது.

---

# Table of contents

General introduction and industrial context .....	1
1. Literature Review .....	7
1.1. Tire manufacturing .....	8
1.1.1. Development of tires .....	8
1.1.2. Parts of a tire.....	9
1.1.3. Formulation of rubber compounds .....	10
1.1.4. Tire manufacturing process .....	12
1.2. Internal mixing .....	13
1.2.1. Banbury mixer .....	13
1.2.2. Flow visualizations with internal mixers.....	15
1.2.3. Modelling the flow behavior in an internal mixer .....	17
1.3. Wall slip and flow regimes.....	20
1.3.1. Wall slip in polymers.....	20
1.3.2. Wall slip characterization techniques .....	22
1.3.3. Thermodependency of wall slip velocities .....	26
1.4. Movement of contact lines/free surfaces .....	27
1.4.1. Contact line dynamics .....	27
1.4.2. Fracture mechanics in viscoelastic fluids .....	28
1.4.3. Viscoelastic trumpet model .....	30
1.5. Adhesion.....	32
1.5.1. Characterization of adhesion energy .....	33
1.5.2. Thermodependency of adhesion energy .....	34
Conclusions .....	37
2. Materials and methods.....	39
2.1. Fluids used in the study .....	40
2.1.1. Rubber products .....	40
2.1.2. Silicone fluid .....	43
2.2. Experimental methods.....	44
2.2.1. Rheometers.....	44
2.2.1.a. Oscillatory rheometers.....	44
2.2.1.b. Capillary rheometer .....	46
2.2.2. Probe tests.....	53
2.3. Transparent flow cells .....	56
2.3.1. Transparent flat die.....	56
2.3.2. Transparent internal mixers .....	58
2.3.2.1. Monocuve mixer.....	59
2.3.2.2. MaCROS mixer .....	61
Conclusions .....	67
3. Rheological and wall slip characterization.....	69
3.1. Oscillatory rheometry.....	70
3.1.1. Silicone fluid .....	70
3.1.2. Rubber products .....	73
3.2. Capillary rheometry.....	77
3.2.1. Study of pre-shearing conditions.....	78
3.2.2. Butadiene Rubber (BR A) behavior .....	80
3.2.3. Styrene Butadiene Rubber A (SBR A) behavior .....	86
3.2.4. Styrene Butadiene Rubber B (SBR B) behavior .....	93
3.2.5. Rubber compound (SBR C) behavior.....	99
3.3. Wall slip characterization .....	103

3.3.1. BR A wall slip velocities .....	103
3.3.2. SBR A wall slip velocities .....	105
3.3.3. SBR B wall slip velocities .....	107
Conclusions .....	110
4. Transparent flow observations .....	113
4.1. Transparent flat die observations.....	114
4.2. Flow observations in the Monocuve mixer .....	117
4.2.1. Flow observations with round rotor .....	117
4.2.2. Flow observations with cam rotor .....	118
4.2.3. Symmetry of the flow outlines in Monocuve mixer .....	124
4.3. Flow observations in MaCROS mixer .....	126
4.3.1. Evaluation of the prototype and identification of model fluid .....	126
4.3.2. Types of flow observations .....	129
4.3.2.1. Counter-rotation condition .....	129
4.3.2.2. Co-rotation condition.....	131
4.4. Steady state flow observations at a small fill factor .....	133
4.4.1. Silicone fluid observations .....	133
4.4.2. Effect of surface properties on stabilization velocities.....	139
4.4.3. Symmetry of the flow outlines in MaCROS mixer .....	141
4.4.4. Rubber products observations .....	142
Conclusions .....	146
5. Influence of adhesion energy on free surfaces during shear flow .....	149
5.1. Probe tests.....	150
5.1.1. Rubber products .....	150
5.1.2. Silicone fluid .....	154
5.2. Modelling the steady state flow observations.....	157
5.2.1. Adhesion model.....	157
5.2.2. Drag model .....	161
5.2.3. Drag model: Prediction of stabilization conditions .....	163
5.3. Finite element simulation of free surface profiles .....	166
5.3.1. Cimlib simulation: Newtonian case.....	166
5.3.2. Cimlib simulation: Non-Newtonian case .....	169
Conclusions .....	172
6. Discussion and conclusion .....	175
6.1. General conclusions .....	176
6.2. Suggestions for future studies .....	178
Bibliographic references.....	181
Appendix .....	I



# General introduction and industrial context

### Need for new rubber formulations

One of the biggest challenges to the transport sector is the reduction of greenhouse gas emissions. Environmental policies are being implemented on industries to cut down on the emission of greenhouse gases, especially that of CO<sub>2</sub>. The transport industry accounts for about 15.5% of the CO<sub>2</sub> emissions in the world and 28.2% in France as of 2016 [Ritchie and Roser, 2020]. An urgent need has risen to find solutions to cut down on greenhouse gas emissions in the transport sector. One way to achieve this is by the reduction of fuel consumption.

Michelin is one of the world's leading tire manufacturers. Research and innovation have always been the core of their strategy. This has led to many inventions such as the removable pneumatic tires, metallic wheels, steel frame tires, radial tires, green tires, cross-climate tires, airless tires, among others. Michelin introduced the first generation of green tires (not to be confused with uncured tires) in 1992. Green tires use silica reinforced rubbers, instead of classically used carbon black reinforced rubbers. These tires improve their energy efficiency by reducing the energy lost due to: 1) the friction generated between the tire tread and the road and 2) the deformation of the material during rolling while maintaining the necessary deformation to grip the road. The energy lost due to rolling resistance accounts for about one-third of fuel consumption [VTT Technical Research Center, 2012]. Diminishing this friction loss will result in a reduction of fuel consumption and ultimately, the emission of greenhouse gases.

With rising awareness on the issue of climate change, there is a push for the development of new tire products to improve fuel efficiency. The development of new tires results in the change of specifications of the different parts of the tire. New rubber formulations are required to meet these new specifications. Thus, the development of new tires necessitates the development of multiple new rubber formulations. Following the development of new rubber formulations, they are tested to ascertain their suitability for the manufacturing process. During this step, the parameters of the manufacturing process are identified and the formulations can be adjusted to facilitate the manufacturing process. This requires repeated industrial trial and error testing, which can be rather time consuming.

### Internal mixing

The tire manufacturing process is quite complex and can be simplified to five stages: i) the compounding/mixing, ii) the milling, iii) the extrusion, iv) tire building and v) vulcanization/curing stage. Over 200 raw materials are used to make a modern commercial tire. Initially, the raw materials of each rubber formulation are mixed in a Banbury or internal mixer (Figure 1).

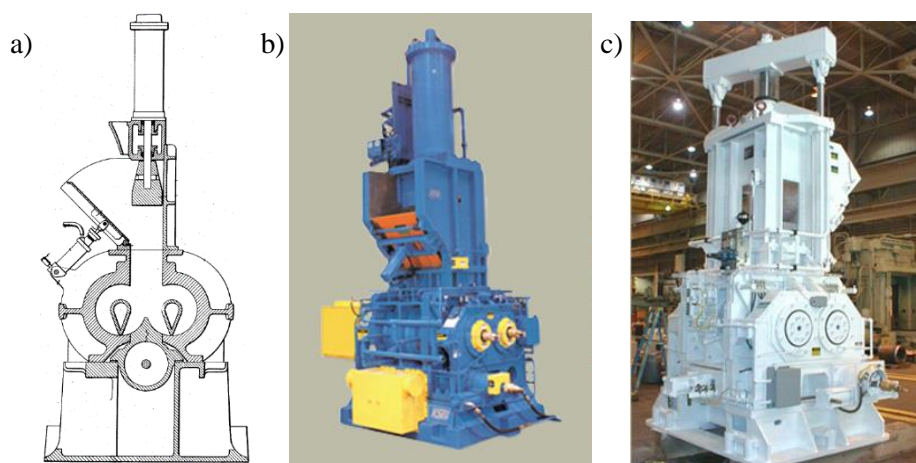


**Figure 1** – a) Schematic representation of a Banbury mixer [Banbury, 1928], b) and c) Industrial Banbury mixers [Kobelco Stewart Bolling, Inc].

At the completion of the mixing cycle, the mixed rubber compound is placed onto a drop mill where the rubber is shaped into flat, long strips by the rotating rolls of the drop mill. The extrusion operation serves to prepare the rubber compounds into sheets of uniform thickness. Belts of fabric and steel are then placed onto the sheets of rubber compounds. The components of the tire are then assembled onto a rotating drum. Finally, the assembled tire is placed into a curing press where steam is used to vulcanize the tire.

The mixing or compounding stage is considered as the most crucial step in the manufacture of multiphase materials ((nano)composites, polymer blends, rubber compounds...) as it is instrumental to the final properties of the product. The mixing process involves the mixing of solid and liquid phases in a partially filled confined volume. The objective is to incorporate, disperse and distribute the components to obtain a homogenous mixture. Hancock [Hancock, 1857] developed the first mixer in 1820 to mix rubber and it consisted of a hollow chamber with a single rotor. Soon, rolls mills became the norm for the mixing and compounding of rubber. However, mill mixing is disadvantageous [Grossman, 1997] due to the:

- 1) length of the mixing cycles,
- 2) dependence on operator skills,
- 3) dust and dirt levels that are atypical,
- 4) difficulty in standardizing subjective procedures,
- 5) difficulty in controlling batch-to-batch uniformity.

The disadvantages of mill mixing outnumber its advantages. As a result, internal mixers were introduced to replace roll mills. Internal mixers typically consist of two counter-rotating rotors enclosed in a mixing chamber. With the invention of the Banbury mixer (Figure 1) in 1916, mill mixers were completely replaced and internal mixing has become the standard mode of mixing till today [White, 1995].

### Interfacial flow behavior in internal mixers

Banbury type internal mixers are still in use today and the mixing process takes place in a confined volume of up to 700 liters. As the mixing occurs in a confined volume, observation of the process is impossible, making it difficult to understand what takes place during the mixing process. Temperature, pressure and torque sensors are used to monitor and control the process. However, this does not provide a complete understanding of the process. The observation of the flow behavior during mixing can be achieved by equipping a lab scale internal mixer with a transparent wall, similar to the works of Freakley and Wan Idris [Freakley and Wan Idris, 1979] and White *et al.* [White *et al.*, 1986]. The observation of the flow behavior of the fluids through the transparent mixers (Figure 2) has helped better understand the flow behavior of the polymers during this process.

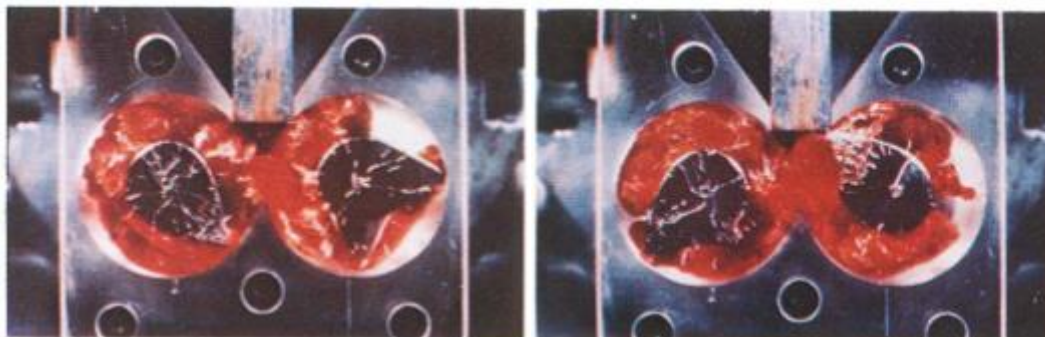


**Figure 2** – Flow observations through a transparent internal mixer [Freakley and Wan Idris, 1979].

Efforts to improve the efficiency of the process (change in geometry of the mixer or a change in mixing parameters) must be carried out by a series of trial and error tests. This can be very time consuming for testing new rubber formulations and can delay the development of new rubber

formulations, like the silica reinforced rubber compounds for green tires. Numerical models have been used to study the behavior of complex processes and provide analytical solutions. A numerical model, which can accurately simulate the flow behavior of the fluids during the internal mixing process, can eliminate the necessity of repeated experimental trials. Such a model would drastically shorten the time required to develop new rubber formulations.

The first efforts to model the internal mixing process were carried out by Ghoreishy [Ghoreishy, 1996] and Dubois *et al.* [Dubois *et al.*, 1996]. Despite numerous advancements over the past few decades, numerical simulation of the internal mixing process has remained an open topic of research. However, these numerical models do not take into account the multiphasic behavior of the rubber compound during the beginning of the mixing cycle, the movements of the interfaces and contact lines. The development of a transparent internal mixer with the objective of observing the flow of the fluids during internal mixing can help characterize the interfacial flow behavior and thus, improve the accuracy of the numerical simulations.

### FUI project OSUM

OSUM (Outil de Scale Up de Mélangeage) is a research project based on a consortium between industrial (Michelin, Lescuyer et Villeneuve and SCC Consultants) and academic partners (ICI-ECN, IMP-SPIN and CEMEF). The FUI project was created with the aim of accelerating the innovation of new rubber formulations and their transition to the production phase.

The repeated industrial trial and error tests required before the transition to the production phase could be replaced by an accurate numerical model. A lab scale mixer, representative of an industrial mixer, is then developed to validate the formulations and subsequently to certify the prediction of the numerical model. Following this phase, a scale up operation is performed on the numerical model to predict the mixing behavior in industrial conditions. The objectives of the project are to:

- i) develop a numerical model of the internal mixing process,
- ii) create a lab scale mixer to test rubber formulations and validate the numerical model,
- iii) define the criteria and validate the steps of scale up.

In this project, the IMP-SPIN team works on the kinetics of impregnation and the multiphasic behavior of the matrix during the beginning of the mixing process. The CEMEF team studies the flow of the elastomers during internal mixing focusing on the interfacial flow behavior and the free surfaces during mixing. The development of a finite element model of the internal mixing process was carried out by the ICI-ECN team. SCC will work in collaboration with the ICI-ECN team to industrialize the numerical model and subsequently, commercialize the simulation software. The lab scale internal mixer for the scale up operation is developed by Lescuyer and Villeneuve. Michelin is responsible for the coordination of the project, testing of the lab scale internal mixer and the validation of the numerical model. In addition, they will also define the criteria, the approach and validate the scale up operation.

### PhD thesis objectives and outline

The efficiency of the mixing process depends on the kinematics of the flow, the bulk rheological behavior of the rubber matrix and also on the interfacial behavior of the matrix at the wall. The modelling of such a process is complex. Few (or no) models take into account the interfacial phenomena at the walls of the mixer. These interfacial phenomena include wall slip, adhesion and the movement of the free surfaces of the fluid during mixing.

Classical transparent internal mixers cannot be used to study the interfacial flow behavior during mixing due to their complex geometry and the transient nature of the observations. A lab scale transparent internal mixer (Monocuve mixer) with a single rotor and a simplified 2D geometry was used to observe the flow behavior of the fluids along the walls of the mixer. In addition, a prototype

mixer called the MaCROS mixer (Malaxeur Contra-Rotatif avec Observation Stationnaire) was developed to conduct steady state flow observations. These observations enable us to study the shape and movement of the free surfaces and interfaces during mixing. A capillary rheometer was used to characterize the rheological and wall slip behavior of the rubber products. The role of the adhesion energy on the free surfaces of the rubber products during mixing was investigated with the help of a numerical model.

The objectives of the thesis were to:

- characterize the rheological and wall slip behavior of the rubber products,
- design and develop a prototype transparent mixer to conduct *in-situ* flow observations in conditions representative of internal mixing,
- conduct and analyze steady state flow observations with the prototype mixer,
- investigate the role of adhesion on the free surfaces of the rubber products during mixing with a numerical model.

This PhD manuscript is divided into six chapters. Chapter 1 provides a brief presentation of the tire manufacturing and the internal mixing processes. A brief literature review on the topics of interest for this PhD work (the determination of rheological and wall slip behavior, the contact line dynamics and the adhesive behavior of viscous fluids) is discussed here.

Chapter 2 presents the different fluids and experimental tools used during the course of this work. The design and development of the transparent tools (transparent flat die and MaCROS mixer) is presented here.

Chapter 3 is dedicated to the rheological characterization of the fluids. The rheological behavior of the model fluid at ambient temperature and rubber products at higher temperatures was determined using oscillatory rheometers. The capillary rheometer was used to characterize the rubber products at different temperatures. From the capillary data, wall slip velocities were estimated using the Shear Rate Difference method.

The flow observations with the transparent tools are discussed in Chapter 4. The steady state flow observations with the MaCROS mixer were conducted in detail under the counter-rotation condition at small fill factors. These observations provide a better observation of the free surfaces of the fluid during shear flow. The stabilization velocities and the free surfaces of the fluid during stabilized shear flow were analyzed.

In Chapter 5, the adhesion energies of the fluids were characterized at their service temperatures. An adhesion model was proposed to estimate the adhesion energy exhibited by the fluids during shear flow in the MaCROS mixer. Subsequently, a finite element model was used to study the influence of adhesion energy on the free surfaces of the fluid during mixing.

The results of this work in the framework of the OSUM project are summarized in Chapter 6. Finally, an non-exhaustive outlook on the future studies is presented here.



# Chapter 1

## Literature Review

### Contents

---

1.1. Tire manufacturing .....	8
1.1.1. Development of tires .....	8
1.1.2. Parts of a tire .....	9
1.1.3. Formulation of rubber compounds .....	10
1.1.4. Tire manufacturing process .....	12
1.2. Internal mixing .....	13
1.2.1. Banbury mixer .....	13
1.2.2. Flow visualizations with internal mixers .....	15
1.2.3. Modelling the flow behavior in an internal mixer .....	17
1.3. Wall slip and flow regimes .....	20
1.3.1. Wall slip in polymers .....	20
1.3.2. Wall slip characterization techniques .....	22
1.3.3. Thermodependency of wall slip velocities .....	26
1.4. Movement of contact lines/free surfaces .....	27
1.4.1. Contact line dynamics .....	27
1.4.2. Fracture mechanics in viscoelastic fluids .....	28
1.4.3. Viscoelastic trumpet model .....	30
1.5. Adhesion .....	32
1.5.1. Contact line dynamics .....	33
1.5.2. Thermodependency of adhesion energy .....	34
Conclusions .....	37

---

### 1.1. Tire manufacturing

#### 1.1.1. Development of tires

The industrial revolution saw the birth and the widespread use of internal combustion engines. Initially, the traction developed by the engines were transmitted by wheels or solid tires. However, the solid tires inflicted severe damage to the vehicle mechanics and the vehicles required frequent maintenance. The drive power and speeds of the vehicles increased over time, making solid tires a source of discomfort for passengers. The rising awareness of the technological applications of rubber compounds provided an alternative for the solid tires. Today, rubber tires are indispensable due to their superior properties [Franta, 1989] such as: 1) great elasticity, 2) low hysteresis loss, 3) good fatigue resistance, 4) resistance to wear, 5) impermeability, 6) considerable chemical resistance, 7) good electrical insulating properties, 8) long service life and 9) their relative low cost.

Natives from Central and South America have used latex from rubber trees to make waterproof clothes and shoes. This was later witnessed by European explorers like Columbus and Cortez. The technological applications of rubber were further explored by de la Condamine in the mid-18<sup>th</sup> century [Schidrowitz and Dawson, 1952]. The discovery of the vulcanization process by Goodyear [Goodyear, 1844] and Hancock [Hancock, 1857] significantly developed the commercial importance of rubber.

Due to the early efforts of Wickham in the late 19<sup>th</sup> century [Collier, 1968], natural rubber is commercially grown in plantations (*hevea brasiliensis*) across the world. In the early 20<sup>th</sup> century, countries which lacked access to rubber plantations, primarily Germany and USA, made efforts to synthesize rubber. In 1906, Hofmann and his co-workers synthesized isoprene rubber [Hofmann and Coutelle, 1911]. Synthetic rubbers were soon used in commercial applications. Today, natural and synthetic rubbers are manufactured in almost similar quantities (47 and 53% respectively) [Garside, 2021; MREPC, 2020] and they are widely used today in applications ranging from tires, gloves, belts, adhesives, etc.

The invention of the pneumatic tire (rubber tires) in 1846 by Thomson saw the tire acting as a circumferential spring which: i) reduces resistance to motion and ii) decreases the shock and fatigue from the vibrations [Tompkins, 1981]. With Dunlop's reinvention of the pneumatic tire in 1888, these tires saw widespread use in the substantial bicycle markets and petrol-powered automobiles. The mass production of automobiles in the early 20<sup>th</sup> century and the advent of both world wars accelerated the tire development and design significantly [French, 1989]. The basic functions of a tire are:

- i) to support the load of the vehicle,
- ii) to transmit the driving, braking and cornering forces applied by the vehicle,
- iii) absorb road shocks,
- iv) prevent the generation of excessive noise within the environment,
- v) maintain performance over a wide range of speeds in dry and wet conditions over long distances,
- vi) maintain and change the direction of movement.

The performance of a tire can be defined by different parameters such as traction, rolling resistance, wear, durability, noise, wet grip, fuel efficiency, etc. These parameters are determined by the ingredients of the tire and the parameters of its manufacturing process. However, the desired performance parameters of the tire can vary based on its application (type of vehicle used, tread construction, load carried, terrain, climate, fuel efficiency, etc.). Figure 1.1 depicts different types of tires based on their application. The development of new tires requires the tailoring of the tire formulation and the parameters of the manufacturing process to obtain the desired performance.

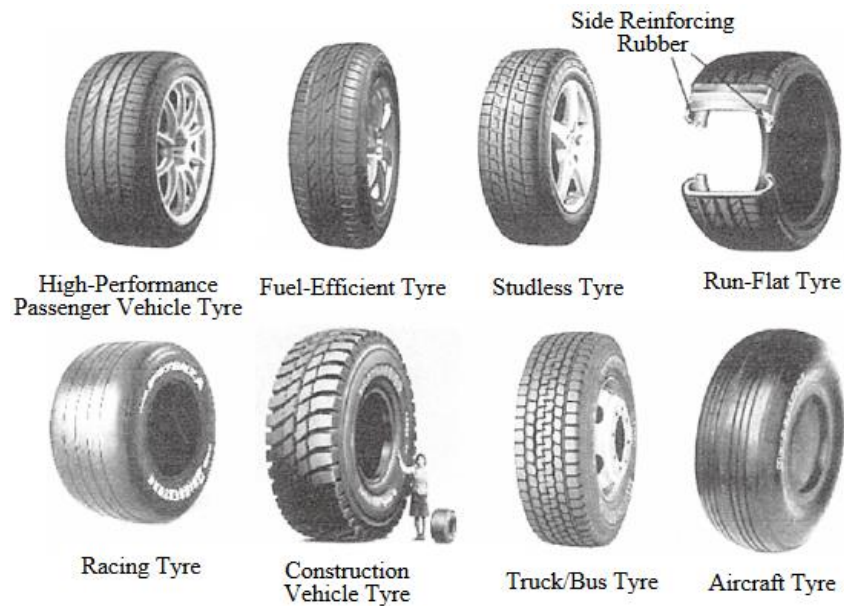


Figure 1.1 – Tires used in different applications [Gomu Rubbers, 2010].

### 1.1.2. Parts of a tire

Commercial tires are manufactured in different shapes and sizes. The different parts of the tire are tailored to provide the desired final properties of the product. The parts are initially manufactured separately and are then assembled on a rotating drum to make the green tire (pre-cured tire). The different parts of a tire are shown in Figure 1.2.

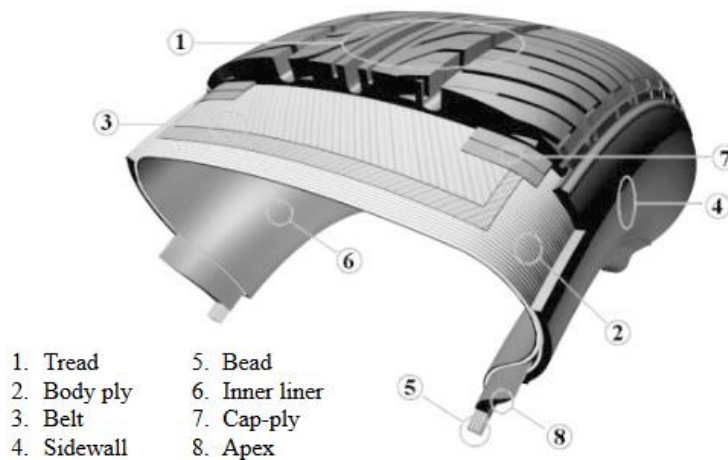


Figure 1.2 – Cross-section of a tire [Evans, 2002].

The important parts of a tire, by their order of assembly, are:

**Inner liner:** This membrane provides an air-tight layer within the structure of the tire, sealing the air at elevated pressures. In some cases (tube tires), this layer is replaced by an impermeable tube of air.

**Body ply:** The body ply consists of twisted parallel cords made of steel, nylon, rayon or polyester. a stiff adhesive rubber compound and adhesion promoters The body ply, also known as the carcass, provides the necessary strength of the tire to bear the stresses as it is loaded and deformed. As the inner liner is inflated, the body ply allows the tire to take its desired profile. During the calendaring process, the cords are coated onto a stiff adhesive rubber compound and adhesion promoters to create a bond between the cords and other tire components.

**Bead:** The bead is a rigid wound hoop of steel coated with rubber. Two beads are placed on either side of the tire, allowing the tire to seat on the rim of the wheel. These beads also act as an anchor for the body ply, preventing it from dislodging. Together, the beads and the body ply provide the necessary strength to carry the load.

**Apex:** The apex membrane provides a stiff connection between the rigid bead coil and the flexible sidewall of the tire. This layer enhances directional stability and steering precision while improving comfort.

**Sidewall:** The sidewall is the flexible part of the tire, which flexes as the tire undergoes shocks and vibrations. It also protects the cord plies and the tire from impacts on the side. Over time, this flexible layer is vulnerable to degradation due to sunlight, excess heat and ozone. Thus, anti-oxidizing and anti-ozone agents are added to its rubber formulation.

**Belt:** This layer consists of layers of steel, fiber glass, rayon and other materials coated with rubber, placed between the tread and the plies. It helps to maintain the tread flat and in contact with the road. This provides the tire with sufficient stiffness to resist the strains of turning and rotation while being flexible enough to absorb deformations caused by obstacles. The tire's mileage performance is reduced by the reduction of rolling resistance and the belt's resistance to punctures.

**Cap-Ply:** This layer of reinforced nylon cords, is embedded to provide comfort and rigidity to the belt. It also improves impact resistance, steering stability and prevents centrifugal stretching of the tire. Polymer cap plies act as a casing, protecting against moisture and restricting the migration of chemicals from the tread into the belt.

**Tread:** The tread is the thickest component of the tire. It is the most critical component of the tire as it is the part of the tire which comes into contact with the ground. The tread transmits the driving forces of the vehicle to the ground and is hence, exposed to rolling resistance and wear. Grooves on the tread surface are used to allow water to escape effectively. The grooves and the tread pattern, provide better traction, turning grip while effectively transmitting the driving forces. This makes it crucial in determining the performance and fuel efficiency of the tire.

Each part of the tire has different functions and dimensions. Based on their individual roles, each part requires different rubber formulations. The development of a new tire results in a change of the tire's desired performance. To provide this performance, the specifications of each part of the tire changes necessitating the need for new rubber formulations. In the next section, the formulation of rubber compounds will be discussed briefly.

### 1.1.3. Formulation of rubber compounds

Due to their difference in function (and hence their formulation), each rubber compound is manufactured separately. As a result, the fabrication of each rubber compound requires different processing conditions. The rubber compounds are formulated with the objective of providing optimum properties at minimum cost and in such a way that they can be efficiently processed. Thus, the ingredients and their concentrations must be chosen prudently. An example of a rubber formulation used in passenger car tires is given in Table 1.1. The concentration of each component is presented in parts per hundred of rubber. A typical rubber compound has the following ingredients:

- polymers,
- fillers,
- oils/Plasticizers,
- anti-degradants,
- processing aids,
- activators,
- vulcanizing agent,

- accelerators.

Ingredients	Concentration (phr)
<i>Polymers</i>	
Styrene Butadiene Rubber (oil extended)	96.3
Butadiene Rubber	30
<i>Filler</i>	
Silica	80
<i>Coupling agent</i>	
	6.4
<i>Oils/Plasticizers</i>	
	28.1
<i>Activators</i>	
Zinc oxide	3.5
Stearic acid	2.0
<i>Anti-degradant</i>	
Antioxidant, antiozonant	2.0
<i>Processing aids</i>	
	3.5
<i>Vulcanizing agent</i>	
Sulfur	1.4
<i>Accelerators</i>	
	4.1

**Table 1.1** – Formulation of a silica based passenger tire tread [Wang *et al.*, 2001].

Natural or synthetic rubber can be used as base polymers in the rubber formulation. Over the years, only a few basic elastomer types have been identified for manufacturing of rubbers. The selection of monomers, the polymerization technique and the architecture of the polymer backbone play a crucial role in determining the final properties of the compound [Evans, 2002].

To reinforce the properties of the base polymers, inorganic fillers are added. Most commonly used materials are carbon black and silica. However, other materials like aluminum trihydrate, clay, chalk, etc are also used to a lesser extent. At low strains, the rubber compound exhibits good stiffness due to a combination of the strength of the cured rubber network, hydrodynamic effect of mixing solid particles in a fluid medium, polymer chain entanglements with the filler network and the strength of the filler-filler network [Evans, 2002]. At higher strains, the filler-filler network breaks and the strength is provided by the polymer-filler network. At higher strain amplitudes, the necessary strength is provided by the covalent links of the polymer chains.

In some cases, coupling agents are required to promote the bond between the fillers and the polymer chains. Oils or plasticizers are added, especially at high filler concentration, to facilitate the mixing of ingredients during the internal mixing phase. Processing aids are required to improve the extrusion and moldability of the compounds. To prevent the degradation of the tire during service, anti-oxidants and anti-ozonates are used for the sidewalls of the tyre. These agents can improve the long-term durability of the tire.

The elasticity of rubber can be greatly improved by the crosslinking of the molecular chains through vulcanization (Figure 1.3a). A network is created by the adjoining of macromolecules of different molecular chains with the use of vulcanization agents. The network results in the improvement of the elasticity, resilience, tensile strength, viscosity, hardness and weather resistance of the compound. In most formulations, the activators and the accelerators are used in tandem with the vulcanization agent. The vulcanization agent, often sulphur, is used to create links between the polymer chains. The activators are used to create more sites in the chain for cross-linking. Vulcanization by sulfur alone is a slow and inefficient process, so accelerators are used to quicken the process (Figure 1.3b).

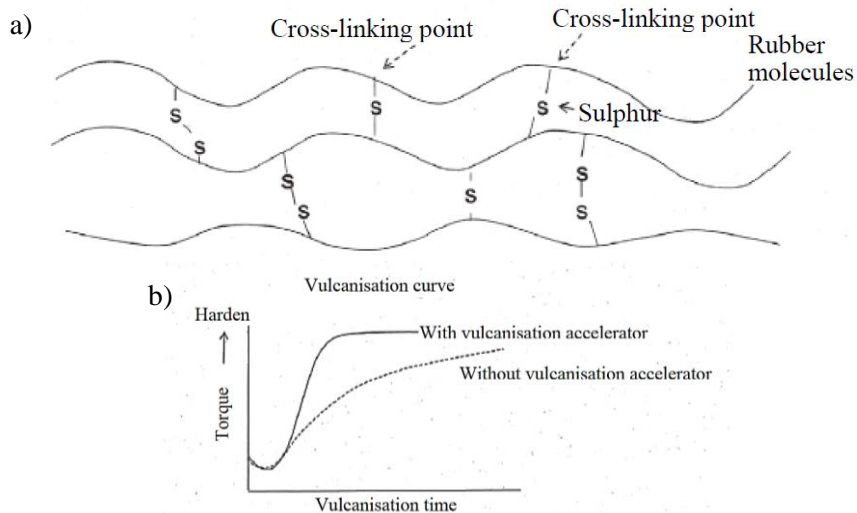


Figure 1.3 – a) Rubber network created through vulcanization and b) the impact of accelerator on vulcanization [Ishikawa, 2011].

### 1.1.4. Tire manufacturing process

A simplified flowchart of the tire manufacturing process is presented in Figure 1.4. Initially, the raw materials required for the manufacturing are acquired and stored. The manufacturing process can be subdivided into five steps. They are:

**Internal mixing:** The ingredients of the rubber formulation are mixed in an internal mixer to produce a homogenized rubber compound. Different parameters such as temperature, rotor speed, etc. are controlled to produce a homogenous rubber compound with optimal incorporation, distribution and dispersion of the ingredients. The vulcanization agent and the accelerators are not added to the compound during this stage.

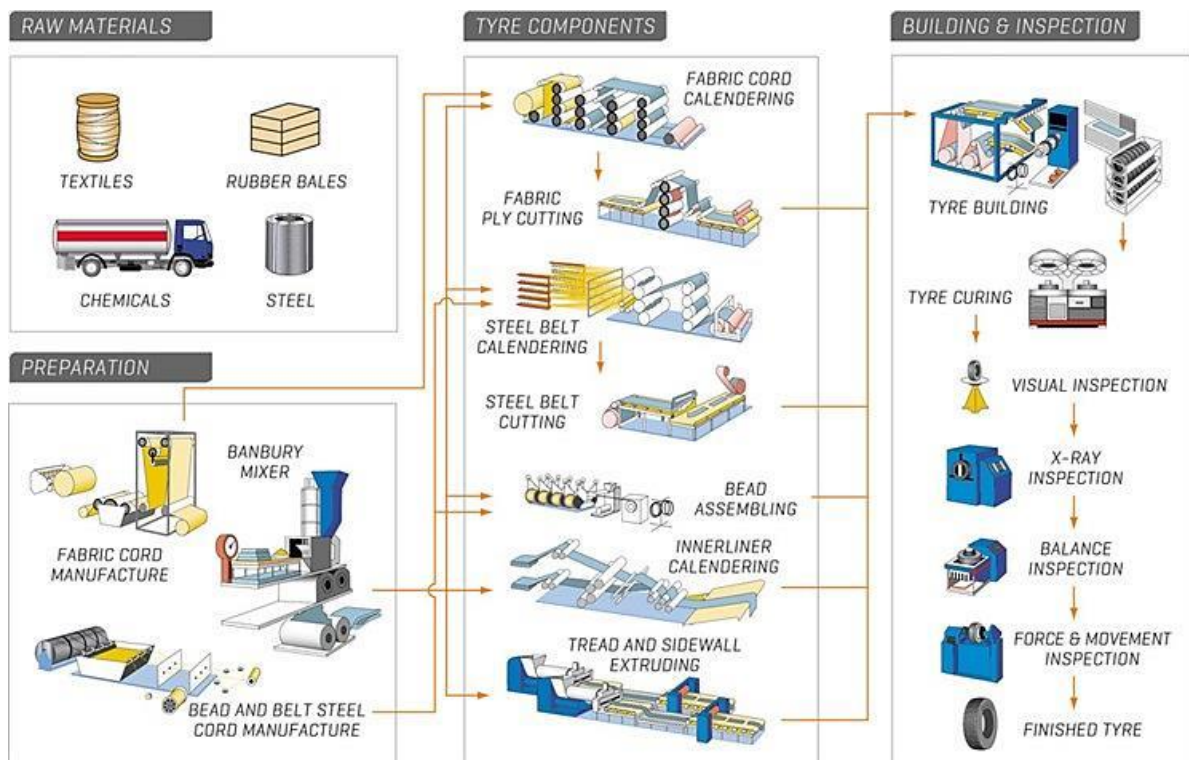


Figure 1.4 – Manufacturing flowchart of the tire manufacturing process [Maxxis tires, 2021].

**Milling:** At the end of the mixing cycle, the rubber is dropped onto drop mills of three or more rollers. The rolls turn in opposite directions to each other. The vulcanization agent and the accelerators are added to the compound as they are shaped into flat, long strips.

**Extrusion:** In this step, uniform sheets of rubber of definite thickness and width are prepared. The extruders are also used to place cords of fabric or steel onto the strips of rubber.

**Assembly:** The various semi-finished products are assembled on the rotating drum. The tire is constructed from the inside out into the pre-cured tire, also known as green tire. The green tire is sprayed with a special fluid to prepare it for the vulcanization process.

**Vulcanization:** The green tire is then placed in a mold where hot steam is used to vulcanize the tire at high temperature and pressure. After a certain length of time, the tire attains its final form and is ready for quality control.

At the end of the manufacturing process, the final product is inspected for defects.

## 1.2. Internal mixing

### 1.2.1. Banbury mixer

The origin of the internal mixer can be traced back to the early efforts of Hancock in 1820 [Hancock, 1857]. His invention, Hancock's pickle, was used to combine strips of rubber in a solution of turpentine, pitch and tar. It is composed of a single cylindrical rotor in a hollow cylindrical chamber with pins on both surfaces. During mixing, he observed that the natural rubber degraded mechano-chemically through the application of high stresses [Porritt and Rogers, 1924]. Roll mills were introduced by Chaffee [Chaffee, 1836] for the mastication and compounding of rubber. They consist of two cylinders moving in opposite directions, similar to modern day calendars. Roll mills were the accepted method for mixing rubber until they were phased out by internal mixers in the 1920s [White, 1995].

In the 19<sup>th</sup> century, twin counter-rotor masticators were developed for crushing, grinding and pulverizing materials. These early 'internal mixers' were originally used in the food processing industry. The rotor design of these masticators was two-dimensional suggesting 2D motion of the materials in the masticator. The first use of intermeshing rotors was recorded in Barden-Crudden's rotary churn (figure 1.5) [Barden and Crudden, 1875]. However, the rotors of such masticators were damaged when highly viscous materials were used [Pfleiderer, 1882]. Pfleiderer's 'kneading and mixing machine's improved on the design of the rotor design to overcome this inconvenience. The improvement of the rotor design imposes a clear three-dimensional flow of the material due to the pumping action of the rotors.

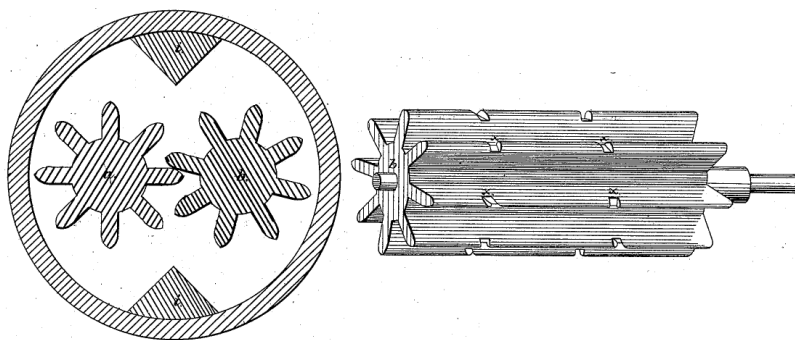


**Figure 1.5** – Intermeshing rotors used in Barden and Crudden's Rotary churn to produce butter [Barden and Crudden, 1875].

With improvements in rubber technology, the rubber compounds used in pneumatic tires became more complex. Large quantities of fine and toxic particles were used in the rubber compounds, making the use of roll mills impractical [Killeffer, 1962]. The fine particles were blown away during mixing due to the lack of an enclosing chamber. These particles in turn endangered the lives of the operators due to their toxicity.

The improved design of the Banbury mixer [Banbury, 1916] eventually made roll mills obsolete. The most remarkable innovations of this machine include the use of double flighted non-intermeshing rotors and the introduction of a ram to hold down the rubber during mixing and seal the mixing chamber. Today, roll mills and continuous mixers are also used to mix rubber compounds. Nevertheless, internal mixing is the most widely used mode of mixing rubber compounds due to the versatility and subsequent improvements of the Banbury mixer. The different parts of a modern-day Banbury mixer are depicted in Figure 1.6.

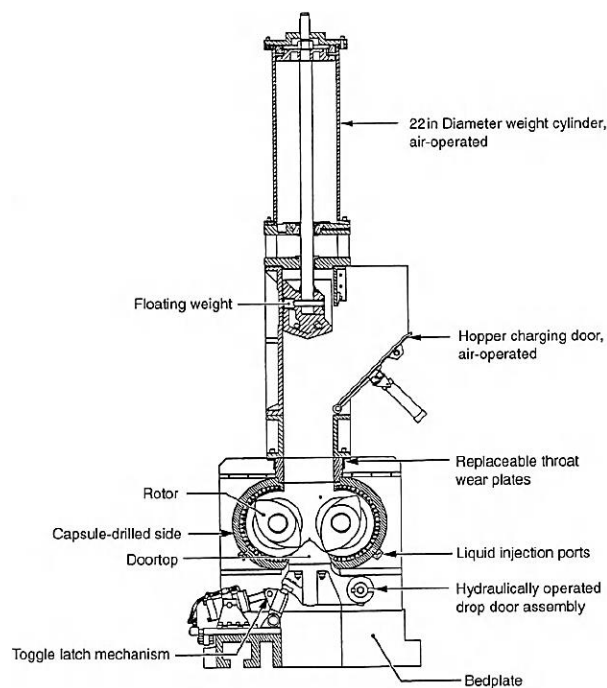


**Figure 1.6** – Parts of a modern-day Banbury mixer [Grossman, 1997].

In a Banbury mixer, the different ingredients are introduced into the mixing chamber through a hopper. The rotors are non-interlocking and rotate at a slight speed differential. Before the beginning of the mixing cycle, the ram is brought down and a pressure is exerted to ensure that the mixing chamber is sealed during mixing. The chamber and the rotor walls are heated through the transfer of a heat transfer fluid. Coolants are used to regulate the temperature of the walls during the mixing process. During mixing, the rotor design ensures that the rubber compound is constantly displaced ensuring that the rubber compound undergoes continuous pressure shear and tear. At the end of the cycle, the material is discharged through the bottom of the mixing chamber. The efficiency of the mixing process is determined by the control of the volume of the batch, sequence of addition of the ingredients, ram pressure, rotor speed, mixing time, temperature and power [Limper, 2012].

Following the invention of the Banbury mixer, Banbury improved the machine design to facilitate the mode of addition of ingredients, cooling of the mixing chamber and the removal of the mixed product. Over the years, many improvements were made to the auxiliary parts and systems (feeding hopper, mixing chamber, temperature control, digital sensors, etc) of the mixer. However, the main focus of research was on the rotor design. In an internal mixer, the rotors have three functions:

- impart shear and elongation to the compound (dispersive mixing),
- distribute ingredients inside the compound (distributive mixing),

- provide high stress and strain to the compound (laminar mixing).

The quality of the mixed product is determined by the quality of these three mixing mechanisms and the processing parameters. The required quality of these mixing mechanisms varies for each rubber product based on their formulation. The quality of mixing is determined by the rotor design and the control of the mixing parameters. Figure 1.7 shows how the rotor wings permit the rubber compound to undergo the three mixing mechanisms. Tangential and intermeshing rotors provide different qualities of mixing [Moribe, 2012] and hence the choice of the type of rotor is crucial. The features of the rotor wings are also tailored to the requirements of the user. The rotor features which influence the quality of mixing are:

- number,
- position,
- length,
- angularity,
- outline,
- tip width.



**Figure 1.7** – Flow paths within the internal mixing due to rotor wing design providing distributive, dispersive and laminar mixing [Limper, 2012].

The central focus of research on the internal mixer was on the improvement of the rotor design. Besides this area of focus, numerous research works were carried out on the influence of the mixing parameters on the efficiency of the mixing cycle. Studies were conducted on the influence of processing parameters on the efficiency of dispersive [Mathews and Haslam, 1932; Jones and Snyder, 1951] and distributive mixing [Griffith *et al.*, 1987]. General reviews [Palmgren, 1975; Funt, 1977; Johnson, 1982] summarizing the role of the processing parameters on the quality of mixing have been published. New rubber formulations are developed every day and studies to determine the right processing parameters are still required today [Narongthong *et al.*, 2018].

### 1.2.2. Flow visualizations with internal mixers

In the second half of the 20<sup>th</sup> century, techniques were being developed to understand the mixing process through ‘visualization’. These techniques were majorly carried out on three axes: static observations, visualization with sensors and flow visualization.

Static observations were carried out by visually examining the product after stopping the internal mixer [Dizon and Papazian, 1977; Boonstra and Medalia, 1963]. Such observations helped ascertain the mixing quality. This type of static flow observations could be conducted with optical microscopes, electron microscopes and electrical conductivity experiments [Lee *et al.*, 1989]. The observation of the compounds after mixing helped understand the flow patterns during mixing and how the rotor dimensions encourage the different mixing mechanisms [Griffith *et al.*, 1987; Kim *et al.*, 1989].

Dynamic flow visualizations with sensors were first carried out by Zakharin *et al.*, [Zakharkin *et al.*, 1966]. They used four dynamometers to measure the normal stress during compounding. Sensors are still used today in internal mixers as a means to control the process. Up until the mid-1970s, ‘visualization’ techniques relied on instruments for monitoring temperature, torque and energy input.

The first direct flow or *in-situ* observations of the internal mixing process were carried out by Freakley and Wan Idris [Freakley and Wan Idris, 1979]. They proposed a more direct method of visualizing the flow process with the use of a lab scale internal mixer fitted with transparent windows. A silicon gum with pigments was mixed in a lab scale Brabender mixer. The stretched eddy patterns observed during the mixing indicated a strong distributive mixing which was attributed to the large wing of the cam rotor. In an effort to find optimal rotor design, Asai *et al.* [Asai *et al.*, 1982] used adjustable rotors to find optimum mixing homogeneity. This study found that two-wing rotors were more effective in distributive mixing than the conventional four-wing rotor design.

Min and White [Min and White, 1985; Min and White, 1987; Min, 1987a; Min, 1987b] were the first to conduct *in-situ* flow observations with compounds representative of those used in industrial internal mixers. These observations showed the difference in flow behavior between the different elastomers (BR, NR and SBR). The experimental setup of the direct flow observations carried out by White *et al.*, [White *et al.*, 1986] is presented in Figure 1.8.

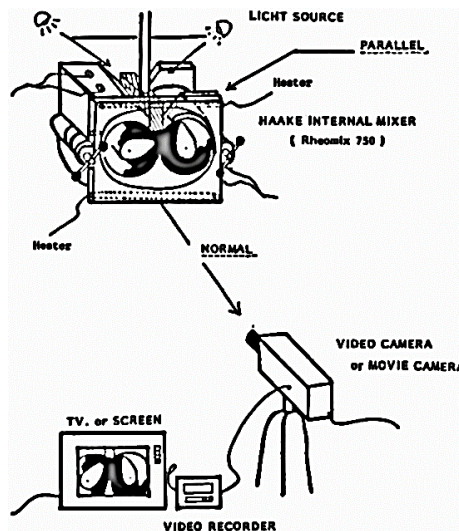


**Figure 1.8** – Experimental setup for direct flow observations of the internal mixing process [White *et al.*, 1986].

Min’s observations [Min *et al.*, 1987b] found that during internal mixing, the rubber compounds exhibited four regimes of mixing similar to those observed during mill mixing [Tokita and White; 1966; White and Tokita, 1968]. Initially, the rubber undergoes tearing and creates powdery fragments. The rubber undergoes stretching and tearing at the thin flow gap of the rotor. Subsequently, a soft layer of rubber adheres to the walls of the mixing chamber. Then the fluid is transferred from one chamber to the other providing distributive mixing.

The direct flow visualization technique highlights the role of the rotor design in mixing. One such example is illustrated in Figure 1.9. In the work of White *et al.* [White *et al.*, 1986], stagnation zones were reported in the mixer where the fluid was not effectively transported from one mixing chamber to the other. No stagnant regions were observed at different fill factors in the work of Freakley and Wan Idris [Freakley and Wan Idris, 1979]. This contrasting behavior during mixing is due to the difference in mixing geometry. These observations show the importance of rotor design and process parameters to the quality of mixing.

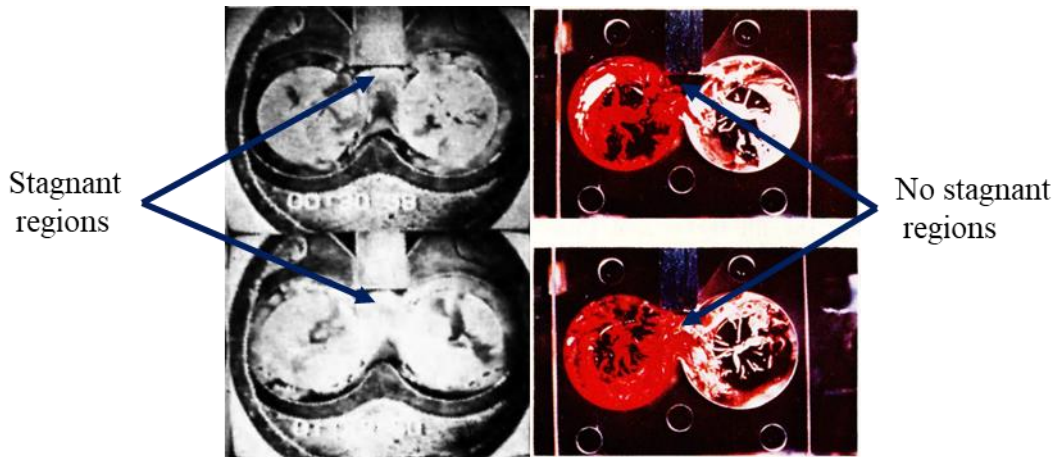


**Figure 1.9** – Direct flow observations of internal mixing [White *et al.*, 1986, Freakley and Wan Idris, 1979] at a fill factor of 0.7.

Later, Min [Min and White, 1987] also used a transparent window on the sides of the chamber wall permitting tangential flow visualization of the mixing process. This showed the accumulation of rubber on the front of the rotor wings while only a small amount was observed behind them (Figure 1.10). The incorporation mechanism of fillers was also studied with this setup. The differences in the incorporation mechanisms were found to be related to the types of materials, but independent of rotor designs. Direct visualization techniques can be used to study the influence of rotor designs, factory cycles [Morikawa *et al.*, 1989], blending of elastomers [Setusa and White, 1991], and blending during a crosslinking reaction [Tokita and White; 1966].

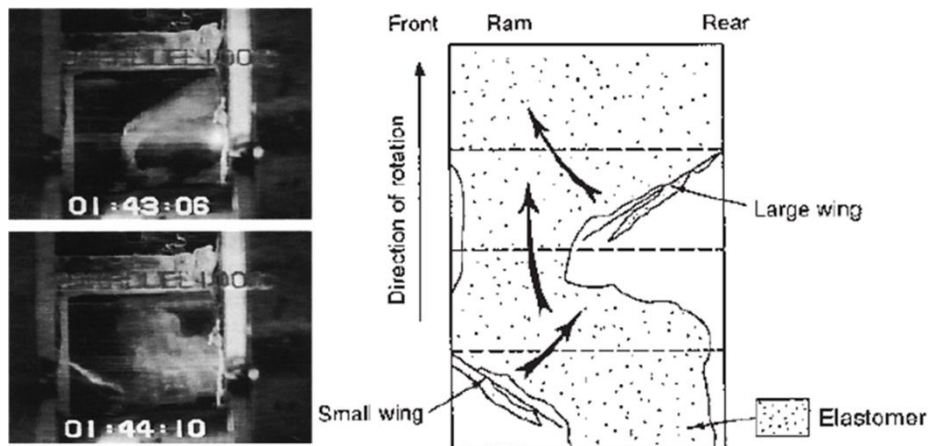


**Figure 1.10** – Transverse flow observations of internal mixing [Min and White, 1987].

Direct flow observations of the internal mixing process have led to numerous improvements of the mixing process. However, the complex 3D flow profile during mixing makes it difficult to focus the flow observations at the interface. Moreover, it is still difficult to observe distributive mixing efficiency near the thin flow gap as well as the quantification of the dispersive and distributive mixing [Manas- Zloczower, 2009]. More sophisticated flow visualization techniques or improved mixer geometries are required to characterize these phenomena.

### 1.2.3. Modelling the flow behavior in an internal mixer

The first efforts to model the flow behavior in an internal mixer [Prager and Talbot, 1959] were carried out on simple single rotor mixers using Reynold's hydrodynamic lubrication theory [Reynolds, 1886]. They considered a Newtonian flow in a completely filled chamber and defined a moving co-ordinate system which was embedded in the walls of the mixing chamber. Bolen and Cowell [Bolen and Colwell, 1958] improved on this model by orienting the concern on the breakup of

agglomerates by taking into account the non-Newtonian shear viscosity and viscous dissipation heating. The modelling of the flow behavior in an internal mixer remains an open topic of research today.

With the advent of cheaper and more robust computers in the early 90's, finite element methods (FEM) were used to simulate the flow behavior in Banbury mixers [Cheng and Manas-Zloczower, 1989; Yagii and Kawanishi, 1990; Nassehi and Freakley, 1991]. Initially, these simulations were carried out on one rotor or half the mixing chamber at completely filled conditions. In an effort to simulate a partially filled internal mixer, Kim and White [Kim and White, 1989] used fractional flow factors. Osswald and co-workers [Gramann *et al.*, 1992; Hutchinson *et al.*, 1999] used the Boundary element method (BEM) rather than FEM to model the flow of particles in a 2D model. This resulted in the evaluation of a dispersive mixing index to determine the efficiency of distributive mixing. Two-dimensional velocity and pressure fields were generated for the flow in the mixing chamber showing a high concentration of shear stress and shear rate at the rotor tips and low values elsewhere in the mixer.

Simulations of the mixing process improved dramatically with the increasing understanding of the mixing process and development of new simulation techniques. Effective predictions of the three-dimensional flow behavior during internal mixing can be obtained today with the aid of modern simulation techniques [Das, 2016] (Figure 1.11). Numerical simulations of the mixing process were not limited to internal mixers. Efforts were also made to simulate the mixing behavior in static and continuous mixers also [Dubois *et al.*, 1996; Mickaily-Huber *et al.*, 1996; Fradette *et al.*, 2006; Rathod and Kokini, 2013; Vyakarnam *et al.*, 2012; Zhu *et al.*, 2014; Valette, 2009]

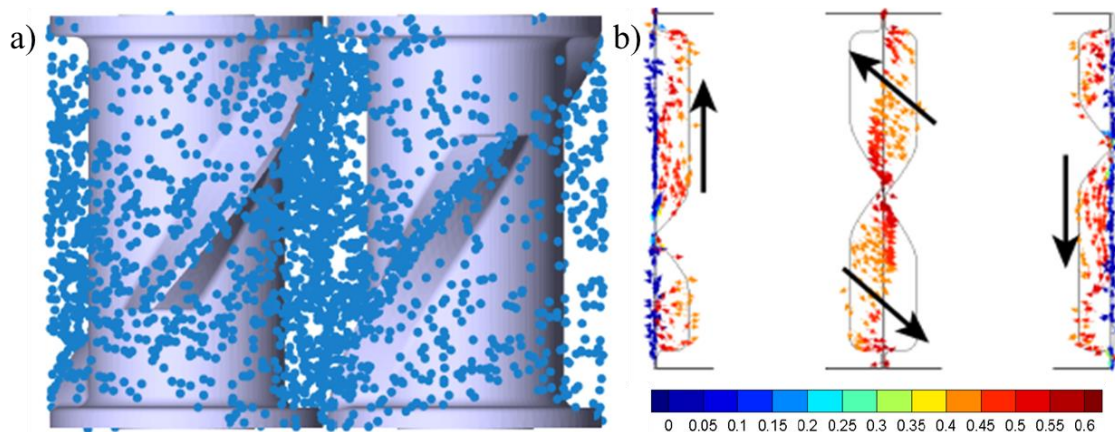


**Figure 1.11** – a) Particle distribution and b) Instantaneous velocity vectors in a Banbury mixer [Das, 2016].

Manas-Zloczower and co-workers analyzed the mixing performance of dispersive and distributive mixing efficiency [Yang and Manas-Zloczower, 1994; Yao and Manas-Zloczower, 1997; Yao *et al.*, 1998] and compared the simulation results against the experimental data. Similarly, Salahudeen *et al.* [Salahudeen *et al.*, 2013] obtained 3D flow fields of the mixing process and conducted distribution studies by correlating the visual observations (Figure 1.12) with the simulation results. These simulations were carried out with intermeshing rotors as well as with different rotor designs.

An important point of critique of these simulations was the lack of incorporation of interfacial phenomena. The first efforts to incorporate these phenomena were carried out by Malkin *et al.* [Malkin *et al.*, 1995] and Nassehi and Ghoreishy [Nassehi and Ghoreishy; 1997]. Nassehi and Ghoreishy used a Volume of Fluid (VOF) model in a Eulerian framework to track the free surfaces of the fluid. Malkin *et al.* modelled the non-isothermal flow of a rubber mixture between the rotor blade and the mixer with the possibility of wall slip boundary condition. These remain the first efforts of integrating interfacial flow behavior in internal mixer simulations.

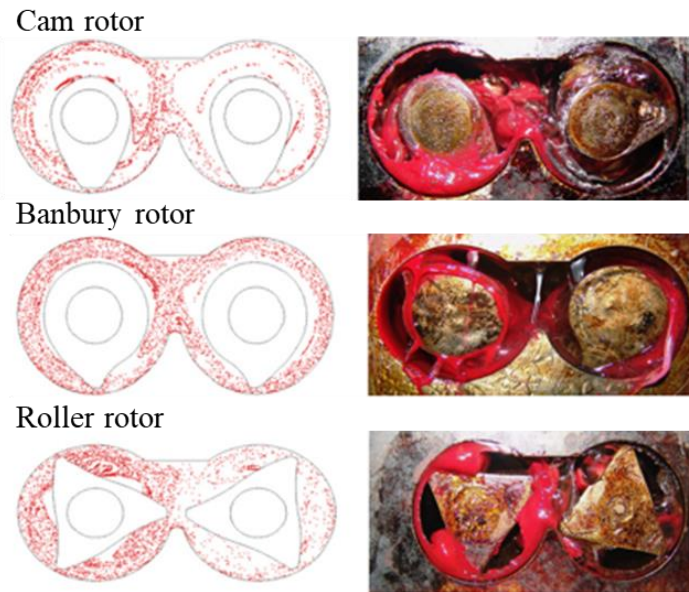


**Figure 1.12** – Simulation of distributive mixing in an internal mixer correlated with static flow observations [Salahudeen *et al.*, 2013].

The quality of the simulation results has improved significantly over the past decade [Das, 2016; Salahudeen *et al.*, 2013; Dhakal *et al.*, 2016; Ahmed *et al.*, 2019; Chen *et al.*, 2017; Liu *et al.*, 2015] provided good predictions of the mixing behavior. Figure 1.13 shows the simulated distribution of rubber in an internal mixer with a no-slip boundary condition [Liu *et al.*, 2015]. However, wall slip is known to affect the local flow rates and hence can impact the form of the free surfaces. Thus, the simulation of the mixing process can be greatly improved by the incorporation of interfacial flow behavior such as wall slip, adhesion/fracture mechanics and the movement of free surfaces.

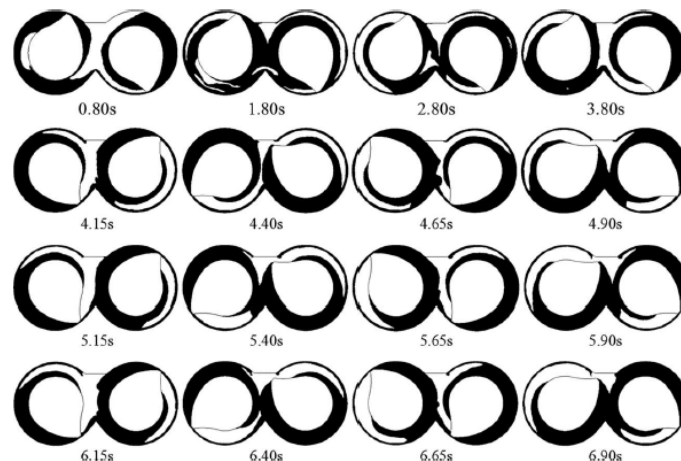


**Figure 1.13** – Distribution of rubber at different intervals of time [Liu *et al.*, 2015].

During shear flow in the mixer, the rubber compound flows along the walls of the mixer which may result in wall slip at the walls of the mixer at shear rates above a critical value ( $\sigma_w$ ) [Hatzikiriakos, 2010]. In addition, adhesion also comes into play as the compound flows along these walls. The free surface is the interface between two homogenous fluids (rubber compound and air in this case). This surface is subject to zero parallel shear stress [Lundgren and Koumoutsakos, 1999]. The movement of this surface is essential to accurately predict the distribution of the compound during mixing. Figure 1.14 shows the manifestation of these phenomena in an internal mixer. As mentioned earlier, interfacial phenomena such as wall slip, free surface movement and adhesion are often neglected during the numerical simulation of the internal mixing process. Sections 1.3, 1.4 and 1.5 are dedicated to a brief literature survey on wall slip, movement of contact lines and adhesion.

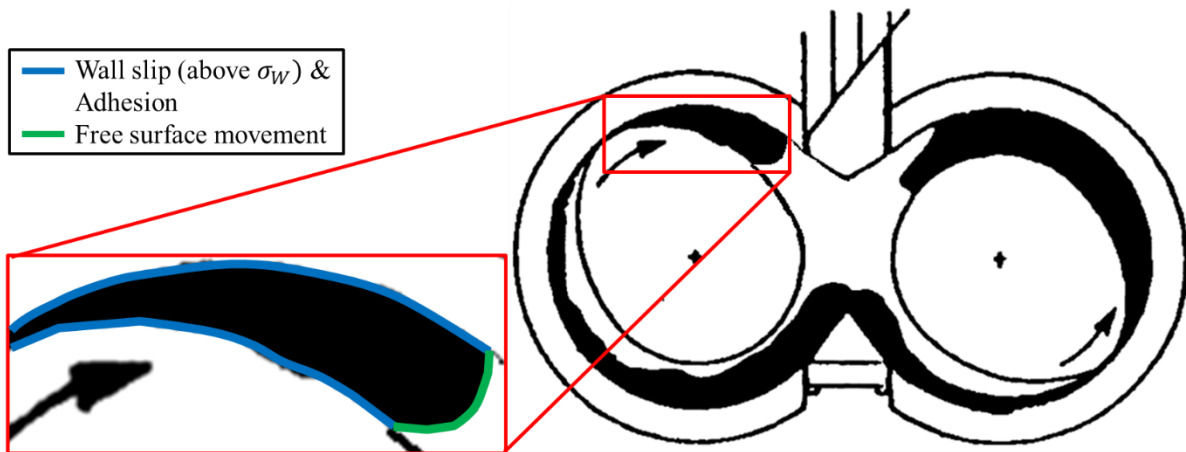


Figure 1.14 – Interfacial phenomena during shear flow in an internal mixer [Cheremisinoff, 2001].

### 1.3. Wall slip and flow regimes

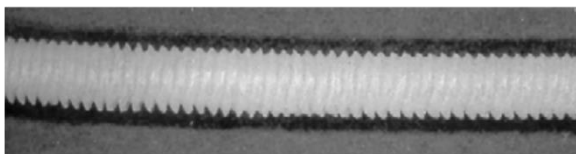
#### 1.3.1. Wall slip in polymers

During industrial processing of polymer materials, the quality of the product is highly sensitive to the flow characteristics, especially at the interface. High molecular weight polymers could exhibit a non-zero flow velocity boundary condition at the interface due to their viscoelastic properties. Alternatively, flow instabilities can occur in extrusion or capillary flow in viscoelastic materials. The characterization of these instabilities is essential as they have been related to the onset of wall slip [Ramamurthy, 1986; Piau *et al.*, 1990]. Yet other researchers [Piau *et al.*, 1990; den Otter, 1970 and 1971] showed that the apparition of a defect and wall slip are not always analogous.

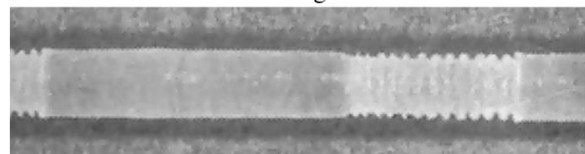
The nature of flow instabilities depends on the nature of the polymer (chemical nature, molecular characteristics, molecular distribution and branch length), presence of some additives, geometry of flow (capillary length, diameter, converging angle and ratio) and operating conditions (temperature, shear rate and pressure). Figure 1.15 presents the extrusion defects encountered during shear flow in polymers. The sharkskin defect consists of repeated cracks on the surface of the extrudate similar to a 'sharkskin'. The oscillating defect appears as a succession of smooth and sharkskin morphologies. The helical defect is a regular defect affecting the entire volume of the extrudate. On the other hand, the chaotic defect is an irregular volume defect.

Surface defects

Sharkskin defect

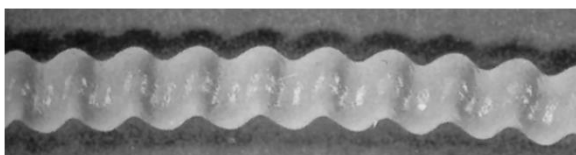


Oscillating defect



Volume defects

Helical defect



Chaotic defect

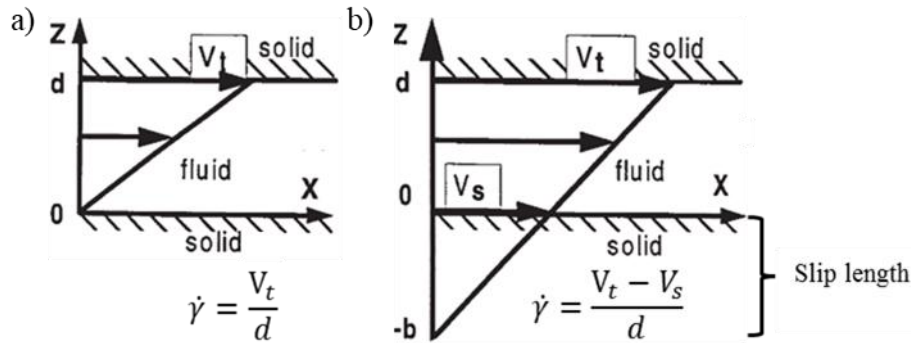


Figure 1.15 – Different types of extrusion defects [Agassant *et al.*, 2014].

On studying the flow extrudates of polyethylene, den Otter [den Otter, 1971] found that low density and high density polyethylene exhibited different behaviors in terms of the onset of flow instabilities. This can be explained by the difference in the branching of the polymer chains between the two

polymers. With increasing shear rates, linear polymers typically exhibit sharkskin, oscillating and chaotic instabilities whereas branched polymers exhibit helical and chaotic instabilities [Vergnes, 2015]. This classification is a simplification and polymers can switch behaviors depending on their polydispersity and molecular weight.

When wall slip occurs, the boundary condition of no-slip is violated and the tangential velocity at the wall is non-zero ( $V_s$ ). It can be assumed that the tangential velocity is zero not at the wall but at a certain length 'b' which can be defined as the slip length (Figure 1.16).



**Figure 1.16** – Velocity field under simple shear with a) no wall slip condition and b) wall slip condition [Léger and Hervet, 2006].

From the Figure 1.16, the slip length can be given by:

$$b = \frac{V_s}{\dot{\gamma}} = \frac{V_s}{V_t - V_s} d \quad \text{Equation 1.1}$$

Hervet and Léger [Hervet and Léger, 2003] studied the evolution of slip length with wall slip velocities. Surface chains were grafted on the top plate, allowing entanglements with bulk chains, so that no slip is possible. On the other hand, wall slip was possible on the lower plate due to the lack of grafted chains. Three different slip regimes were identified on plotting the slip length in function of wall slip velocity ( $V_s$ ) (Figure 1.17). These slip regimes can be summarized as:

- i) At low shear rates, the slip length is independent of the slip velocity.
- ii) Above a critical slip velocity,  $V^*$ , the slip length increases exponentially following a power law  $b \sim V_s^\alpha$ .
- iii) At higher shear rates, a linear relation between slip length and slip velocity can be observed.

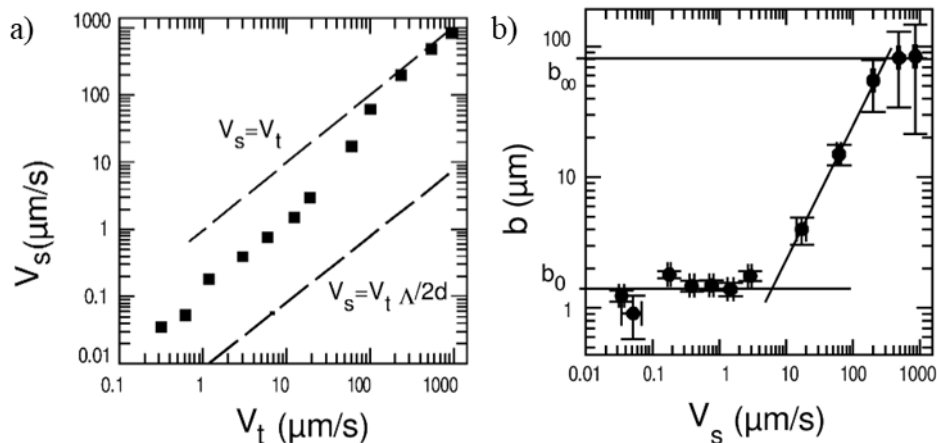


**Figure 1.17** – a) Slip velocity and b) slip length in function of the tangential velocity of a PDMS, flowing against a silica surface covered with end grafted PDMS chains [Hérvet and Léger, 2003].

Brochard-Wyart and de Gennes developed a molecular model describing how polymer entanglements and grafting on a solid surface can affect the boundary condition for the velocity at the polymer–solid interface [Brochard-Wyart and de Gennes, 1992]. This model provides a good explanation of the previously described slip regimes.

**Regime i):** They hypothesized that polymer entanglements with the polymer chains grafted to the surface act as obstacles to the flow of the bulk chains. They can produce a large friction between the dragged chains and the grafted chains at low shear rates. Under the effect of friction, the grafted chains can deform and an elastic restoring force develops. In steady state, the elastic and friction forces balance each other. In this regime, the slip length is small and independent of the slip velocity.

**Regime ii):** Under large deformations, the grafted chains become large enough that they disentangle from the bulk chains. In this regime, the friction force decreases strongly with slip velocity and the grafted chains re-entangle. The shear force is fixed and independent of the slip velocity while the frictional coefficient ( $k$ ) is inversely proportional to the slip velocity. Thus, the slip length ( $b \sim 1/k$ ) increases exponentially with the slip velocity.

**Regime iii):** Once the loading frequency is further increased, grafted chains do not have time to re-entangle and the friction becomes small and independent of slip velocity. This gives us the third regime of wall slip where the slip length depends linearly on the wall slip velocities.

### 1.3.2. Wall slip characterization techniques

The classical method to characterize wall slip is through rheological measurements. This can be achieved by the measurement of the pressure drop as a function of flow rate for different flow geometries in capillary rheometers [El Kissi and Piau, 1990; Kalika and Denn, 1987; Denn, 2001] or as a function of the thickness of the liquid in rotational rheometers [Hatzikiriakos and Delay, 1991]. More recent studies use velocimetry techniques [Atwood and Schowalter, 1989] or the direct measurement of the local velocity near the walls (100nm) [Léger *et al.*, 1994]. These investigations show that the onset of wall slip depends on the nature of the polymer and the wall surface. In this section, the Mooney and Shear Rate Difference methods are presented while other techniques are mentioned.

#### Mooney method

One of the essential hypotheses of capillary rheometry is the lack of slip at the walls during flow. This can be contravened in certain flow conditions due to the polymer’s behavior. Mooney [Mooney, 1931] was the first to observe slip in capillary rheometry and established a method to demonstrate the phenomenon of wall slippage. He devised a method to characterize wall slip velocities which is by far the most widely used method today. Mooney hypothesized that shear stress ( $\sigma_w$ ) is the unique motor of the phenomenon of slip. When the slip velocity ( $V_s$ ) is only dependent on the shear stress ( $\sigma_w$ ), the flow rate ( $Q_{total}$ ) is a function of two components (Figure 1.18): one related to the shear stress ( $Q_{shear}$ ) and another component related to the slip ( $Q_{slip}$ ).

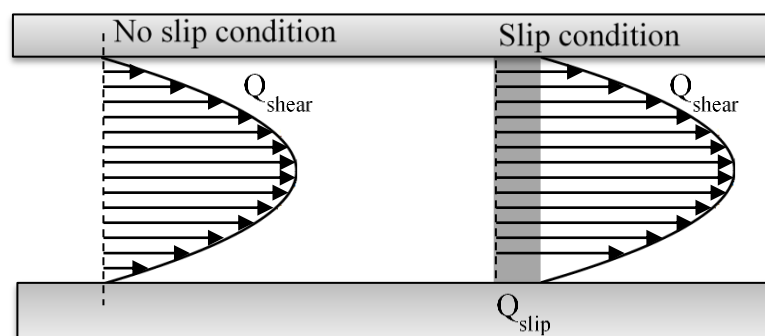


Figure 1.18 – Flow in no slip and slip conditions at the same shear stress.

This definition gives us:

$$Q_{total} = Q_{shear} + Q_{slip} \quad \text{Equation 1.2}$$

If the fluid adheres perfectly to the walls, the geometry of the capillary must not impact the shear stress developed for a given shear rate. Thus, for a given shear rate, the wall shear stress developed for capillary dies of different diameters must be the same. When plotting the wall shear stress in function of the wall shear rate for capillaries of different diameters (Figure 1.19), a master curve (superimposed curves) is obtained in the case of no-slip conditions. However, if the curves are not superimposed and numbered according to increasing diameters (Figure 1.20), we assume that it is due to wall slip.

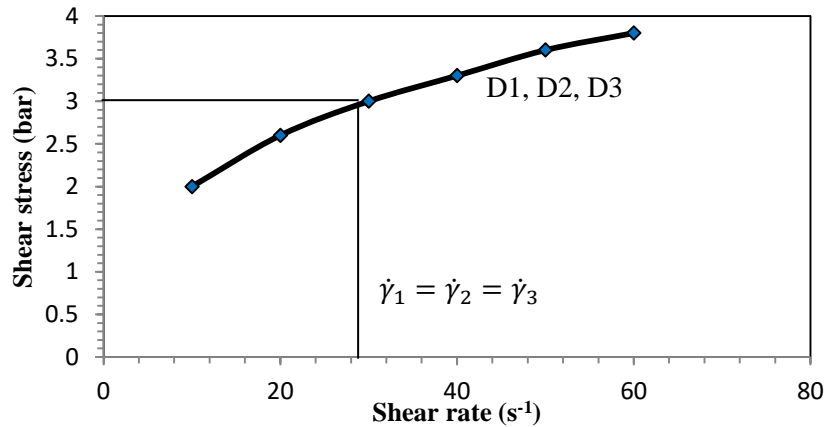


Figure 1.19 – Evidence of lack of slip according to Mooney.

From Equation 1.2, it can be deduced that:

$$\dot{\gamma}_a = \dot{\gamma}_{corrected} + 4V_s \frac{1}{R} \quad \text{Equation 1.3}$$

where  $\dot{\gamma}_a$  is the apparent shear rate, R is the radius of the capillary and  $\dot{\gamma}_{corrected}$  is the apparent shear rate corrected for wall slip.

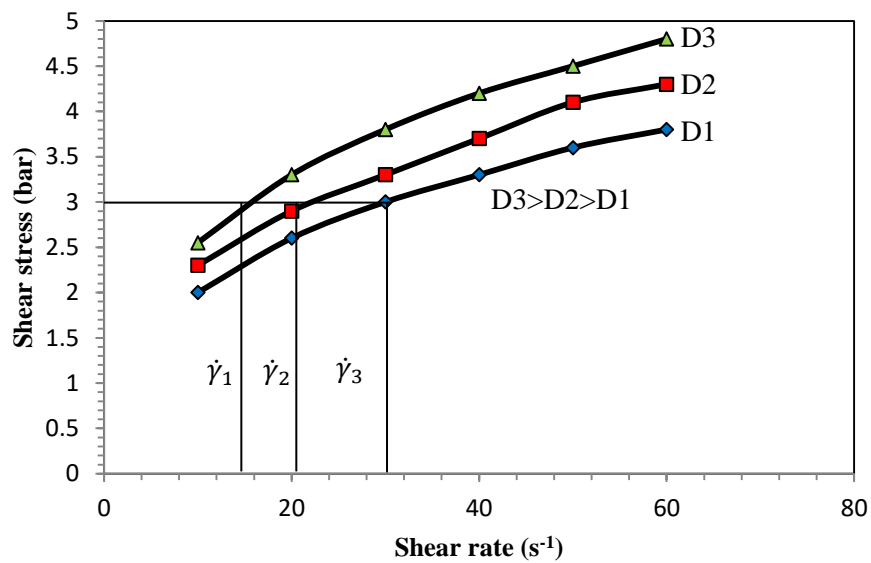


Figure 1.20 – Evidence of slip according to Mooney ( $\sigma_w$ ).

Equation 1.3 points out that the slip velocity can be obtained by plotting the apparent shear rate as a function of  $1/R$  for constant shear stress. Plotting these curves should give straight curves with a slope of four times the slip velocity ( $V_s$ ). As a consequence, we can obtain the slip velocities for different values of shear stresses ( $\sigma_w$ ). Extrapolating these curves should give a y-intercept which provides the value of  $\dot{\gamma}_{corrected}$  for the corresponding shear stress. Mooney's method to determine the slip velocities is presented in Figure 1.21.

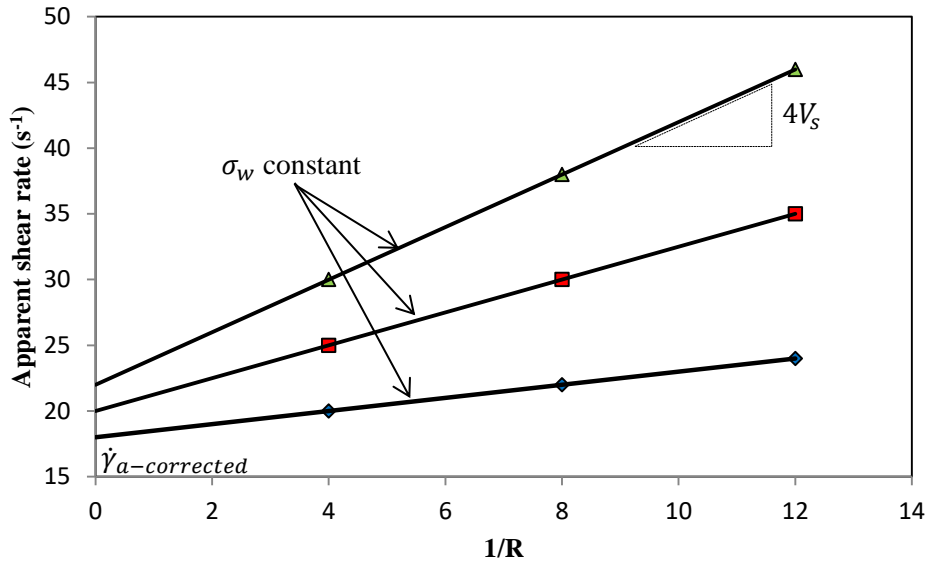


Figure 1.21 – Mooney's method to determine the slip velocities.

### Shear Rate Difference method

The Shear Rate Difference method is based on Mooney's hypothesis that the total flow rate is the sum of flow rate due to shear and wall slippage (Equation 1.2). This method can be applied when different flow regimes exist, characterized by a change in slope of the flow curves as shown in Figure 1.22. The flow curves experience a change in slope at a critical shear stress ( $\sigma_c$ ). This critical shear stress is defined as the stress above which the fluid experiences wall slip. Hence, the flow curve at shear stresses below the critical shear stress is considered to be slip free (Regime I) and at shear stresses above the critical shear stress is considered to be slip flow (Regime II).

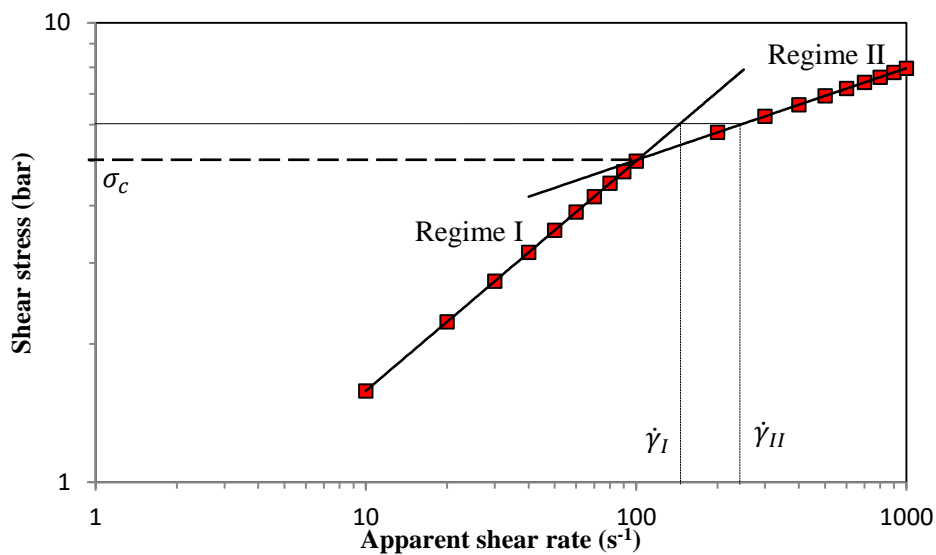


Figure 1.22 – Example of the Shear Rate Difference method.

Thus, for a constant shear stress, the difference in shear rate of the slip regime (Regime II) and slip free regime (Regime I) should give the slip velocity. One stark difference of the Shear Rate Difference method from the Mooney method is the dependence of wall slip velocities with the die geometry. The wall slip velocity obtained by the Shear Rate Difference method is given by:

$$\dot{\gamma}_{II} - \dot{\gamma}_I = 4 \frac{V_S}{R} \quad \text{Equation 1.4}$$

where  $\dot{\gamma}_I$ , and  $\dot{\gamma}_{II}$  are the shear rates of the flow regimes.

The trend lines of the two flow regimes are traced and extrapolated. Normally, the trend lines of these two flow regimes intersect only at the critical shear stress. For a given shear stress, the x-intercepts of the trend lines ( $\dot{\gamma}_I$  and  $\dot{\gamma}_{II}$ ) are determined and are used in Equation 1.4 to obtain the slip velocity.

### Other characterization techniques

The major inconvenient of the Mooney method is the attainment of straight curves and non-negative intercepts with the y-axis (Figure 1.21). As the Mooney method does not provide realistic results in some cases, alternative methods have been proposed by several authors [Wiegrefe, 1991; Mourniac *et al.*, 1992; Geiger, 1989; Karam, 1995]. These wall slip characterization techniques are briefly presented below:

**Geiger:** Geiger [Geiger, 1989] questioned the Mooney method and proposed that the wall slip velocity is a function of shear stress and the die geometry. With the help of a slit die rheometer, he expressed the wall slip velocity relation as:

$$V_S(\sigma_W, h) = h \cdot g(\sigma_W) \left[ \exp\left(\frac{f(\sigma_W)}{h}\right) - 1 \right] \quad \text{Equation 1.5}$$

where h is the thickness of the die and  $\sigma_W$  is the wall shear stress.

Thus, the plot of apparent shear rates ( $\dot{\gamma}_{app}$ ) in function of (1/h) for a given shear stress ( $\sigma_W$ ) will provide the wall slip velocities.

**Wiegrefe:** Wiegrefe [Wiegrefe, 1991] added on Mooney's hypothesis by suggesting, without evidence, that the wall slip velocities are inversely proportional to the radius of the die. Thus, the apparent shear rates ( $\dot{\gamma}_{app}$ ) are plotted in function of (1/R<sup>2</sup>) instead of (1/R), as was the case with the Mooney method. The slope of this curve provides  $4 \frac{V_S}{R}$ .

**Mourniac:** Mourniac *et al.* [Mourniac *et al.*, 1992] observed that the Mooney method (Equation 1.4) did not work for carbon black filled SBR compounds with a flat die rheometer. He found that that the wall slip was not only a function of the shear stress but also of the local geometry (gap or diameter of the die). Again, Mooney's hypothesis of total flow rate (Equation 1.2) was used to obtain the relation for the wall slip velocities. The wall slip velocities for a power law fluid are given by:

$$V_S = R \left( \frac{m_{app}}{3m_{app} + 1} \left( \frac{\sigma_W}{K_{app}} \right)^{\frac{1}{m_{app}}} - \frac{m}{3m + 1} \left( \frac{\sigma_W}{K} \right)^{\frac{1}{m}} \right) \quad \text{Equation 1.6}$$

where  $V_S$  is the wall slip velocity, R is the radius of the die,  $m_{app}$  and  $K_{app}$  are the apparent pseudoplastic index and consistence while m is the actual pseudoplastic index.

### 1.3.3. Thermodependency of wall slip velocities

The influence of temperature (T) on wall slip can be quantified with the relation of slip length (b) and temperature (Equation 1.7) [Hénot *et al.*, 2018]. However, the wall slip length is often neglected during numerical simulations.

$$b \sim \exp\left(\frac{E_{Visc} - E_{Friction}}{RT}\right) \quad \text{Equation 1.7}$$

where R is the gas constant,  $E_{Visc}$  and  $E_{Friction}$  are the activation energies of the molecular process taking place in the bulk and at the interface.

In order to simulate the local flow field at the interface, a relation between the temperature and the evolution of wall slip velocities is required. For the purposes of numerical simulation, such laws have been defined [ANSYS, 2017]. Though, these relations do not hold any physical significance. Researchers [Hatzikiriakos and Dealy, 1991; Karam *et al.*, 1998; Turner and Moore, 1980] have studied the influence of temperature on wall slip velocities. In general, higher wall slip velocities were encountered at higher temperatures. However, these researchers were not able to define a relation between wall slip velocities and temperature. Figure 1.23 presents the evolution of wall slip velocities at different temperatures.

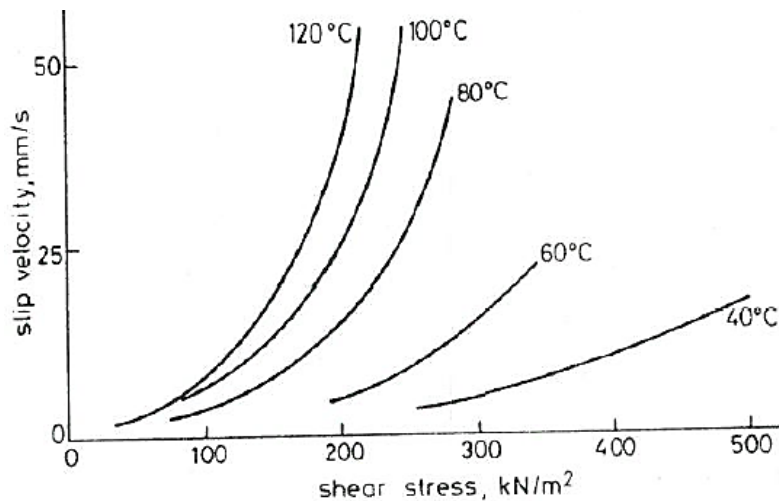
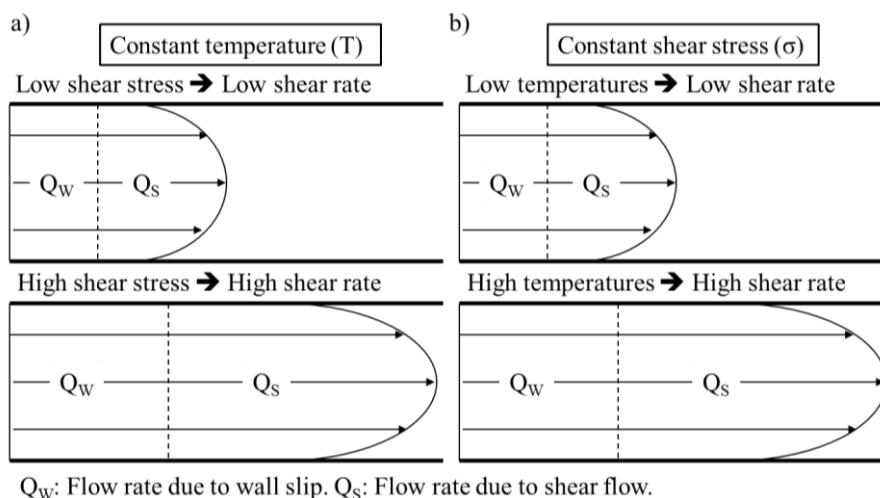


**Figure 1.23** – Effect of temperature and shear stress on wall slip with a formulated EPDM [Turner and Moore, 1980].



$Q_w$ : Flow rate due to wall slip.  $Q_s$ : Flow rate due to shear flow.

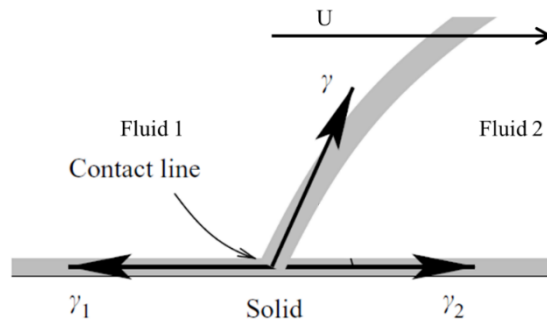
**Figure 1.24** – a) Interpretation of wall slip with shear stress [Dimier *et al.*, 2002] and b) interpretation of wall slip with temperature.

Figure 1.24 (above) shows the interpretation of wall slip with shear stress and temperature. Dimier *et al.* [Dimier *et al.*, 2002] illustrated (Figure 1.24a) that at a constant temperature, wall slip velocities increase with shear stress. At high shear rates, the flow rate due to wall slip ( $Q_w$ ) and shear flow ( $Q_s$ ) increase simultaneously. On the other hand; the increase in wall slip velocities with temperature can be attributed to the increased mobility of the polymer chains. At lower temperatures, the polymer chains are more rigid. They resist the flow better at low temperatures than at higher temperatures. At higher temperatures, the polymer chains are more mobile which gives us higher shear rates and thus increased wall slip velocities (Figure 1.24b).

## 1.4. Movement of contact lines/free surfaces

### 1.4.1. Contact line dynamics

The displacement of one fluid by another fluid over a solid surface results in the movement of the three-phase contact line i.e., interfacial line separating the solid surface and the two immiscible fluids (Figure 1.25). In the case of simple fluids, the fluid near the solid is considered to not move nor slip relative to the solid surface [Dryden *et al.*, 1956]. The movement of the contact line violates this hypothesis. The understanding of the contact line dynamics is crucial to industrial applications such as coating, contact dispensing, inkjet printing, spray cooling, and the application of agrochemicals [Zhang and Ren, 2016].



**Figure 1.25** – Moving contact line formed between the displacement of two fluids across a solid surface [Zheng and Ren, 2016].

In static systems, the ability of the fluid to wet the surface (wettability) is determined by the molecular forces of surface tension. The equilibrium shape of the meniscus is determined by the surface tension, and the capillary length ( $l_c = \sqrt{\frac{\gamma}{\rho g}}$ ). The equilibrium contact angle,  $\theta$  (Figure 1.26), is given by Young's law [Young, 1805].

$$\cos \theta = \frac{\gamma_{SV} - \gamma_{SL}}{\gamma} \quad \text{Equation 1.8}$$

where  $\gamma_{SV}$ ,  $\gamma_{SL}$  and  $\gamma$  is the surface tension between the solid-vapor interface, solid-liquid interface and liquid-gas interface respectively.

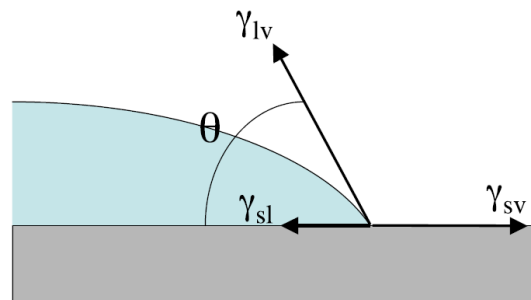


**Figure 1.26** – Determination of the equilibrium angle ( $\theta$ ) [Bonn *et al.*, 2009].

The first experimental observations of the flow near dynamic contact lines were conducted by West [West, 1911] and Yarnold [Yarnold, 1938]. They studied the resistance to motion of an isolated mercury index in an air-filled capillary tube. A pressure difference was applied across the capillary tube. Yarnold argued that the fluid must undergo a rolling flow similar to a ‘fountain’. Such a flow was later observed by Schwartz *et al.* [Schwartz *et al.*, 1964] with the use of tracers.

When the contact line moves (velocity,  $U$ ) with respect to the substrate, the system is no longer in equilibrium. The stress experienced by the fluid near the interface is proportional to the local velocity gradient. This leads to a viscous stress ( $\eta U/r$ ) where  $\eta$  is the dynamic viscosity and  $r$  is the distance from the contact line. As we approach the three-phase contact line (gas/liquid/metal) at  $r = 0$ , the viscous stress tends towards infinity resulting in a non-physical singularity [Huh and Scriven, 1971]. This problem was analytically solved by Huh and Scriven using similarity solutions and no-slip boundary condition. To resolve the dynamic singularity, many mechanisms have been proposed such as mesoscopic precursor film, molecular film, Navier slip, nonlinear slip, surface roughness, shear thinning, diffuse interface, normal stresses, evaporation and condensation [Bonn *et al.*, 2009].

The viscosity induced pressure at the three-phase line results in a strong curvature of the contact line [Dussan 1979]. The dimensionless Capillary number,  $Ca$ , is used to describe the balance between the viscous and capillary forces.

$$Ca = \frac{U\eta}{\gamma} \quad \text{Equation 1.9}$$

The capillary number of viscous fluids indicates that the thermodynamic forces of adhesion cannot influence the movement of the contact lines. In the case of polymers, the energy required to move the three-phase line is greater by an order of  $10^3$  to  $10^4$  than the thermodynamic work of adhesion due to its surface tension. For viscous fluids, the loss of contact from the substrate can occur by other mechanisms like the propagation of a crack along the interface or the extensive deformation in the bulk volume of the fluid. Strong dissipative mechanism can act on the bulk volume even in cases of localised fracture. Thus, the understanding of the fracture mechanics of polymers is crucial to tackle the problem of moving contact lines

### 1.4.2. Fracture mechanics in viscoelastic fluids

One of the unique features of fracture mechanisms in polymers is the rate of fracture propagation. To study this phenomenon, Inglis [Inglis, 1913] studied the propagation of fractures in a thin plate with an elliptical hole (Figure 1.27).

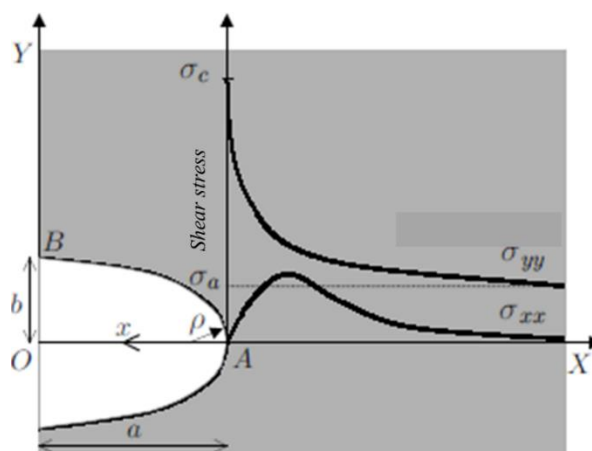


Figure 1.27 – Qualitative evolution of shear stresses along the OX axis during Inglis’s experiments [Inglis, 1913].

When a perpendicular shear stress ( $\sigma_a$ ) is applied, he noticed the concentration of local shear stress at the extremity of the hole (A). From Figure 1.27, we can see that the shear stress attains a maximum value at the extremity ( $\sigma_c$ ) and it diminishes towards the applied shear stress ( $\sigma_a$ ) towards infinity. The transverse shear stress reaches a maximum value slightly above  $\sigma_a$  and diminishes to zero at infinity. This amplification ( $K_t$ ) at the local region, is given by:

$$K_t = \frac{\sigma_c}{\sigma_a} = 1 + \frac{2a}{b} \quad \text{Equation 1.10}$$

where a and b are the short and long axes of the ellipse respectively.

The factor of amplification ( $K_t$ ) was highly dependent of the geometry of the crack, specifically the length of the fracture and the local curvature at the extremity. The factor also depends on the crosslinking ratio and the degree of entanglements in the polymer. The mode of the application of pressure is also an important factor which comes into play.

Three modes of fractures can be distinguished based on the mode of pressure [Rice, 1968] (Figure 1.28). The mode I corresponds to the most common mode where the separation occurs in the normal direction of the surface, mode II corresponds to a longitudinal propagation and mode III is the parallel shear of the fracture. In some cases, more than one mode of pressure can take place.

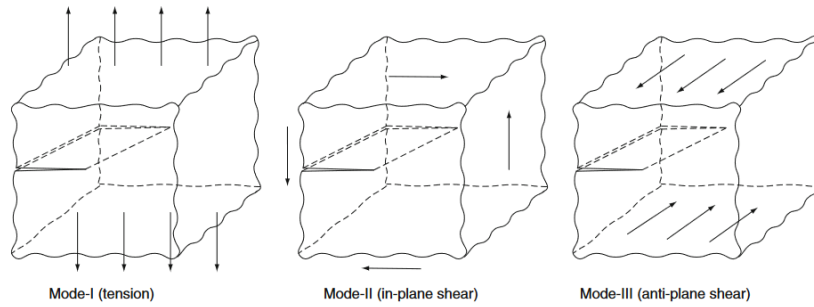


Figure 1.28 – Three modes of fracture [Wang and Chung, 2013].

Inglis's work explained the localization of stress at the extremities of the fracture. However, it does not explain the phenomenon of larger fractures propagating faster than smaller fractures, which seems to be in violation with the dependence of the amplification factor ( $K_t$ ) and the ratio of a/b (Equation 1.10). To resolve this contradiction, Griffith [Griffith, 1920] proposed a fracture mechanics theory based on an energy criterium. He considered a static fracture as a reversible thermodynamic system. A fracture can propagate only if it liberates more energy than it absorbs. The critical energy required to propagate the fracture is given by:

$$\delta W \geq \delta U_e + \delta T \quad \text{Equation 1.11}$$

where  $\delta W$  represents the work of external forces,  $\delta U_e$  is the variation of the elastic energy due to the extending crack and  $\delta T$  is the energy necessary to increase the free surfaces of the crack.

Griffith defined the critical shear stress ( $\sigma_c$ ) above which the crack propagates. The critical shear stress for the propagation of a crack to provide an extension of  $\delta a$  is expressed as:

$$\sigma_c = \sqrt{\frac{2E'\gamma_s}{\pi a}} \quad \text{Equation 1.12}$$

where  $E'$  is the young's modulus in the shear plane and  $\gamma_s$  is the surface tension of the substrate.

Griffith [Griffith, 1924] obtained the relation  $\sigma_c \sqrt{a} = 0.26 \text{ MPa.m}^{1/2}$  while studying fracture dynamics with glass. Modern techniques used to estimate the surface energies show that this relation was a good prediction. Experiments with polystyrene and polymethyl acrylate show the dependence of  $\sigma_c$  with  $1/\sqrt{a}$ . However, the estimation of the surface energy of these polymers was found to be too high (magnitude of  $10^2$  to  $10^3$ ).

Griffith's theory was found to be valid on the absence of plastic deformation. The overestimation of the surface energy can be due to factors such as the adsorption of molecular chains and the interdiffusion of chains with the substrate. Thus, the surface energy term was replaced by a more global term ( $G_0$ ). This term corresponds to the energy liberated per unit length of crack propagated. From this, we obtain:

$$G_0 = \frac{\pi a \sigma_c^2}{E} \quad \text{Equation 1.13}$$

Irwin [Irwin, 1957] developed an alternative method to Griffith's approach to analyze the local shear field around the crack. The shear ( $\sigma_{ij}(r, \theta)$ ) and deformation ( $u_{ij}(r, \theta)$ ) relation obtained from this method is presented below:

$$\sigma_{ij}(r, \theta) = \frac{K_I}{\sqrt{2\pi r}} g_{ij}(\theta) \quad \text{Equation 1.14}$$

$$u_i(r, \theta) = \frac{K_I}{2E} \sqrt{\frac{r}{2\pi}} h_i(\theta) \quad \text{Equation 1.15}$$

where  $K_I$  is the intensity factor,  $E$  is the Young's modulus,  $g_{ij}(\theta)$  and  $h_i(\theta)$  are universal functions.

Again, the stress is proportional to  $1/\sqrt{r}$ , which creates a non-physical singularity at the extremity of the crack. However, in reality, the localized dissipative phenomena such as plastic deformation with fibril formation or the extraction of chains occur between the two faces of the crack.

On studying the influence of temperature and velocities on the adhesion energy, researchers [Andrews and Kinloch, 1973; Kaelble, 1969] found that a time-temperature equivalence can be established for the fracture energy of viscoelastic fluids. At temperatures above the glass transition temperature ( $T_g$ ), the energy of the fracture increases with the crack propagation velocity and decreases with the temperature. This time-temperature equivalence doesn't hold true at temperatures below the glass transition temperature as the polymers exhibit a solid like behavior and thus, no viscous dissipation.

### 1.4.3. Viscoelastic trumpet model

In 1988, de Gennes [de Gennes, 1988] developed a qualitative model to describe the crack propagation in the linear viscoelastic domain of the fluid called the 'Viscoelastic Trumpet' model. He considered a slightly crosslinked polymer whose static elastic modulus ( $\mu_0$ ) is inferior to the modulus at high frequencies ( $\mu_\infty$ ).

$$\mu(\omega) = \mu_0 + (\mu_\infty - \mu_0) \frac{i\omega\tau}{1 + i\omega\tau} \quad \text{Equation 1.18}$$

where  $\omega$  is the frequency and  $\tau$  is the characteristic time of the material.

Also,  $\lambda$  was defined as the ratio between high and low frequency moduli.

$$\lambda = \frac{\mu_\infty}{\mu_0} \quad \text{Equation 1.19}$$



At large velocities ( $V > L/(\lambda\tau)$ ),  $G_v(V)$  decreases with an increase in crack propagation velocity.

$$\frac{G_v(V)}{G_0} \sim \frac{L}{V\tau} \quad \text{Equation 1.21}$$

From these results, the viscous contribution ( $G_v$ ) to the fracture energy can be represented as a function of the crack propagation velocity (Figure 1.30).

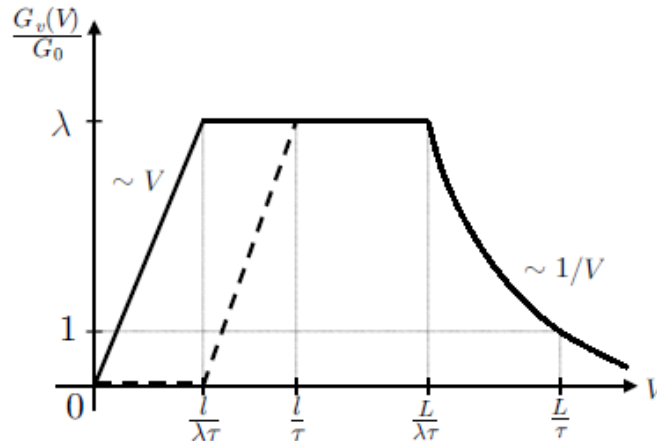


Figure 1.30 – Variation of  $G_v/G_0$  as a function of the crack opening velocity [Saulnier, 2003].

### 1.5. Adhesion

Adhesion is the tendency of dissimilar surfaces to cling to one other and is used as one of the methods of assembling materials. Adhesive bonding is advantageous due to its cost, lightness, absence of mechanical piercing, improved fatigue resistance, improved stiffness, improved shock resistance and their ability to join complex shapes. The adhesion energy of simple fluids is dominated by the inter and intramolecular forces. In order to achieve a good and effective adhesive/cohesive joint, we require clean surfaces with high energy states, surface roughness, good wettability, resistance to phase separation, adhesive solidification and adequate flow [Marshall *et al.*, 2009]. The work required to separate the interface between two phases (1 and 2) is the work of adhesion (Figure 1.31).

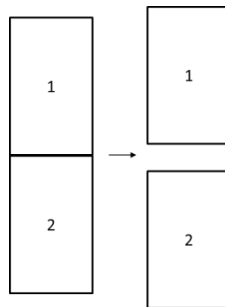


Figure 1.31 – Work of adhesion.

Dupré [Dupré, 1869] proposed that the work ( $W_A$ ) required to separate the phases is given by:

$$W_A = \gamma_1 + \gamma_2 - \gamma_{12} \quad \text{Equation 1.22}$$

where  $\gamma_1$ ,  $\gamma_2$  is the surface tension of phase 1 and 2 and  $\gamma_{12}$  is the interfacial tension between phase 1 and 2.

Interfacial attraction is important only in cases where the fracture is reversible. In reality, interfacial attraction is unimportant and wetting is the only requirement for a strong adhesive bond [Eley, 1961]. It is essential to distinguish the thermodynamically reversible work of adhesion as a result of

intermolecular forces from the adhesion energy exhibited by the fluids. S. Abbot [Abbott, 2015] shows that the influence of surface energy on adhesion is negligible and that entanglement of polymer chains together with energy dissipation determines the adhesion energy (Figure 1.32). For example, the thermodynamically reversible work of adhesion for a SBR polymer in contact with a glass surface can account for an order of  $50 \text{ mJ/m}^2$  of adhesion energy while the adhesive strength of such a contact can be of the order of  $200 \text{ J/m}^2$ .

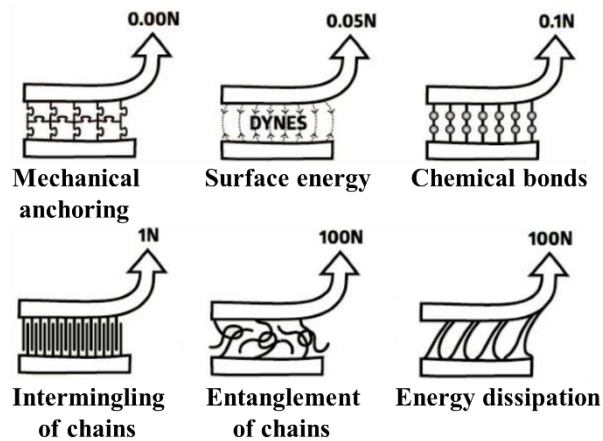


Figure 1.32 – Contribution of different mechanisms to adhesion energy [S. Abbot, 2015].

In general, adhesives can be classified into three categories based on their structure: i) thermosets, ii) thermoplastics and iii) pressure sensitive adhesives or polymer melts. Thermosets usually consist of a polymer dissolved in a solvent and crosslinking is achieved through the evaporation of the solvent. Thermoplastics usually contain precursors that will polymerize at the surface to create a strong bond. Finally, pressure sensitive adhesives are polymer melts that create a reversible adhesion depending on environmental conditions (temperature, pressure and contact time). The fluids used in this study behave like polymer melts which are sensitive to pressure i.e. pressure sensitive adhesives.

### 1.5.1. Characterization of adhesion energy

Various tests are used to determine the mechanical strength of an adhesive joint. These tests can be used to obtain the fracture strength and fracture energy of an adhesive joint. The adhesion tests are of either the crack initiation or crack propagation type. During crack propagation tests (peel and cantilever tests), a pre-existing crack is put under dynamic load and the rate at which the crack propagates is analyzed. With crack initiation tests (tensile and lap tests), a uniform adhesive layer is put under dynamic load. Figure 1.33 presents some of the adhesive tests used for adhesive joints (thermosets and thermoplastics).

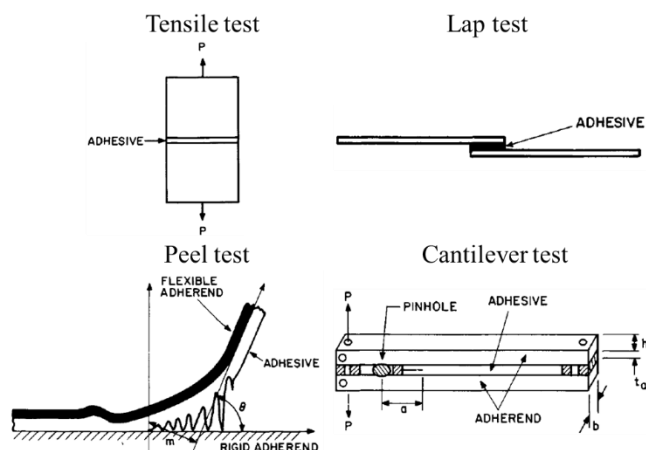


Figure 1.33 – Different types of adhesive tests [Wu, 1982].

In this study, tensile tack tests (probe tests) were carried out on the fluids. A brief literature on the tensile tests used on adhesive joints and polymer melts is presented here.

### Tensile tests on adhesive joints

During tensile tests, the adhesive undergoes pure mode I rupture. These tests are comparatively simple and convenient and are often used in industrial tests. Moreover, when the modulus of the adhesive and substrate are not similar, the adhesive layer undergoes non-uniform tensile stress with superimposed shear stress. Stress concentrations can also occur due to the lateral contraction of the adhesive layer during tension. The strength of the adhesive joint increases with decreasing thickness. Thick adhesive layers exhibit lower adhesive strengths as they have a larger probability of experiencing a critical flaw [Bikerman and Huang, 1959] and they experience more contractive shear stress than thinner layers [Gordon, 1967].

### Tensile tests on polymer melts

Probe tests, tensile tests with a compression cycle, are usually used to characterize the adhesion energy of polymer melts. The adhesion energy of polymer melts depends on conditions such as temperature, pressure and contact time. A layer of polymer melt is placed on the holding substrate and a pressure is exerted on it by a cylindrical substrate. After a pre-set contact time, the cylindrical probe is removed from the molten polymer at a constant velocity and the force response is measured as a function of time and displacement. The advantage of such tests is the application of a uniform compressive force on the polymer melt before debonding and a uniform displacement field to the polymer melt during debonding. The effect of the compression stage is often ignored [Shull and Creton 2004]. The typical force response measured during a tensile tack test is presented in Figure 1.34. Probe tests can be carried out with a plane-plane or sphere-plane geometry. The advantages of the sphere-plane geometry are its sensitivity to small misalignments of the sample and the good crack propagation geometry. However, these advantages are offset by the complex stress field obtained with highly viscoelastic fluids. As a result, the plane-plane geometry is used extensively for viscoelastic fluids [Zosel, 1985; Lakrout *et al.*, 1999; Poivet *et al.*, 2003; Shull and Creton, 2004].

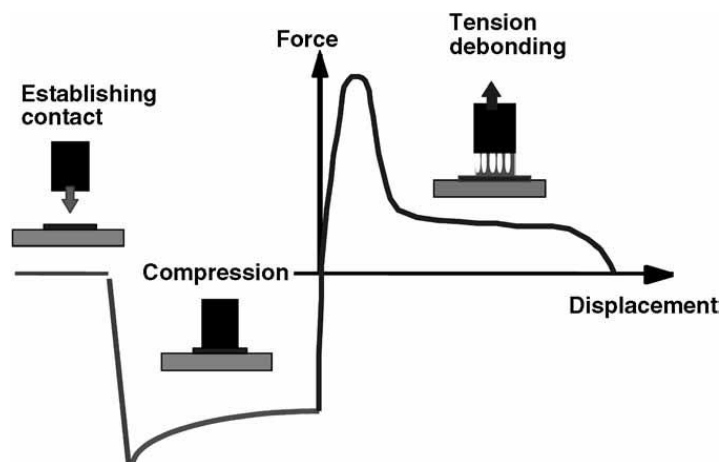


**Figure 1.34** – Typical force response measured during tensile tack experiments [Creton, 2003].

### 1.5.2. Thermodependency of adhesion energy

The influence of temperature on the adhesion energy was investigated by Zosel [Zosel, 1985] for uncross-linked and slightly cross-linked polymers. Being viscoelastic materials, the mechanical properties of polymers are dependent on the temperature and the time scale of the experiment. During this investigation, Zosel carried out creep experiments over a large range of temperatures (-100 to 250°C) in the linear visco-elastic regime. The creep compliance ( $D = \text{Strain}/\text{Shear stress}$ ) was measured at different times and a master curve was obtained by multiplying the creep compliance by a

factor of  $T/T_0$  and the time by  $1/a_T$ . Figure 1.35 presents the creep compliance and the master curve of creep compliance for polyisobutylene.

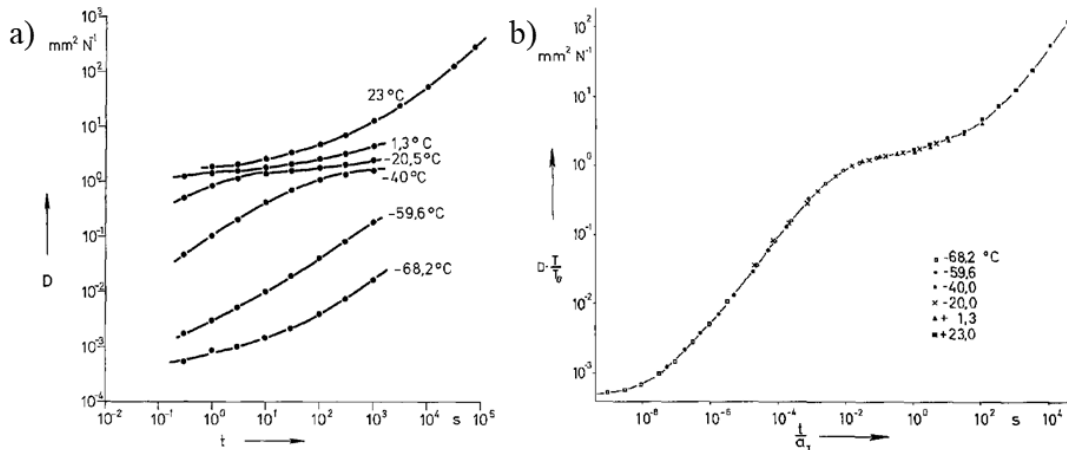


**Figure 1.35** – a) Creep compliance and b) the mastercurve of creep compliance for polyisobutylene [Zosel,1985].

A good time-temperature superposition of the creep compliance could be obtained. At short times, glass-like behavior was observed at time intervals ( $t/a_T$ ) of  $10^{-8}$  and  $10^{-2}$  s. This zone (linear visco-elastic domain) is influenced by the entanglement of chains, where a minor dependence of creep compliance ( $D$ ) with time ( $t$ ) is found. At long times, the creep compliance increases linearly with  $t$ . Subsequently, he studied the relationship between adhesion energy and temperature (Figure 1.36).

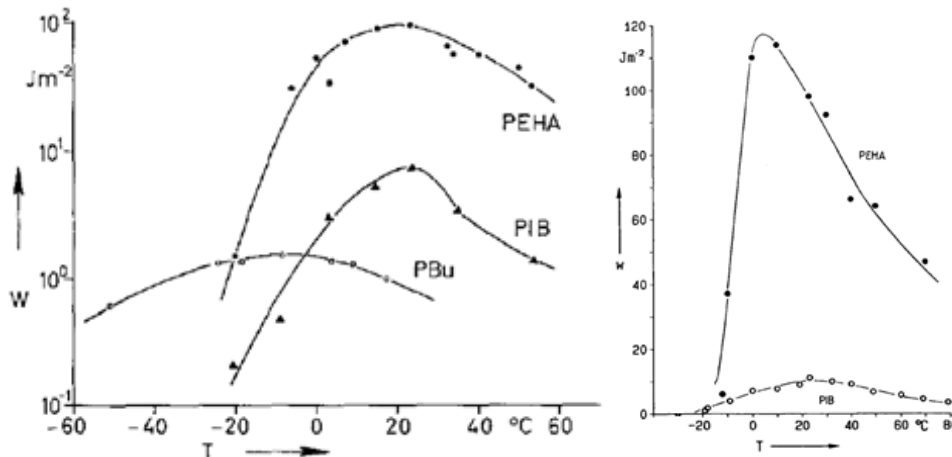


**Figure 1.36** – Adhesive fracture energy ( $w$ ) in function of temperature for polyethylhexylacrylate (PEHA), polybutadiene (PIB) and polyisobutylene (PIB) [Zosel,1985 and 1989].

Dahlquist [Dahlquist, 1970] was the first to detail the influence of elasticity and viscosity with the tack energy. On plotting the work adhesive energy in function of the temperature (Figure 1.36) [Zosel, 1985; Zosel, 1989] observed a maximum peak adhesion energy. This peak adhesion energy was found to occur at a temperature of about  $70^\circ\text{C}$  from the glass transition temperature ( $T_g$ ). In some cases, this peak was reported at  $50$  to  $70^\circ\text{C}$  above the glass transition temperature [Zosel, 1985]. Zosel observed that the peak adhesion energy was found to occur near the gel point temperature for crosslinked polymers [Zosel, 1991].

The nature of the Adhesion energy vs Temperature curves varies from one material to the other and is a function of the polymer architecture. On applying pressure on the molten polymer, the viscoelastic material creeps on the roughness of the substrate. At temperatures close to the glass transition temperature ( $T_g$ ), the mobility of the polymer chains is low and they do not allow any mechanical anchoring of the material. The material exhibits typically low adhesion energies of the order of

molecular interaction forces. An increase in temperature results in an increase of the mobility of chains allowing the material to better creep on to the surface roughness of the material. Thus, the adhesive strength increases with temperature till it reaches the peak value. The peak adhesion energy of the fluid is thus a result of an equilibrium between the creep and disentanglement of the chains. At higher temperatures, the increased mobility results in the disentanglement of the chains with surface and it behaves like a ‘fluid’. Thus, at these temperatures, the adhesion energy of the fluid is of the order of the surface tension of the material.

A typical Tack vs Temperature curve is shown in Figure 1.37. In order to extrapolate the adhesion energy at other temperatures, we take the liberty of distinguishing four different zones in the Tack vs Temperature curve. This predictive method is based on the adhesive behavior described by Zosel [Zosel 1986, 1989 and 1991]. However, this type of extrapolation should only be used as a predictive method to estimate the range of adhesion energies at a certain temperature rather than as a means to acquire a precise prediction. For this prediction, we define the Zosel temperature ( $T_{Zosel} = T_g + 70^\circ\text{C}$ ) as the peak adhesion temperature or the temperature above which the adhesion energy drops. The four different zones of this curve are:

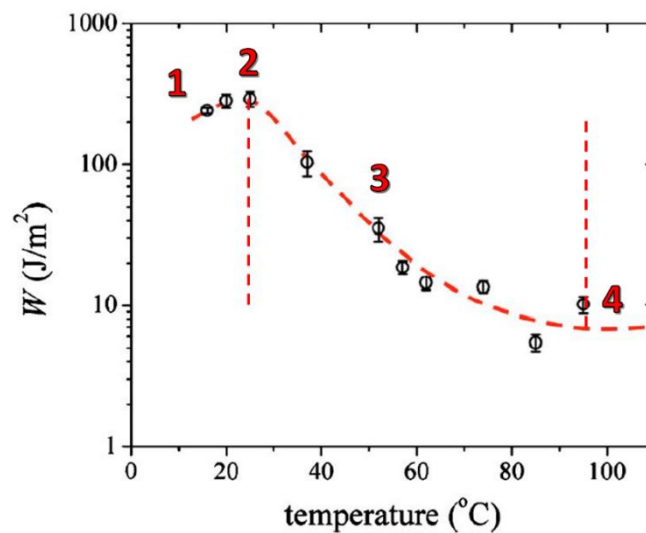


Figure 1.37 – Four zones of a Tack vs Temperature curve [Moon *et al.*, 2005].

**Zone 1 ( $T_g < T < T_{Zosel}$ ):** In this zone, the adhesion energy increases with temperature. For extrapolation purposes, we define this dependence as more or less linear. Thus, an increasing linear thermodependent law can be defined to predict the adhesion energy in this zone.

**Zone 2 ( $T = T_{Zosel}$ ):** This point corresponds to the peak adhesion energy. We consider that this peak occurs at  $70^\circ\text{C}$  above the glass transition temperature.

**Zone 3 ( $T > T_{Zosel}$ ):** Above the Zosel temperature, the adhesion energy drops with an increase in temperature. Again, we define this dependence as more or less linear for extrapolation purposes. A decreasing linear thermodependent law can be defined to predict the adhesion energy in this zone.

**Zone 4 ( $T \gg T_{Zosel}$ ):** At these temperatures, the melt behaves like a fluid. The measured tack energy corresponds to values close to the surface energy of the polymers. Thus, the adhesion energy can be explained to behave like a plateau like behavior at these temperatures.

### Conclusions

Since the invention of the Banbury mixer in 1916, the internal mixing process is the most widely used method of mixing rubber compounds. The rotor design and the process parameters influence the quality of the final product. Research is actively carried out today to improve the rotor design and the determination of the process parameters for new rubber formulations.

In an effort to understand the process, direct flow visualization techniques were developed. Such observations of the internal mixing process have greatly improved the understanding of the mixing process leading to numerous improvements of the mixing process. Due to the complex geometry and 3D flow behavior in the internal mixer, the observation of the interfacial phenomena in the mixer remains difficult.

With increasing understanding of the mixing process and development of new simulation techniques, numerical simulations which effectively simulate the 3D flow behavior during internal mixing can be obtained today. However, the contribution of interfacial phenomena such as wall slip, free surface movement and adhesion are often neglected in these simulations. The quality of these numerical models can greatly improve with the incorporation of these phenomena such as: wall slip, movement of contact line and adhesion.

During industrial processing, the polymers may experience wall slip above the critical shear stress ( $\sigma_w$ ). The onset of wall slip can be linked to the onset of flow instabilities though this is not always the case. The nature of flow instabilities depends on the nature of the polymer, geometry of flow and operating conditions. However, the branching of the polymer chains remains the dominant factor in the types of flow instabilities encountered. The classical method to characterize wall slip velocities is through the measurement of the pressure drop as a function of flow rate for different flow geometries in capillary rheometers. Researchers found that the wall slip velocities increase with a rise in temperature, for a given shear stress above  $\sigma_c$ . However, a relation between the wall slip velocities and temperature could not be defined.

The displacement of one fluid by another over a solid surface results in the movement of the three-phase contact line, violating the no slip boundary condition. This movement also results in a stress singularity at the contact line. Many models have been proposed to solve this singularity problem. In the case of polymers, the thermodynamic forces of adhesion cannot influence the movement of the contact lines. For viscous fluids, the loss of contact from the substrate can occur due to the crack propagation along the interface or the bulk deformation of the fluid.

For polymers, the contact line movement problem can be addressed as a fracture mechanics problem. Griffith [Griffith, 1920] proposed that a crack can propagate only if it liberates more energy than it absorbs. This again results to a non-physical singularity at the extremity of the crack as the stress is inversely proportional to the crack width. A time-temperature equivalence can be established for the fracture energy where the fracture energy increases with the propagation velocity and decreases with the temperature. The viscoelastic trumpet model by de Gennes [de Gennes, 1988] provides the adhesive behavior of the polymer at different length-scales of the crack.

The phenomenon of adhesion is often treated as a problem of inter and intramolecular forces for simple fluids. However, for polymers, the viscoelastic dissipation significantly dominates over the molecular forces. In this study, probe tests were used to characterize the adhesion energy of the fluids. The influence of temperature on the adhesion energy was investigated by Zosel [Zosel, 1985]. From this study, the Adhesion energy vs Temperature curve can be split into four distinct zones. The adhesion energy of the polymer increases linearly with temperature till it reaches a peak at about  $T_g + 70^\circ\text{C}$  where  $T_g$  is the glass transition temperature. After this peak, the adhesion energy drops linearly till it reaches a plateau at high temperatures. These trends can be used to estimate the adhesion energy of the adhesive at other temperatures.

### Résumé en français

Le mélangeur interne est le procédé le plus utilisé pour mélanger les mélanges de caoutchouc depuis l'invention du mélangeur Banbury en 1916. La qualité du produit final est fortement influencée par la conception du rotor et les paramètres du procédé. Des recherches sont activement menées de nos jours pour améliorer la conception du rotor et la détermination des paramètres de procédé pour les nouvelles formulations de caoutchouc. Afin de comprendre le procédé, des techniques de visualisation directe d'écoulement ont été développées. Ces observations ont aidé à mieux comprendre le procédé, conduisant à des nombreuses améliorations de celui-ci. À cause de la géométrie complexe du mélangeur et de l'écoulement 3D dans le mélangeur interne, l'observation des phénomènes interfaciaux reste difficile.

Une meilleure compréhension du procédé et le développement des nouvelles techniques de simulation, ont amené à des simulations numériques qui peuvent effectivement simuler l'écoulement 3D des élastomères dans un mélangeur interne. Néanmoins, la contribution des phénomènes interfaciaux comme le glissement à la paroi, mouvement des surfaces libres et l'adhésion sont souvent négligés dans ces simulations numériques. L'incorporation des phénomènes comme le glissement à la paroi, le mouvement des surfaces libres et l'adhésion, peut améliorer la qualité des simulations numérique du procédé de mélange interne.

Au cours du traitement industriel, les polymères peuvent subir un glissement à la paroi pour des contraintes supérieures à la contrainte critique ( $\sigma_w$ ). L'apparition du glissement à la paroi peut être liée à l'apparition d'instabilités d'écoulement bien que ce ne soit pas toujours le cas. L'apparition de ces instabilités dépend de la nature du polymère, la géométrie d'écoulement et des paramètres du procédé. Cependant, le branchement des chaînes polymères reste le facteur dominant pour l'apparition de ces instabilités. La méthode classique pour caractériser les vitesses de glissement à la paroi est par la mesure de la perte de charge en fonction du débit pour différentes géométries de filière avec un rhéomètre capillaire. Des chercheurs ont trouvé que les vitesses de glissement croissent avec la température pour une contrainte donnée ( $> \sigma_c$ ). Malgré ces résultats, aucune relation thermodépendante des vitesses de glissement a été déterminée.

Le déplacement d'un fluide par un autre à travers une surface solide entraîne le mouvement de la ligne triple, violant la condition des limites d'aucun glissement. Le mouvement de la ligne triple mène à une singularité non-physique de contrainte. Plusieurs modèles ont été proposées pour résoudre cette singularité. Dans le cas des polymères, les forces thermodynamiques d'adhésion ne peuvent pas influencer le mouvement des lignes triples. Pour les fluides visqueux, la perte de contact avec le substrat peut se produire en raison de la propagation des fissures le long de l'interface ou de la déformation au coeur du fluide.

Le problème du mouvement de la ligne triple peut être traité comme un problème de mécanique de la rupture pour des polymères. Griffith [Griffith, 1920] a proposé qu'une fissure peut se propager à la condition qu'elle libère plus d'énergie qu'elle absorbe. Cette condition cause une singularité non-physique à l'extrémité de la fissure où la contrainte est inversement proportionnelle à la largeur de la fissure. Une équivalence temps-température peut être établie pour l'énergie de fracture. Cette énergie croit avec la vitesse de propagation et diminue avec la température. Le modèle de trompette viscoélastique de de Gennes [de Gennes, 1988] prédit un le comportement adhésif du polymère à différentes zones de la fissure.

L'adhésion est souvent traitée comme un problème de forces inter et intramoléculaires pour les fluides simples. Dans le cas des polymères, la dissipation viscoélastique domine significativement sur les forces moléculaires. L'énergie d'adhésion peut être quantifiée à l'aide de différentes techniques de caractérisation. L'influence de la température sur l'énergie d'adhésion a été étudiée par Zosel [Zosel, 1985]. Sur la base de ces travaux, une méthode de prédiction a été proposée pour prédire l'énergie d'adhésion à différentes températures.

## Chapter 2

# Materials and methods

### Contents

---

2.1. Fluids used in the study .....	40
2.1.1. Rubber products .....	40
2.1.2. Silicone fluid .....	43
2.2. Experimental methods .....	44
2.2.1. Rheometers .....	44
2.2.1.a. Oscillatory rheometers .....	44
2.2.1.b. Capillary rheometer .....	46
2.2.2. Probe tests .....	53
2.3. Transparent flow cells .....	56
2.3.1. Transparent flat die .....	56
2.3.2. Transparent internal mixers .....	58
2.3.2.a. Monocuve mixer .....	59
2.3.2.b. MaCROS mixer .....	61
Conclusions .....	67

---

## 2.1. Fluids used in the study

During the course of this work, two types of fluids were studied. The rubber products were chosen so as to work with fluids representative of those used in internal mixers. A silicone fluid was also used as a model fluid to perform *in-situ* observations during shear flow experiments in the MaCROS mixer at ambient temperature.

### 2.1.1. Rubber products

Three pure elastomers and a rubber compound were investigated during this work. The pure elastomers were chosen for their use in the manufacture of tires [Arlanxeo, 2020; Trinseo, 2020] and their commercial availability. These elastomers were also chosen as they were more transparent than most pure rubbers. The transparency of these elastomers could aid the observation of the flow across the width of the transparent flow geometries. The pure elastomers are a Butadiene Rubber (BR A), a functionalized Styrene Butadiene Rubber (SBR A) and a Styrene Butadiene Rubber (SBR B). These materials will be mentioned by their abbreviations henceforward. The physicochemical properties of these elastomers are presented in Table 2.1.

	BR A	SBR A	SBR B
Molecular weight $M_w$ (kg/mol)	505	434	248
Polydispersity index	3.22	4	9.05
Density (kg/m <sup>3</sup> )	900	930	950
Glass transition temperature (°C)	-108	-62	-48

**Table 2.1** – Physicochemical properties of the elastomers [Jugo Viloría, 2017; Arlanxeo, 2020; Trinseo, 2020].

SBR and BR are commercially available synthetic elastomers. They were developed in the early 20<sup>th</sup> century as a means to replace the utilization of Natural Rubber. The development of synthetic elastomers was a product of the rapid expansion of the tire industry at that time and the almost complete halt of production of Natural Rubber during World War II. The emergence of polymer chemistry in the 1920s accelerated the production of synthetic elastomers [Curchod, 1984]. The research in synthetic rubber was pioneered by countries which lacked access to rubber plantations (unlike U.S.A., U.K., France and the Netherlands).

### Styrene Butadiene Rubber

Styrene Butadiene Rubber is a copolymer of styrene and butadiene. The ratio of butadiene (x) and styrene (y) can vary from 60 to 84% and from 16 to 40% respectively. An increase in content of butadiene or styrene influences the elastomeric and thermoplastic behavior of the copolymer, respectively. The best equilibrium of mechanical properties is obtained for 23.5% of styrene (x = 66.5% and y = 23.5%). The chemical formula of SBR is presented in Figure 2.1.

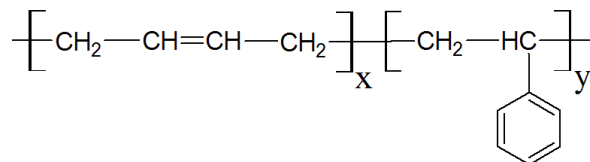


**Figure 2.1** – Chemical formula of SBR.

The SBR is synthesized by two methods:

- polymerization in solution,
- polymerization in emulsion, comprising two methods:
  - hot processing at 50° C (original process),
  - cold processing at 5°C (most common process today).

As of today, the SBR is the most widely used synthetic elastomer. The hot emulsion polymerization method was mastered in 1929 in which the macromolecular copolymer is polymerized with styrene and butadiene. At present, the most common methods of SBR production are the “cold” emulsion polymerization and the solution method, in that order. In solution polymerization, the polymerization occurs in dry hydrocarbon solvent with anionic methyl-lithium catalyst. These methods influence the properties of the SBR considerably. They can also influence the structure of the macromolecular chain. Four molecular structural units exist in SBR, of which three are the molecular chain variations of butadiene. The macromolecular structures units of SBR are presented in Figure 2.2.

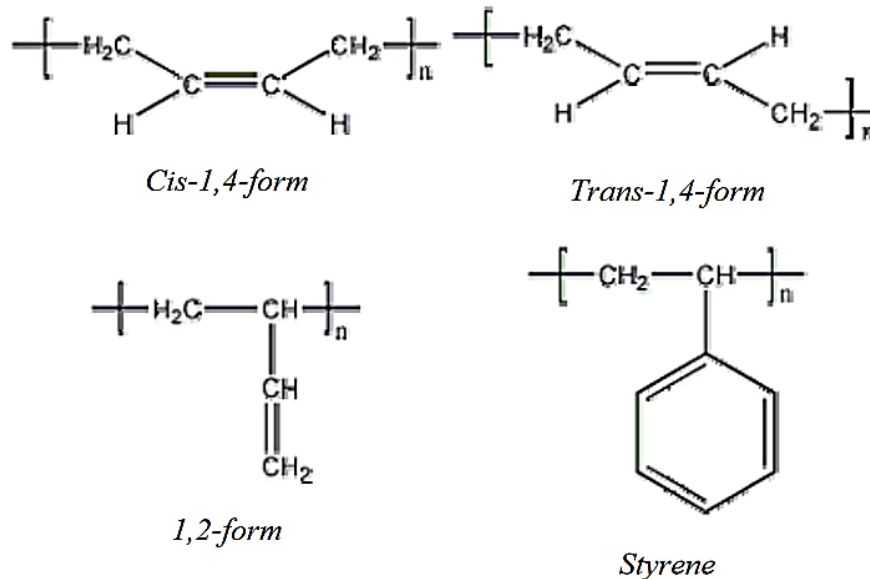


Figure 2.2 – Macromolecular structural units of SBR.

**SBR A:** SBR A is a functionalized SBR, commercially available under the name SPRINTAN™ SLR 3402-SCHKOPAU. It is manufactured by Trinseo, formerly known as Sprintan™, by anionic solution polymerization using an organo-lithium initiator. SBR A is partially coupled with a generation 2 functionalization for polymer/filler interaction with carbon black and silica. The functions are an alkoxysilane group and a thiol group [Jacoby *et al.*, 2016; Isitman *et al.*, 2017; Pavon Sierra *et al.*, 2016]. Its chemical composition is given by:

- styrene: 15%,
- 1,2-vinyl butadiene: 30%,
- 1,4 butadiene: 55%.

**SBR B:** SBR B is a solution Styrene Butadiene rubber (S-SBR) which is commercially sold under the name Buna® SBR 2300 by ARLANXEO. Its chemical composition is given by:

- styrene: 27 %,
- 1,2-vinyl butadiene: 18 %,
- 1,4-cis butadiene: 22 %,
- 1,4-trans butadiene: 33%.

### Butadiene Rubber

With the emergence of polymer physics in 1920, BR was the first artificially synthesized elastomer. The development of SBR replaced BR in most of its applications. However, BR is widely used in certain applications, like retreading and tire threads, for its superior elastic properties. BR is available today, both in emulsion and solution form. The chemical composition of BR is presented in Figure 2.3.

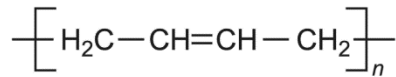


Figure 2.3 – Chemical formula of Butadiene Rubber.

BR was originally polymerized in emulsion form with sodium (Na) and was called as BuNa. BR can also be polymerized in solution form by the use of Ziegler-Natta catalysis. Ziegler worked on the development of catalysts for polymerization reactions. These reactions paved the way for new and highly industrial processes, for which he was awarded the Nobel Prize in Chemistry. Using Ziegler-Natta catalysts in a non-polarizing environment exclusively with one of three catalytic associations (Ti/Al, Co/Al or Ni/Al), solution BR can be obtained. As presented in Figure 2.2, BR can have three different structural units.

**BR A:** BR A is a solution BR, synthesized with Ziegler-Natta catalysis and a Neodymium catalyst. The synthesis procedure is described in detail in the patent WO 2007045417 [Parola *et al.*, 2007]. BR A is mostly in 1,4-cis form (98.8%) (Figure 2.2).

### Rubber compound (SBR C)

In addition to the pure rubber products, a rubber compound was formulated during the course of this work. The formulation was chosen to be representative of industrial rubber compounds and provide high adhesion energies. Its objective was to be used in the study as a rubber compound similar to those used in industrial internal mixers. Besides, the rubber compound was designed to exhibit a superior adhesive behavior than the pure rubber products at elevated temperatures. SBR C was formulated with the SBR A as base elastomer. Its formulation is presented in Table 2.2. The concentration of each component is represented in phr or parts per hundred of rubber.

Function	Ingredient	Concentration (phr)
Base elastomer	SBR A	100
Resin	Wingtack® STS	85
Filler	Silica	63.2
Coupling agent	Silane	4.9
Anti-oxidant	6PPD	1.6
Anti-ozone	Wax anti-ozone	1.1
Activator	Stearic Acid	2
Activator	Zinc oxide	1.5
Accelerator	DPG	1.15

Table 2.2 – Formulation of SBR C compound.

The formulation of SBR C contains common compounding ingredients that can be found in an industrial rubber compound. The SBR C was designed to have a greater adhesion energy by altering its glass transition temperature ( $T_g$ ) and thus its Zosel temperature ( $T_{Zosel}$ ). The Zosel temperature ( $T_g + 70^\circ\text{C}$ ) [Zosel, 1985] of SBR A ( $T_g = -62^\circ\text{C}$ ) is  $8^\circ\text{C}$ . SBR A was mixed with the Wingtack® STS resin ( $T_g = 44^\circ\text{C}$ ) [Total] to increase the glass transition temperature ( $T_g$ ) of the compound and hence its Zosel temperature. The Fox equation [Fox, 1956] can be used to determine the  $T_g$  of a polymer blend.

$$\frac{1}{T_g} = \frac{w_1}{T_{g,1}} + \frac{w_2}{T_{g,2}} \quad \text{Equation 2.1}$$

where  $T_{g,1}$ ,  $T_{g,2}$ ,  $w_1$  and  $w_2$  are the transition temperatures and weight fractions of components 1 and 2, respectively.

The Fox equation is used to determine the glass transition temperatures of rubber compounds composed uniquely of elastomers. This gives us a  $T_g$  of  $-24^\circ\text{C}$ . Due to the presence of other ingredients in the rubber compound (fillers, activators, coupling agents, etc), the actual  $T_g$  of the

compound can vary. Differential scanning calorimetry (Calorimetry (DSC Perkin Elmer 4000)) was carried out on SBR C (Figure 2.4). The  $T_{eg}$  of SBR C was determined to be  $-42^{\circ}\text{C}$ , giving a Zosel temperature of  $28^{\circ}\text{C}$ .

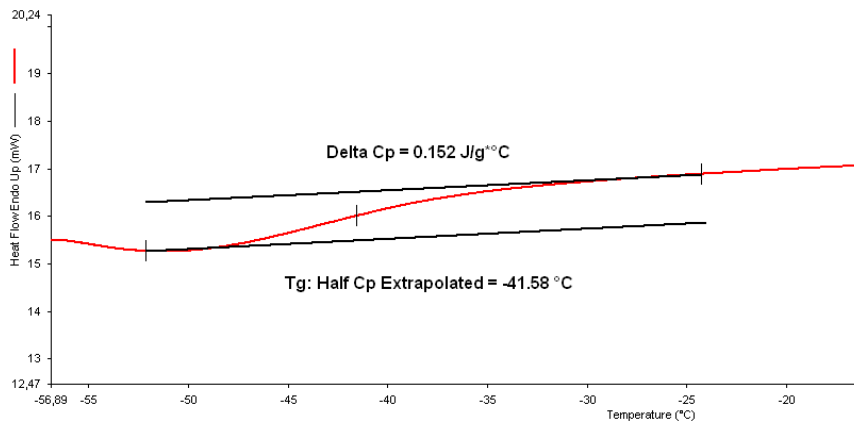


Figure 2.4 – Phase transformation of SBR C ( $50^{\circ}\text{C}/\text{min}$ ).

### 2.1.2. Silicone fluid

To study the flow behavior of viscous fluids in the MaCROS prototype at ambient temperature, a model fluid was required. It is simpler to operate the prototype at ambient temperature as the heating system is not required and any potential changes in viscosity of the fluid due to uneven heating of the surfaces or other temperature related inconsistencies can be avoided. The required properties of a fluid to conduct these experiments are presented in Chapter 4.3.1. A silicone fluid was chosen to study the steady state flow conditions with the MaCROS prototype.

The silicone fluid is commercially sold under the brand “Liquid Glass Thinking Putty<sup>®</sup>” by Crazy Aaron, Nebraska, USA. This fluid shows complete transparency. It exhibits a shear viscosity plateau of  $22600\text{ Pa}\cdot\text{s}$  at ambient temperature (Equation 3.1). The chemical composition of the fluid was unknown. Hence, Attenuated Total Reflectance-Fourier Transform Infrared Spectrometers (ATR-FTIR) analysis was carried out on the silicone fluid. ATR-FTIR analysis is a sampling technique used with infrared spectroscopy to examine the samples without further preparation in the solid or liquid state. FTIR spectra were acquired with a Nicolet iS50 FTIR by using attenuated total reflection mode with GladiATR equipment from PIKE Technologies (ICN, University of Nice-Sophia Antipolis). The spectra were collected between  $4000$  and  $600\text{ cm}^{-1}$ , with 32 scans and a resolution of  $4\text{ cm}^{-1}$ . Automatic background subtraction was applied. FTIR spectra for the silicone fluid are presented in Figure 2.5.

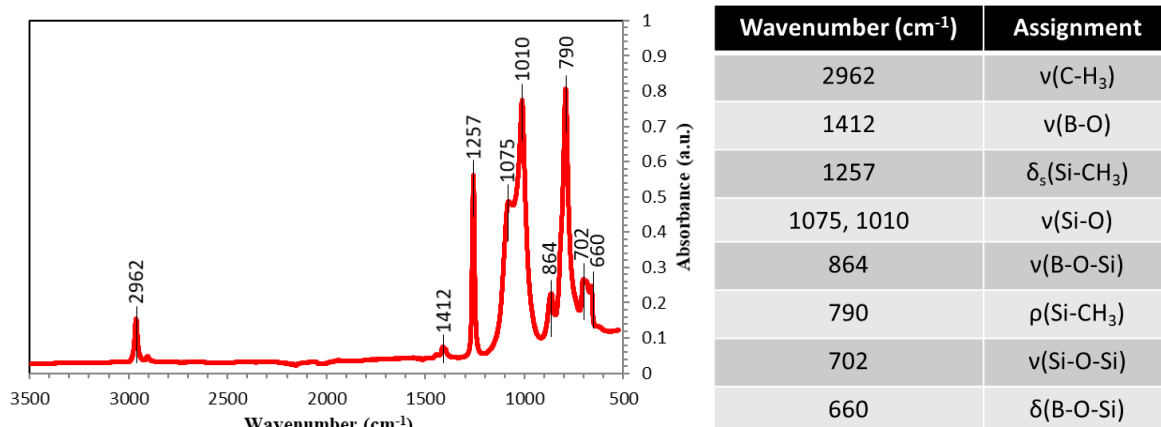


Figure 2.5 – ATR-FTIR spectrum of the silicone fluid at a resolution of  $4\text{cm}^{-1}$  (with 32 scans).

The ATR-FTIR analysis indicates the presence of bonds of polydimethylsiloxane (PDMS) such as Si-O-Si, Si-O, C-H<sub>3</sub> and Si-CH<sub>3</sub> bonds. The presence of  $\nu(\text{B-O})$ ,  $\nu(\text{B-O-Si})$  and  $\delta(\text{B-O-Si})$  peaks were also detected. This confirms the use of boric acid or borax as crosslinking agent, as claimed in the Silly Putty patent [Minuto, 1983]. The chemical structure of PDMS chain and that of PDMS cross-linked with borax are presented in Figure 2.6. Thus, we can identify the silicone fluid is a PDMS cross-linked with borax.

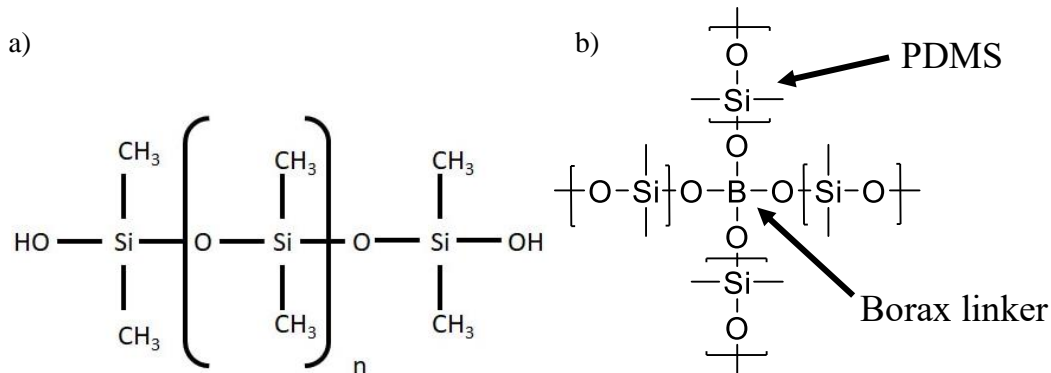


Figure 2.6 – Chemical structure of a) PDMS and b) PDMS cross-linked with Borax.

## 2.2. Experimental methods

During the course of this work, three types of tools were used. Rheological characterization of the fluids was achieved with the help of oscillatory and capillary rheometers. The adhesion energy of the fluids was characterized with probe tests. Flow observations were carried out with a transparent flat die and two transparent lab scale mixers. The development and design of these transparent flow cells will be presented in Chapter 2.3.

### 2.2.1. Rheometers

The most commonly used rheometers are oscillatory and capillary rheometers. Oscillatory rheometers work at small deformations (in the linear viscoelastic domain). The oscillatory rheometers can provide information on the viscoelastic character of the polymer and on its molecular structure. Capillary rheometers work at large deformations. Alternatively, capillary rheometers are used to characterize the flow behavior at shear rates comparable to those used in industrial processing.

#### 2.2.1.a. Oscillatory rheometers

In oscillatory rheometry, the fluid is first placed between a stationary plate and an oscillating plate, as shown in Figure 2.7. It is then sheared between two parallel plates to measure the viscoelastic behavior. A sinusoidal shear strain ( $\epsilon(t) = \epsilon_0 \cdot \sin(\omega t)$ ) is induced to the fluid by the oscillating plate. The frequency ( $\omega$ ) determines the time scale period. The stress response to the induced shear deformation is measured as a function of time,  $\sigma(t)$ , with the help of a torque sensor on the oscillating plate. The experimental data are analyzed while working in the linear viscoelasticity domain and thus, the induced strains must be within this domain. The stress response is given by:

$$\sigma(t) = G'(\omega)\epsilon_0 \sin(\omega t) + G''(\omega)\epsilon_0 \cos(\omega t) \quad \text{Equation 2.2}$$

where  $G'$  and  $G''$  are the elastic and viscous moduli, and  $\epsilon_0$  is the amplitude of the strain.

In the case of elastic solids, the stress response is in phase with the applied sinusoidal strain. However, with viscous fluids, the stress and the strain are out of phase by  $\delta = \pi/2$ . Viscoelastic fluids exhibit an intermediate flow behavior with a phase shift of  $0 < \delta < \pi/2$ . The determination of the phase shift can be used to determine the viscous and elastic components of the viscoelasticity. The complex dynamic modulus,  $G$ , is given by:

$$G = G' + iG'' \quad \text{Equation 2.3}$$

$$G' = \frac{\sigma_0}{\varepsilon_0} \cos\delta \quad \text{Equation 2.4}$$

$$G'' = \frac{\sigma_0}{\varepsilon_0} \sin\delta \quad \text{Equation 2.5}$$

where  $\sigma_0$ ,  $\varepsilon_0$  are the stress and strain amplitudes, and  $\delta$  is the phase shift.

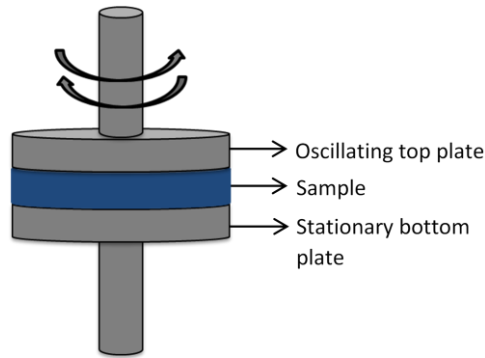


Figure 2.7 – Principle of oscillatory rheometers.

The complex viscosity ( $\eta^*$ ) can be obtained from the elastic and viscous moduli by the equation:

$$|\eta^*| = \frac{\sqrt{G'^2 + G''^2}}{\omega} \quad \text{Equation 2.6}$$

The evolution of  $G'$  and  $G''$  with the amplitude of the strain (Amplitude sweep tests) allows us to identify the zone of linear viscoelasticity where the stress is proportional to the strain. Figure 2.8 represents the behavior of a typical viscoelastic fluid in the frequency sweep and amplitude sweep tests. The evolution of the moduli with the frequency (Frequency sweep tests) helps us to study the time-dependent behavior of the fluid in the linear viscoelasticity zone. Frequency sweep tests allow us to obtain information on the structure and long-term stability of the fluid.

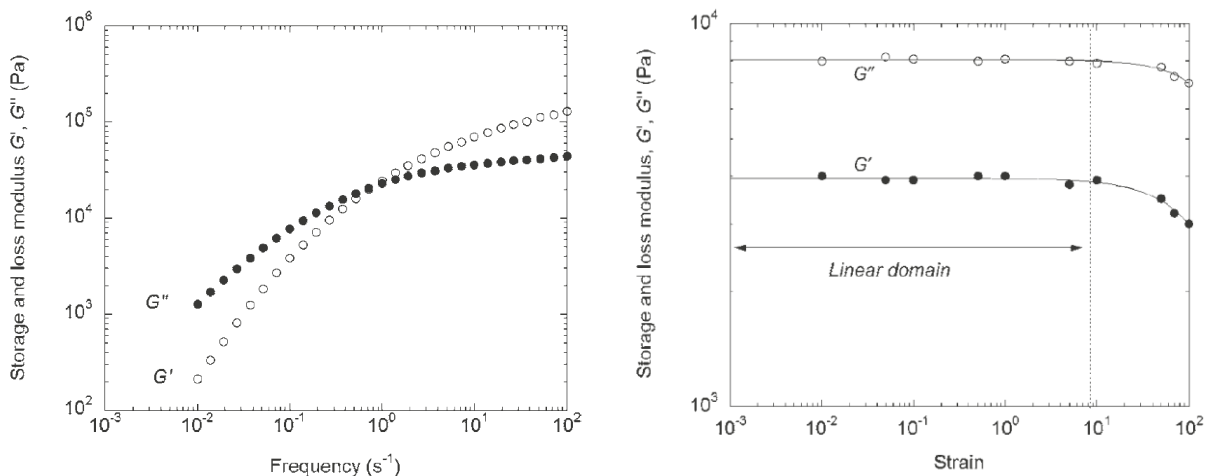


Figure 2.8 – a) Frequency and b) amplitude sweep tests of polystyrene at 180°C [Agassant *et al.*, 2014].

Sample preparation for oscillatory rheometers

The silicone fluid samples were prepared by deforming the fluid between the plates of the oscillatory rheometer. The fluid is placed on one plate and the plates were moved to create a gap of 2 mm. The excess fluid on the sides of the plates was removed to create a uniform sample of 2 mm thickness.

Samples for the rubber products were prepared with the help of a hydraulic press and a mold. The required volume, 20 cm<sup>3</sup> (10 cm \* 10 cm \* 2 mm), of the rubber product was introduced into the mold and heated to 110°C by the hydraulic press for 30 minutes. A pressure of over 8 bar was applied on the mold at 110°C for 90 minutes to create the film. To prevent any swelling of the film, the pressure on the mold was maintained as the mold was cooled down to ambient temperature. The rubber film was ejected from the mold. The sample was cut from the film for its use in the oscillatory rheometer.

Three oscillatory rheometers were used in this study. The ARES rheometer from TA Instruments was used to characterize the silicone fluid. It imposes a constant deformation while measuring the stress response. On the other hand, the MCR-302 rheometer from Anton Paar and ARES G2 rheometer were used to characterize the rubber products. They impose a constant shear stress while measuring the stress response. It is important to note that no residual stress must be present in the sample before launching the oscillatory tests. This was especially a problem while working with the rubber products. The MCR-302 and ARES G2 rheometers can impose a negligible normal force while introducing the fluid between the parallel plates thus aiding the fluid to relax the residual stresses faster.

2.2.1.b. Capillary rheometer

Capillary rheometers are widely used in the industry as they can work at comparably high shear rates (1 to 10<sup>4</sup> s<sup>-1</sup>). This range of shear rates is representative of those encountered in industrial processes (Figure 2.9). A capillary rheometer can be used to investigate the flow of fluids and the appearance of extrusion defects.

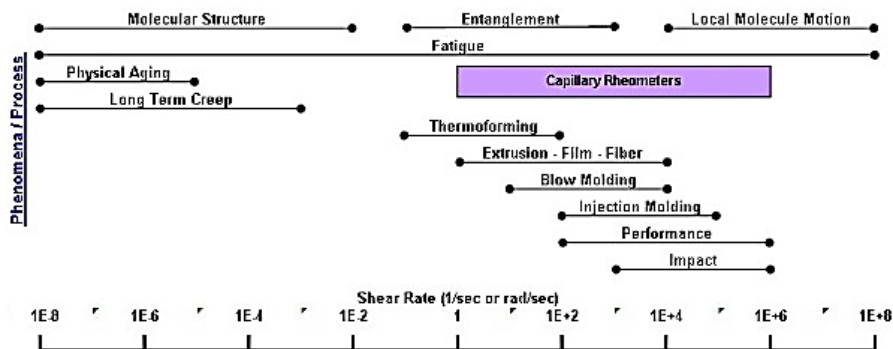
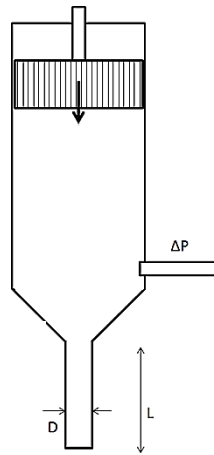


Figure 2.9 – Shear rates encountered during polymer processing [TA Instruments, 2015].

A capillary rheometry consists of a chamber equipped with a piston and a die at the exit of the chamber. The polymer in the solid state is introduced into the chamber and heated to the desired temperature. After reaching the molten state, the polymer is pushed through the capillary chamber and the die by the piston. The pressure drop developed is measured with the help of a pressure transducer. The schematic representation of a classical capillary rheometer is presented in Figure 2.10. The analysis of the pressure drop enables us to determine the fluid viscosity. During this work, a capillary rheometer equipped with a pre-shearing chamber called the RhéoART<sup>TM</sup> is used.



**Figure 2.10** – Schematic representation of a capillary rheometer.

### **RhéoART™**

Rheoplast was a capillary rheometer developed by a group of scientists from the Centre de Mise en Forme (CEMEF), Sophia-Antipolis, France. The RhéoART™ is the electric version of the hydraulic Rheoplast and is commercialized by ART Technologies (Saint Etienne, France). It is the result of successive developments over the last 35 years based on the original work of Avenas and his colleagues [Avenas *et al.*, 1975; Villemaire *et al.*, 1989; Villemaire *et al.*, 1994]. The RhéoART™ was designed to overcome two major difficulties posed by classical capillary rheometers.

The long processing time required to plasticize or melt the fluid can be problematic for fluids which are incompatible with their thermal stability. To overcome this problem, the processing time must be reduced or stabilizers must be added to the fluid. The addition of stabilizers in the fluid influences the rheological behavior.

Another difficulty with capillary rheometers is the encapsulation of air bubbles in the fluid during the feeding/melting step. These pockets of air can perturb the pressure measured by the transducer making the analysis of these measurements inadequate.

In order to avoid these difficulties, the RhéoART™ is equipped with a shearing chamber. The fluid is sheared (pre-shear) in the RhéoART™ before it is introduced into the injection chamber. It is sheared by the combined motion of the feeding and injection pistons. The injection chamber is heated to the required temperature. The pre-shearing action leads the fluid to undergo self-heating. The fluid is thus heated by both self-heating and conduction. This leads the fluid to attain the processing temperature sooner than in the case of a classical rheometer. The pre-shearing action greatly reduces the presence of air bubbles in the molten fluid. Thus, it permits the measurement of viscosity in conditions which are closer to the processing conditions.

The schematic representation of RhéoART™ is presented in Figure 2.11. The RhéoART™ consists of three chambers: a feeding chamber, a shearing chamber and an injection chamber. The fluid is introduced into the feeding chamber. Then the injection piston is rotated and the feeding piston is moved down. This results in the fluid being pre-sheared in the shearing chamber before its introduction into the injection chamber. When the chamber is filled, the fluid is extruded through the die. The injection chamber is equipped with electrical heaters and thermocouples to control the temperature. A pressure transducer is situated near the entry of the capillary die. Dies of different dimensions and shapes can be used.

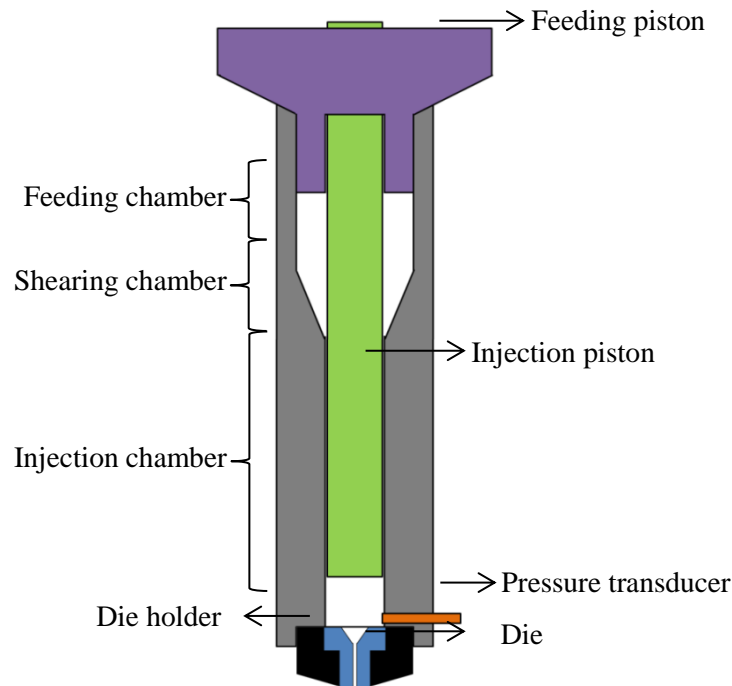


**Figure 2.11** – Schematic representation of RhéoART™.

Experimental measurements carried out using the RhéoART™ can be subdivided into six stages. They are:

- 1) feeding stage,
- 2) pre-shearing stage,
- 3) purge stage,
- 4) relaxation stage,
- 5) extrusion stage,
- 6) initialization stage.

The different stages of the experiment are presented in Figure 2.12 (page 48).

**Feeding stage:** At this stage, the feeding and injection pistons are in their initial/upper positions. The machine is set to the processing temperature. The fluid is introduced through the hopper into the feeding chamber. For better processing, the elastomer is introduced in the form of small blocks (of about 1 cm<sup>3</sup>) through the hopper.

**Pre-shearing stage:** Following the feeding stage, the pre-shearing of the fluid takes place, where the fluid is compressed and sheared. The feeding piston descends at a pre-defined speed ( $V_d$ ) while the injection piston rotates at a pre-defined speed ( $V_r$ ). The fluid is sheared and homogenized and transferred to the injection chamber as a result of the motion of these two pistons. The pre-shearing prevents the encapsulation of the air bubbles. The downward motion of the feeding piston forces the fluid to move from the feeding to the shearing and finally to the injection chamber. At the end of the pre-shearing stage, the injection chamber is completely filled.

**Purge stage:** The objective of the purge stage is to evict the fluid present in the capillary die from the previous experiment. At the beginning of the purge stage, the feeding piston stops descending and the injection piston stops rotating. Then the injection piston descends to evict the fluid at a pre-defined speed, called the purging speed ( $V_p$ ). Then the injection piston stops and we move on to the relaxation stage. The total volume of the injection chamber is 12.17 cm<sup>3</sup>. In order to purge the fluid remaining from the previous experiment (fluid remaining in the capillary die and around the pressure transducer),

3.17 cm<sup>3</sup> of fluid is purged from the injection chamber. 9 cm<sup>3</sup> of fluid is left for the extrusion stage and experimental analysis.

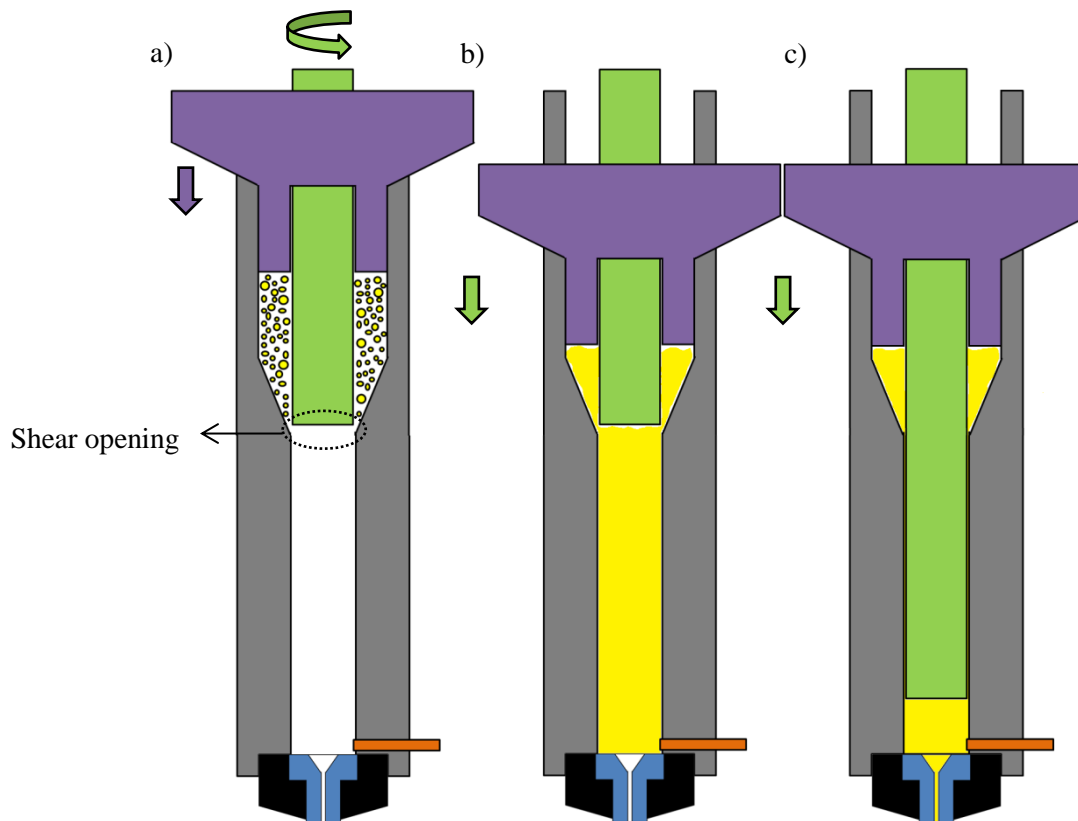


Figure 2.12 – a) Pre-shearing stage, b) Purge stage and c) Extrusion stage.

Relaxation stage: Now, the fluid is left to relax for a certain time ( $t_r$ ) to homogenize the temperature and relax the pressure developed during the previous stages.

Extrusion stage: After the relaxation time, the injection piston starts descending again at speeds imposed by the user. The evolution of the pressure signals is recorded by the software during this stage.

Initialization stage: At the end of the extrusion stage, the injection piston, followed by the feeding piston, go back to their initial/upper positions.

The first four stages of the RheoART<sup>TM</sup>'s procedure correspond to the pre-shear step. It is defined by four parameters, depicted in Figure 2.12a. They are:

- i) rotation speed of the injection piston ( $V_r$ ),
- ii) descending speed of the feeding piston ( $V_d$ ),
- iii) relaxation time ( $t_r$ ) and
- iv) shear opening ( $O$ ).

Increasing the rotation and descending speeds of the feeding piston ( $V_r$ ,  $V_d$ ) provides more shear to the fluid during the pre-shearing stage. Increasing the relaxation time ( $t_r$ ) gives the fluid more time to eliminate residual stresses and homogenize its temperature. The shear opening corresponds to the gap created between the injection piston in its initial/upper position and the injection chamber (Figure 2.12a). The shear opening relates to the geometry of the zone of transition between the shear and injection chamber. A small shear opening restricts the transfer of fluid and increases the shear rate. Increasing the shear opening facilitates the transfer of fluid but decreases the shear encountered by the fluid during this transition.

Cylindrical dies are the most common type of dies used in capillary rheometers. They are made of tungsten carbide with an entrance angle of 90°. For the rheological characterization, dies of different dimensions are used. Dies of different lengths are used to vary the L/D ratio of the die. This variation allows us to carry out pressure corrections. Dies of different diameters are used to highlight the slip phenomenon and consequently determine wall slip velocities. The influence of the geometry (die length and diameter) on the flow curves is presented in Chapter 3.2. The dimensions of the different dies used in this work are mentioned in Table 2.3.

Diameter (mm)	Length (mm)	L/D ratio
0.93	0	0
	3.72	4
	7.44	8
	14.88	16
1.39	0	0
	5.56	4
	11.12	8
	22.24	16
2	0	0
	8	4
	16	8
	32	16

**Table 2.3** – Dimensions of the cylindrical dies.

### Data analysis of capillary rheometer measurements

The experiments conducted on the RhéoART™ are governed by the input parameters and the aforementioned pre-shearing conditions. The input and pre-shear conditions of the RhéoART™ are:

#### Input conditions

- 1) Temperature (T),
- 2) Die geometry,
- 3) Purging speed ( $V_p$ ),
- 4) Shear rates imposed ( $\dot{\gamma}_a$ ) and
- 5) Duration of each cycle of shear rate (t).

#### Pre-shear conditions

- 1) Rotation speed of injection piston ( $V_r$ ),
- 2) Descending speed of feeding piston ( $V_d$ ),
- 3) Relaxation time ( $t_r$ ) and
- 4) Shear opening (O).

#### Result/Output

Pressure drop ( $\Delta P$ ).

After setting the input and pre-shear conditions, the elastomer is put under flow and it experiences shear stress at the walls. The pressure drop ( $\Delta P$ ) is measured in function of time by the pressure transducer. This evolution is used to obtain the shear stress. The elastomer is considered to be in steady state when the pressure drop stops evolving as a function of time. When the elastomer is sheared at the given shear rate, the pressure drop increases for a certain amount of time and it stops evolving. The elastomer is considered to be in the steady state at this moment. A plateau is attained and this value is considered as the corresponding pressure drop for data analysis purposes. Therefore, for each shear rate imposed, a suitable duration of shearing time must be chosen for the elastomer to attain the steady state. An example of the steady state values obtained from the evolution of pressure drop as a function of time is presented in Figure 2.13.

For the purposes of data analysis, the pressure drop is measured only in steady state conditions. Cylindrical dies are the most common type of dies used in capillary rheometers. For cylindrical dies, the apparent shear stress ( $\sigma_a$ ) and apparent shear rate ( $\dot{\gamma}_a$ ) are given by:

$$\sigma_a = \frac{R}{2L} \Delta P \quad \text{Equation 2.7}$$

$$\dot{\gamma}_a = \frac{4Q}{\pi R^3} \quad \text{Equation 2.8}$$

$$\dot{\gamma}_a = \frac{4V_d \cdot R_B^2}{R^3} \quad \text{Equation 2.9}$$

where  $R$  is the radius of the cylindrical die,  $L$  is its length,  $Q$  is the volume flow rate,  $R_B$  is the radius of the injection chamber and  $V_d$  is the descending speed of the injection piston.

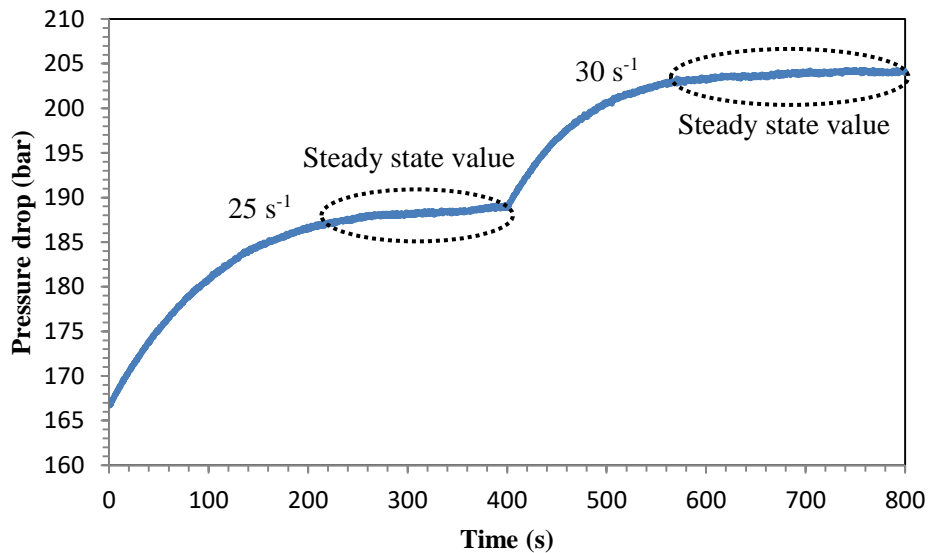


**Figure 2.13** – Evolution of pressure drop for SBR A using a die of diameter (D) 1.39 and length (L) 22.24 mm, at different shear rates.

To obtain the real wall shear stress ( $\sigma_w$ ) and the real shear rate ( $\dot{\gamma}_r$ ), the shear-thinning behavior of the fluid and the additional pressure drop due to the position of the pressure transducer must be taken into account. Bagley and Rabinowitsch corrections are used to obtain the real shear stress and real shear rate respectively.

### Bagley corrections

The pressure transducer is present at the end of the injection chamber. It cannot measure the pressure at the end of the capillary die. The additional pressure drop due to the position of the pressure transducer can be corrected with the use of Bagley corrections. Also, the constriction between the injection chamber and the capillary die is neglected. Moreover, the die swell at the exit of the capillary die is not taken into account by the pressure transducer (Figure 2.14).

The Bagley corrections take into account the inlet and outlet components of pressure to obtain the corrected pressure value. However, these corrections can only be carried out under specific assumptions (capillary assumptions), which are:

- flow is incompressible and well established,
- product is homogeneous,
- no slip at the wall,
- no influence of the pressure on the viscosity.

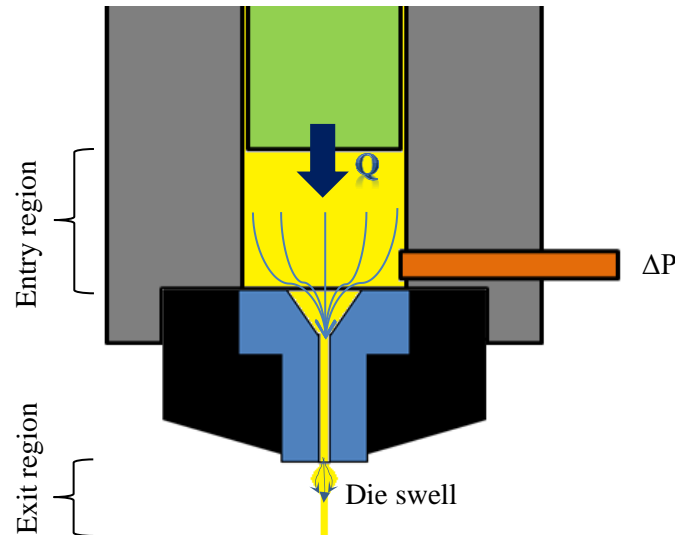


**Figure 2.14** – Converging flow at the capillary inlet and velocity profile at the outlet.

Bagley corrections were carried out at a given flow/shear rate by plotting the pressure drop as a function of the  $L/D$  ratio for a given capillary die. For each shear rate, a straight line must be obtained intersecting the y-axis on its positive side and the x-axis on its negative side. The y-axis intercept ( $\Delta P_o$ ) is considered as the entrance pressure correction while the x-axis intercept ( $e$ ) is considered as the added capillary length. This fictitious length corresponds to the additional capillary length required to obtain a pressure drop of  $\Delta P_o$ . An example of a typical Bagley corrections curve is shown in the Figure 2.15.

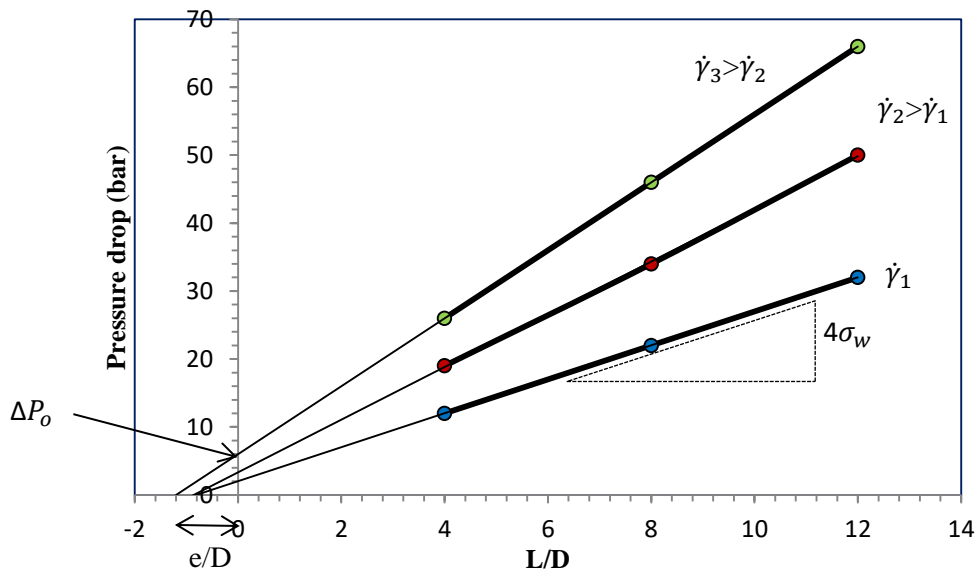


**Figure 2.15** – Bagley corrections principle.

Bagley corrections remove the influence of the capillary length ( $L/D$ ) on the shear stress developed in the die by providing a single value of corrected shear stress for the capillaries dies of the same diameter. The corrected pressure drop ( $\Delta P_c$ ) and the corrected wall shear stress ( $\sigma_w$ ) obtained through the Bagley corrections are given by:

$$\Delta P_c = \Delta P - \Delta P_o \quad \text{Equation 2.10}$$

$$\sigma_w = R \frac{\Delta P}{2(L + e)} \quad \text{Equation 2.11}$$

Similar to the Mooney method, the most important difficulty of the Bagley method is the attainment of linear curves. The non-linearity of these curves is probably a result of a lack of respect to the capillary assumptions. Deviation from the assumptions can result in the invalidity of the Bagley method. Such invalid curves can lead to significant errors on the wall shear stress estimations. Consequently, at least three dies (more than two) of different L/D ratios and same diameter are used while applying the Bagley corrections. The slope of the  $\Delta P$  vs L/D curves for a given shear rate is equal to four times the real wall shear stress. Thus, the corrected shear stress is obtained for each apparent shear rate through the Bagley corrections.

### Rabinowitsch corrections

The shear-thinning behavior of the fluid is taken into account by the Rabinowitsch corrections. These corrections use the real wall shear stress value. Thus, they are used after the Bagley corrections to obtain the real shear rate ( $\dot{\gamma}_r$ ). In this method, the wall shear stress ( $\sigma_w$ ) is plotted as a function of the apparent shear rate ( $\dot{\gamma}_a$ ) as shown in Figure 2.16. Rabinowitsch corrections are valid only in the cases of validity of the capillary assumptions. The real shear rate is determined by:

$$\dot{\gamma}_r = \frac{3m + 1}{4m} \dot{\gamma}_a \quad \text{Equation 2.12}$$

where  $m = \frac{\partial[\log(\sigma_w)]}{\partial[\log(\dot{\gamma}_a)]}$  is the shear-thinning index.  $m$  usually varies from 0.2 to 0.6 for polymers and from 0.1 to 0.3 for elastomers.

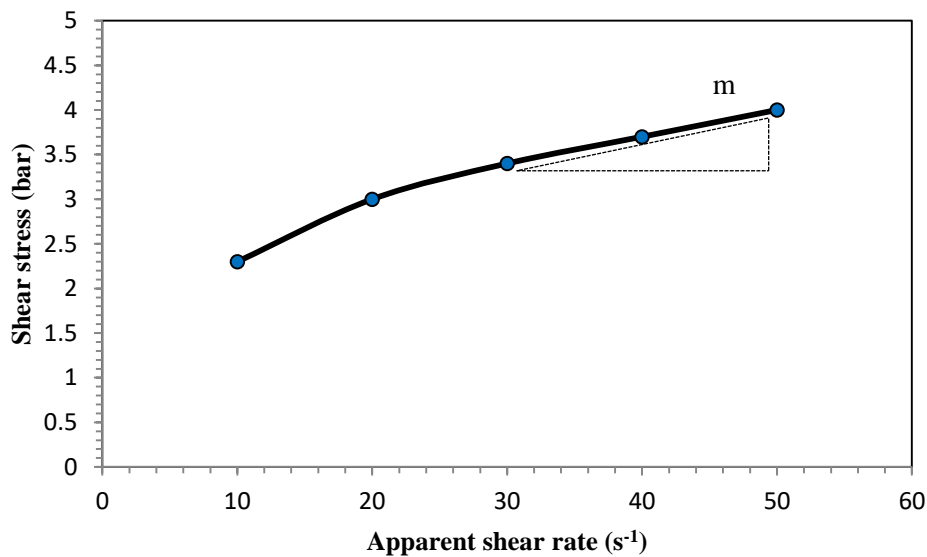


Figure 2.16 – Principle of Rabinowitsch corrections.

The corrected shear stresses and shear rates obtained through these corrections permit us to calculate the real viscosity ( $\eta_r$ ) of the elastomer. The relationship to obtain the viscosities is given by:

$$\eta_r = \frac{\sigma_w}{\dot{\gamma}_r} \quad \text{Equation 2.13}$$

### 2.2.2. Probe tests

In this work, probe tests were carried out to predict the amount of energy required to break the adhesive bonds between the molten polymer and the walls of the internal mixer during internal mixing. Considering the geometry and the mode of mechanical stress loading (shear) in an internal mixer, adhesive shear tests are more appropriate to characterize the adhesion energy. However, it is

difficult to construct a geometry which is similar to the flow channels observed in internal mixers. As it is difficult to reproduce the type of shear that is experienced in the internal mixer, the adhesion energy was characterized with tensile tests. Tensile tests were chosen over shear tests due to the ease of use and their simple geometry which is simpler to fabricate in comparison to shear tests. The probe tests were carried out not to obtain the exact adhesion energy values of the fluids during internal mixing but rather to obtain an order of magnitude of this energy.

As the operating temperatures of the molten polymers are different, two different equipment were used to characterize energy of adhesion of the molten polymers. The rubber products were characterized at high temperatures with the help of an Instron machine equipped with a heating system. On the other hand, the silicone fluid was characterized at ambient temperature with the help of a Zwick tensile machine. The Instron and Zwick apparatuses are presented below.

### Instron apparatus

The Instron apparatus consists of an Instron tensile machine equipped with a heating system and a 100 N force sensor. The adhesion energy of the rubber products could be characterized at 100°C, the reference temperature of the rheological characterization, with the plane-plane geometry (Figure 2.22a). However, a layer of adhesive or backing is used with this geometry. The use of backing layers is not encouraged as they can provide superior adhesion energies.

Alternatively, the sphere-plane geometry can be used (Figure 2.22b). But at 100°C, the thermal expansion of the polymer melt is significant resulting in the lack of perfect adherence with the contact substrate. Thus, probe tests were carried out at 40°C, 60°C and 80°C. The prediction technique described in Chapter 1.5.2 can be used to find the adhesion energy of the fluids at 100°C.

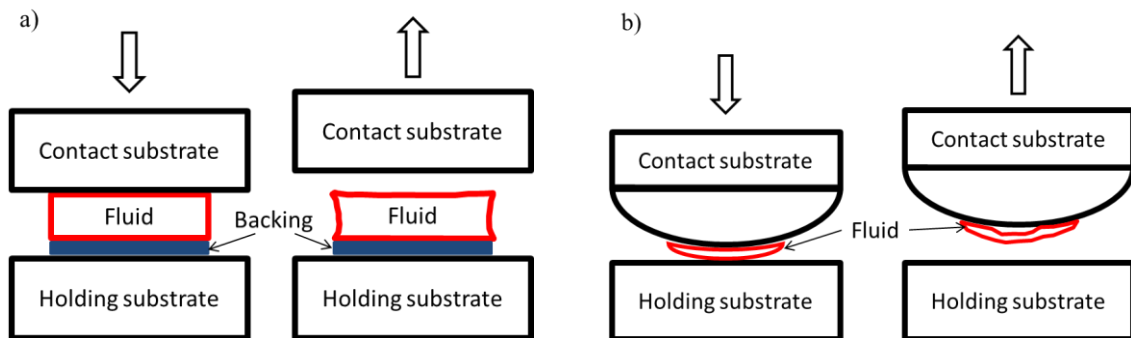


Figure 2.22 – a) Plane-plane and b) Sphere-plane geometry of tack tests with Instron apparatus.

Initially, the contact and holding substrates were heated to the desired temperatures. The molten polymer sample was placed in contact with the contact substrate and a pre-defined contact pressure was applied on the molten polymer for a pre-defined contact time by the descending contact substrate. After the contact time has passed, a displacement was exerted on the molten polymer by the ascending contact substrate. The resistance of the material to undergo tension, corresponding to the adhesion energy, was measured by the force sensor as a function of time ( $F(t)$ ). The total force required to break the adhesion can be calculated by integrating the force response (Figure 1.34) during the tensile stage. This resistance corresponds to the energy of adhesion ( $\Delta E$ ) and the energy is given by:

$$\Delta E = \int_0^{\infty} \frac{F(l) \cdot dl}{S} \quad \text{Equation 2.14}$$

where  $l$  is the displacement and  $S$  is the apparent surface area of the substrate.

The evolution of the force response during the tensile stage can be used to determine the nature of the contact failure (adhesive or cohesive failure). A clean break in the Force vs Time graph (red curve of Figure 2.23) indicates an adhesive failure between the two substrates whereas the signature of

cavitation and fibrils in the graph (blue curve of Figure 2.23) can indicate a cohesive failure. Additionally, the presence of any macroscopic or microscopic traces on either substrate indicates a cohesive failure.

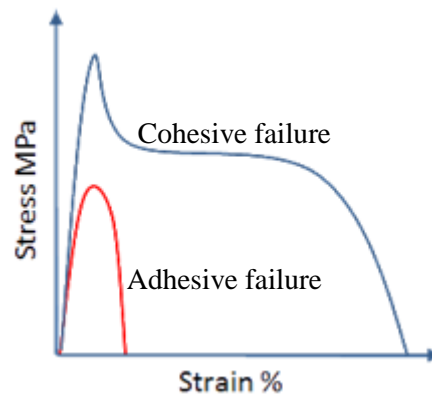


**Figure 2.23** – Example of a Stress vs Strain graph for an adhesive and cohesive material [Abbott, 2015].

The plane-plane geometry provides a uniform contact pressure across the surface of the sample. On the other hand, the sphere-plane geometry provides a maximum stress at the center of contact. The contact pressure varies with  $1/r$  across the rest of the sample surface, where  $r$  is the distance from the center of contact. Using these methods, we obtain two different estimations of the adhesion energy of the rubber products at  $100^{\circ}\text{C}$ . The energy of adhesion obtained from two different tack tests cannot be compared as they do not provide similar results [Duncan and Lay, 1999; Creton and Ciccotti, 2016]. Four stark differences exist between these two methods: 1) the shape of the contact, 2) the presence or absence of the backing layer, 3) the dimensions of the contact substrate and 4) the dimensions of the molten polymer sample.

For the plane-plane geometry tack tests, the molten polymer samples were prepared in the form of a cylinder of 4 mm length and 16 mm in diameter. One side of the molten polymer sample is glued to the contact substrate. Care was taken to use the appropriate amount of glue required for these experiments. The dimension of the molten polymer samples for the sphere-plane geometry tests are that of a cylinder of 4 mm length and 14 mm diameter.

### Zwick apparatus

The Zwick apparatus consists of a Zwick tensile machine equipped with a 100 N force sensor. Substrates of steel and brass were used to study the influence of the substrate material on the adhesion energy of the molten polymer. The substrates were machined to provide a circular contact area whose diameter is 40 mm providing a contact area of  $5.024\text{ cm}^2$ . No backing layer was used on either substrate of the Zwick apparatus. Figure 2.24 depicts the different steps of the tack test.

A layer of molten polymer was placed on the stationary holding substrate (Figure 2.24a). The thickness of this molten polymer is 6 mm. The contact substrate was then brought into contact with the molten polymer at a pre-defined speed (Compression speed). The molten polymer was compressed to a thickness of 4 mm (Figure 2.44b). The contact substrate was maintained in contact with the molten polymer for a certain time (Contact time). After the contact time has passed, a tensile force was exerted on the molten polymer by the contact substrate as it moves in the opposite direction at a pre-determined speed (Tensile speed). The experiment was stopped when the force response saturates.

The initial (6 mm) and final thickness (4 mm) of the samples were maintained as constants during the experiments. The parameters which were varied during the experiment are:

- i) substrates used,

- ii) compression speed,
- iii) relaxation time and
- iv) tensile speed.

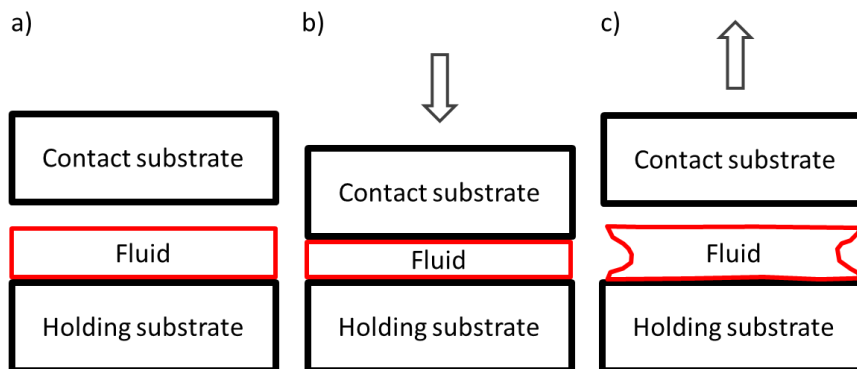


Figure 2.24 – Different stages of the tack test with Zwick apparatus.

### 2.3. Transparent flow cells

During the course of this work, two types of transparent flow cells were used to conduct flow observations. These tools include a transparent flat die and two transparent internal mixers. The transparent flat die was designed and developed to be fixed at the exit of the RhéoART™. The transparent walls of the flat die permit the flow observation of the elastomers along the flow channel. The objective of the transparent flat die was to obtain velocity field estimations under wall slip conditions to measure the wall slip velocities.

Two transparent internal mixers were used during the course of this work to conduct flow observations of the elastomers in an internal mixer. The design of these mixers varies from the traditional design of transparent internal mixers used for flow observations [Freakley and Wan Idris, 1979; Asai *et al.*, 1982; Sato *et al.*, 1981; Min and White, 1985, 1987 and Min, 1987a]. The Monocuve mixer, developed by Michelin, was used to conduct flow observations similar to those conducted by the aforementioned researchers. The simple geometry of the MaCROS mixer was used to conduct steady state observations of the free surfaces of viscous fluids. The geometry of the MaCROS mixer can be best described as a transparent counter-rotation Couette cell

The transparent flat die and the MaCROS internal mixer were developed in CEMEF by the workshop team during the course of this work.

#### 2.3.1. Transparent flat die

Flat dies, after cylindrical dies, are the second most common type of dies used in capillary rheometers. The transparent flat die developed is presented in Figure 2.25. It is mounted at the exit of the RhéoART™. While conducting experiments on the RhéoART™, the elastomer is extruded from the injection chamber through the flat die at an entry angle of 180°. The transparent flat die is heated with the help of heating elements and a thermocouple is used to measure the temperature of the metallic walls of the flat die. The observation of the flow across the die should permit the:

- observation of the melt flow front,
- determination of the velocity field,
- measurement of the flow velocities in steady state conditions and
- measurement of slip velocities along the metallic walls.

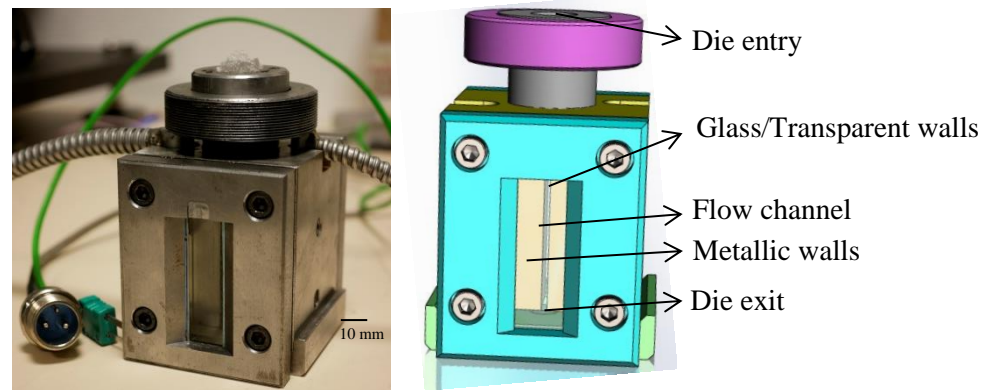


Figure 2.25 – The transparent flat die developed in CEMEF.

The flow channel of the flat die is in the form of a cuboid of length  $L$ , width  $W$  and thickness ‘ $h$ ’ (Figure 2.26b). The fluid enters the flow channel through the die entry. The fluid flows through the flat die along the four rectangular walls. The flow across the flow channel is observed through the transparent glass walls along the  $Lh$  planes of the flow channel. The transparent walls are made of annealed borosilicate glass and are sufficiently resistant to the stresses developed inside the flow channel. The  $WL$  planes are covered by two metallic walls made of 42CrMo4 steel with an average surface roughness ( $R_a$ ) of  $0.2 \mu\text{m}$ . These metallic walls are naturally opaque. The experimental setup for the observation of flow in the transparent flat die is presented in Figure 2.26.

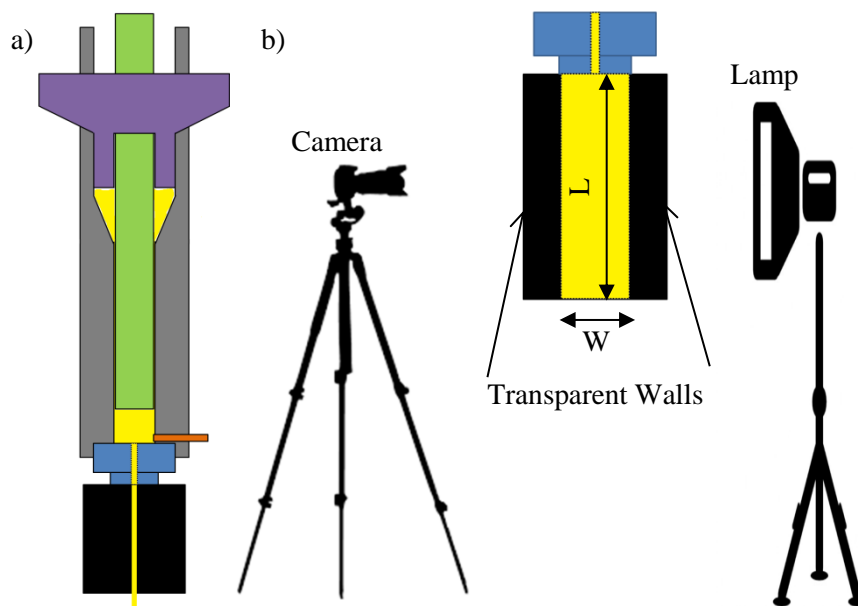


Figure 2.26 – a) Transparent flat die connected to the exit of the RhéoART™. b) Experimental setup of the transparent flat die.

The flow across the die was observed through the transparent borosilicate glasses with the help of a Panasonic G80 camera with an Olympus M.Zuiko (30 mm  $f/3.5$  Macro) objective. This camera was used for all the observation studies of this PhD work. The camera was positioned in front of one of these glass walls and a monochromatic lamp was placed on the other side (Figure 2.26b). The illumination provided by the monochromatic lamp can be controlled by adjusting its intensity or the distance between the flat die and the lamp. The quality of the video recording can be improved by controlling the aperture and shutter speed of the camera as well as adjusting the position of the camera with respect to the flat die. Appropriate illumination and recording conditions are required to obtain interpretable recordings of the elastomer flow.

To carry out viscosity measurements with a flat die, the following assumptions must be respected:

- Flow is incompressible and well established,
- Product is homogeneous,
- No slip at the wall,
- No influence of the pressure on the viscosity,
- The flow is not perturbed by the presence of lateral walls (a large W/h ratio is required),
- The pressure profile is linear.

To ensure that the pressure profile inside a flat die is linear, at least three pressure sensors should be placed within the flat die. However, due to the compact nature (small length) of the transparent flat die, it was difficult to place multiple heating elements and pressure sensors along the length of the lateral walls. Thus, the pressure drop ( $\Delta P$ ) across the transparent flat die was measured by the pressure transducer which is situated in the injection chamber of the RhéoART™. When the capillary assumptions are respected, the shear rates and wall shear stress can be obtained by:

$$\dot{\gamma}_a = \frac{6Q}{Wh^2} \quad \text{Equation 2.15}$$

$$\sigma_w = \frac{h}{2(1 + \frac{h}{W})} \frac{\Delta P}{L} \quad \text{Equation 2.16}$$

$$\dot{\gamma}_r = \frac{3m + 1}{4m} \dot{\gamma}_a \quad \text{Equation 2.17}$$

where  $m = \frac{\partial[\log(\sigma_w)]}{\partial[\log(\dot{\gamma}_a)]}$ ,  $Q$  is the volume flow rate,  $\dot{\gamma}_a$  is the apparent shear rate,  $\dot{\gamma}_r$  is the real shear rate and  $\sigma_w$  is the wall shear stress.

The dimensions of the transparent flat die were chosen as:

- Length (L): 50 mm,
- Width (W): 20 mm,
- Thickness (h): 2 mm.

In order to attain steady state flow in a flat die, a long flow channel is required. 50 mm was chosen as the length of the flow channel to provide a sufficiently long flow channel. A long flow channel also facilitates the flow observation as it provides a comparatively large zone of observation and longer observation times. The measurement of the pressure drop by the pressure transducer, situated in the injection chamber of the RhéoART™, allows us to know if the elastomer has achieved steady state or not. A thickness of 2 mm was chosen for the flat die to obtain high shear rates. One of the assumptions taken into account while working with flat dies is that the flow is considered to take place between two infinitely parallel plates (limited side wall effects). Flat dies with aspect ratios (W/h) of 10 or higher can be considered as infinitely parallel plates [Mourniac *et al.*, 1992; Silva *et al.*, 2015; Han, 1976]. Thus, a width of 20 mm, i.e. W/h=10, was chosen for the flat die.

### 2.3.2. Transparent internal mixers

The free surfaces of the fluid during mixing could be observed with the help of transparent internal mixers. However, these observations are complex and transient in nature. Two different transparent lab-scale internal mixers were used during the course of this work. The complexity of the observed free surfaces can be overcome with the simplified geometry of the Monocuve mixer. This geometry also gives transient flow observations. The MaCROS mixer was designed to carry out steady state observations of the free surfaces during mixing.

**2.3.2.1. Monocuve mixer**

The continual transfer of fluid from one mixing chamber to the other and the complex geometries of the rotors (Figure 2.27) makes the observations of free surfaces difficult. The use of a single mixing chamber with a simplified rotor geometry can overcome this complexity. The Monocuve mixer, developed by Michelin, overcomes this problem with the use of a single mixing chamber rather than two. This prevents the transfer of fluid from chamber to chamber simplifying the flow kinematics in the mixer.



**Figure 2.27** – Example of the rotor and mixing chamber geometry used in lab scale mixers [Mirshahidi, 2011].

Two different rotors were used with the Monocuve mixer (Figure 2.28). These rotors have a simple 2D profile. The flow observations observed with 2D rotors will be simpler in comparison to those observed with 3D rotors. Thus, the use of a single mixing chamber and simplified rotor geometries can simplify the flow behavior during mixing. The Monocuve mixer was equipped with two different rotors with a simplified 2D profile (Figure 2.28). The cam rotor is better equipped to shear the fluid due to: i) its small thin flow gap and ii) constricting flow channel at the tip. On the other hand, the round rotor provides low shear rates and displaces the fluid in the mixer.

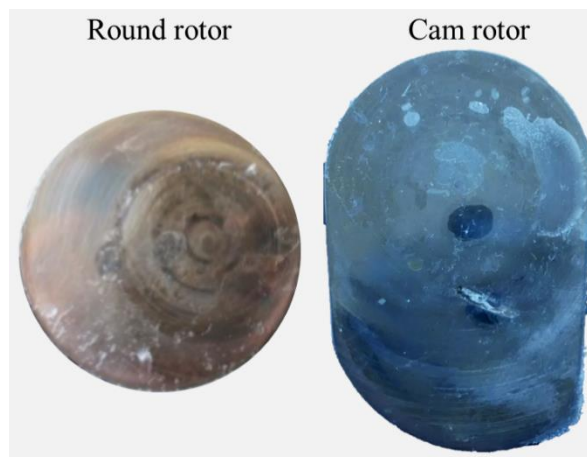


**Figure 2.28** – Round and cam rotor of the Monocuve mixer.

The thin flow gap of an internal mixer represents the smallest gap between the rotor blades and the walls of the mixing chamber. The fluid, as it flows through the constricting zone between the rotor blades and the walls of the mixer, undergoes the maximum shear at the thin flow gap. A 2D flow permits the better observation of the flow behavior of the rubber at the walls of the mixer. The objective of the Monocuve mixer is to observe simplified flow to discern the free surfaces of the fluid at the interface (fluid/metal/gas contact line) during flow, as shown in Figure 2.29.

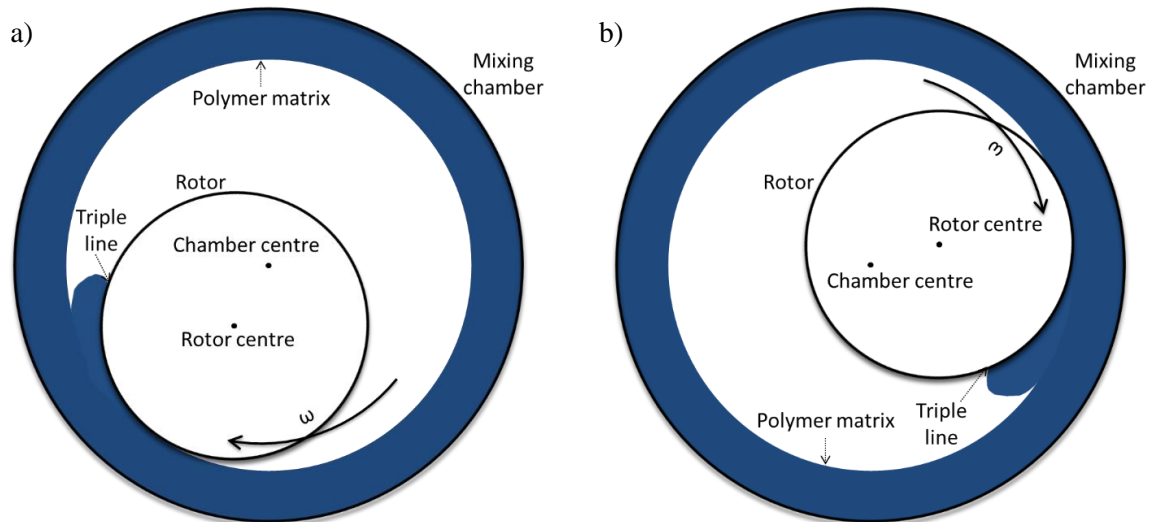


**Figure 2.29** – Principle of Monocuve mixer. a) Position 1 of the rotor and b) Position 2 of the rotor.

The Monocuve mixer has a static cylindrical mixing chamber. It has a diameter of 100 mm with a thickness of 30 mm. The mixing chamber is equipped with a transparent window for observation. The transparent window comprises of a circular sheet of polycarbonate (PC) supported by a cylindrical quartz block. The PC sheet and the quartz block are transparent and permit the flow observation with the help of the camera and a lamp for illumination. The PC sheet is screwed on to the quartz block to provide the necessary physical support to resist the high stresses. The rigid quartz block can fracture if the rotor rubs across its surface during rotation. The PC sheet prevents this contact, protecting the quartz block from such damage. The PC sheet is worn out over a series of tests and must be replaced.

The rotors rotate around the chamber center in the clockwise direction and their maximum rotation speed is limited to 150 rpm. The round rotor has a diameter of 60 mm and a thickness of 30 mm. The center of the round rotor is 10 mm eccentric from the center of the mixing chamber. Thus, the use of the round rotor provides a thin flow gap of 10 mm. The dimensions of the cam rotor are confidential and will not be shared here. The cam rotor provides a thin flow gap of 2 mm and its axis of rotation is the center of the mixing chamber.

The rotors and the mixing chamber are made out of 42CrMo4 steel and are tempered with oil to obtain a hardness of 54 HRC. The temperatures of the rotor and the chamber are regulated by the flow of a thermo-regulated fluid bath (oil). Thermocouples present at the surfaces of the rotor and the chamber measure the surface temperature of both surfaces. These temperatures are used as a feedback to control the temperature of the thermo-regulated fluid. Illumination of the transparent window is achieved with the help of a lamp. The experimental setup of the Monocuve mixer is presented in Figure 2.30. As it can be seen, the hopper can be used to introduce the fluid in the mixing chamber. The fluid can be introduced before or during the rotor's rotation. The fluid is cut into small blocks before being introduced through the hopper to facilitate its processing.

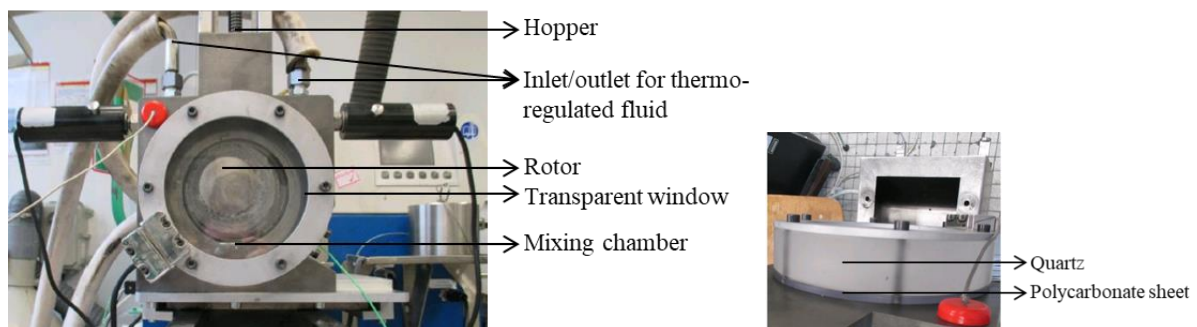


**Figure 2.30** – Experimental setup of Monocuve apparatus.

### 2.3.2.2. MaCROS mixer

Couette cells are typically used in applications where they are completely or nearly completely filled [de Haas *et al.*, 1998; Kasolang *et al.*, 2012]. The geometry of the MaCROS mixer can be best described as an eccentric counter-rotation transparent Couette cell. The principle of the MaCROS mixer is to use counter-rotation cylinders to stabilize the position of the fluid permitting steady state observations of the free surfaces during shear flow. While working in counter-rotation conditions, the fluid's position can be stabilized at optimal angular cylinder velocities.

To observe the free surfaces of the viscous fluid under shear flow, we work at fill factors lower than those used in industrial mixers. By varying the fill factor of the fluid introduced in to the prototype, the free surfaces can be observed between i) the inner cylinder surface and a layer of fluid, ii) both the inner and outer cylinder surfaces. These types of observations are obtained at large and small volume fill factors respectively (Figure 2.31a and 2.31b). Transparent windows on either side of the cylinders permit the flow observation by the transmission of light. The two cylinders rotate around their respective centers. The eccentricity of the axes of rotation of the cylinders provides a thin flow gap as small as 3 mm to obtain high shear rates.

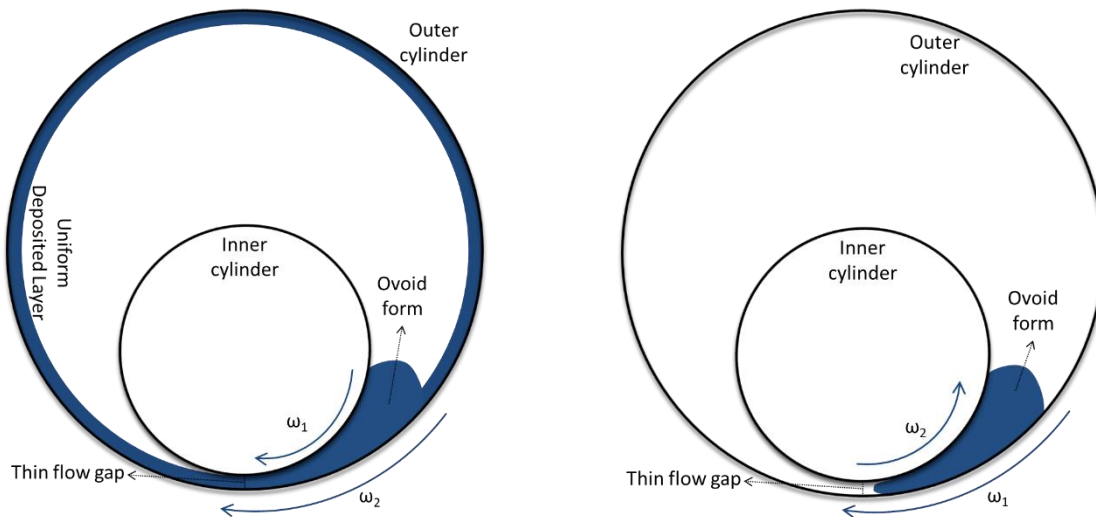


**Figure 2.31** – Schematic representation of a) large volume stabilization and b) small volume stabilization.

The computer-aided design (CAD) of the prototype is presented in Figure 2.32. The MaCROS mixer and its auxiliary systems are presented in Figure 2.33. The main components of the mixer are:

- Outer cylinder,
- Inner cylinder,
- Transparent windows,
- Heating system,
- Recording system,
- Power control,
- Interface and recording system.

Additional views of the CAD design are presented in Appendix I.

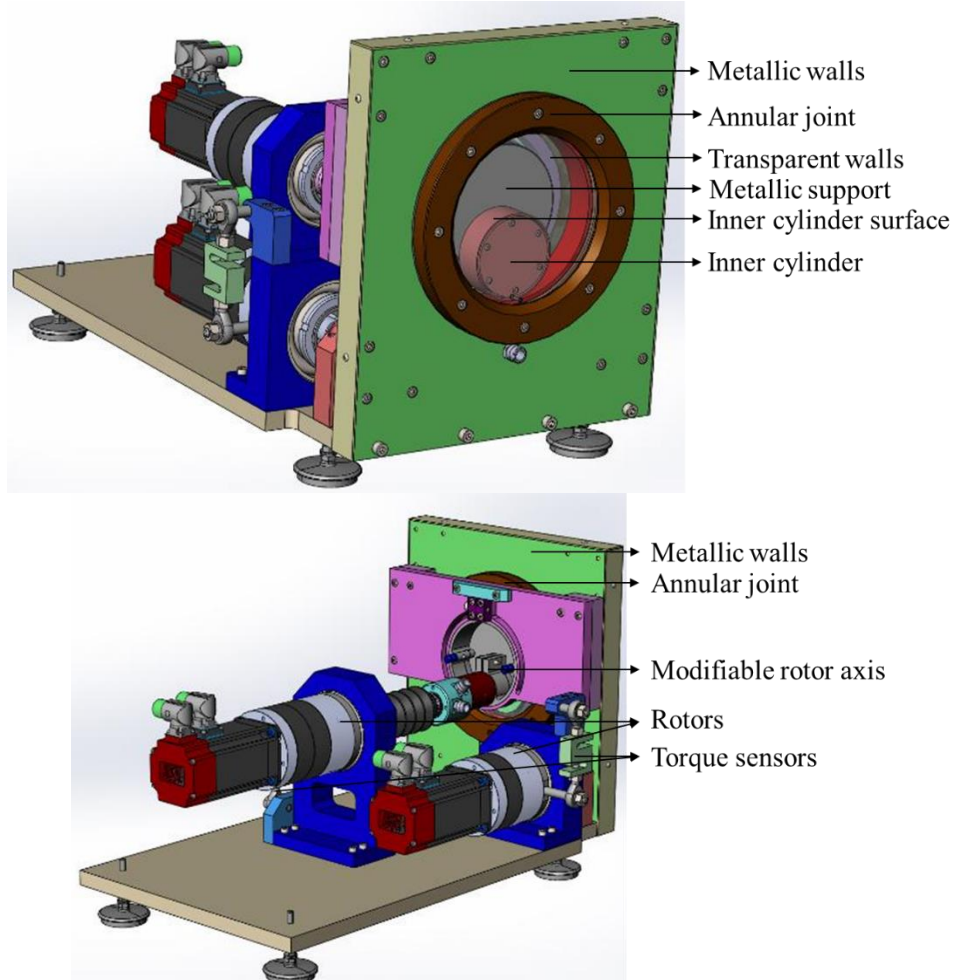


Figure 2.32 – CAD design of the MaCROS mixer.

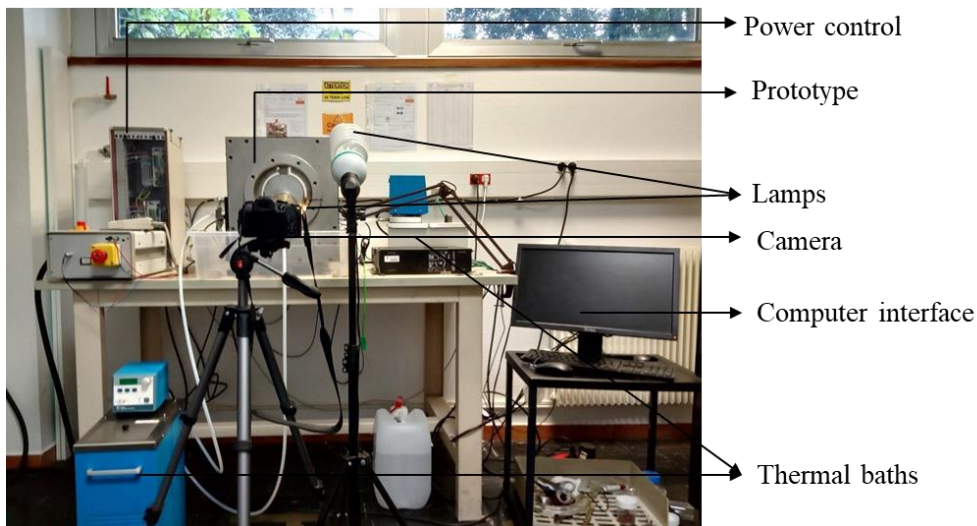


Figure 2.33 – MaCROS mixer and its auxiliary systems.

Outer cylinder:

The outer cylinder consists of an annular surface which is welded onto a gear (Figure 2.34). The gear, along with the outer cylinder surface, is set in rotation by the motor whose axis of rotation is shown in Appendix I. The motor is a brushless gear motor from MDP company (Neyron, France) which can provide a maximum torque of 100 Nm. As the motor is set to rotation, the gear and the annular outer

cylinder surface. The rotational axes of the inner and outer cylinder surfaces were chosen to be perpendicular to the gravitational axis to facilitate flow observations. As the influence of gravity on the flow behavior of the viscous fluids is negligible, this does not impact the flow behavior.

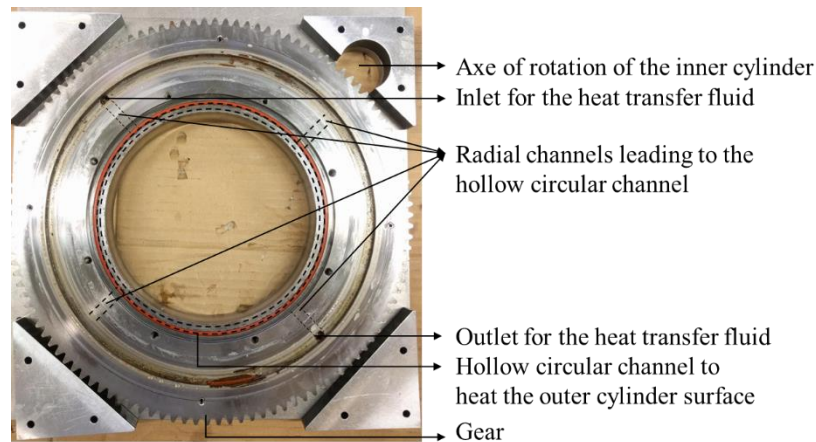


Figure 2.34 – Outer cylinder system of the MaCROS mixer.

The annular surface has a thickness ( $W$ ) of 30 mm and is made up of 42Cd4 steel. A small thickness was chosen for the outer cylinder surface to limit the torque required to shear the viscous fluids between the cylinder surfaces. A radius ( $R_1$ ) of 89.5 mm was chosen to have a large zone of observation for the observations. The gear and the outer cylinder surface are enclosed within two metallic walls.

A reservoir behind the outer cylinder surface allows the heat transfer fluid to heat the surface by heat conduction. The reservoir is equipped with an inlet and outlet canal to create a closed-circuit flow for the heat transfer fluid. The roughness of the outer cylinder surface can be corrected to study the impact of surface roughness on the interfacial flow behavior.

#### Inner cylinder:

The different parts of the inner cylinder are presented in Figure 2.35. The inner cylinder consists of a hollow cylinder with a shaft (depicted in green). The shaft is driven by a brushless rotor from MDP company which can provide a maximum torque of 50 Nm. The surface of the inner cylinder (depicted in red) is heated with the closed-circuit flow of the heat transfer fluid. The shaft is equipped with an inlet and outlet valve for the heat transfer liquid to enter and exit this hollow space. A perforated plate is used to ensure the flow of the heat transfer fluid to the surface of the inner cylinder. The inner cylinder surface is a removable surface which can be used to change the surface. For this work, two inner cylinder surfaces were prepared with 42Cd4 steel and CuZn40Pb3 brass.

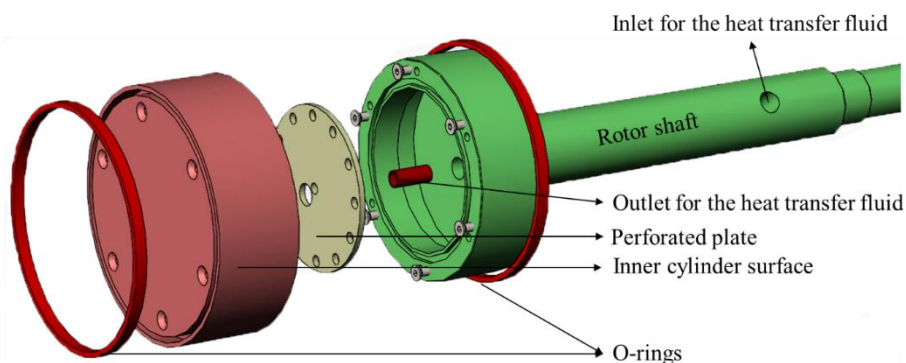


Figure 2.35 – Exploded view of the inner cylinder system.

This permits us to work under:

- i) Similar surface condition: 42Cd4 steel surface for the inner and outer cylinders,
- ii) Dissimilar surface condition: 42Cd4 steel for the outer cylinder and CuZn40Pb3 brass surface for the inner cylinder.

These surface conditions permit us to study of the impact of the nature of surface on the interfacial flow behavior. In addition, the roughness of the cylinder surfaces can be varied to study the influence of roughness on the interfacial flow behavior. The roughness of the brass inner cylinder surface cannot be varied by polishing the surfaces with emery sheets.

To prevent the contact between the inner cylinder surface and the transparent windows, a small gap is provided between the two surfaces. The contact of these surfaces during rotation could result in the generation of a large amount of friction. The fluid tends to enter this gap during the rotation of the cylinders. The motors would require a substantial amount of torque to shear the fluid within this minute gap. This should be avoided for two purposes:

- i) the fluid in the gap creates friction which leads to a rise in torque required,
- ii) a significant amount of fluid is lost in the gap during the course of the experiment.

To prevent the fluid from entering this gap, special O-rings made of brass were designed (Figure 2.35). Trenches were machined on the front and the back of the inner cylinder surface to place the O-rings. Springs are inserted between the O-rings and the trenches to limit the friction developed between the O-rings and the transparent windows while maintaining the contact between the two surfaces.

The inner cylinder surface comprises a cylindrical surface ( $R_2$ ) of 43.75 mm radius. The thickness of the inner cylinder is similar to that of the outer cylinder ( $W = 30$  mm). The radii of the outer ( $R_o$ ) and inner cylinder ( $R_i$ ) were chosen to have a ratio ( $R_o/R_i$ ) of almost 2:1. The rotational axis of the inner cylinder is 42.75 mm below the rotational axis of the outer cylinder. This provides a thin flow gap ( $h_0$ ) of 3 mm, to obtain shear rates similar to those found in industrial mixers. The minimum thin flow gap was chosen so that we have a  $W/h_0$  ratio of 10. Normally, at such ratios, the influence of side walls can be neglected [Han, 1976]. Nevertheless, this is not true in cases of rotating side walls/windows.

A variable thin flow gap can be achieved by moving the axis of rotation of the inner cylinder. A double eccentric joint is used to displace the rotation axis of the inner cylinder (Figure 2.36). An exploded view of this setup is presented in Appendix I. The eccentricity of the axes of rotation can be varied from 34.75 to 42.75 mm providing a thin flow gap varying from 3 to 11 mm. A circular bridle of 90 mm diameter (Figure 2.36) is provided to ensure the rigidity of the entire inner cylinder system.

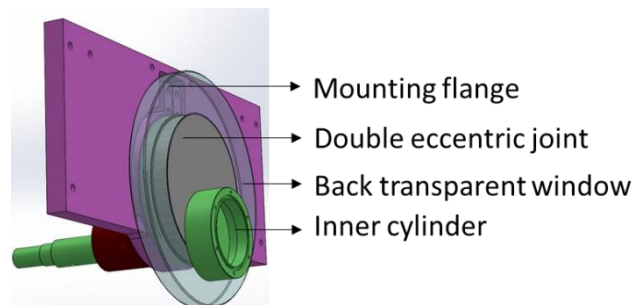


**Figure 2.36** – Movable axe of rotation.

Transparent windows:

The observation of the fluid flow is ensured through the transmission of light through the front and back transparent windows. The transparent windows are made of annealed borosilicate glass to resist

the stresses developed at the high operating temperature ( $>100^{\circ}\text{C}$ ). The transparent windows are fixed to the rotating gear of the outer cylinder with the help of screws and annular joints (Figure 2.34). Thus, the transparent windows rotate at the same velocity as the rotating gear. It was difficult to design stationary windows due to the compact geometry and the different moving parts of the MaCROS mixer. The rotation of the transparent windows creates a drag effect on the flow, thus creating a 3D flow field. This drag effect will be presented in Chapter 4.4.1.

The introduction of the fluid into the mixer is achieved by dismantling the front window, introducing the fluid and then reassembling the front window. The front transparent window is circular with a thickness of 15 mm and a diameter of 205 mm. The front window is equipped with a small hole to permit a thermocouple to pierce the fluid at the end of the experiment (when the cylinders are at rest) and measure the fluid temperature. Care was taken to provide easy assembly and disassembly of the front transparent window to facilitate the introduction of the fluid and for cleaning purposes. The back transparent window has an annular form (inner diameter = 115 mm; outer diameter = 205 mm) with the same thickness (15 mm) as the front transparent window. The bridle is fixed to the annular back transparent window.

### Heating system:

The inner and outer cylinder surfaces are heated by the conduction of heat by the flow of the heat transfer fluid. Two thermal baths are used to transfer the heat transfer fluids to the reservoirs of the inner and outer cylinder. The heat regulation is controlled by two thermocouples placed in each thermal bath. The heat transfer fluid is a silicone based fluid commercially sold as Julabo™ 8940114. It is transmitted with the help of Teflon tubes to the inlets and the outlets of the reservoirs of the inner and outer cylinder.

### Recording system:

The flow observations can be recorded with the camera, which is placed on a tripod. The position of the tripod can be adjusted to focus on the desired zone. The observation zone is illuminated with the help of two lamps placed on either side of the transparent windows. The illumination of the fluid from the front and the back enables us to effectively identify the shape of the stabilized fluid. The brightness and position of the lamps can be controlled to provide the optimal conditions of observation.

### Power control:

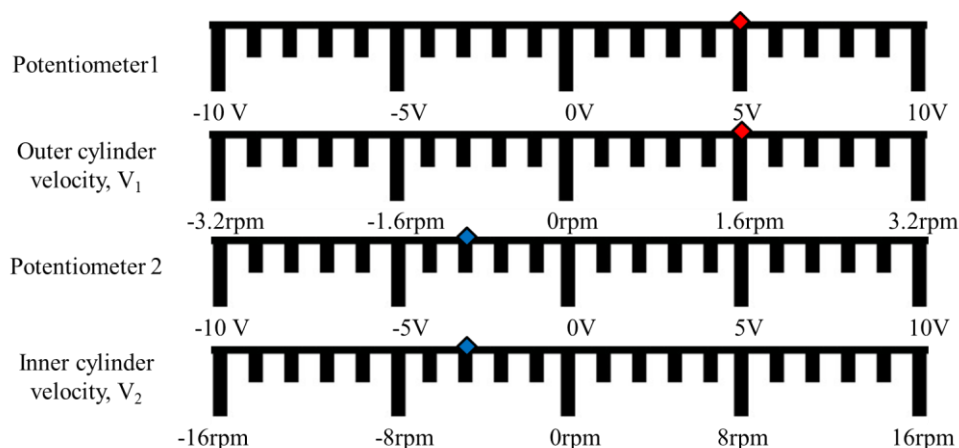


**Figure 2.37** – Velocity control of cylinders with adjustable potentiometers ( $V_1 = -1.6 \text{ rpm}$   $V_2 = 4.8 \text{ rpm}$  in this example).

Brushless motors from the MDP company are used to control the cylinder velocities. The rotational speeds of the motors are measured with the help of tachymeters. In order to have precise control of the cylinder speeds, the rotational speeds of the inner and outer cylinder were limited to 16 and 3.2 rpm

respectively. The rotor movements (rotational speeds and direction) are independent and shear rates up to  $15 \text{ s}^{-1}$  could be obtained in the counter-rotation condition. The velocity of both the cylinders could be adjusted with independent potentiometers. The potentiometers can deliver a tension of -10 to 10 V to their respective variators. To control the velocities of the cylinders, the tension provided by the potentiometers was scaled with the LabVIEW software. Figure 2.37 (above) shows how the velocity of the cylinders are controlled with the potentiometers.

### Interface:

A LabVIEW program was created to act as an interface to display and record the different variables measured by the sensors (cylinder velocities, temperatures and torques). The information from these sensors (two tachymeters, two torque sensors and the three thermocouples) are displayed on a personal computer and can be recorded as a function of time to study the evolution of these variables during the experiment. The rotational speeds and directions of the cylinders are measured with the help of two tachymeters and controlled with the help of a joystick. The torque, corresponding to the resistance exerted by the fluid to flow, is measured on each motor axis with load sensors via 100 mm lever arms.

In addition to the two thermocouples placed in the thermal baths, two thermocouples are placed on the hollow spaces of both cylinders to measure the temperature of the heat transfer fluid in these spaces. The temperatures of the heat transfer fluid recorded inside the reservoir are considered as the temperature of the cylinder surfaces. A third thermocouple can be inserted through the front transparent window to measure the temperature of the fluid at rest at the end of the experiment.

The design of the prototype can be used to observe the free surfaces of the fluid at the interface of the inner and outer cylinder under the counter-rotation conditions. The prototype enables us to perform flow observations under different conditions of:

- fluid used,
- volume of fluid introduced,
- rotational speeds,
- rotational directions,
- thin flow gaps,
- temperature of the inner and outer cylinder surfaces,
- roughness of the inner and outer cylinder surfaces,
- nature of the inner cylinder surface.

### Conclusions

In order to characterize the flow behavior at the interface of rubber products, three pure rubber products and a rubber compound were chosen. The pure rubber products were chosen for their use in tire manufacturing and their commercial availability. They were also comparatively transparent to most rubber products. To investigate the influence of adhesion on the flow behavior at the rubber/metal interface, a rubber compound was formulated to provide a superior energy of adhesion to the pure rubber products. A silicone fluid was used as a model fluid to conduct observations under shear in the MaCROS mixer at ambient temperature.

Oscillatory rheometers were used to characterize the viscoelastic behavior of the fluids. The RhéoART capillary rheometer was used to characterize the flow behavior of the rubber products at large deformation rates. Analytical methods, like the classic Mooney method, can be used to estimate the wall slip velocities. A transparent flat die was designed and developed during the course of this work to observe the flow of the elastomers along the thickness of its flow channel and conduct velocity field estimations.

The estimation of the energy of adhesion of the fluids is crucial to understand the influence of adhesion during the interfacial flow behavior of the fluids. Probe tests can be used to estimate the energy of adhesion exhibited by the fluids. Adhesive shear tests are more appropriate to characterize the adhesion energy exhibited by the fluids during mixing. However, it is difficult to construct a geometry for the tack tests which is similar to that observed in internal mixers. Probe tests were chosen to estimate the energy of adhesion of fluids due to their simplicity and ease of use. Due to the difference in the operating temperatures of the fluids, two different equipment were used to characterize adhesion energy of the fluids at their respective operating temperatures.

Lab-scale internal mixers equipped with a transparent window, can be used to conduct *in-situ* flow observations of the process. However, the observation of the free surfaces of the fluid at the interface with transparent internal mixers is difficult. This is due to the complexity and transient nature of the flow observations. The complexity of the observations could be avoided by working with a single mixing chamber and a 2D rotor, similar to the Monocuve mixer developed by Michelin. To conduct steady state flow observations in internal mixing conditions, an eccentric counter-rotation Couette cell (MaCROS mixer) was designed and developed. The MaCROS mixer can be used to characterize the free surfaces of the fluid and the interfaces with metal walls (fluid/metal/gas contact lines) under different conditions of: i) fluid used, ii) volume of fluid, iii) shear rates (rotational speeds), iv) thin flow gaps, v) surface temperatures, vi) roughness of the surfaces and vii) nature of the surfaces.

The different fluids, characterization tools and transparent flow geometries described in the chapter were used to study the wall slip behavior (Chapter 3), movement of free surfaces (Chapter 4) and the role of adhesion during shear flow (Chapter 5).

### Résumé en français

Afin de caractériser l'écoulement interfacial des caoutchoucs, quatre produits ont été choisis : trois caoutchoucs purs et un mélange de caoutchouc. Les caoutchoucs purs ont été choisis pour leur utilisation dans les pneus et leurs disponibilités commerciales. Ils sont aussi relativement transparents en comparaison avec la plupart des caoutchoucs. Le mélange de caoutchouc a été formulé avec l'objectif d'étudier l'influence de l'adhérence sur l'écoulement à l'interface caoutchouc/métal. La formulation de ce mélange doit fournir une énergie d'adhésion supérieure aux caoutchoucs purs. Un fluide silicone a été choisi comme fluide modèle pour effectuer des observations sous cisaillement dans le mélangeur MaCROS à température ambiante.

L'estimation de l'énergie d'adhésion des fluides est cruciale pour la compréhension de l'influence de l'adhésion sur le comportement d'écoulement interfacial des fluides. Les tests d'adhérence peuvent être utilisés pour estimer l'énergie d'adhésion présentée par les fluides. Les essais en cisaillement sont plus appropriés pour la caractérisation de l'énergie d'adhésion. Cependant, il est difficile de construire des tests d'adhérence avec une géométrie similaire à celle d'un mélangeur interne. Les tests de tack en traction ont été choisis pour estimer l'énergie d'adhérence des fluides en raison de leur simplicité et facilité d'utilisation. Les caoutchoucs et le fluide silicone ont été caractérisés à différentes températures. À cause de cette différence, deux équipements différents ont été utilisés pour la caractérisation de l'énergie d'adhérence.

La visualisation directe du mélange interne est réalisée avec des mélangeurs internes à l'échelle laboratoire équipé des fenêtres transparentes. Cette visualisation fournit des informations cruciales pour comprendre et améliorer le procédé. Pourtant, ces observations sont complexes et transitoires. De plus, l'observation des surfaces libres du fluide à l'interface est difficile.

Cette complexité de géométrie peut être évitée en travaillant avec une géométrie simplifiée, comme le mélangeur Monocuve développé par Michelin. Les observations en régime permanent peuvent être exécuté avec une cellule de Couette excentrique à contre-rotation (mélangeur MaCROS). Ce prototype a été conçu et développé au cours de ces travaux. Le mélangeur MaCROS permet de caractériser les surfaces libres du fluide et les interfaces avec les parois métalliques (ligne fluide/métal/gaz) dans différentes conditions de: i) fluide utilisé, ii) volume de fluide, iii) taux de cisaillement ( vitesses de rotation), iv) des entrefers d'écoulement minces, v) de température de surface, vi) rugosité des surfaces et vii) nature des surfaces.

Les différents fluides, outils de caractérisation et géométries d'écoulement transparents décrits dans ce chapitre ont été utilisés pour cibler les objectifs de la thèse : déterminer des vitesses de glissement à la paroi (Chapitre 3), étudier le comportement d'écoulement interfacial aux parois (Chapitre 4) et étudier l'influence de l'adhésion sur ce comportement (Chapitre 5).

## Chapter 3

# Rheological and wall slip characterization

### Contents

---

3.1. Oscillatory rheometer .....	70
3.1. Silicone fluid .....	70
3.2. Rubber products .....	73
3.2. Capillary rheometer .....	77
3.2.1. Study of pre-shearing conditions .....	78
3.2.2. Butadiene Rubber (BR A) behavior .....	80
3.2.3. Styrene Butadiene Rubber A (SBR A) behavior .....	86
3.2.4. Styrene Butadiene Rubber B (SBR B) behavior .....	93
3.2.5. Rubber compound (SBR C) behavior .....	99
3.3. Wall slip characterization .....	103
3.3.1. BR A wall slip velocities .....	103
3.3.2. SBR A wall slip velocities .....	105
3.3.3. SBR B wall slip velocities .....	107
Conclusions .....	110

---



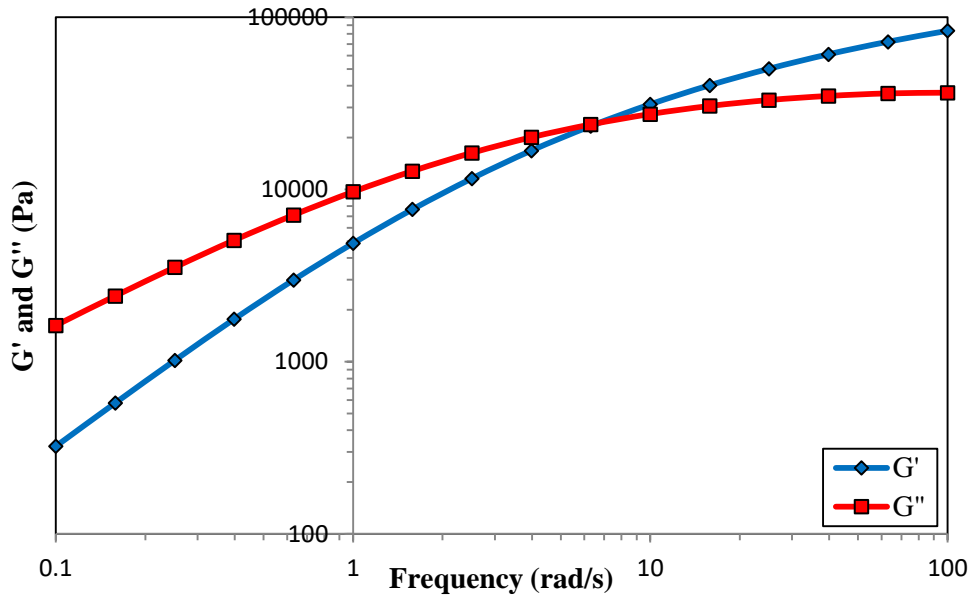


Figure 3.2 – Frequency sweep test of silicone fluid at ambient temperature at 1% strain.

During the flow observations, the fluid is exposed to shear between the cylinders for an extended period of time (up to 1 hour). These observations are quite time consuming as it is difficult to find the appropriate conditions to stabilize the fluid between the cylinder surfaces. It is essential that the properties of the fluid do not change during the course of the experiment. A change in rheology of the fluid during the course of the experiment could make it difficult to stabilize the fluid for long durations. Thus, it is essential to investigate the evolution of the fluid’s rheology over time.

Moreover, the transparency of the silicone fluid was lost during the experiment. This is due to the presence and mixing of impurities which in turn could result in a change of fluid properties. The evolution of the rheological properties over time at a frequency of 1 and 100 rad/s is presented in Figure 3.3. The silicone fluid exhibits good rheological stability for durations of up to 1 hour. The stabilization experiments with the MaCROS mixer were conducted at significantly smaller timescales. Thus, the rheology of the silicone fluid will not evolve during these experiments.

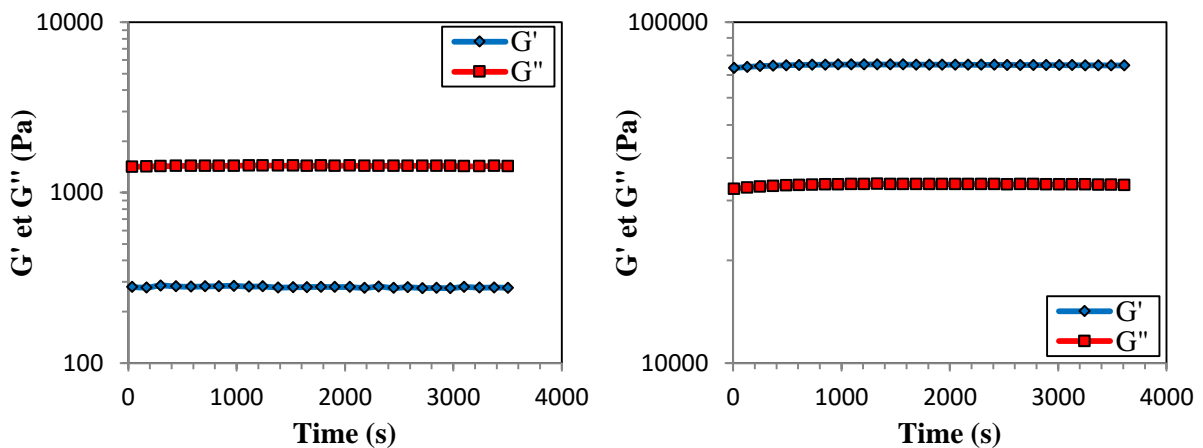


Figure 3.3 – Evolution of elastic ( $G'$ ) and viscous moduli ( $G''$ ) of silicone fluid at 1 rad/s (left) and 100 (right) rad/s over 1 hour.

To confirm this, the rheology of the fluid before and after the stabilization experiments were tested by carrying out a frequency sweep test at 1% deformation (Figure 3.4). From Figures 3.3 and 3.4, it can be inferred that the rheological properties of the fluid do not vary during the course of the flow observations. Efforts were made to measure the impact of temperature on the rheological behavior. However, the emission of bad odors was noticed at higher temperatures (40°C) indicating possible

degradation of the fluid with temperature. Thus, the silicone fluid was only used for flow observations at ambient temperature.

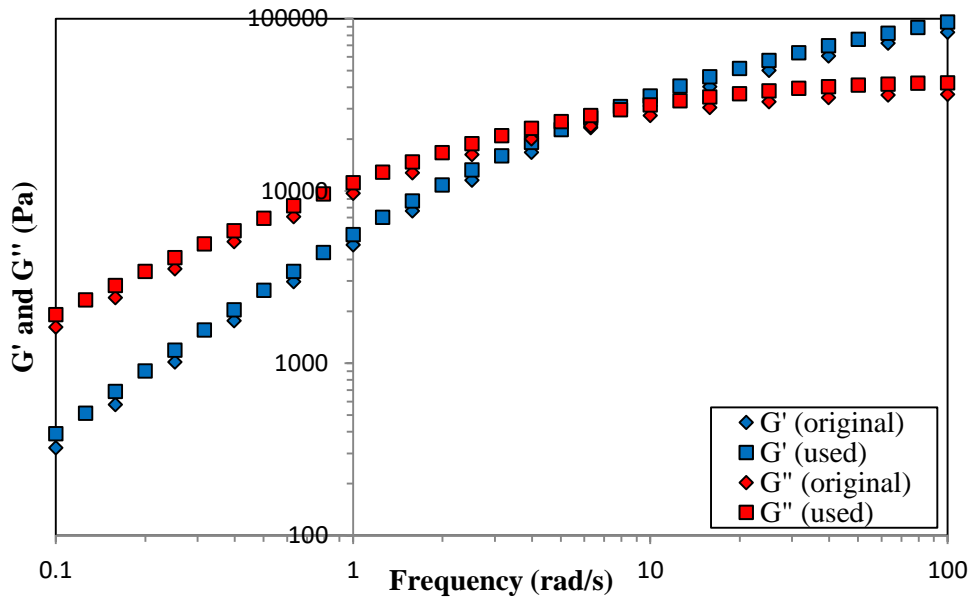


Figure 3.4 – Frequency sweep test of silicone fluid before and after flow observations at ambient temperature.

The complex viscosity curve of the silicone fluid is presented in Figure 3.5.

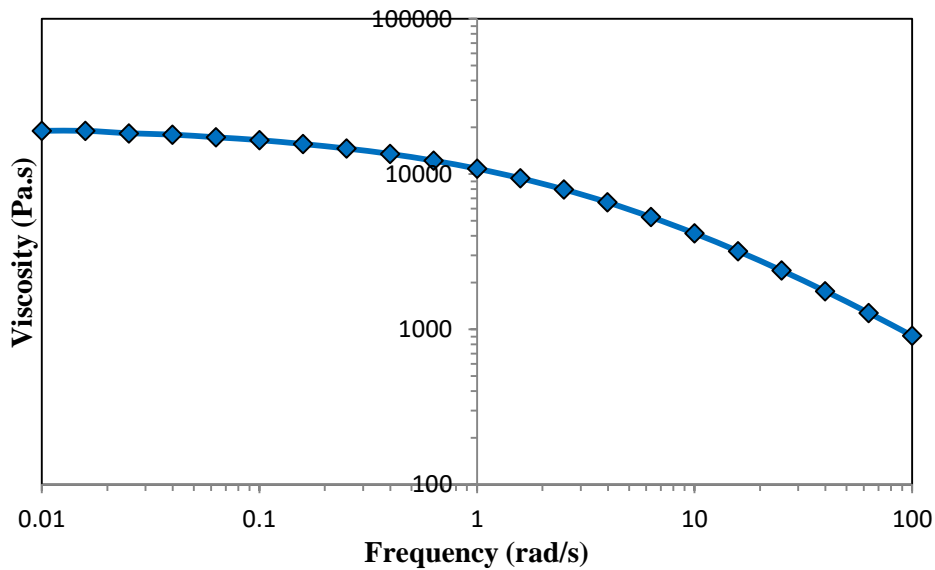


Figure 3.5 – Complex viscosity curve of silicone fluid at ambient temperature.

As the silicone fluid tends to exhibit a Newtonian plateau at low frequencies ( $< 0.1$  rad/s), the complex viscosity ( $\eta$ ) can be fitted with a Carreau-Yasuda law [Carreau, 1968; Yasuda, 1979]:

$$\eta = \eta_0 (1 + (\lambda \dot{\gamma})^a)^{\frac{n-1}{a}} \quad \text{Equation 3.1}$$

where  $\dot{\gamma}$  is the shear rate,  $\eta_0 = 22600$ ,  $\lambda = 0.86$ ,  $a = 0.69$  and  $n = 0.36$  for the silicone fluid. The determination of the different parameters from dynamic rheological measurements assumes the validity of the Cox-Merz rule for this fluid which is the case for linear polymer chains [Snijkers and Vlassopoulos, 2014]. The complex viscosity of the silicone fluid was also fitted with a power law (Equation 3.2) at frequencies ranging from 1 to 100 rad/s.

$$\eta = K\dot{\gamma}^{m-1} \quad \text{Equation 3.2}$$

where  $K$  is the consistency and  $m$  is the index of pseudoplasticity. For the silicone fluid, we find  $K = 14200 \text{ Pa}\cdot\text{s}^m$  and  $m = 0.49$ .

### 3.1.2. Rubber products

#### SBR A

The viscoelastic behavior of the different rubber products was characterized by carrying out frequency sweep tests. Measurements were performed for a range of frequencies from 0.01 to 100 rad/s at a deformation of 1%, which is in the linear viscoelastic domain. The rheology of the different rubber products was tested at 100°C. To differentiate the rheology of the linear and branched SBRs, SBR A and SBR B were tested at different temperatures. The frequency sweep tests of SBR A at different temperatures are presented in Figure 3.6.

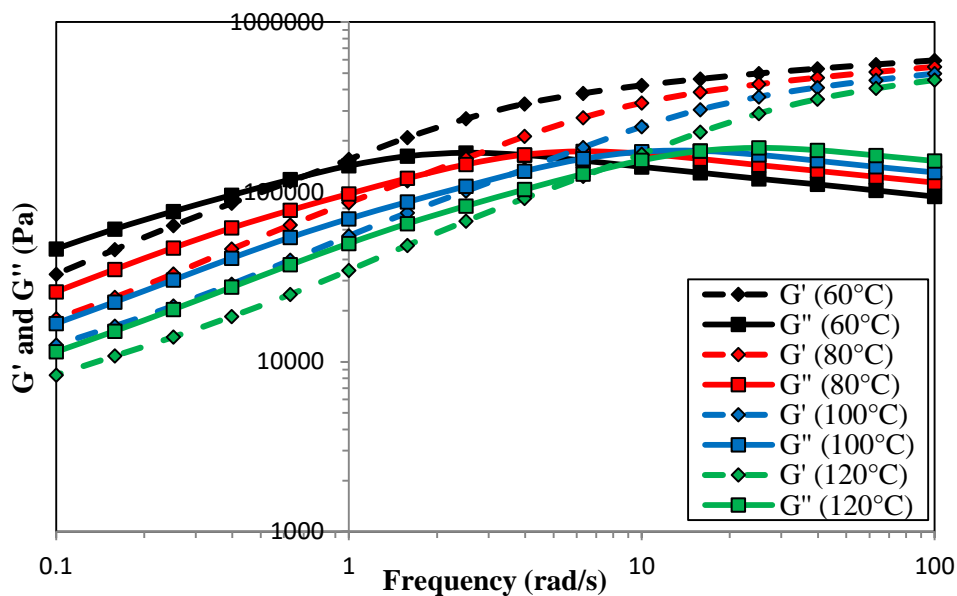


Figure 3.6 – Evolution of elastic ( $G'$ ) and viscous ( $G''$ ) moduli of SBR A at different temperatures.

The thermodependent flow behavior of the fluid can be fitted with a time-temperature superposition (TTS) [Ferry, 1980]. The TTS was performed by applying horizontal shifts followed by vertical shifts on the frequency sweep test. The horizontal shifts were performed by using a thermodependent shift factor ( $a_T$ ) on the shear rate (Frequency for Frequency sweep tests). However, some researchers [Ferry, 1980; Tobolsky and Andrews, 1945; Griffith, 1980] observed that for thermorheologically complex materials, an additional vertical shift factor ( $b_T$ ) was required. The temperature dependency of the vertical shift factor ( $b_T$ ) is significantly weaker than that of the horizontal shift factor ( $a_T$ ) [Guedes, 2011; Delay and Plazek, 2009; Vananroye *et al.*, 2011]. By considering 100°C as the reference temperature, a master curve was obtained for the SBR A (Figure 3.7).

The shift factors ( $a_T$  and  $b_T$ ) for the different temperatures are presented in Table 3.1. The thermal dependence of  $a_T$  is well described by an Arrhenius law. An activation energy of 41.75 kJ/mol was estimated for SBR A. This activation energy was found to be in the range of values estimated for pure SBRs (33 – 42 kJ/mol [Leblanc 1996], 44 kJ/mol [Mongruel and Cartault 2006]).

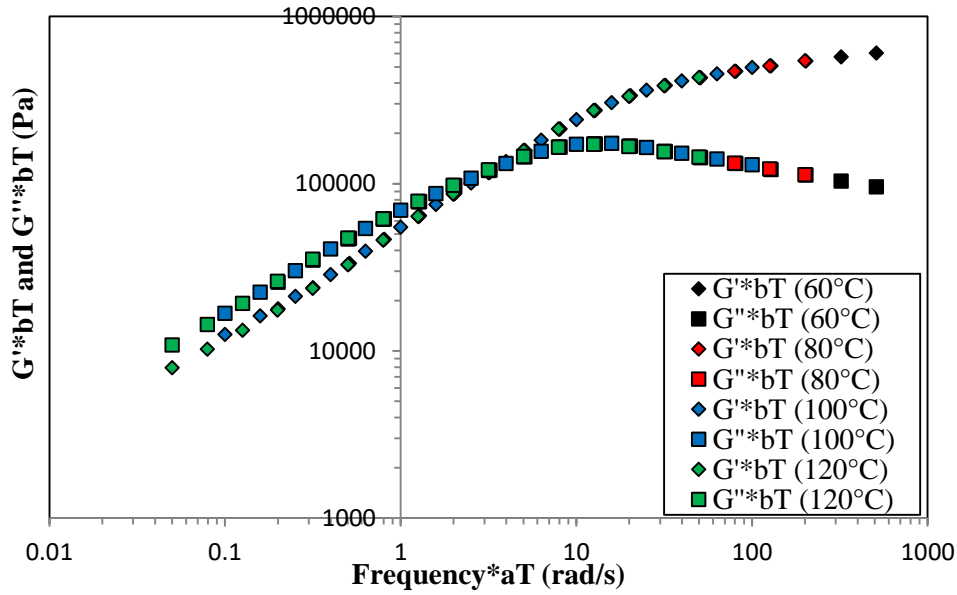


Figure 3.7 – Time-temperature superposition of the frequency sweep tests of SBR A.

Temperature	$a_T$	$b_T$
60°C	5.1	1.02
80°C	2	1
100°C	1	1
120°C	0.5	0.95

Table 3.1 – Shift factors of SBR A at different temperatures.

The viscosity curves at different temperatures and the master viscosity curve of SBR A are presented in Figure 3.8. The viscosity curves do not present a Newtonian plateau in these range of frequencies. The viscosity curves are fitted by a power law (Equation 3.2). The thermodependency of the complex viscosity is given via the thermal dependence of the consistency (Equation 3.3).

$$K(T) = K_0 \cdot \exp\left[\frac{mE}{R} \left(\frac{1}{T} - \frac{1}{T_{ref}}\right)\right] \quad \text{Equation 3.3}$$

where  $K$  is the consistency,  $K_0$  is the consistency at the reference temperature,  $m$  is the index of pseudoplasticity. For SBR A, we have  $K_0 = 80500 \text{ Pa}\cdot\text{s}^m$ ,  $m = 0.48$ ,  $R = 8.314 \text{ J}\cdot\text{mol}^{-1}\cdot\text{K}^{-1}$ ,  $T_{ref} = 373 \text{ K}$  and  $E = 41.8 \text{ kJ/mol}$ .

### SBR B

The crossover frequency of  $G'$  and  $G''$  curves was found to occur at lower frequencies ( $< 0.1 \text{ rad/s}$ ) for SBR B which is found to be in concurrence with results obtained from other studies conducted on SBRs [Boudimbou, 2011; Tassieri *et al.*, 2016]. This crossover occurs at higher frequencies for SBR A (0.5 to 8 rad/s at 60 to 120°C). This may be due to the presence of functionalized groups in the polymer [Jacoby *et al.*, 2016; Isitman *et al.*, 2017; Pavon Sierra *et al.*, 2016].

Time-temperature superposition (TTS) was carried out on the SBR B flow curves while considering 100°C as the reference temperature. The shift factors ( $a_T$  and  $b_T$ ) for the different temperatures are presented in Table 3.2. An activation energy of 50.8 kJ/mol was estimated for SBR B. The complex viscosity curves at different temperatures and the master viscosity curve of SBR B are presented in Figure 3.10.

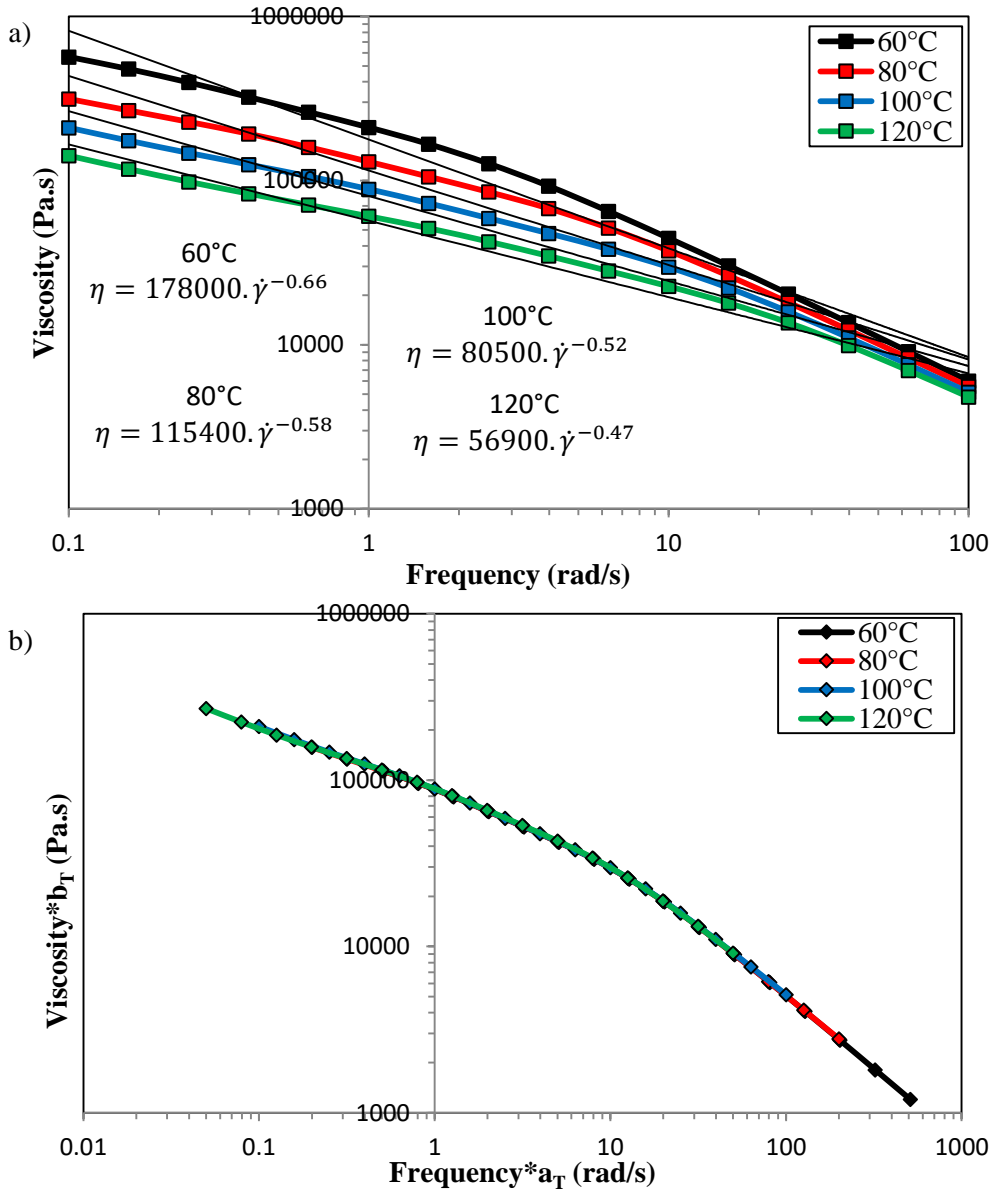


Figure 3.8 – a) Viscosity curves at different temperatures of SBR A. b) Master viscosity curve of SBR A at  $T_{ref} = 100^\circ\text{C}$ .

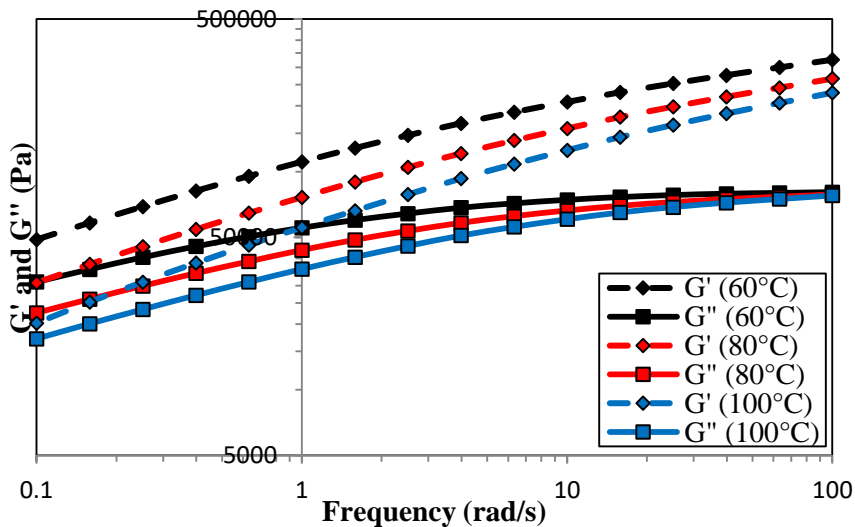


Figure 3.9 – Evolution of elastic ( $G'$ ) and viscous ( $G''$ ) moduli of SBR B at different temperatures.

Temperature	$a_T$	$b_T$
60°C	8	1.04
80°C	2.9	1.06
100°C	1	1

Table 3.2 – Shift factors of SBR B at different temperatures.

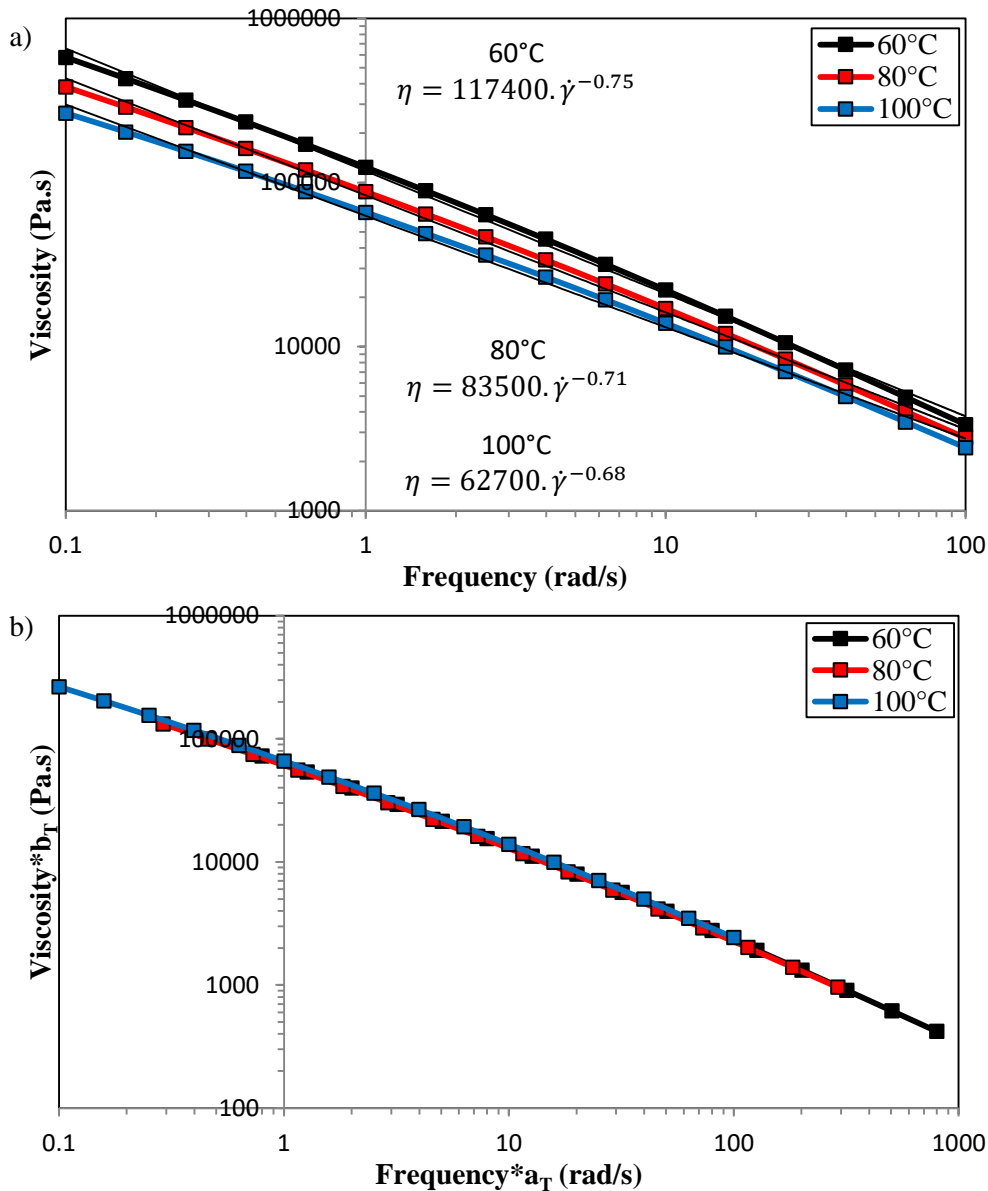
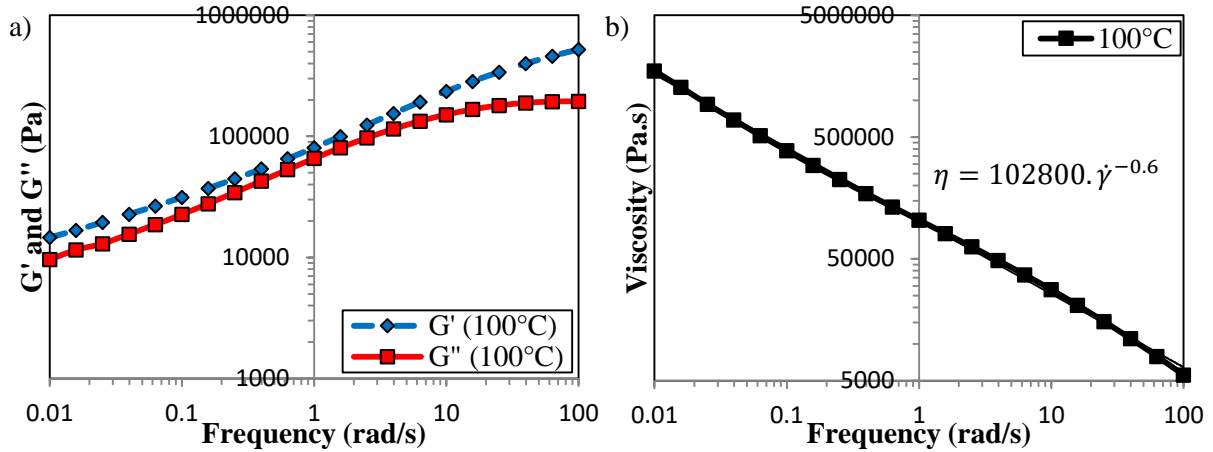


Figure 3.10 – a) Viscosity curves at different temperatures of SBR A. b) Master viscosity curve of SBR B at  $T_{ref} = 100^\circ\text{C}$ .

### BR A and SBR C

The rheological behavior of BR A and SBR C were carried out at  $100^\circ\text{C}$  (reference temperature of SBR A and SBR B characterization). The evolution of the storage and loss moduli and the complex viscosity flow curves of BR A and SBR C are presented in Figures 3.11 and 3.12. A dominance of the elastic modulus ( $G'$ ) over the viscous modulus ( $G''$ ) was observed for BR A and SBR C at these frequencies.



**Figure 3.11** – a) Evolution of elastic ( $G'$ ) and viscous moduli ( $G''$ ) of BR A at 100°C. b) Viscosity curve of BR A at 100°C.

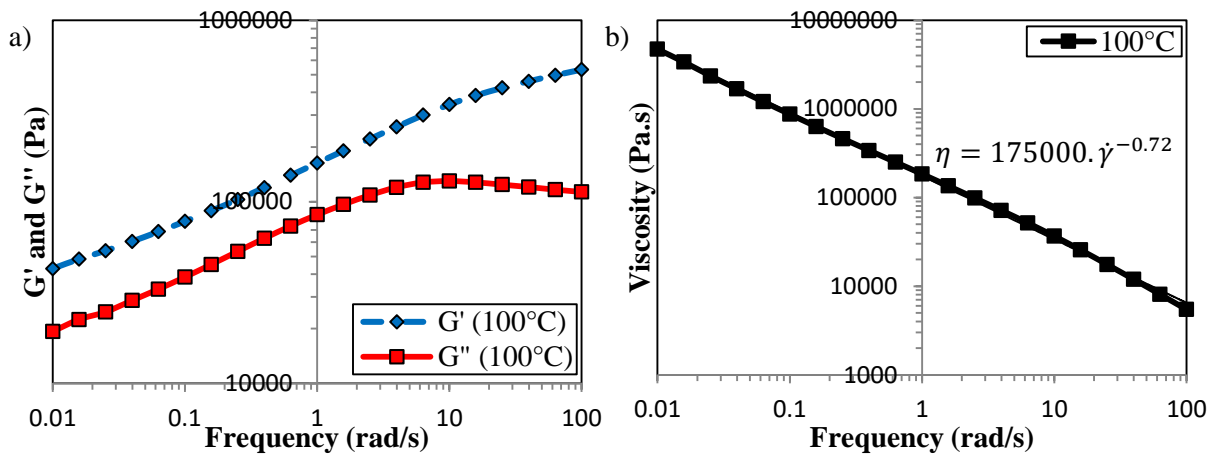


**Figure 3.12** – a) Evolution of elastic ( $G'$ ) and viscous moduli ( $G''$ ) of SBR C at 100°C. b) Viscosity curve of SBR C at 100°C.

The complex viscosity curves of SBR B, SBR C and BR A were fitted by a power law. The values of the parameters of the rubber products at 100°C are summarized in Table 3.3.

Viscosity, $\eta = K\dot{\gamma}^{m-1}$		
Fluid	K	m
SBR A	80500	0.48
SBR B	62700	0.32
BR A	102800	0.40
SBR C	175000	0.29

**Table 3.3** – Viscosity laws of the rubber products at 100°C.

The viscosity laws of the fluids used in this study obtained by oscillatory rheometry are compared in Appendix II.

### 3.2. Capillary rheometry

The RhéoART<sup>TM</sup> was used to characterise the rheological behavior of the rubber products at shear rates ranging from 1 to 800 s<sup>-1</sup>. While estimating the pressure drop ( $\Delta P$ ) values at a given shear rate, a maximum error of 0.5 bar was encountered. This corresponds to an error of 0.14 to 2%, depending on the conditions, of the estimated pressure drop value.

During internal mixing, the rotors and the chamber walls are heated to 50-80°C [Le *et al.*, 2003]. Due to the self-heating phenomenon, the temperature of the rubber mix can rise up to 160°C [Jin *et al.*, 2020] during the mixing cycle [Majesté and Vincent, 2015]. The rheological behavior of the different rubber products was investigated at 100°C with the RhéoART™. This permits a comparison of the oscillatory and capillary behavior of the rubber products. The SBR A and SBR B were characterised at different temperatures to investigate the influence of temperature on the evolution of wall slip velocities.

### 3.2.1. Study of pre-shearing conditions

The influence of the pre-shearing conditions on the measured pressure drops was investigated prior to the measurements. This study was carried out on SBR B at 100°C using a cylindrical die of diameter (D) 2 mm and length (L) 64 mm. The pre-shearing conditions were varied (Table 3.4) and the evolution of the pressure drop was studied at shear rates ranging from 5 to 300 s<sup>-1</sup>. Each pre-shear parameter was varied independently, the others being constant. The influence of each pre-shearing conditions on the pressure drop evolution is presented in Figures 3.13-3.16.

Pre-shearing conditions	Values used for the study
Rotation speed of injection piston ( $V_r$ )	30, 60, 100, 150 rpm
Descending speed of feeding piston ( $V_d$ )	0.5, 1, 2.5, 5 mm/s
Relaxation time ( $t_r$ )	30, 75, 150, 300 s
Shear opening (O)	1, 2, 4, 8 mm

Table 3.4 – Values used for testing the pre-shearing conditions.

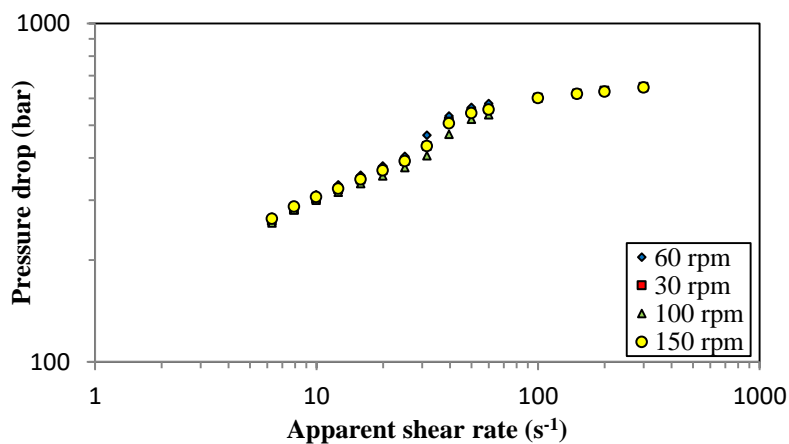


Figure 3.13 – Influence of the rotation speed ( $V_r$ ) of injection piston on the pressure drop evolution.

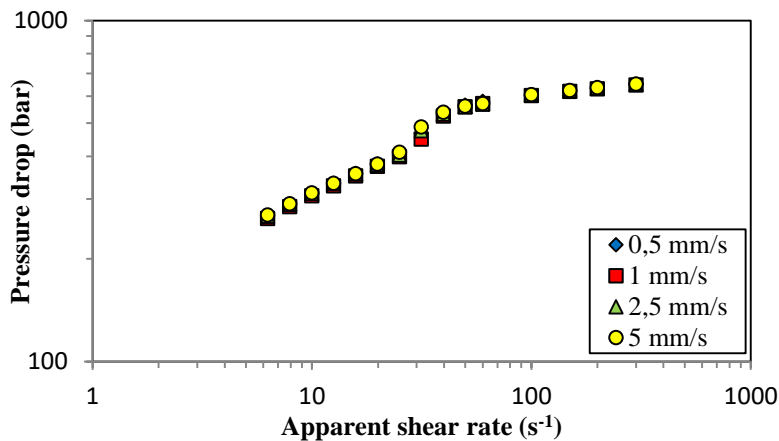


Figure 3.14 – Influence of the descending speed ( $V_d$ ) of feeding piston on the pressure drop evolution.

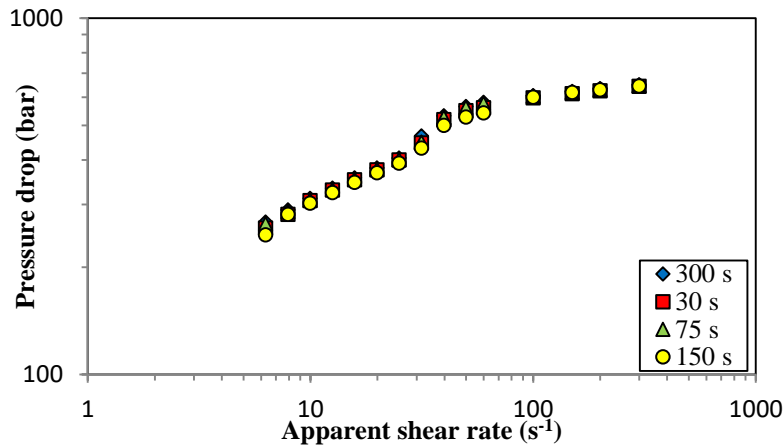


Figure 3.15 – Influence of the relaxation time ( $t_r$ ) on the pressure drop evolution.

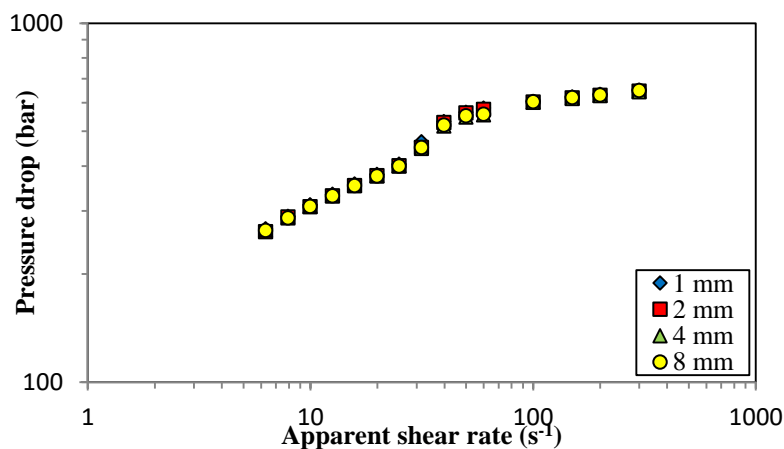


Figure 3.16 – Influence of the shear opening ( $O$ ) on the pressure drop evolution.

From these figures, we can observe that the variation of pre-shearing conditions has no impact on the evolution of pressure drop. Jugo Viloría [Jugo Viloría 2017], while working with the RhéoART™ arrived at the same conclusion. As there is no effect of the pre-shearing process on the pressure drop evolution, the pre-shearing conditions were chosen to facilitate the processing of the elastomers. The pre-processing conditions chosen for the rheological characterization are presented in Table 3.5. These values provide sufficient shear to the fluid before it is pushed to the injection chamber and sufficient time for the fluid to eliminate any residual pressure.

Pre-shear conditions	Values
Rotation speed of injection piston ( $V_r$ )	60 rpm
Descending speed of feeding piston ( $V_d$ )	0,5 mm/s
Relaxation time ( $t_r$ )	300 s
Shear opening ( $O$ )	1 mm

Table 3.5 – Pre-shear conditions chosen for the rheological characterization.

The amount of shear provided to the elastomers can be controlled by varying:

- 1) the rotation speed of the injection piston ( $V_r$ ),
- 2) the descending speed of the feeding piston ( $V_d$ ) and
- 3) the flow of the elastomers through the small shear opening ( $O$ ).

Increasing the rotation speed of the injection piston ( $V_d$ ) and constricting the shear opening ( $O$ ) can impose more shear stress on the fluid. A shear opening ( $O$ ) of 1 mm, the lowest possible setting, was chosen. Imposing high rotation speeds ( $\geq 100$  rpm) was found to cause too much noise and vibration in the machine. To avoid damaging the machine, a moderate rotation speed ( $V_r$ ) of 60 rpm was chosen. The pre-shearing process comes to an end when the feeding piston finishes its descent. A relatively slow feeding speed ( $V_d$ ) of 0.5 mm/s was chosen to extend the duration of the pre-shearing process. To eliminate the residual pressure provided to the fluid, a sufficiently long relaxation time of 300 s was chosen. These pre-shearing conditions were used as constants during the rheological characterization.

### 3.2.2. Butadiene Rubber (BR A) behavior

#### Pressure drop evolution:

The first step in the capillary data analysis is to study the evolution of the pressure drop in function of time. Figure 3.17 shows an example of the pressure drop evolution in function of time, as the shear rate is increased, for the BR A (using a capillary of  $L/D = 8$  and  $D = 2$  mm). When different shear rates are applied, the fluid experiences different shear stresses which are represented by a change in the pressure drop signal. For every change in shear rate, the pressure drop changes with time and after a sufficient amount of time, a steady state value in the pressure drop is attained. These steady state values can be used to determine the shear stress, viscosity and slip velocities with the help of capillary data analysis.

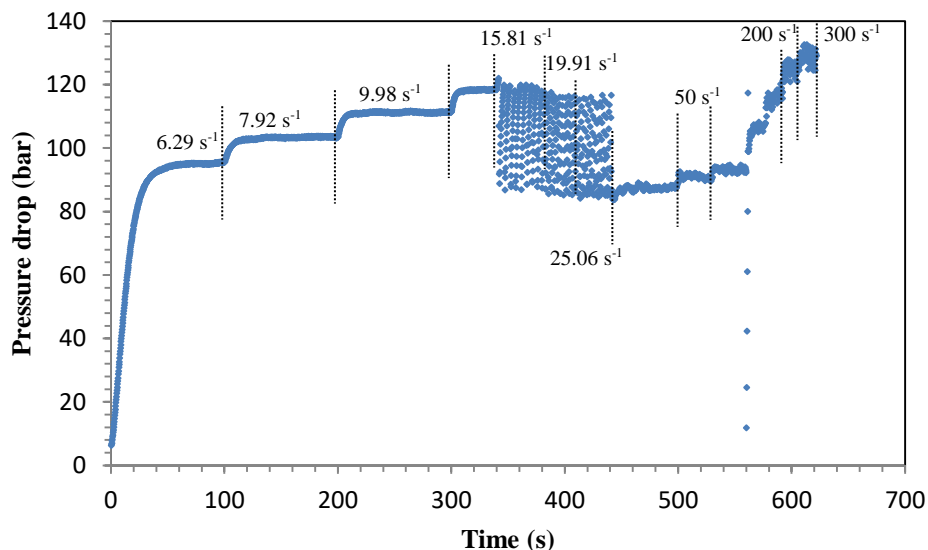


**Figure 3.17** – Evolution of pressure with time for different shear rates of BR A at 100°C for a capillary of  $L/D = 8$  and  $D = 2$  mm.

Pressure oscillations are observed for a certain range of shear rates. In such cases, the pressure drop oscillates between two steady state values. The period of oscillation decreases with an increase of shear rate. It was observed that pressure oscillations occurred at shear rates of 15 to 40  $s^{-1}$ . The magnitude of the pressure oscillations was found to be as high as 40 bars. Steady state values of pressure drop were observed at the other shear rates.

BR A exhibits two stable zones where the pressure drop achieves a steady state, separated by an unstable zone where the pressure drop oscillates between two steady state values. This behavior is typical of the behavior exhibited by linear polymer chains [Vergnes, 2015]. This behavior was also observed while working with other capillary dies. However, no pressure oscillations were observed while working with capillary dies of  $L/D = 0$ . This is due to the lack of compressibility in these dies ( $L/D = 0$ ).

The different flow regimes exhibited by BR A can be identified by plotting the steady state value of pressure drop in function of the apparent shear rates (Figure 3.18). The flow regimes can be identified by the observation of any change in slope of the flow curve (log-log plot). Figure 3.18 shows that the rheological behavior of BR A is similar to that of the pure Butadiene Rubber characterised by Jugo Viloría [Jugo Viloría, 2017]. At low shear rates, a stable flow regime exists where the pressure drop increases exponentially (linearly in log-log scale) with the apparent shear rate. This evolution is interrupted by the onset of pressure oscillations. This zone of oscillating flow is followed by another stable flow regime where the pressure drop also increases exponentially with the apparent shear rate. The zone of pressure oscillations, separating the stable flow regimes, is called as the oscillating flow regime. The stable flow regime present at low shear rates is called as Regime I while that present at high shear rates is called as Regime II.

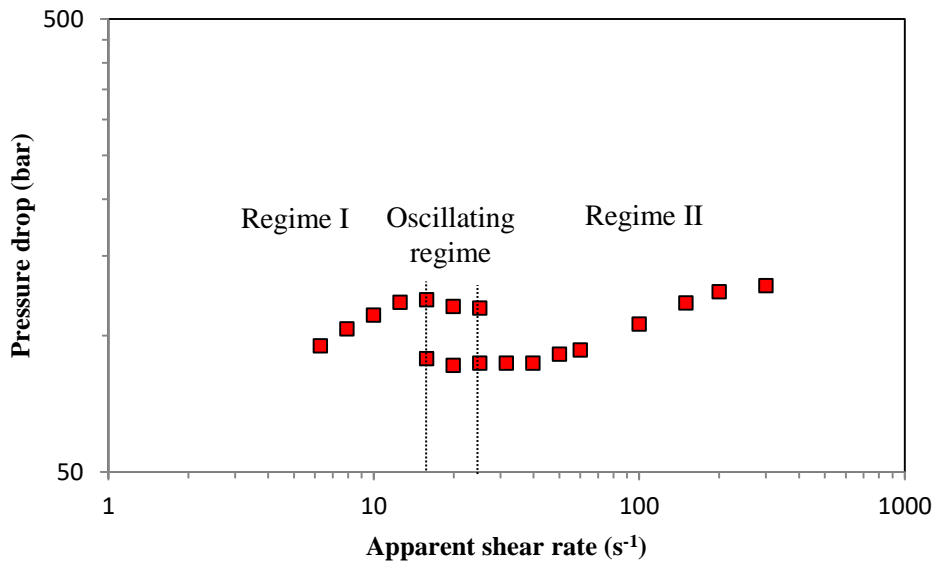


**Figure 3.18** – Evolution of pressure drop with apparent shear rate of BR A at 100°C and their corresponding flow instabilities for a capillary of  $L/D = 8$  and  $D = 2$  mm.

When we observe the two stable flow regimes, Regime I and Regime II, we found that the slope of the Regime II curve is inferior to that of the Regime I. This reduction in slope must be a result of some restraining/damping phenomenon like the wall slip phenomenon. Additionally, the pressure oscillations of the oscillating flow regime are a product of the stick-slip instability. In this case, the fluid oscillates between slip free flow and slip flow. The critical shear stress ( $\sigma_c$ ) is the shear stress at which wall slip is observed. In this case, it corresponds to the shear stress at the onset of pressure oscillations. Another approach to perceive the change in flow behavior is the observation of the flow extrudates morphology.

### Flow extrudates morphology

A change in the flow regime can also manifest itself via a modification of the flow extrudates morphology. The correlation between the aspect of the flow extrudates morphology and the flow behavior was presented in Chapter 1.3.1. Three types of flow morphologies, corresponding to the three flow regimes, were observed for BR A. The observed flow morphologies are:

- i) Sharkskin instability → Regime I
- ii) Stick slip instability → Oscillating regime
- iii) Chaotic instability → Regime II

The flow instabilities correlated with their flow regimes are presented in Figure 3.19. Examples of corresponding flow extrudates of BR A at different shear rates are presented in Figure 3.20. Similar flow instabilities were reported by Jugo Viloría while working with a pure BR [Jugo Viloría, 2017].

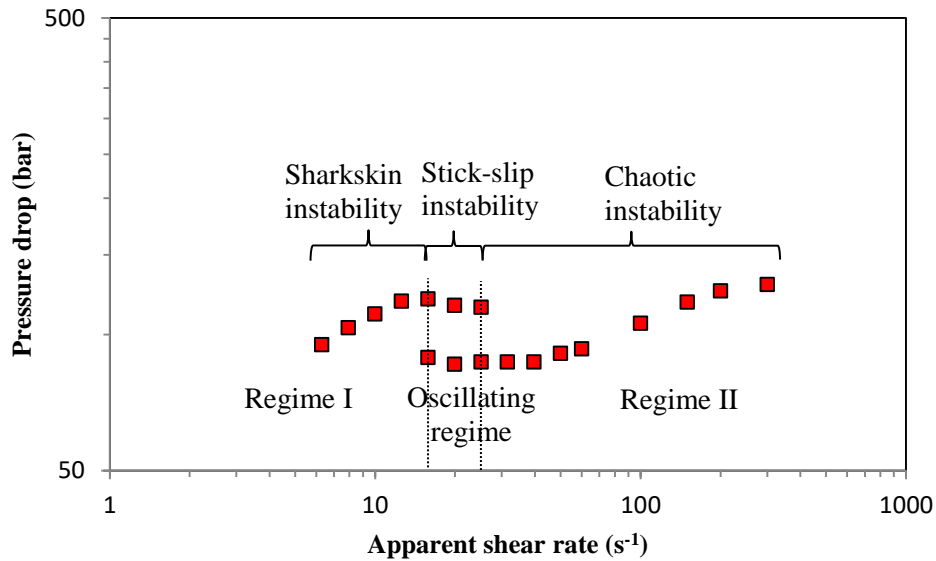


**Figure 3.19** – Flow regimes and their corresponding flow instabilities for BR A at 100°C for a capillary of  $L/D = 8$  and  $D = 2$  mm.

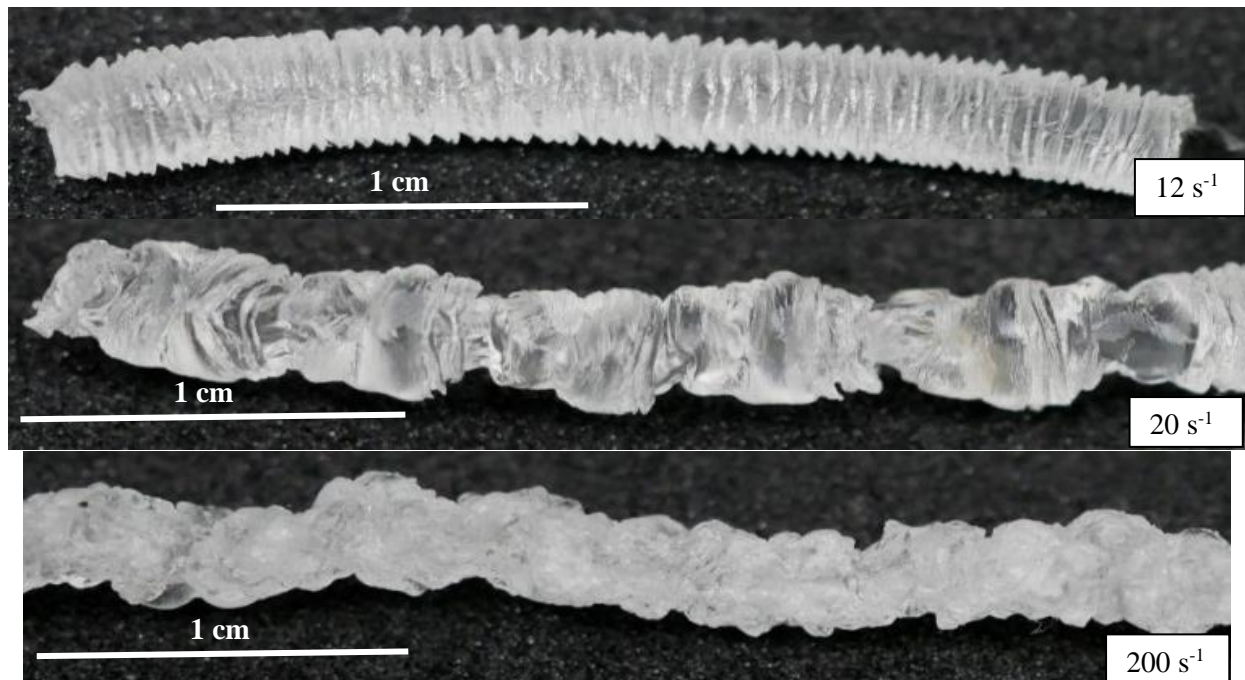


**Figure 3.20** – Flow extrudates of BR A at 100°C for a capillary die of  $L/D = 8$  and  $D = 2$  mm.

From Figure 3.20, at  $20 \text{ s}^{-1}$ , the flow extrudate seems to indicate a volume defect. BR A undergoes stick-slip flow with short frequencies. As a result, the zones representing the slip and no-slip behavior are too short. This gives the appearance of a volume defect but observation of the flow extrudates shows that irregularities in the flow extrudate occur at regular intervals indicating stick-slip flow.

### Influence of capillary geometry

The pressure drop evolutions of BR A in function of shear rate for capillary dies of different lengths and diameters are presented in Figure 3.21. The influence of the dimensions of the capillary die on the flow curves is due to the compressibility of the dies [Jugo Vilorja, 2017]. The die compressibility can be defined as the degree to which the dimensions of the die constrict the flow of the fluid. Thinner dies (smaller diameters) and longer dies (higher  $L/D$  ratios) produce more compressibility and hence exhibit larger pressure drop values. This behavior is observed in Figure 3.21.

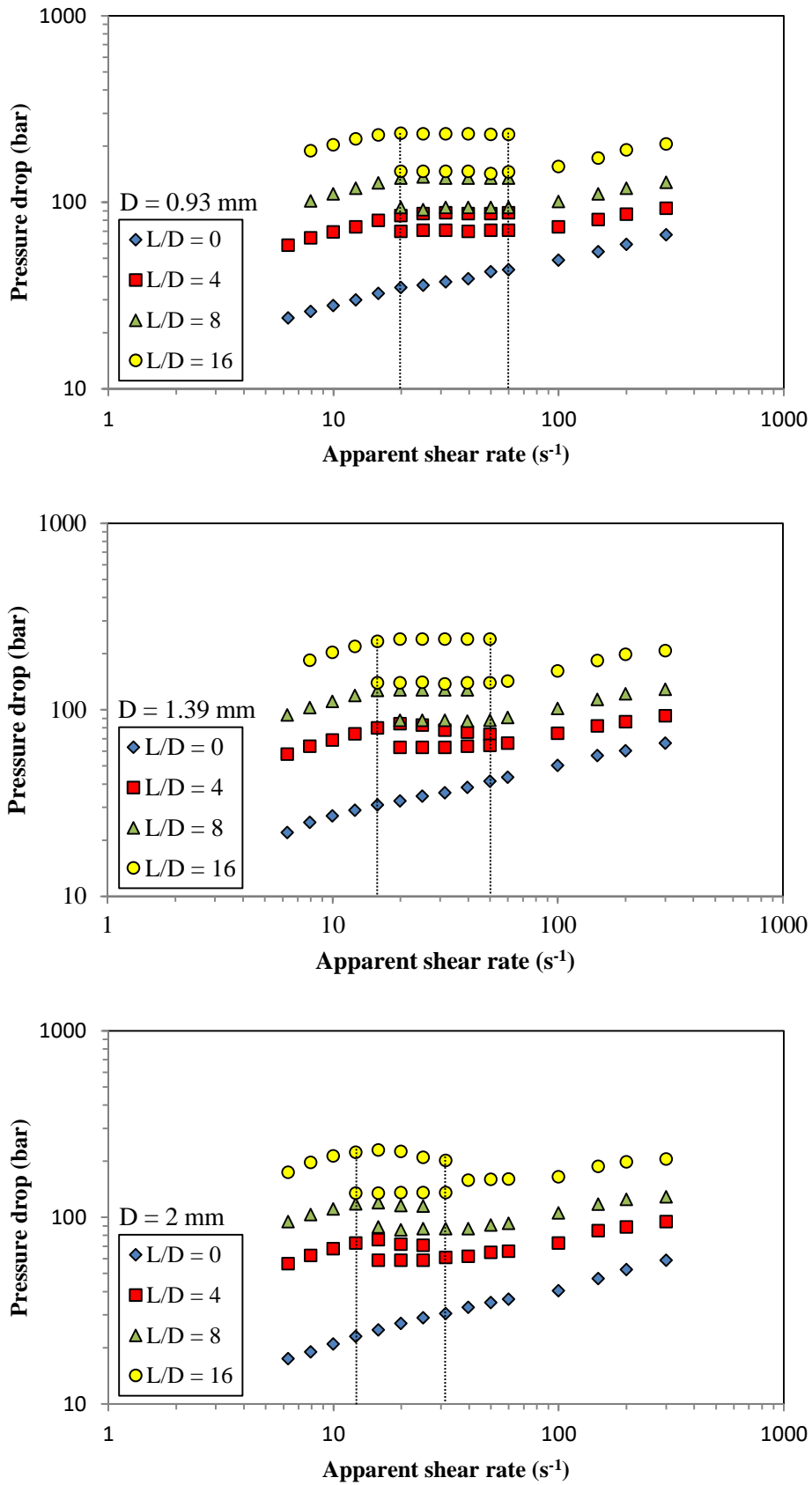


**Figure 3.21** – Pressure drop evolutions in function of apparent shear rates of BR A at 100°C for different capillary die diameters ( $D = 0.93, 1.39$  and  $2$  mm) and  $L/D$  ratios (0, 4, 8, 16).

The pressure drop evolutions for different L/D ratios of BR A at 100°C is presented in Appendix III. The magnitude of the pressure oscillations increases with the compressibility of the die (Figure 3.21). Capillary dies of zero length (L/D = 0) exhibit no pressure oscillations as they are unable to exhibit any compressibility (zero length). The onset of the pressure oscillations of BR A was found to occur between 15 to 20 s<sup>-1</sup> for the different capillary die while the onset of the Regime II flow varies between 40 to 60 s<sup>-1</sup>. The slope of the Regime II flow was inferior to that of the Regime I flow. From Figure 3.21, we find that the onset of the pressure oscillations occurs at smaller shear rates for longer capillary dies (L/D = 16), whereas the onset of Regime II flow occurs at smaller shear rates for larger diameters (D = 2 mm).

**Shear stress and viscosity curves:**

The measured pressure drop values are used to calculate the wall shear stress with the help of the Bagley method [Bagley, 1957]. An example of how the shear stresses are calculated for BR A with the Bagley method is presented in Figure 3.22. It is essential that the curves provide a very good linear regression (R<sup>2</sup>). Thus, curves with a regression coefficient below 0.99 are considered as invalid in this study. The slope of these curves is equal to four times the shear stress.

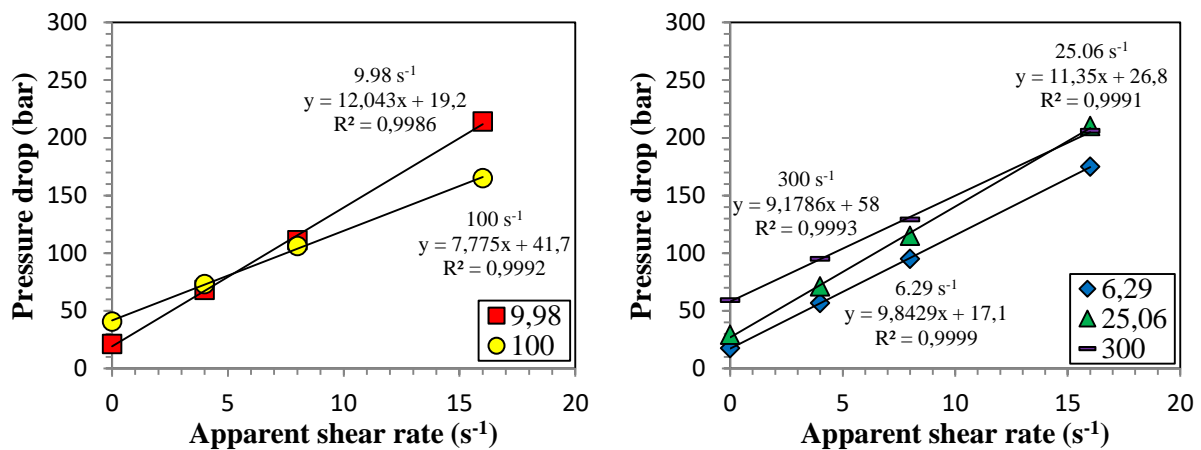
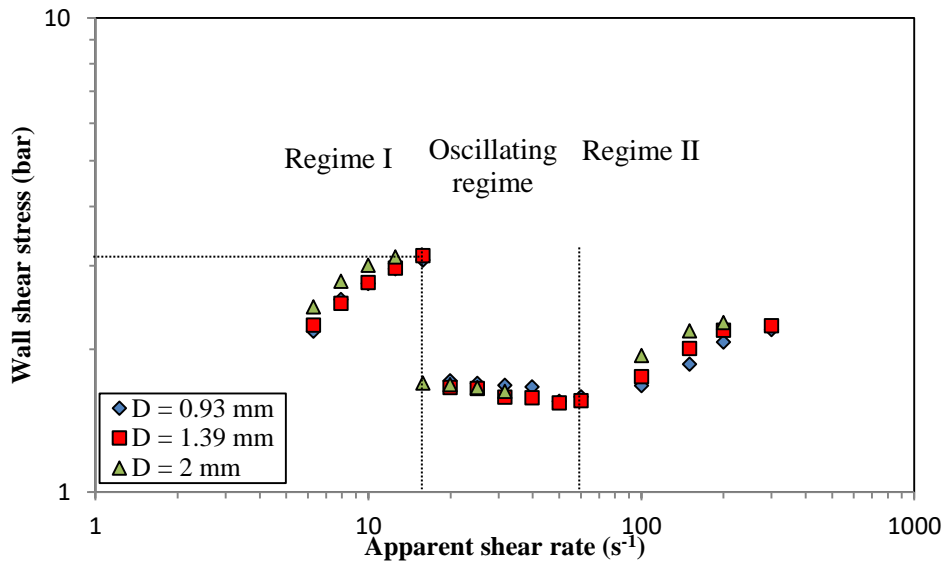


Figure 3.22 – Estimation of wall shear stress with Bagley method for BR A at 100°C (D = 2 mm).

The wall shear stresses can be easily calculated for Regime I and Regime II. However, the pressure drop oscillates between two steady state values during the oscillating flow regime (Figure 3.21). This is because the shear stress of the fluid oscillates between the critical shear stress and another stable flow regime. To find the shear stress of this lower state, the lower value of the pressure drop is used in the Bagley method. This was done to find the shear stress to which the fluid oscillates to aid the identification of the transition from the oscillating regime and verify that the stress experienced by the fluid does not exceed the critical shear stress during the oscillating flow regime. The wall shear stresses obtained through the Bagley method are plotted in Figure 3.23. The wall shear stresses are obtained for each diameter and hence the impact of the capillary length on the flow curve is removed through the Bagley corrections.

Regime I flow terminates at a critical wall shear stress ( $\sigma_c$ ) around 3.2 bar. The same critical shear stress was observed for all the diameters. The Regime I flow curves for the different diameters do not superimpose, but were ranked arbitrarily. We assume that it is due to the inaccuracy of some measurements and we consider a no-slip or weak slip condition in this regime. As the Regime I curves for the three diameters are quite close to each other, they are used to estimate the viscosity. At higher shear rates, the fluid enters the oscillating regime where the shear stress oscillates between two levels. Regime II starts at a shear stress of around 1.5 bar, which is lower than that of the critical shear stress. The Regime II flow curves do not superimpose and were ranked in the order of increasing diameters and this regime can be considered as a regime of considerable wall slip. Thus, with increasing apparent shear rates, we have a no or weak wall slip (Regime I), followed by a regime of stick-slip flow (Oscillating flow regime) and a flow regime of strong wall slip (Regime II).



**Figure 3.23** – Evolution of wall shear stress in function of the shear rates of the BR A at 100°C for capillaries of different diameters ( $D = 0.93, 1.39$  and  $2$  mm).

Following the Bagley corrections, the Rabinowitsch correction [Rabinowitsch, 1929] is performed to obtain the real shear rates in Regime I. It is used to estimate the shear-thinning index ( $m$ ). This is later used to obtain the real shear rate (Equation 2.12) and the viscosity (Equation 2.13). An example of the Rabinowitsch correction is provided in Figure 3.24.

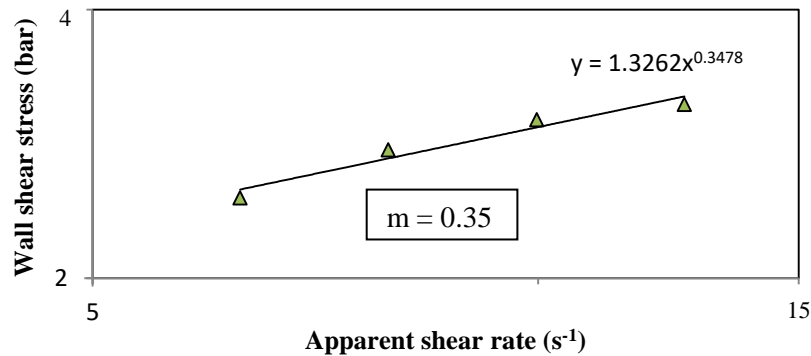


**Figure 3.24** – Rabinowitsch corrections on BR A at 100°C for a capillary die of  $D = 2$  mm.

Figure 3.25 presents the viscosity curves of BR A at 100°C.

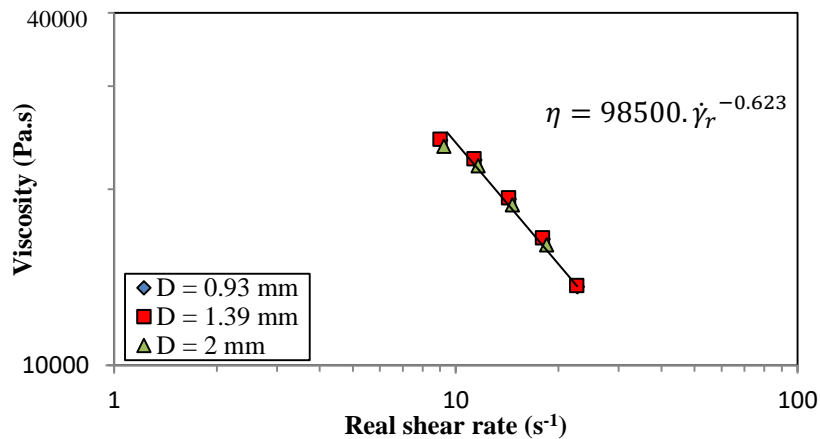


**Figure 3.25** – Evolution of viscosity of BR A at 100°C for capillary dies of  $D = 0.93, 1.39$  and  $2$  mm.

From Figure 3.24, the shear-thinning index is calculated for the three diameters to obtain 3 sets of real shear rates. The real shear stress and real shear rate values for each diameter are used to obtain the viscosity evolution for each diameter (Figure 3.25). The viscosity curves for the different diameters were found to be close to each other. The viscosity law is obtained by fitting a power law on the viscosity curves for the three diameters. The viscosity law obtained by combining the data from the three curves of Figure 3.25, provide a power law equation with  $K = 98500 \text{ Pa}\cdot\text{s}^m$  and  $m = 0.38$ .

The viscosity curve from the oscillatory data, is compared with the viscosity curve from the capillary data in Figure 3.26 to test the validity of the Cox-Merz principle. The viscosity curves obtained from the two methods were found to be comparable although the viscosity from the oscillatory data was found to be slightly larger to that from the capillary data. However, the viscosity laws from the two methods can be considered as close enough to be used interchangeably to describe the rheological behavior of BR A in the condition of no wall slip.

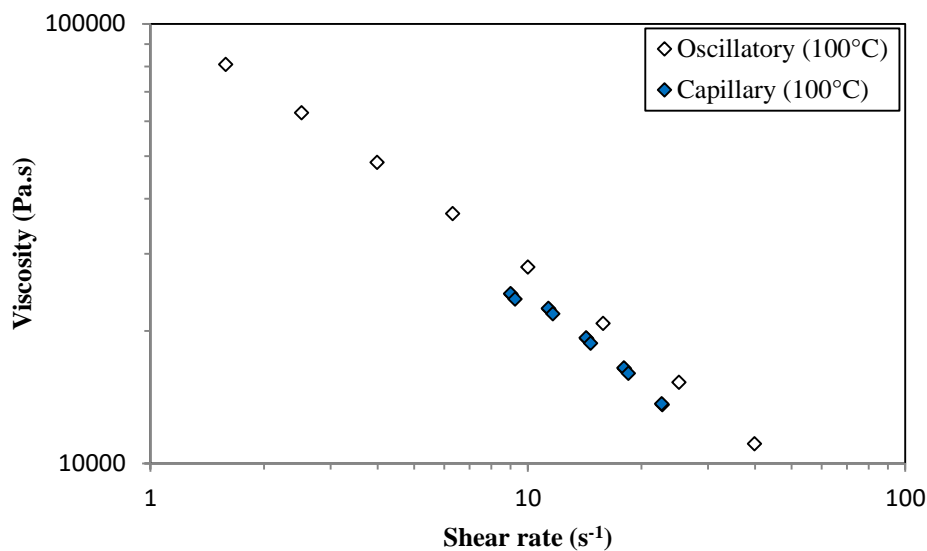


**Figure 3.26** – Viscosity curves of BR A at 100°C obtained with oscillatory and capillary rheometers.

The wall slip velocities of BR A and other rubber products are presented in Chapter 3.3. The wall slip behavior of the rubber products were characterized at 100°C, the reference temperature for the rheological characterization. The influence of temperature on the wall slip velocities of elastomers was investigated with the SBR A and SBR B. These fluids were chosen for this study due to their different molecular structures and chemical similarity (SBR elastomers). SBR A was characterized at 100, 120 and 140°C while SBR B was characterized at 60, 80 and 100°C. These temperatures were chosen to obtain sufficient data points in the Regime I and Regime II flow regimes. These data points were in turn used to obtain the wall slip velocities for different shear stresses with the Shear Rate Difference method.

#### 3.2.3. Styrene Butadiene Rubber A (SBR A) behavior

##### Pressure drop evolution

The evolution of the pressure drop in function of time of the SBR A at 100°C (for a capillary of  $L/D = 8$  and  $D = 2 \text{ mm}$ ) is presented in Figure 3.27. Similar to BR A, pressure oscillations were observed in SBR A. The presence of an oscillating flow regime indicates that SBR A behaves like a linear structured polymer. The magnitude of these oscillations was found to be of the order of a few bar. These oscillations are not visible in Figure 3.27 due to their small amplitude. A zoom of the pressure evolution is presented in Figure 3.28 to show the pressure oscillations. Pressure oscillations were observed at other temperatures and with other non-zero length capillary dies. These pressure

oscillations do not have a constant amplitude or frequency. This difference in stick-slip behavior might be due to the functionalization of SBR A.

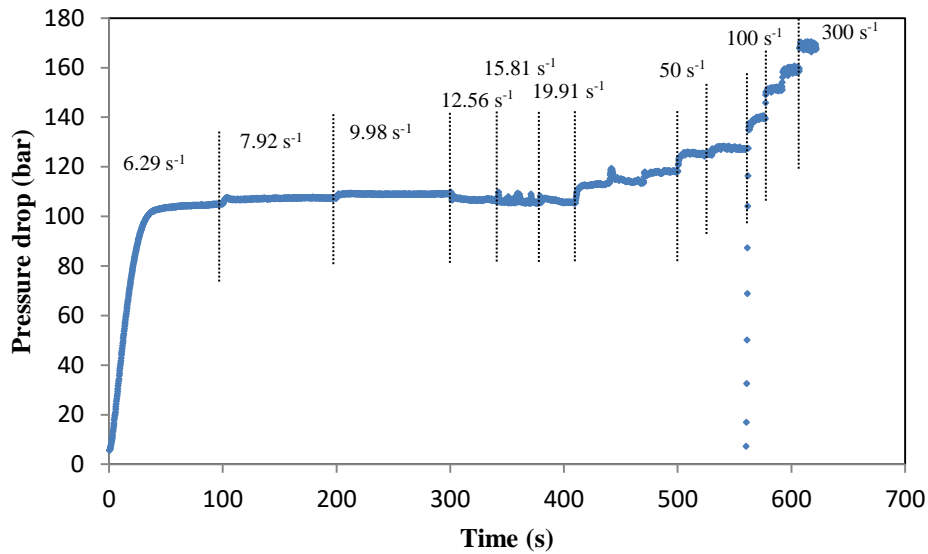


**Figure 3.27** – Evolution of pressure drop with time for different shear rates of SBR A at 100°C using a capillary of  $L/D = 8$  and a  $D = 2$  mm.

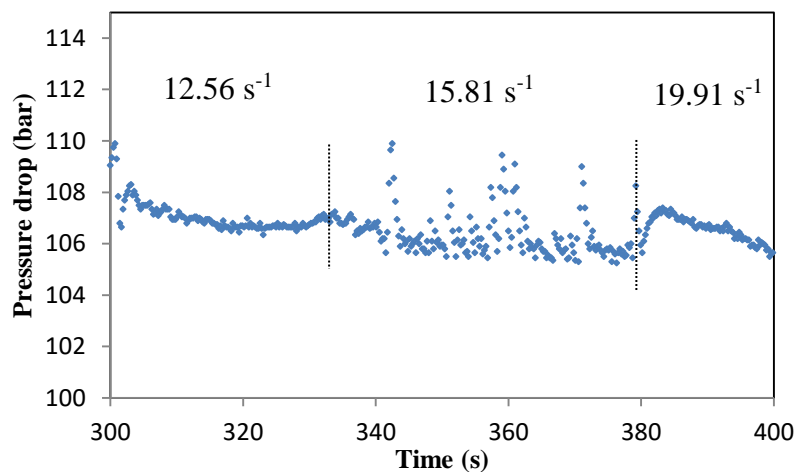


**Figure 3.28** – Pressure oscillations at different shear rates of SBR A at 100°C using a capillary of  $L/D = 8$  and a  $D = 2$  mm.

The pressure drop evolution of SBR A at 100°C using a capillary of  $L/D = 8$  and a  $D = 2$  mm (Figure 3.29) highlights three flow regimes. In the increasing order of shear rates, SBR A exhibits two stable flow regimes separated by an oscillating flow regime. The transition from Regime I to the oscillating flow regime takes place at comparatively small shear rates (between 6 and 8  $s^{-1}$ ). The transition from the oscillating flow regime and Regime II takes place between 20 to 40  $s^{-1}$  for the different capillary dies. Another effect of the compressibility of dies is the onset of pressure oscillations. The pressure oscillations could be observed at higher shear rates (40  $s^{-1}$ ) for smaller dies ( $D = 0.93$  mm) compared to the larger dies ( $D = 2$  mm).

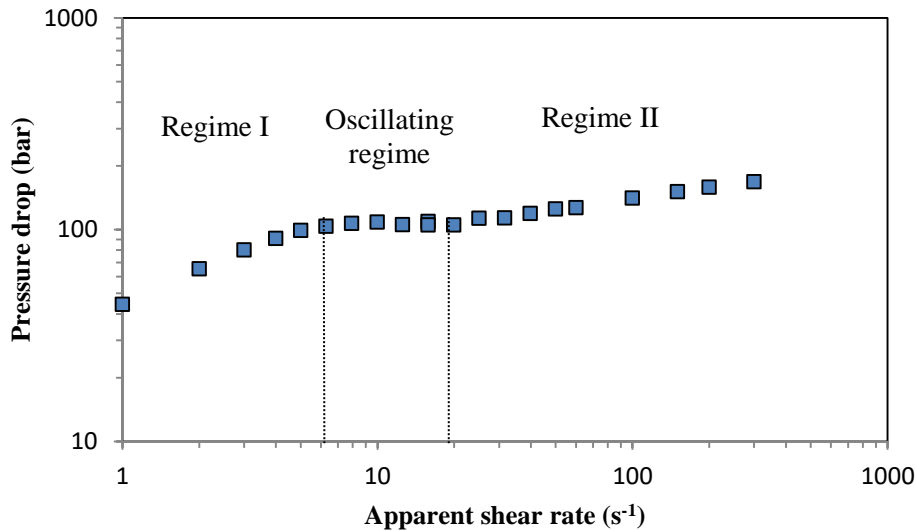


**Figure 3.29** – Evolution of pressure drop with time for different shear rates of SBR B at 100°C using a capillary of  $L/D = 8$  and a  $D = 2$  mm.

SBR A was found to exhibit a stable flow regime at small apparent shear rates ( $< 8 \text{ s}^{-1}$ ) at 100°C before the onset of stick-slip flow. The onset of wall slip occurs at smaller shear rates for smaller temperatures [Crié, 2014]. Thus, the rheological characterization was carried out at higher temperatures (120 and 140°C) rather than at lower temperatures. Figure 3.30 presents the pressure drop evolutions for a capillary die of  $L/D = 8$  and  $D = 2$  mm at 100; 120 and 140°C. As expected, the onset of wall slip (demonstrated by a change in slope), occurs at higher shear rates as the temperature is increased. At higher temperatures, the polymer melt is more fluid in nature. As a result, it requires higher shear rates to attain the same shear stress.

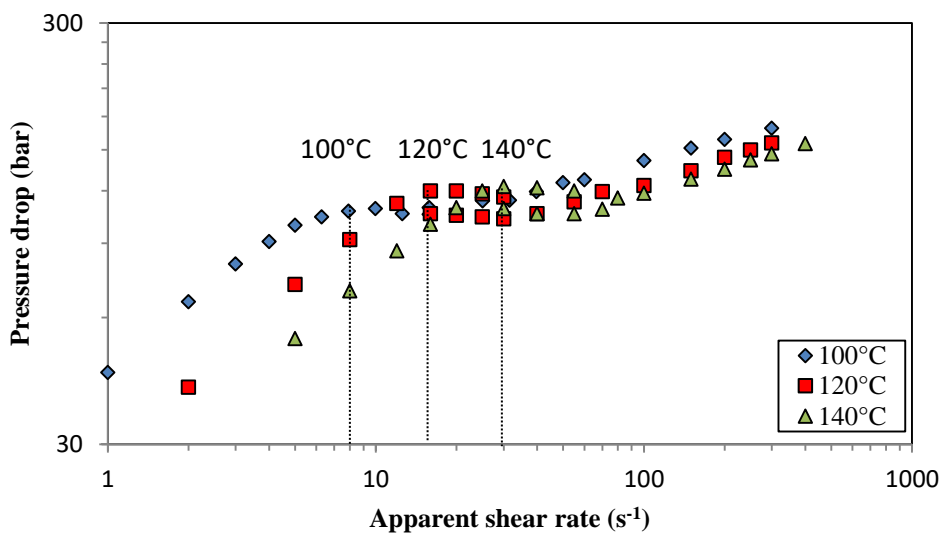


**Figure 3.30** – Evolution of pressure drop with time for different shear rates of SBR A at 100, 120 and 140°C for a capillary of  $L/D = 8$  and a  $D = 2$  mm.

### Flow extrudates morphology

Four types of flow extrudates morphologies were observed with SBR A. At small shear rates, corresponding to the Regime I, smooth profiles were observed on the flow extrudates (Figure 3.32) at small shear rates followed by sharkskin defect. During the oscillating flow regime, stick-slip instability was observed, which is typical of this flow regime. At higher shear rates, corresponding to the Regime II flow, the extrudate presents a chaotic aspect. This instability is not a surface but a

volume defect. The flow regimes and the aspects of their corresponding flow extrudates are summarized in Figure 3.31. Examples of the flow extrudates of SBR A at different shear rates are presented in Figure 3.32. Similar extrudates were observed for SBR A at 120 and 140°C. Each flow regime was marked with a change in slope of the Pressure drop Vs Apparent shear rate curves and a change in the aspect of the flow extrudates.

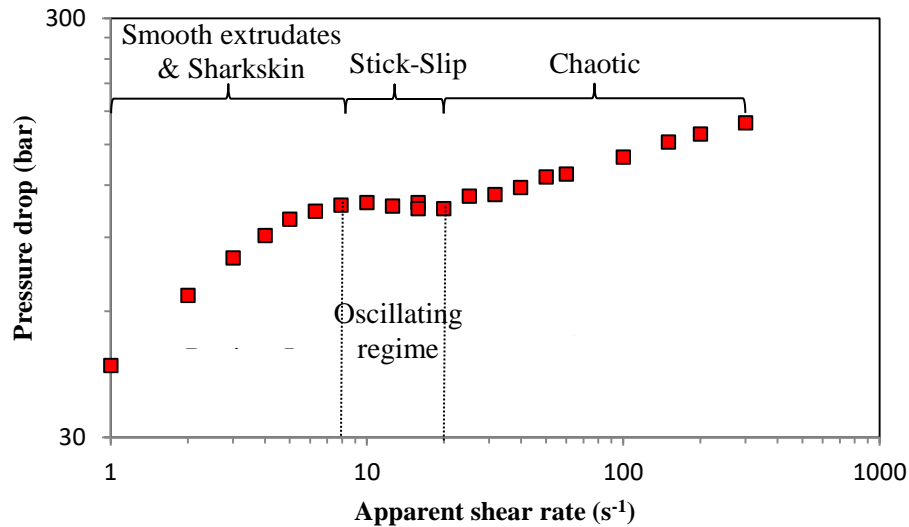


**Figure 3.31** – Flow regimes and their corresponding flow extrudates of SBR A at 100°C for a capillary die of  $L/D = 8$  and  $D = 2$  mm.

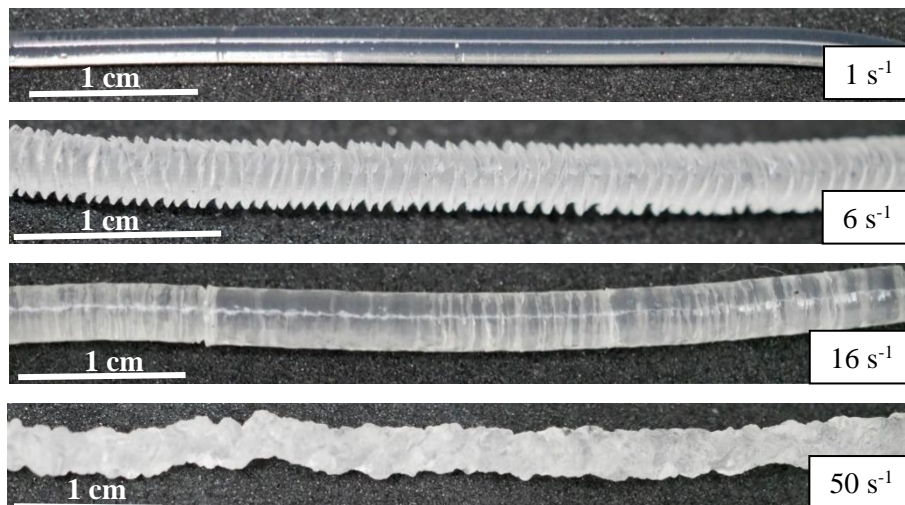


**Figure 3.32** – Flow extrudates of SBR A at 100°C for a capillary die of  $L/D = 8$  and a  $D = 2$  mm.

### Influence of capillary geometry

The pressure drop evolutions in function of shear rate for capillary dies of different lengths and diameters are presented in Figure 3.33. The flow behavior is similar to that of BR A. However, it was observed that the magnitude of the pressure oscillations were quite small and sometimes negligible. At some shear rates, the pressure drop remained constant exhibiting a plateau like behavior. At higher shear rates, the flow transitions to Regime II where the pressure drop increases with the shear rate with a slope inferior to that of Regime I. The pressure drop curves present the same features but the transition of regimes occurs at higher shear rates as the temperature is increased. The pressure drop evolutions for different  $L/D$  ratios of SBR A at 100°C is presented in Appendix IV. The pressure drop evolutions of SBR A at 120 and 140°C are presented in Appendix V and VI respectively.

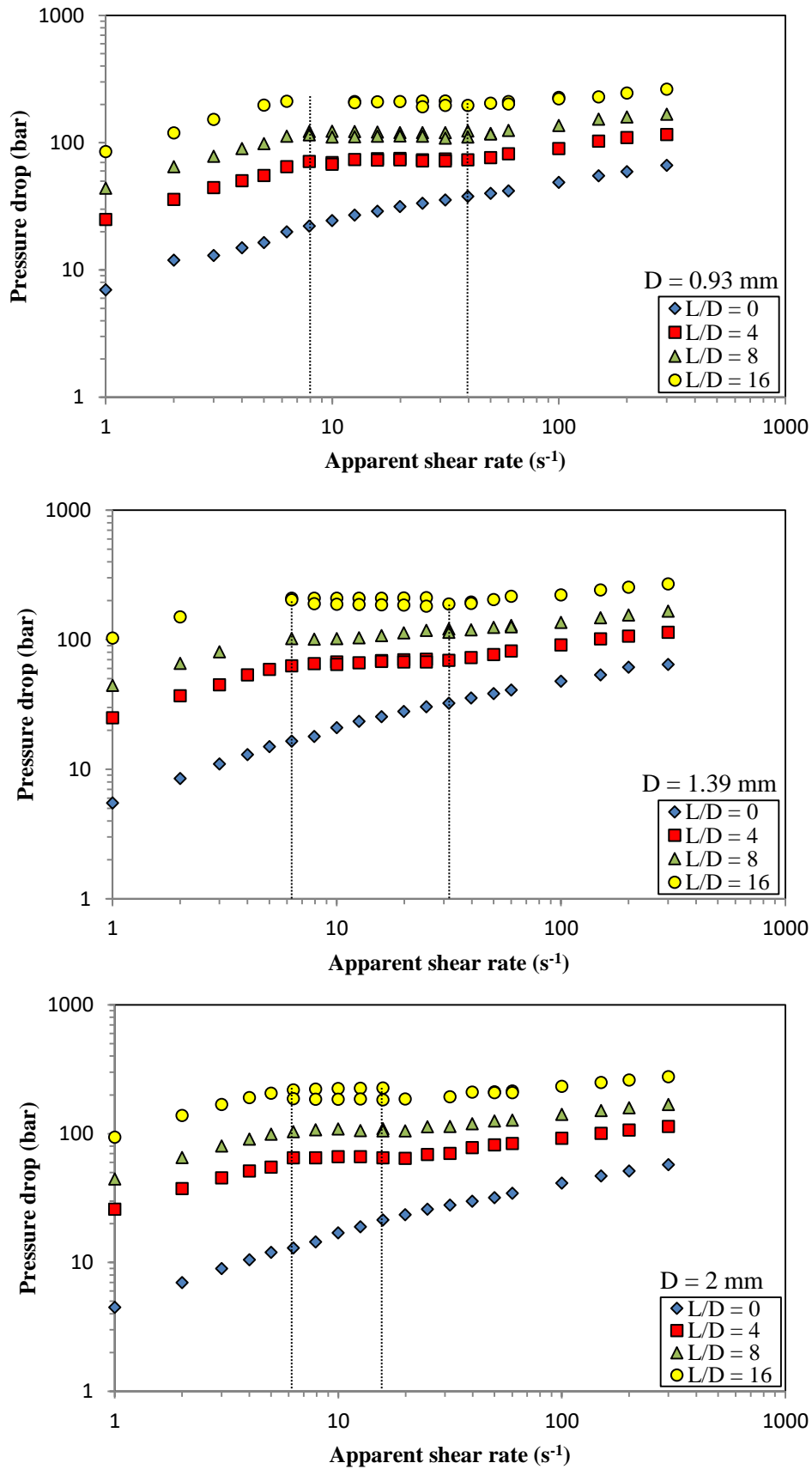


**Figure 3.33** – Pressure drop evolutions in function of apparent shear rates of SBR A at 100°C with different capillary die diameters ( $D = 0.93, 1.39$  and  $2$  mm) and  $L/D$  ratios (0, 4, 8 and 16).

Shear stress and viscosity curves:

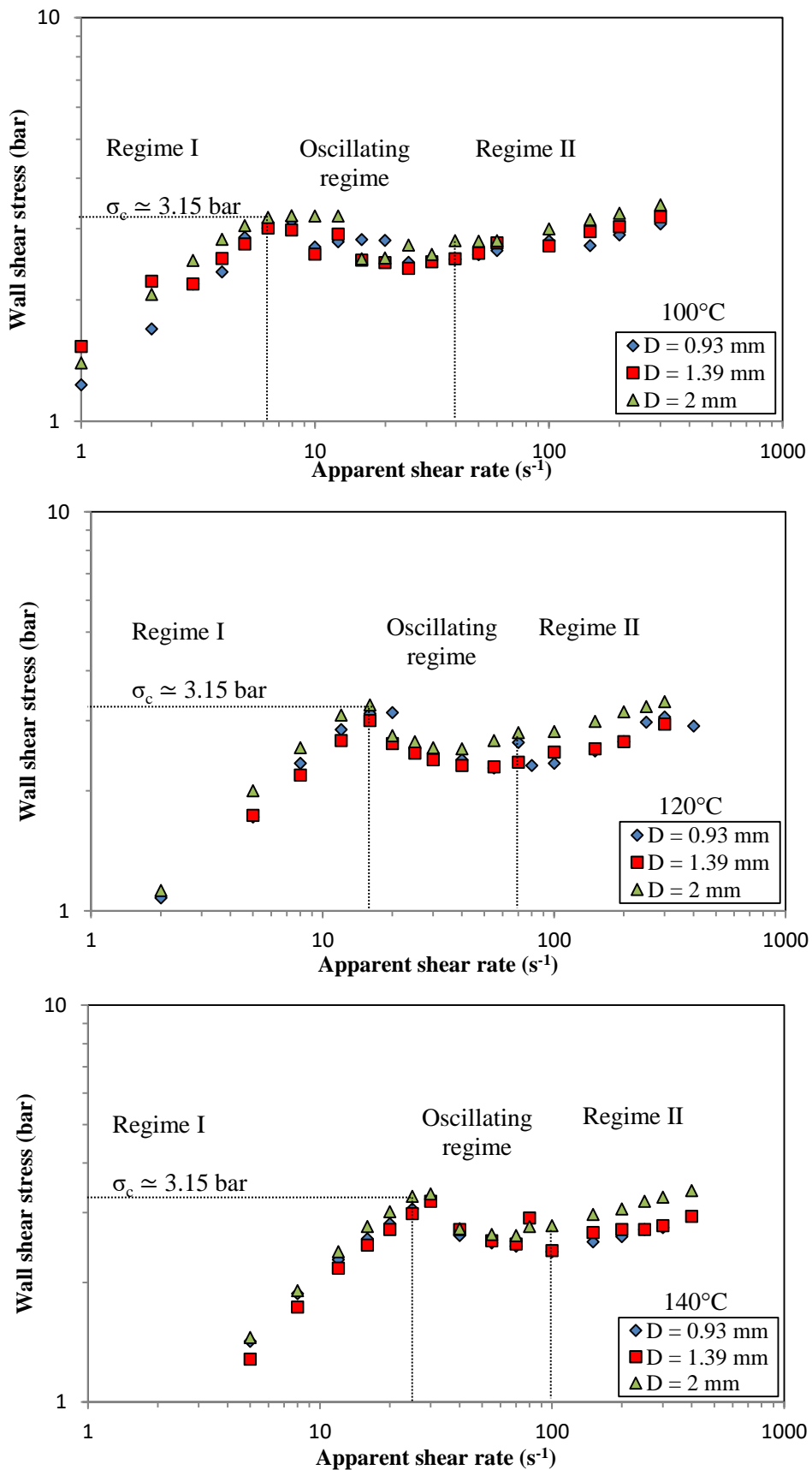
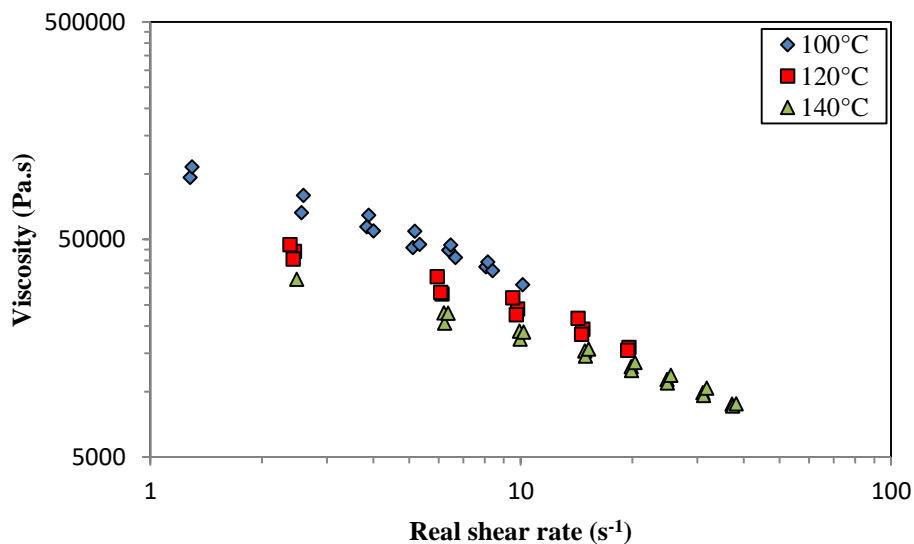


Figure 3.34 – Real shear stresses in function of the shear rates of the SBR A) at 100, 120 and 140°C for capillaries of different diameters (D = 0.93, 1.39 and 2 mm).

The Bagley corrections were carried out on the SBR A flow curves to obtain the wall shear stress. The wall shear stress in function of the apparent shear rate for different capillary diameters at different temperatures is presented in Figure 3.34 (page 91). The different curves of Regime I were found to not superimpose. A lack of superposition of flow curves can be considered to be due to wall slip, yet the curves were not ranked in the order of increasing diameter. Thus, the lack of superposition of flow curves in Regime I must be due to some inaccuracies in the measurements and not wall slip. Regime I is considered as a regime of no-slip or weak slip.

The wall shear stresses for the oscillating flow regimes were calculated by considering the lower pressure drop value of the oscillations as its steady state pressure drop. A critical shear stress ( $\sigma_c$ ) of around 3.15 bar is observed. The critical shear stress was found to be independent of the temperature. The principal difference of the flow curves at different temperatures was the shear rates at which the transitions of the flow regimes occur. The onset of the subsequent flow regimes occurred at higher shear rates at higher temperatures. The Regime II curves were found to be ranked in the order of increasing diameter confirming that this regime exhibits wall slip.

The Rabinowitsch corrections were carried out on the Regime I flow curves to obtain the real shear rates and subsequently the viscosities of SBR A. The evolution of the viscosity in function of the real shear rate at different temperatures is presented in Figure 3.35. A viscosity law for each temperature in the form of a power law was obtained by combining the data of the three diameters.



**Figure 3.35** – Evolution of viscosity of SBR A in function of real shear rates at 100, 120 and 140°C for capillary dies of  $D = 0.93, 1.39$  and  $2$  mm.

A time-temperature superposition was carried out on the capillary data. The master viscosity curves of SBR A are presented in Appendix VII. The shift factor  $a_T$  for the different temperatures is presented in Table 3.6. An activation energy of 42 kJ/mol was obtained with the capillary data, which was comparable to the activation energy obtained with the oscillatory data. The values of the power law constants of the viscosity curves of SBR A at different temperatures are presented in Table 3.7.

Temperature	$a_T$
100°C	1
120°C	0.45
140°C	0.27

**Table 3.6** – Shift factors of SBR A at 100, 120 and 140°C.

Temperature (°C)	Consistency, K (Pa.s <sup>m</sup> )	Shear-thinning index (m)
100	121000	0.45
120	68500	0.53
140	55800	0.5

**Table 3.7** – Power law constants of the viscosity laws of SBR A at 100, 120 and 140°C.

The viscosity curves obtained with oscillatory and capillary rheometers at 100 and 120°C are compared in Figure 3.36. The rheological behavior obtained by the two methods was found to be very close to each other. The viscosity curves at 120°C were very well superimposed. Capillary data at 100°C was found to be slightly superior to the oscillatory data, indicating a potential failure of Cox-Merz principle. Such a failure was reported to be observed for some systems on a certain range of shear rates [Snijkers and Vlassopoulos, 2014]. The viscosity laws determined from oscillatory or capillary rheometer are close enough to be used indifferently for SBR A.

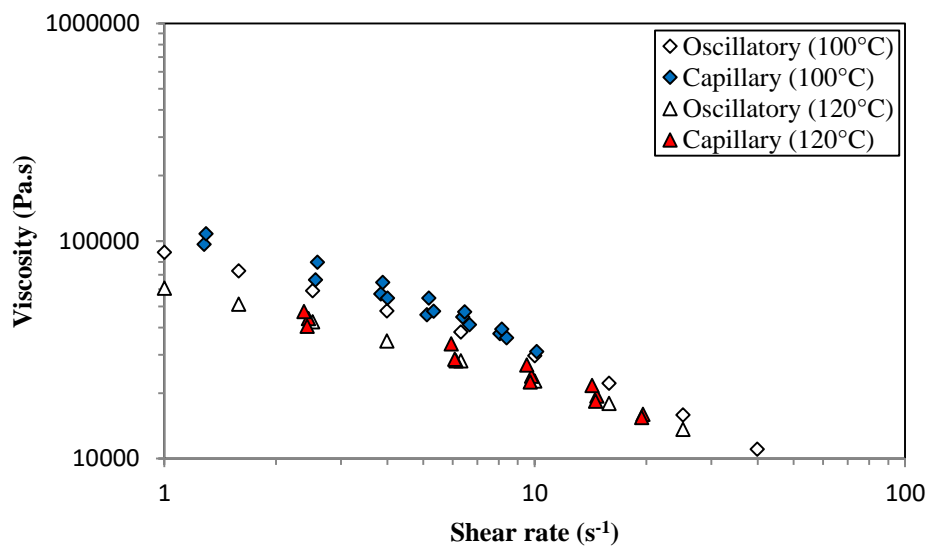


**Figure 3.36** – Viscosity curves of SBR A at 100 and 120°C obtained with oscillatory and capillary rheometers.

### 3.2.4. Styrene Butadiene Rubber B (SBR B) behavior

#### Pressure drop evolution

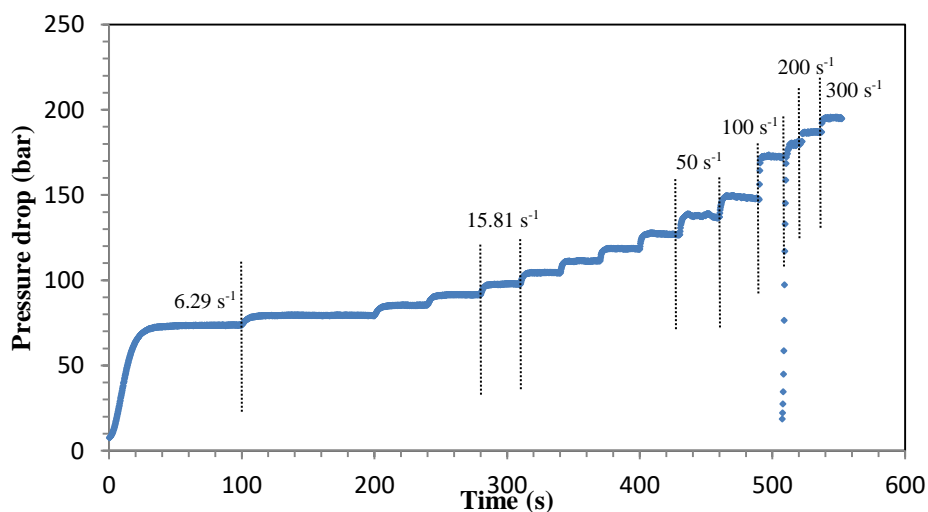


**Figure 3.37** – Evolution of pressure drop with time for different shear rates of SBR B at 100°C using a capillary of  $L/D = 8$  and a  $D = 2$  mm.

The evolution of the pressure drop in function of time of the SBR B (for a capillary die of  $L/D = 8$  and  $D = 2$  mm) at  $100^\circ\text{C}$  is presented in Figure 3.37 (page 93). Contrary to BR A and SBR A, pressure oscillations were not observed with SBR B. This was also the case while working at other temperatures and with other capillary dies. The pressure drop is plotted in function of the apparent shear rate (Figure 3.38) to identify the different flow regimes.

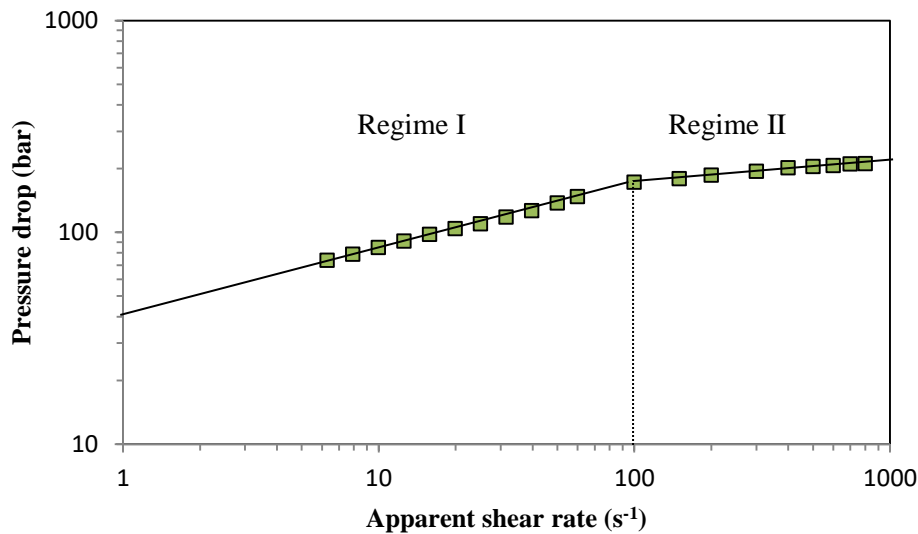


**Figure 3.38** – Evolution of pressure drop with apparent shear rate of SBR B at  $100^\circ\text{C}$  using a capillary of  $L/D = 8$  and a  $D = 2$  mm.

This rheological behavior of SBR B was found to be similar to the behavior of the pure SBRs characterized by Jugo Viloría and Crié [Jugo Viloría, 2017; Crié, 2014]. Two distinct flow regimes, marked by a change in the slope of the flow curve, were observed with SBR B. The change in slope was found to occur at about  $100\text{ s}^{-1}$  for all the capillary dies. After  $100\text{ s}^{-1}$ , the pressure drop continues to increase exponentially (linearly in log-log scale). The change of slope can be attributed either to wall slip or upstream flow instabilities. At higher temperatures, the onset of Regime II should occur at higher shear rates. These shear rates might be beyond the operating limit of RhéoART™. Consequently, obtaining data points at these shear rates might be problematic. Hence, the rheological characterization was carried out at lower temperatures ( $60$  and  $80^\circ\text{C}$ ). Figure 3.39 presents the pressure drop evolutions for a capillary die of  $L/D = 8$  and  $D = 2$  mm at  $60$ ,  $80$  and  $100^\circ\text{C}$ . Again, two flow regimes marked by a sharp change in slope were observed for SBR B at  $60$ ,  $80$  and  $100^\circ\text{C}$ .

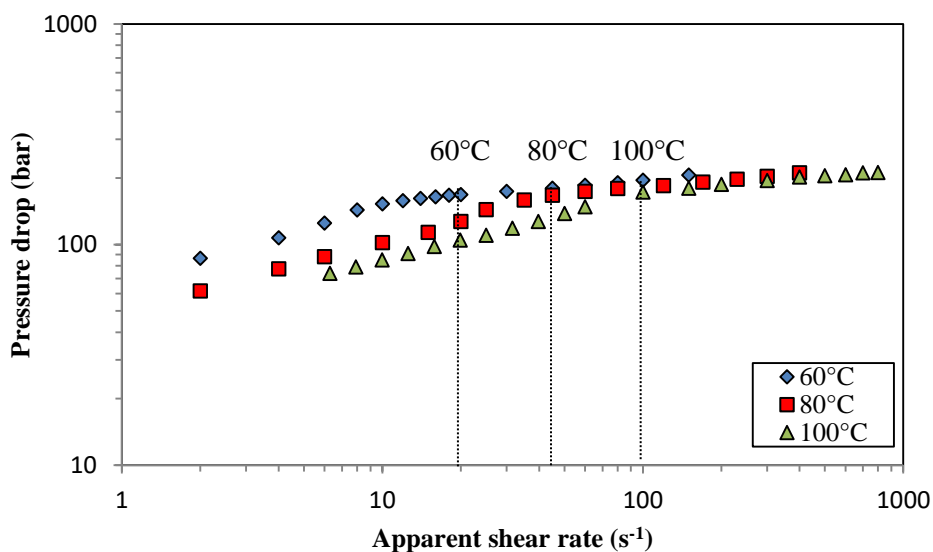


**Figure 3.39** – Evolution of pressure drop with time for different shear rates of SBR B at  $60$ ,  $80$  and  $100^\circ\text{C}$  for a capillary of  $L/D = 8$  and a  $D = 2$  mm.

Flow extrudates morphology

The flow extrudates morphology of SBR B at 100°C using a capillary die of  $L/D = 8$  and a  $D = 2$  mm are presented in Figure 3.41. Two types of instabilities were observed. Sharkskin instabilities were observed at low shear rates, corresponding to Regime I flow. These instabilities were found to become more chaotic in nature with increasing shear rates. At higher shear rates, corresponding to Regime II flow, a volume change was observed with the aspects of the extrudates. The Regime II flow was found to be dominated by chaotic instabilities. The flow regimes and their corresponding nature of flow extrudates of SBR B at 100°C is presented in Figure 3.40. Similar flow extrudates were observed at 60 and 80°C where sharkskin instabilities become more chaotic in nature at higher shear rates before transitioning to chaotic instabilities when they reach Regime II flow. Upstream flow instabilities are reported to create a slight and delicate change of slope which usually corresponds to the beginning of the volume defect. This phenomenon is highlighted by the change in slope being more prominent with shorter capillaries [den Otter, 1971]. This tendency was not observed in the measurements indicating that the change of slope is rather due to the transition from a branch of no-slip or weak slip to a branch of considerable slip.

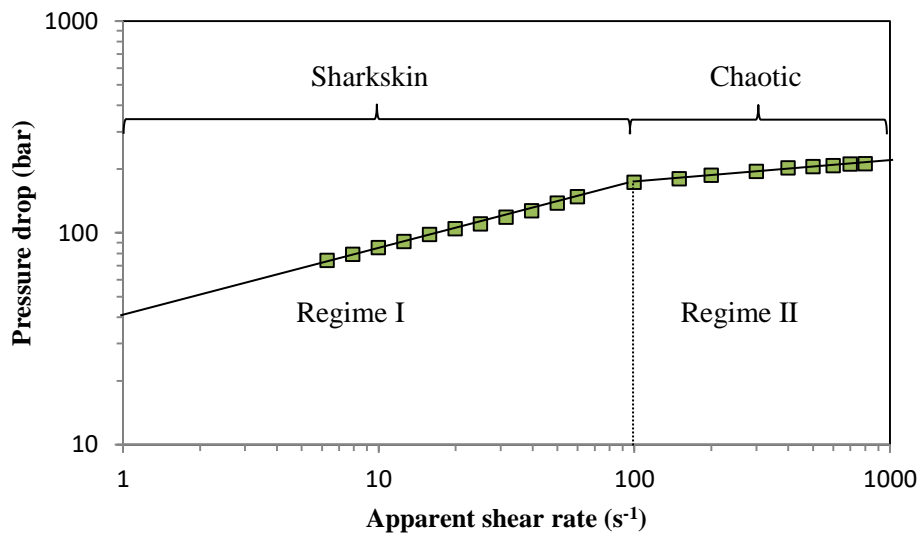


Figure 3.40 – Flow regimes and their corresponding flow extrudates of SBR B at 100°C for a capillary die of  $L/D = 8$  and  $D = 2$  mm.



Figure 3.41 – Flow extrudates of SBR B at 100°C for a capillary die of  $L/D = 8$  and  $D = 2$  mm.

A continuous flow curve is typical of branched or highly elastic polymers [Vergnes, 2015]. However, the extrudates in regime I show a sharkskin defect which is not usually observed with branched polymers. The dynamic rheology already questioned about the potential presence of star chains within linear ones. A blend of linear and star chains may explain this particular behavior.

Influence of capillary geometry

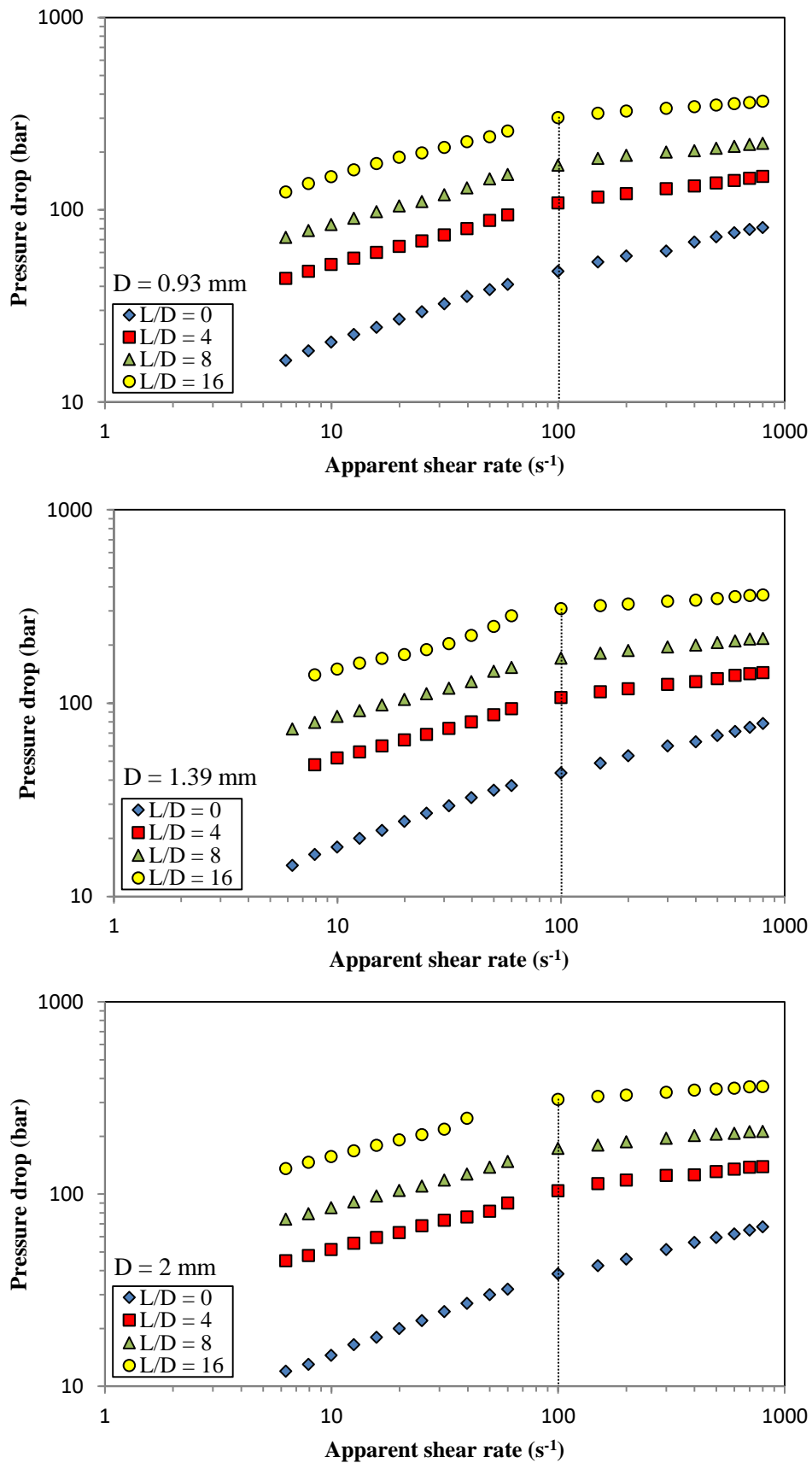


Figure 3.42 – Pressure drop evolutions in function of apparent shear rates of SBR B at 100°C with different capillary die diameters ( $D = 0.93, 1.39$  and  $2$  mm) and  $L/D$  ratios (0, 4, 8 and 16).

The pressure drop evolutions of SBR B in function of apparent shear rates for capillary dies of different lengths and diameters at 100°C are presented in Figure 3.42 (page 96). A significant change in slope was observed for all non-zero length capillary dies at 100 s<sup>-1</sup>. The zero length dies (L/D = 0) witnessed, in comparison, only a small change in slope. However, a change in slope also occurs at 100 s<sup>-1</sup>. Thus, the onset of Regime II flow of SBR B was unaffected by the die geometry at 100°C. The pressure drop evolutions for different L/D ratios of SBR B at 100°C is presented in Appendix VIII. The pressure drop evolutions of SBR B at 60 and 80°C are presented in Appendix IX and X respectively.

Shear stress and viscosity curves

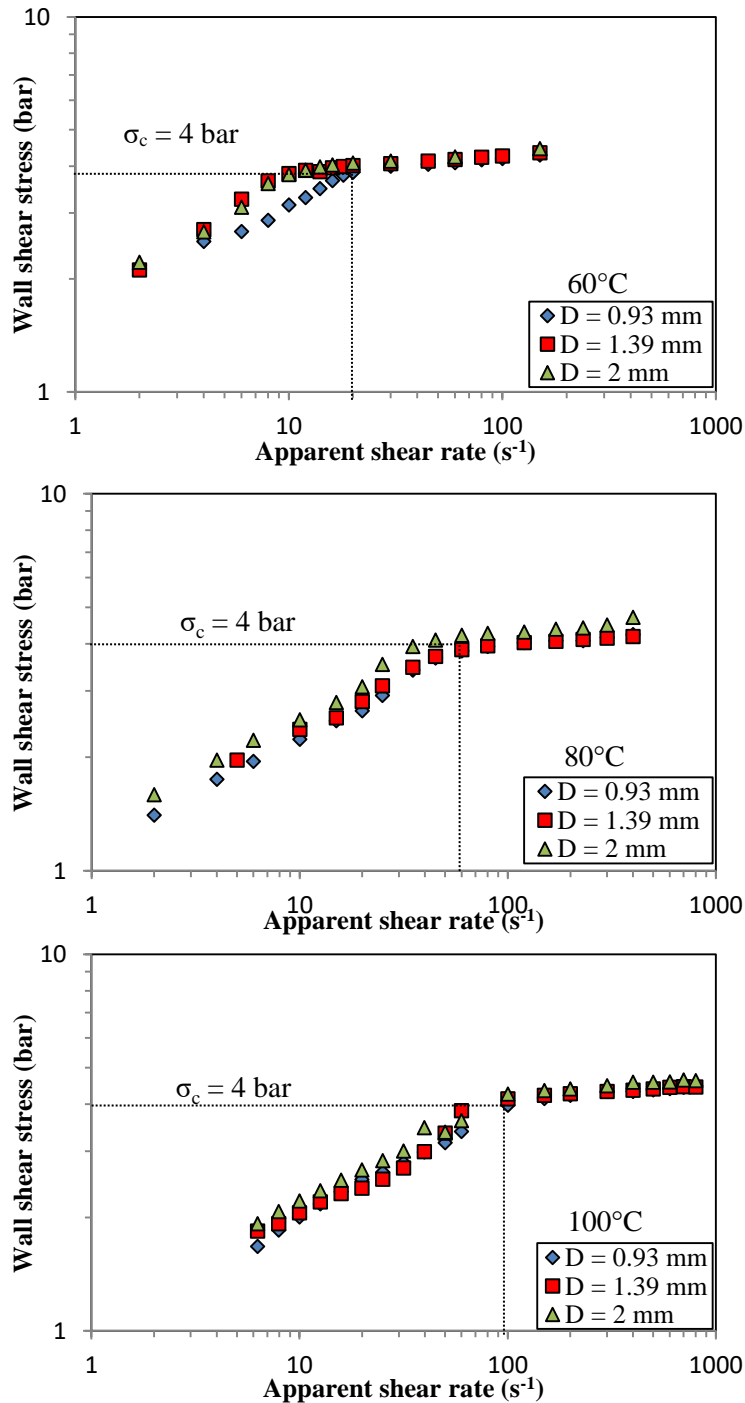


Figure 3.43 – Real shear stresses in function of the shear rates of the SBR B at 60, 80 and 100°C for capillaries of different diameters (D = 0.93, 1.39 and 2 mm).

Following the Bagley corrections, the evolution of wall shear stress in function of the apparent shear rate at different temperatures is presented in Figure 3.43 (page 97). A critical shear stress ( $\sigma_c$ ) of about 4 bars was obtained, independent of the temperature. As with SBR A, the onset of the Regime II was found to occur at higher shear rates with increasing temperature. The Regime I flow curves, at the different temperatures were found to not superimpose but are rather ranked in an arbitrary order. Based on the aspect of the flow extrudates (Figure 3.41), no slip or weak slip was assumed in Regime I. The Regime II flow curves were ranked in the order of increasing diameters (Figure 3.44).

At 60°C, the Regime I flow curve for one diameter ( $D = 0.93$  mm) was found to have a different behavior to the other curves ( $D = 1.39$  and 2 mm). Though the flow curve ( $D = 0.93$  mm) transitions to Regime II at a critical shear stress ( $\sigma_c$ ) of 4 bars, the shear rate at which this transition took place was found to be abnormal. This curve was not considered in the following analysis. Similar to SBR A, the onset of the Regime II flow was found to occur at higher shear rates with increasing temperature.

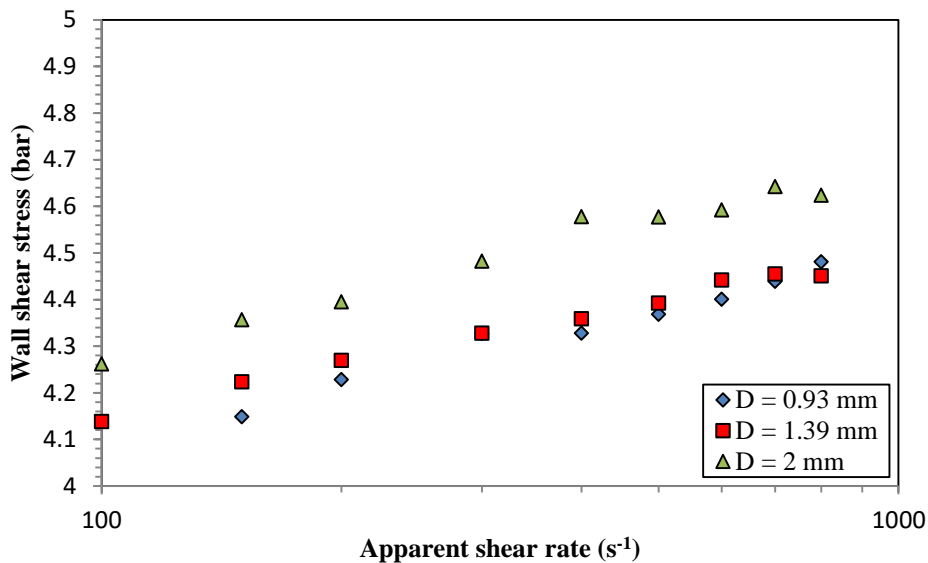


Figure 3.44 – Zoom of the Regime II curve of SBR B at 100°C for capillaries dies of different diameters ( $D = 0.93, 1.39$  and 2 mm) and  $L/D$  ratios (0, 4, 8 and 16).

Following the Rabinowitsch corrections, the viscosity curves of SBR B at different temperatures could be plotted in function of the real shear rate (Figure 3.45).

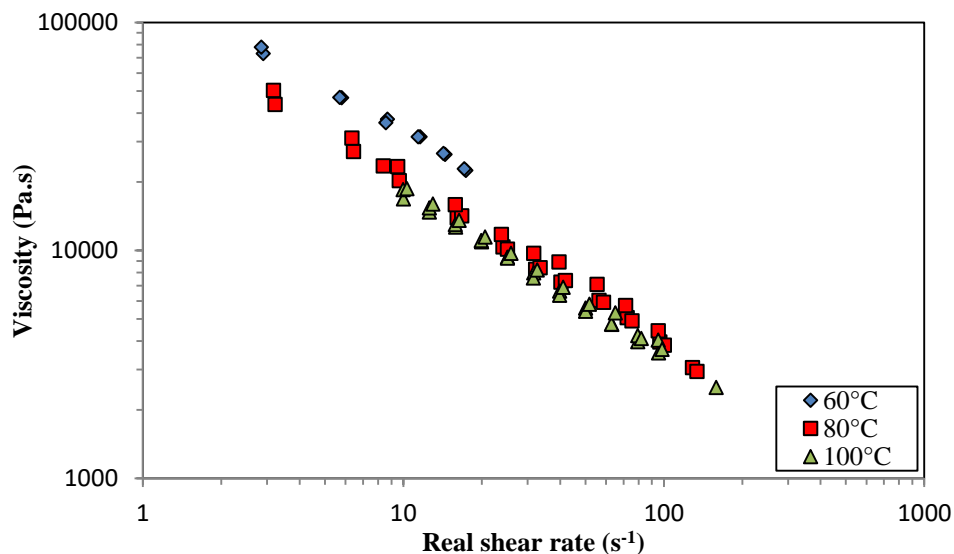


Figure 3.45 – Evolution of viscosity in function of real shear rates of SBR B at 60, 80 and 100°C for capillary dies of  $D = 0.93, 1.39$  and 2 mm.

### Chapter 3: Rheological and wall slip characterization

The time-temperature superposition was carried out on the capillary data of SBR B. The master viscosity curves of SBR B are presented in Appendix VII. The shift factor,  $a_T$  for the different temperatures is presented in Table 3.8.

Temperature	$a_T$
60°C	6.8
80°C	1.6
100°C	1

**Table 3.8** – Shift factors of SBR A at 60, 80 and 100°C.

An activation energy of 49.9 kJ/mol was obtained with the capillary data. This energy is comparable to the activation energy obtained with the oscillatory data. The values of the power law constants of the viscosity laws for the different temperatures are presented in Table 3.9.

Temperature (°C)	Consistency, K (Pa.s <sup>m</sup> )	Shear-thinning index (m)
60	150000	0.35
80	109200	0.28
100	92600	0.29

**Table 3.9** – Power law constants of the viscosity laws of SBR B at 60, 80 and 100°C.

The viscosity curves obtained from the oscillatory and capillary rheometers, at 60, 80 and 100°C, are compared in Figure 3.46. The curves obtained from the two methods do not superimpose but were found to be quite close with similar slopes. The viscosity obtained from the capillary rheometer was found to be slightly superior to that of the oscillatory rheometer. Since the Cox-Merz rule did not hold, the viscosity laws of the capillary data were chosen to describe the flow behavior of SBR B.

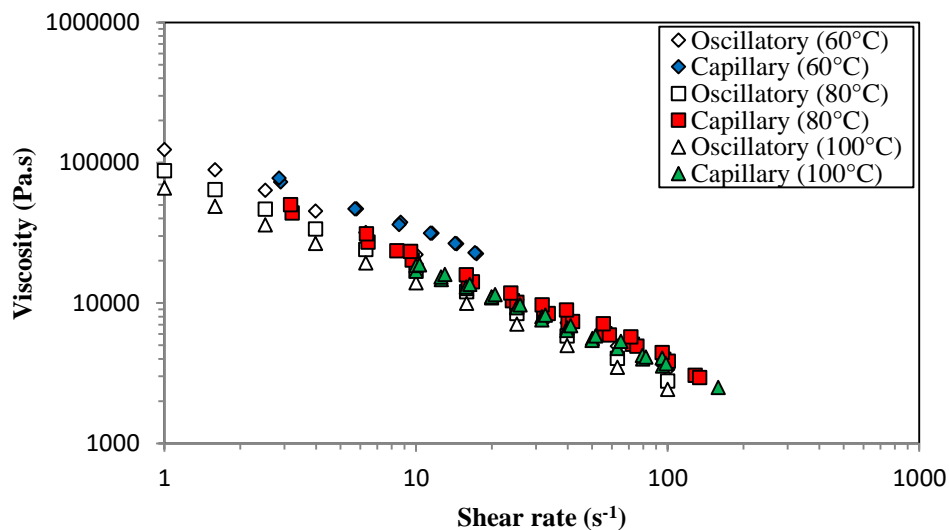


**Figure 3.46** – Viscosity curves of SBR B at 60, 80 and 100°C obtained with oscillatory and capillary rheometers.

#### 3.2.5. Rubber compound (SBR C) behavior

##### Pressure drop evolution

The evolution of the pressure drop in function of time of the SBR C (for a capillary die of  $L/D = 8$  and  $D = 2$  mm) at 100°C is presented in Figure 3.47. No pressure oscillations were observed and steady state values could be identified at the different shear rates with all the capillary dies. The pressure drop evolution of SBR C at 100°C is presented in Figure 3.48. No significant change in slope of the pressure drop evolution was observed with the flow curves. A single flow regime (Regime I) was observed at the characterized shear rates (10 to 300 s<sup>-1</sup>).

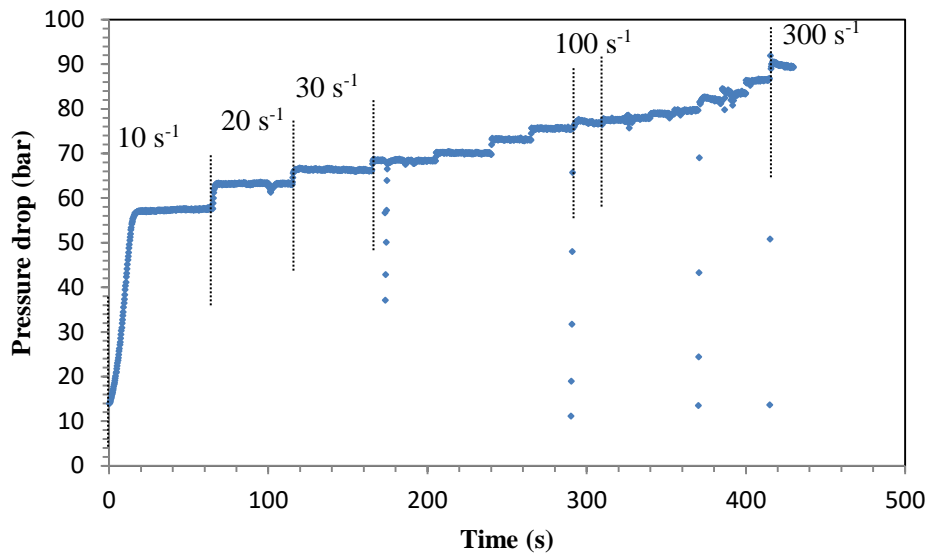


**Figure 3.47** – Evolution of pressure drop with time for different shear rates of SBR C using a capillary of  $L/D = 8$  and a  $D = 2$  mm at  $100^{\circ}\text{C}$ .

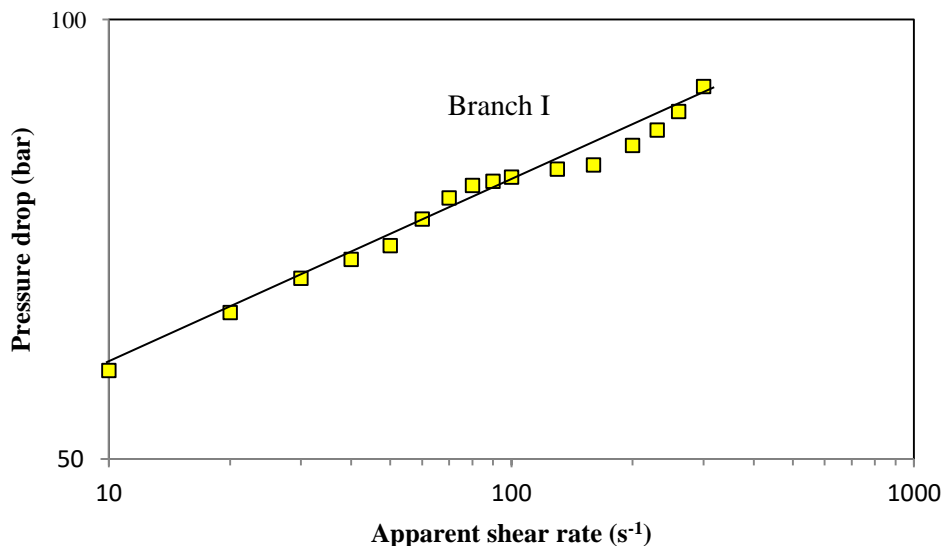


**Figure 3.48** – Evolution of pressure drop with apparent shear rate of SBR C at  $100^{\circ}\text{C}$  using a capillary of  $L/D = 8$  and a  $D = 2$  mm.

### Flow extrudates morphology

The flow extrudates of SBR C at  $100^{\circ}\text{C}$  using a capillary die of  $L/D = 8$  and a  $D = 2$  mm are presented in Figure 3.49. Smooth extrudates were observed shear rates ranging from  $10$  to  $300\text{ s}^{-1}$ . No flow instabilities, nor aspect modifications were observed on examining the flow extrudates. The evolution of shear stress curves will indicate if Regime I accounts for no slip or strong slip regime.

Note: A difference in contrast of the flow extrudates is observed in Figure 3.49. This is because dust particles stuck to the SBR C flow extrudate at  $100\text{ s}^{-1}$ , giving it a lower contrast than the flow extrudate at  $300\text{ s}^{-1}$ .

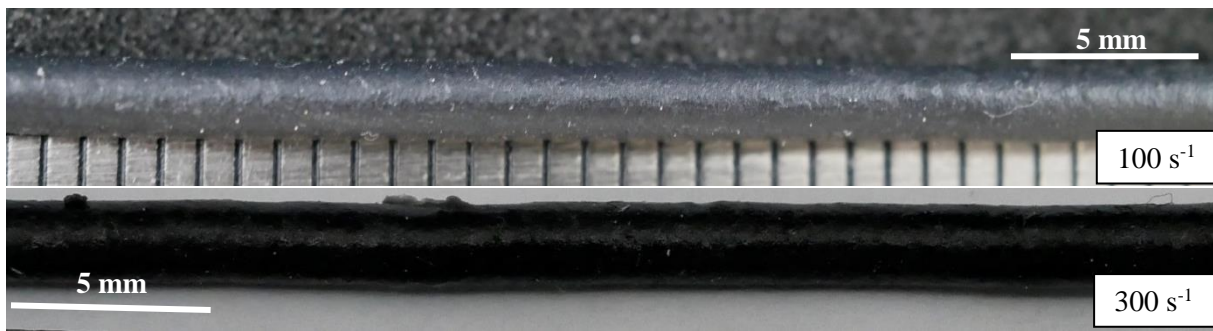


Figure 3.49 – Flow extrudates of SBR C at 100°C using a capillary die of  $L/D = 8$  and a  $D = 2$  mm.

Influence of capillary geometry

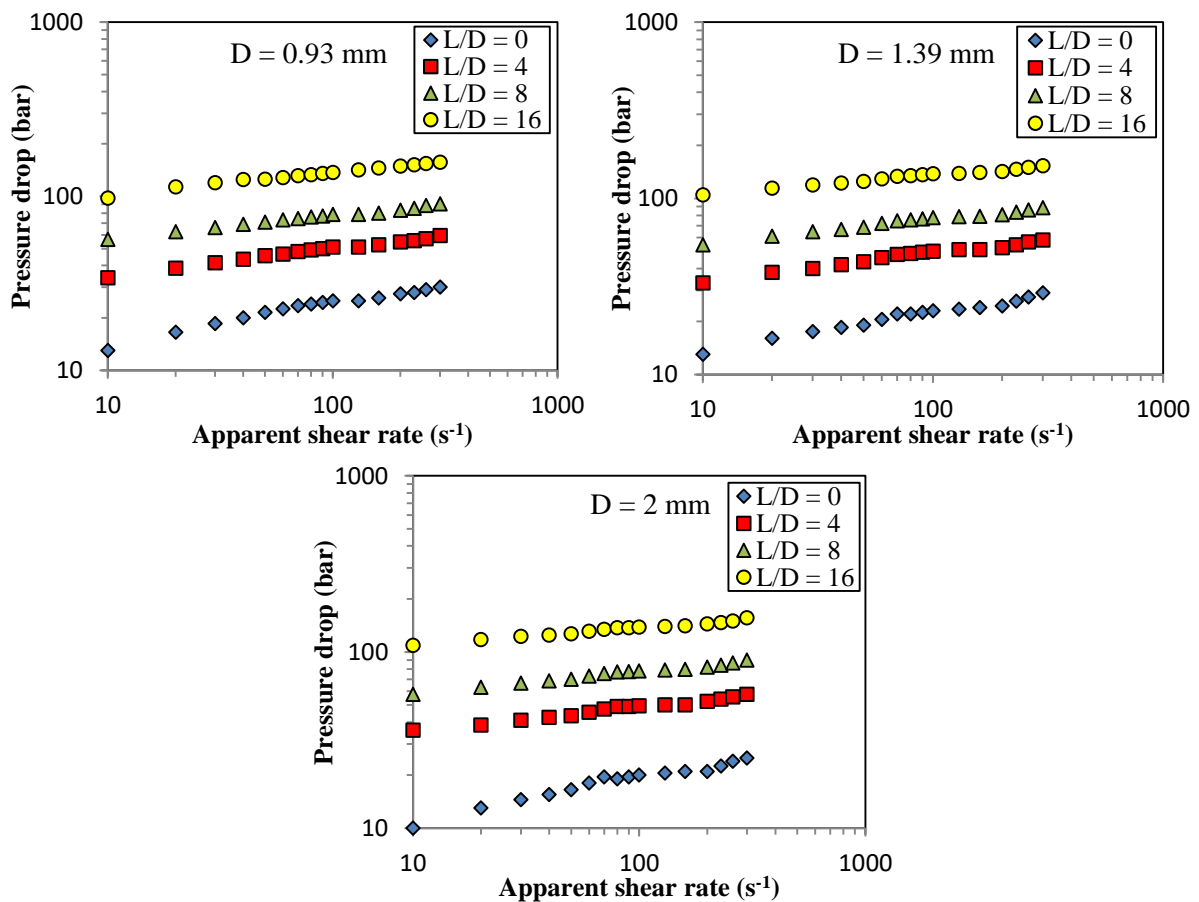


Figure 3.50 – Pressure drop evolutions in function of apparent shear rates of SBR C at 100°C with different capillary die lengths ( $D = 0.93, 1.39$  and  $2$  mm).

The pressure drop evolutions of SBR C in function of the apparent shear rates for capillary dies of different lengths and diameters at 100°C are presented in Figure 3.50. A single flow regime is observed for all  $L/D$  ratios. Thus, SBR C exhibits a single flow regime at these shear rates, probably without wall slip. The pressure drop evolutions for different  $L/D$  ratios of SBR C at 100°C is presented in Appendix XI. It was found that for the same  $L/D$ , the flow curves were found to superimpose each other. Thus, for all non-zero length dies, the impact of the diameter is negligible. However, for zero-length capillary dies, the measured pressure drop was ranked in the order of decreasing diameters or increasing compressibility of the die.

Shear stress and viscosity curves:

The evolution of the shear stress of SBR C at 100°C is presented in Figure 3.51. The curves of the different diameters do not superimpose but were found to be close to each other. These curves cannot be ranked in the order of increasing diameter. Thus, the flow can be considered to be a flow without considerable wall slip i.e. no slip or weak slip flow regime. The lack of wall slip experienced by SBR C at 100°C could be due to its superior adhesive properties. Following Rabinowitsch corrections, the viscosity curves of SBR C is presented in Figure 3.52. A viscosity law was obtained in the form of a power law. A shear-thinning index of close to 0.1 was also obtained by other researchers [de Valle et Aramburo 1981; Crié, 2014] while working with rubber compounds. The constants of the power law equation are:  $K= 93300 \text{ Pa}\cdot\text{s}^m$  and  $m =0.11$ .

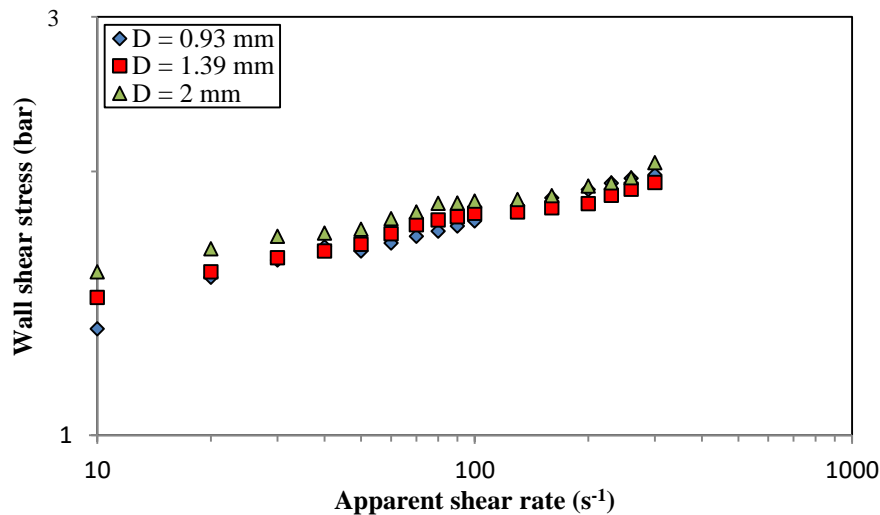


Figure 3.51 – Real shear stresses in function of the shear rates of the SBR C at 100°C for capillaries of different diameters ( $D = 0.93, 1.39$  and  $2 \text{ mm}$ ).

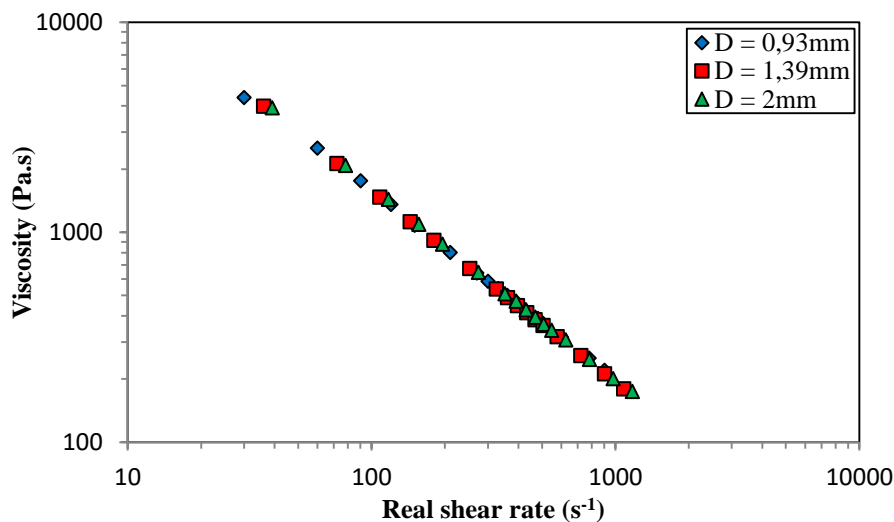


Figure 3.52 – Evolution of viscosity in function of real shear rates of SBR C at 100°C for capillary dies of  $D = 0.93, 1.39$  and  $2 \text{ mm}$ .

The viscosity curve obtained from the oscillatory and the capillary data are compared in Figure 3.53. A lack of correlation between the two viscosity curves was observed. This could be attributed to the presence of fillers in the compound. At small deformations, the rheology of the fluid is influenced by the presence of fillers. Thus, SBR C exhibits a significantly superior viscosity with the oscillatory data in comparison to the viscosity obtained with the capillary data. The viscosity laws of the fluids used in this study obtained by capillary rheometry are compared in Appendix II.

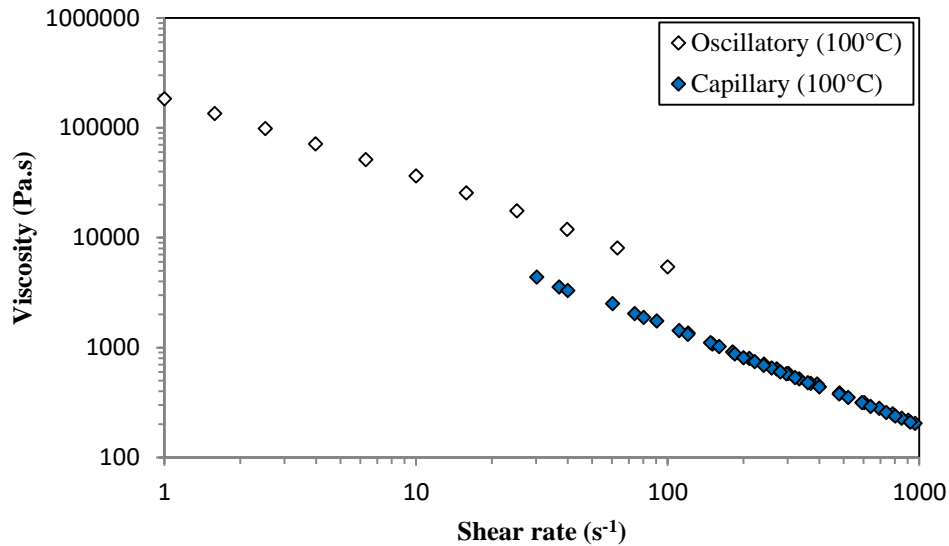


Figure 3.53 – Viscosity curves of SBR C at 100°C obtained with oscillatory and capillary rheometers.

### 3.3. Wall slip characterization

In this section, the wall slip behavior of the rubber products were characterized at 100°C. As SBR C does not exhibit wall slip up to shear rates of 300 s<sup>-1</sup>, there will be no discussion on its wall slip behavior. The influence of temperature on the wall slip velocities was investigated with SBR A and SBR B. Wall slip velocities can be determined using the Shear Rate Difference method.

#### 3.3.1. BR A wall slip velocities

The critical shear stress of BR A is 3.2 bar. After the oscillating flow regime, BR A exhibits wall slip behavior at lower shear stresses. Thus, the wall slip velocities were calculated from the onset of Regime II flow, corresponding to a shear stress of 1.5 bar (Figure 3.23). The Regime I and Regime II flow curves of the shear stress evolution curves of BR A (Figure 3.23) were used to obtain the wall slip velocities. An example of the Shear Rate Difference method is illustrated in Figure 3.54.

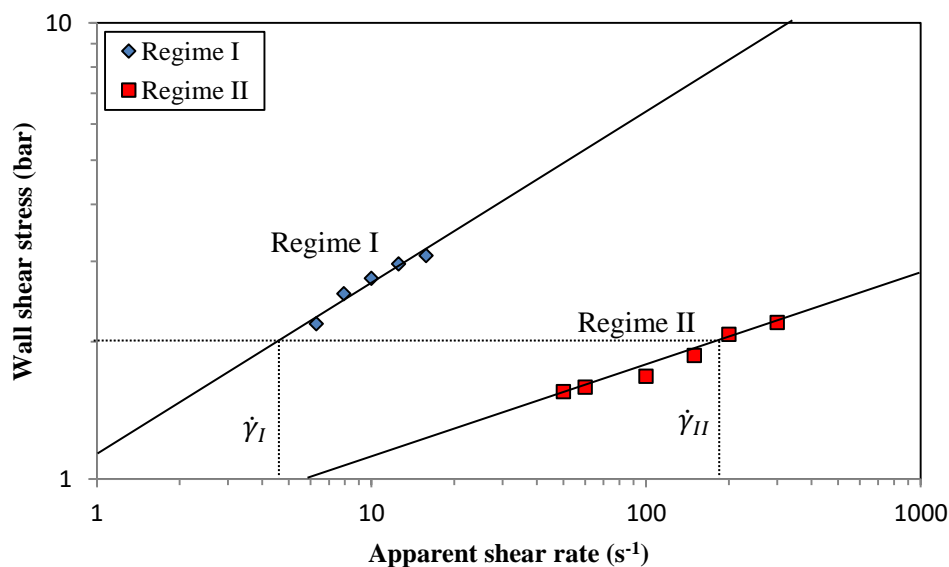
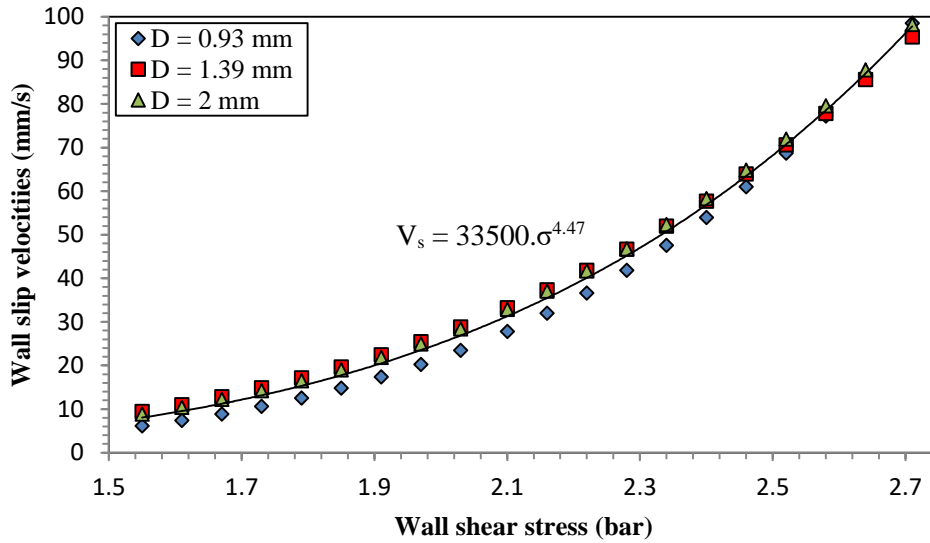


Figure 3.54 – Shear Rate Difference method for BR A at 100°C for a capillary of D = 0.93 mm.

Trend lines were defined for Regime I and Regime II flow curves for each diameter. The Regime I and Regime II flow curves were fitted with a power law.  $\dot{\gamma}_I$  and  $\dot{\gamma}_{II}$  values were obtained for each shear stress. Equation 2.16 provides the wall slip velocity for each shear stress value. Figure 3.55 shows the evolution of wall slip velocities of BR A at 100°C.



**Figure 3.55** – Evolution of wall slip velocity obtained through the Shear Rate Difference method for BR A at 100°C with capillary dies of D = 0.93, 1.39 and 2 mm.

In this case, the wall slip velocity curves for the different diameters were found to superpose quite well. A wall slip velocity for BR A could be obtained by defining a single law for the combined data of the three diameters. This wall slip law was found to fit well when defined as a power law equation of the form:

$$V_s = A \cdot \sigma^b \quad \text{Equation 3.4}$$

where  $V_s$  is the wall slip velocity (mm/s),  $\sigma$  is the wall shear stress (MPa), A and b are constants.

The values of the constants (A and b) depend on the units chosen for the variables. If Equation 3.4 is expressed in SI units, the constant ‘A’ would provide values of very small magnitude ( $10^{-26}$ ) which can be difficult to integrate into the simulation code. By representing wall slip velocities in mm/s and wall shear stress in MPa, the constants show values of acceptable magnitudes. The power law constants of the wall slip velocity law of BR A (Equation 3.4) are:  $A = 33500 \text{ mm.MPa}^b \cdot \text{s}^{-1}$  and  $b = 4.47$ .

### Use of wall slip velocity law for linear and branched polymers

Branched polymers:

Due to the structure of the polymers, linear and branched polymers undergo different types of slip behavior. In the case of branched polymers, no pressure oscillations are encountered and wall slip can occur only at shear stresses above the critical shear stress ( $\sigma_c$ ). Thus, the wall slip velocity law is only applicable for shear stresses above this critical value. The wall slip velocity is considered as zero below the critical shear stress.

Linear polymers:

For linear polymers, wall slip can occur in Regime II at shear rates below the critical shear stress. Thus, shear stress at which the Regime II transition occurs ( $\sigma_{c*}$ ) is also noted. We assume that the wall slip velocity is zero below this shear stress ( $\sigma_{c*}$ ). The slip velocity law is applicable from this shear

stress. Different slip mechanisms are encountered in the loading (increasing  $\sigma_w$ ) and unloading condition (decreasing  $\sigma_w$ ).

In the loading condition, no wall slip is encountered till the critical shear stress ( $\sigma_c$ ). On increasing the shear stress above this value, the slip velocity is given by Equation 3.4 and we encounter high slip velocities (Figure 3.56). In the unloading condition, the slip velocity is applicable till the critical shear stress corresponding to Regime II transition ( $\sigma_{c^*}$ ). The wall slip velocity is considered as zero below this shear stress. Table 3.10 summarizes the different slip phenomenon experienced by the fluid in these conditions.

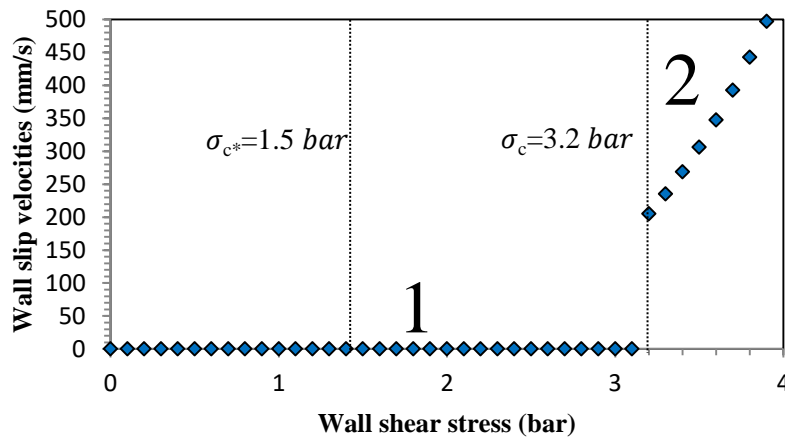


Figure 3.56 – Wall slip velocity law of a linear polymer during the loading condition.

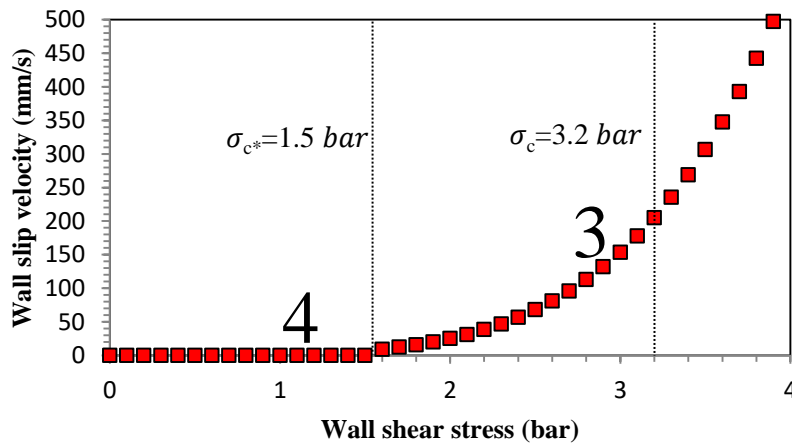


Figure 3.57 – Wall slip velocity law of a linear polymer during the unloading condition.

Loading condition (increasing shear stress)		
1	$\sigma \uparrow; 0 < \sigma < \sigma_c$	The fluid undergoes slip free flow.
2	$\sigma \uparrow; \sigma_c < \sigma$	The fluid slips while obeying the wall slip velocity law.
Unloading condition (decreasing shear stress)		
3	$\sigma \downarrow; \sigma_{c^*} < \sigma$	The fluid slips while obeying the wall slip velocity law.
4	$\sigma \downarrow; \sigma < \sigma_{c^*}$	The fluid exhibits no wall slip.

Table 3.10 – Wall slip behavior of linear polymers during loading and unloading condition.

### 3.3.2. SBR A wall slip velocities

The critical shear stress ( $\sigma_c$ ) of SBR A is 3.15 bar while the Regime II transition occurs at 2.3 bar ( $\sigma_{c^*}$ ). The wall slip velocities are estimated from 2.3 bar. The evolution of wall slip velocities of SBR A at 100, 120 and 140°C are presented in Figure 3.58. At 100°C, the curves of the different diameters were found to be close to each other. At 120°C, the  $D = 1.39$  mm curve was found to deviate from the other

curves. Similarly, the  $D = 2$  mm curve at  $140^{\circ}\text{C}$  deviates from the other curves. We cannot conclude that there is an effect of geometry on the wall slip velocities at  $120$  and  $140^{\circ}\text{C}$ . In such a case, the wall slip velocities curves must be ranked in increasing order of diameters. Thus, this discrepancy in the data must be due to the inaccuracy of some measurements.

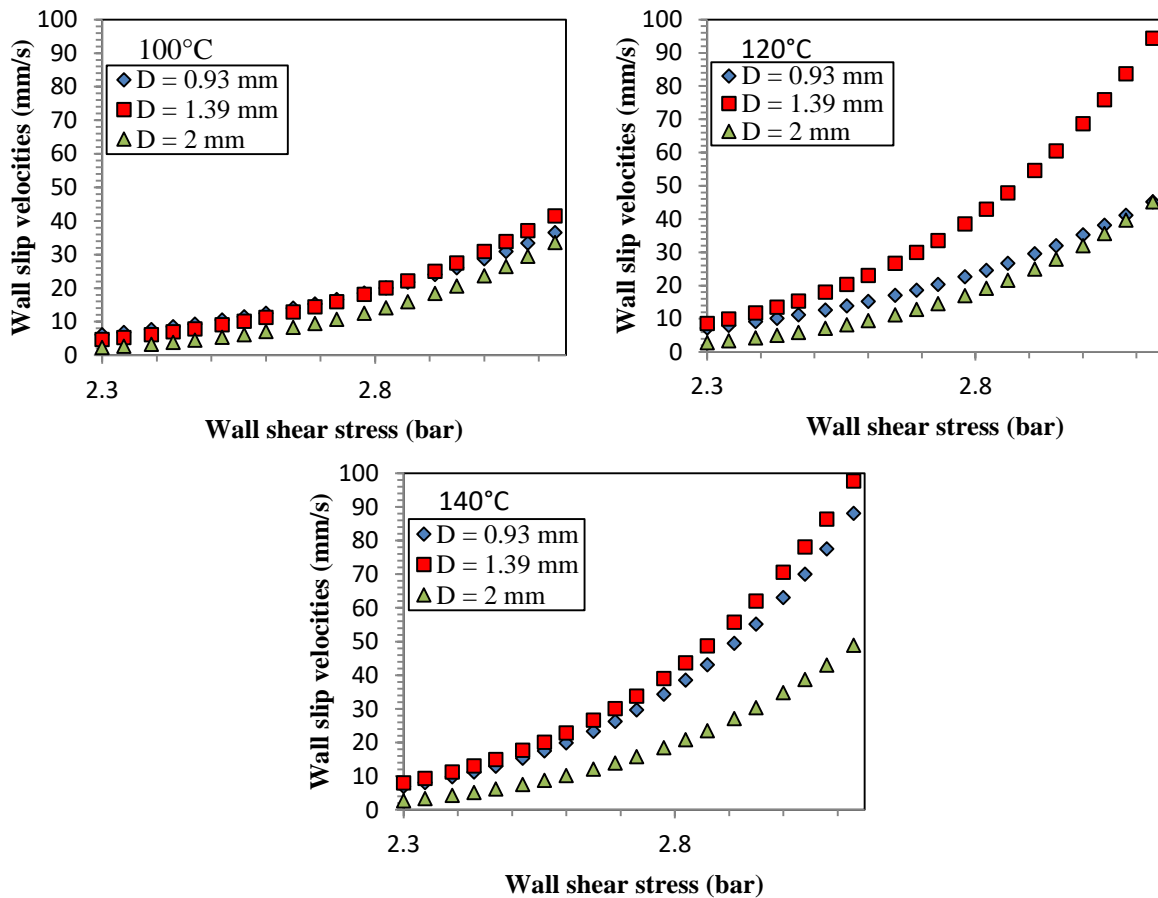


Figure 3.58 – Wall slip velocities of SBR A determined by the Shear Rate Difference method at  $100$ ,  $120$  and  $140^{\circ}\text{C}$  for capillary dies of  $D = 0.93$ ,  $1.39$  and  $2$  mm.

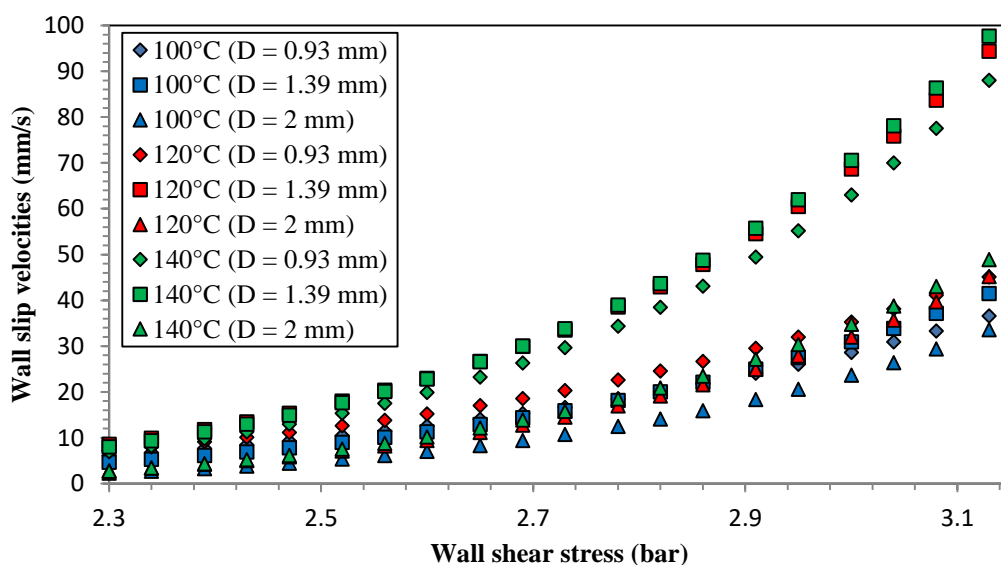


Figure 3.59 – Wall slip velocities of SBR A determined by Shear Rate Difference method at different temperatures for capillary dies of  $D = 0.93$ ,  $1.39$  and  $2$  mm.

Figure 3.59 (page 106) plots the wall slip velocities curves of SBR A at different temperatures on the same graph. A general trend of increasing wall slip velocities with increasing temperature can be observed. The two exceptions to this trend are the  $[D = 1.39 \text{ mm}, 120^\circ\text{C}]$  and  $[D = 2 \text{ mm}, 140^\circ\text{C}]$  curves. Due to the inaccuracies of these measurements, accurate slip velocity laws cannot be defined for SBR A at 120 and 140°C.

However, for the purposes of numerical simulation of the mixing process, we define wall slip velocity laws at 120 and 140°C by neglecting the data from the two erroneous curves. As a result of this choice, it is important to note that the wall slip velocities at 120 and 140°C are not accurate. Consequently, we refrain from defining a thermodependent slip velocity law based on this data. Table 3.11 presents the constants of the wall slip velocity laws of SBR A at 100, 120 and 140°C.

Temperature (°C)	Slip velocity law constants	
	A (mm.MPa <sup>b</sup> .s <sup>-1</sup> )	b
100	$6.6 \cdot 10^3$	6.34
120	$2.1 \cdot 10^5$	7.25
140	$1.2 \cdot 10^6$	8.12

Table 3.11 – Constants of the wall slip velocity laws for SBR A at 100, 120 and 140°C.

### 3.3.3. SBR B wall slip velocities

The critical shear stress for SBR B is 4 bars. Due to the lack of pressure oscillations, the wall slip velocities are estimated from this value. The evolution of wall slip velocities of SBR B at 60, 80 and 100°C are presented in Figure 3.60.

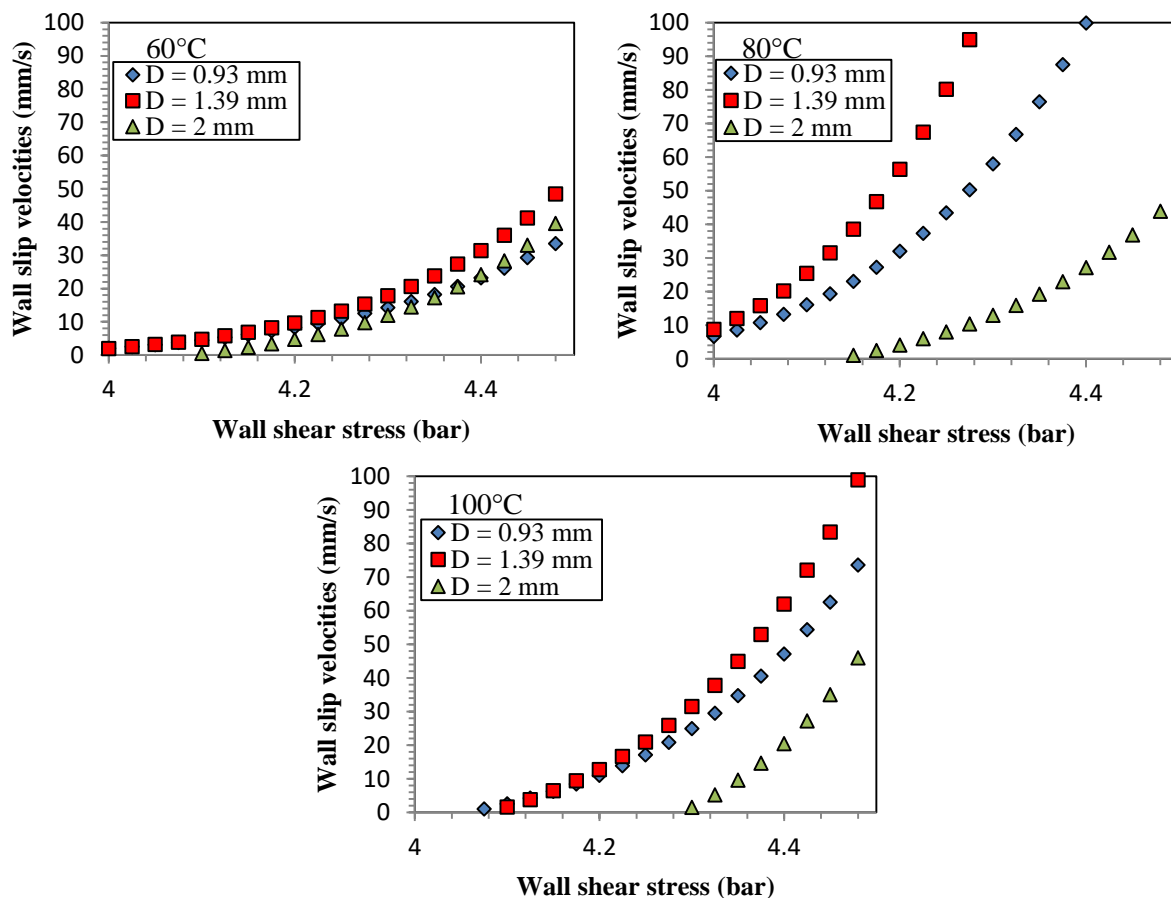


Figure 3.60 – Wall slip velocities of SBR B determined by Shear Rate Difference method at 60, 80 and 100°C for capillary dies of  $D = 0.93, 1.39$  and  $2 \text{ mm}$ .

The curves of the different diameters were found to be close to each other at 60°C. This was not the case at 80 and 100°C. On plotting all the wall slip velocity curves (Figure 3.61), we find that none of the curves at 80°C are not close to each other. At 100°C, the D = 0.93 mm and D = 1.39 mm curve are close to each other. For simulation purposes, wall slip velocities are defined at 60 and 100°C by neglecting the [D = 2 mm, 100°C] curve.

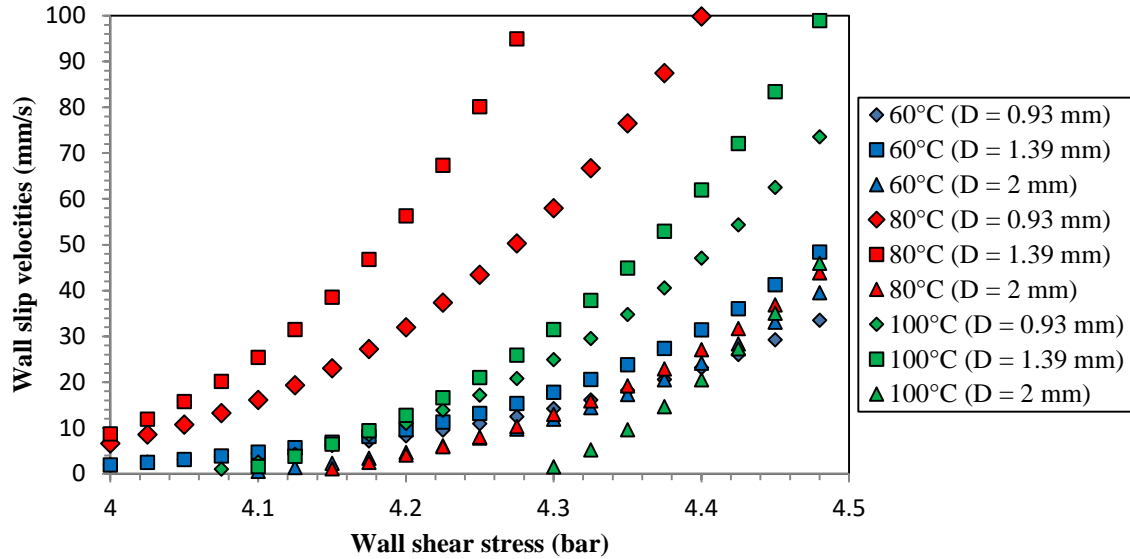


Figure 3.61 – Wall slip velocities of SBR B determined by Shear Rate Difference method at different temperatures for capillary dies of D = 0.93, 1.39 and 2 mm.

Table 3.12 presents the constants of the wall slip velocity laws for SBR B at 60, and 100°C. SBR B exhibits unrealistically high values for the exponent ‘b’. This is due to the stark change of slope between the Regime I and Regime II curves (Figure 3.43). From Figure 3.59 and 3.61, we find that the estimation of wall slip velocities with the indirect method can provide slip velocity values which are not realistic. It is advised to carry out direct estimations of the wall slip velocities to obtain accurate slip velocity laws. The thermo-dependence of wall slip behavior can be better studied with the determination of the evolution of slip lengths with temperature [Bäumchen *et al.*, 2012].

Temperature (°C)	Slip velocity law constants	
	A (mm.MPa <sup>b</sup> .s <sup>-1</sup> )	b
60	5.2 * 10 <sup>6</sup>	23.23
100	2.8 * 10 <sup>9</sup>	30.05

Table 3.11 – Constants of the wall slip velocity laws for SBR A at 100, 120 and 140°C.

### Comparison of wall slip velocities for the different elastomers

To show the contrasting slip behavior of BR A, SBR A and SBR B, the wall slip velocity law of these products is compared in Figure 3.62. The main difference between these curves is the shear stress at which the onset of wall slip occurs. The exponent of the wall slip velocity laws of BR A and SBR A were found to be comparable to those obtained by Gierlowski [Gierlowski, 2002] and Jugo Viloria [Jugo Viloria, 2017]. The exponent of the wall slip velocity of SBR B was found to be very high.

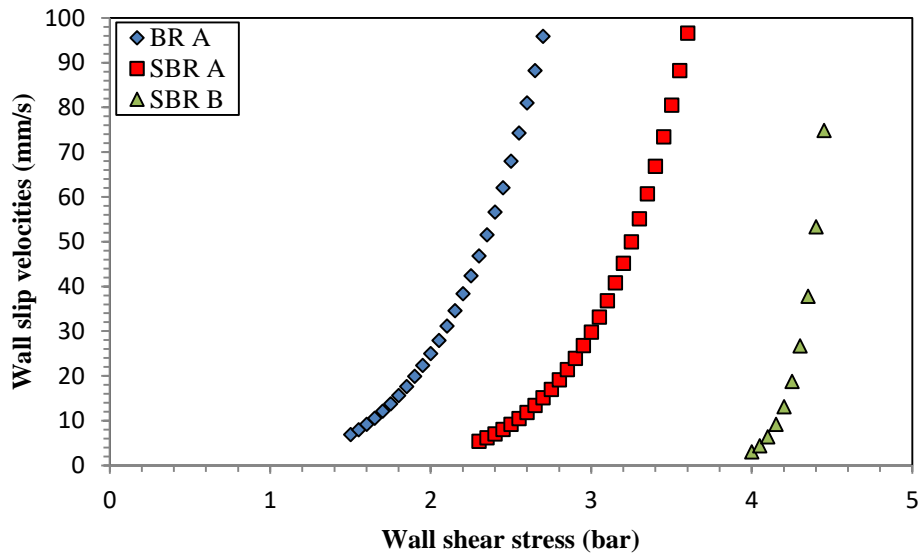


Figure 3.62 – Comparison of the wall slip velocity laws of BR A, SBR A and SBR B at 100°C.

## Conclusions

The rheological and wall slip behavior of the different products of the study were characterized using oscillatory and capillary rheometry. The oscillatory rheometer was used to identify the required properties of the fluid for the flow observations. The silicone fluid was identified for this purpose. Subsequently, the viscoelastic behavior of the silicone fluid and the different rubber products was characterized with the oscillatory rheometer.

The different flow regimes, flow instabilities and slip behavior experienced by the products were characterized with the capillary rheometer. The viscosity curves of the oscillatory and capillary data were compared and were found to be in relative agreement for the pure rubber products with the exception of SBR C. The rheological behavior of the different products is summarized in Table 3.13. Due to the lack of correlation of oscillatory and capillary data of SBR C, the viscosity laws obtained from the capillary data were chosen over those obtained with the oscillatory data.

	BR A	SBR A	SBR B	SBR C
<b>Molecular Structure</b>	Linear	Branched	Linear	Compound
<b>Flow Regimes</b>	Regime I Oscillating Regime II	Regime I Oscillating Regime II	Regime I Regime II	Regime I
<b>Critical shear stress (bar)</b>				
<b>Regime I (<math>\sigma_c</math>)</b>	3.2	3.15	4	-
<b>Regime II (<math>\sigma_{c*}</math>)</b>	1.5	2.3		
<b>Critical shear rate (s<sup>-1</sup>)</b>				
<b>Regime I</b>	15-20	6-8	100	-
<b>Regime II</b>	40-60	20-40	-	

**Table 3.13** – Comparison of the rheological behavior of the rubber products at 100°C.

Wall slip velocities were estimated with the Shear Rate Difference method. Moreover, the influence of temperature on the wall slip velocities with SBR A and SBR B was investigated. A general trend of increasing wall slip velocities with increasing temperature was observed. Due to some data inaccuracies, it was difficult to define wall slip velocity laws at all temperatures with accuracy. No thermodependent wall slip velocity law could be obtained for the rubber products due to these inaccuracies. Wall slip velocity laws could be obtained for the rubber products at 100°C. The viscosity and wall slip velocity laws of the different rubber products are summarized in Table 3.14.

	BR A		SBR A		SBR B		SBR C	
	<b>K</b> (Pa.s <sup>m</sup> )	<b>m</b>						
<b>Viscosity law</b> $\eta = K \cdot \dot{\gamma}^{m-1}$	98500	0.38	121000	0.45	92600	0.29	93300	0.11
<b>Activation energy (E<sub>a</sub>)</b>	-		42 kJ/mol		49.9 kJ/mol		-	
<b>Wall slip velocity law</b> $V_s = A\sigma^b$ with $V_s$ (mm/s) and $\sigma$ (MPa)	<b>A</b>	<b>b</b>	<b>A</b>	<b>b</b>	<b>A</b>	<b>b</b>	<b>A</b>	<b>b</b>
	33500	4.47	69800	6.44	2.8.10 <sup>12</sup>	30.05	-	-

**Table 3.14** – Viscosity and wall slip velocity laws for the rubber products at 100°C.

At 100°C, BR A and SBR A undergo wall slip at relatively small shear rates and shear stress. These fluids can be used to carry out wall slip observations. On the other hand, SBR B undergoes wall slip at high shear rates and shear stress at 100°C. This makes it an ideal choice for transparent flow observations. BR A exhibits wall slip in the intermediate range in comparison to the two SBRs. SBR C was found to exhibit no wall slip at high shear rates, probably due to its adhesive nature. It can be used in tandem with SBR B to contrast the difference in flow behavior due to increased adhesive behavior.

Résumé en français

Le rhéomètre oscillatoire a été utilisé pour identifier les propriétés requises du fluide pour les observations d'écoulement avec le MaCROS. Un fluide silicone a été identifié comme fluide modèle. Par la suite, le comportement viscoélastique du fluide silicone et des différents élastomères a été caractérisé avec le rhéomètre oscillatoire.

La caractérisation avec le rhéomètre capillaire à grandes déformations a permis l'identification des différents régimes d'écoulement, instabilités d'écoulement et comportement de glissement des élastomères. Les lois de viscosité obtenues avec les données oscillatoires et capillaires ont été comparées et sont relativement en accord pour les caoutchoucs purs, mais pas pour le SBR C. Les régimes d'écoulement des différents fluides est résumé dans le tableau 3.15. En raison du manque de corrélation des données oscillatoires et capillaires de SBR C, les lois de viscosité obtenues à partir des données capillaires ont été choisies pour les élastomères (Tableau 3.16).

	BR A	SBR A	SBR B	SBR C
<b>Structure moléculaire</b>	Linéaire	Branché	Linéaire	Mélange
<b>Régime d'écoulement</b>	Regime I Oscillant Regime II	Regime I Oscillant Regime II	Regime I  Regime II	Regime I
<b>Contrainte critique (bar)</b>				
<b>Regime I (<math>\sigma_c</math>)</b>	3.2	3.15	4	-
<b>Regime II (<math>\sigma_{c*}</math>)</b>	1.5	2.3		
<b>Taux de cisaillement critique (s<sup>-1</sup>)</b>				
<b>Regime I</b>	15-20	6-8	100	-
<b>Regime II</b>	40-60	20-40	-	

Tableau 3.15 – Comparaison du comportement rhéologique des produits caoutchoucs à 100°C.

Les vitesses de glissement des parois ont été estimées à l'aide de la méthode de différence de taux de cisaillement. L'influence de la température sur les vitesses de glissement du SBR A et du SBR B a été étudiée. Une tendance générale d'augmentation des vitesses de glissement avec la température a été observée. Cependant, il était difficile de définir avec précision les lois de vitesse de glissement des parois à toutes les températures. En raison de ces imprécisions, une loi thermodépendante de vitesse de glissement à la paroi n'a pu être obtenue. Des lois de vitesse de glissement de paroi peuvent être obtenues pour les caoutchoucs à 100°C. Les lois de viscosité et de vitesse de glissement à la paroi des différents produits en caoutchouc sont résumées dans le tableau 3.16.

	BR A		SBR A		SBR B		SBR C	
	K (Pa.s <sup>m</sup> )	m	K (Pa.s <sup>m</sup> )	m	K (Pa.s <sup>m</sup> )	m	K (Pa.s <sup>m</sup> )	m
<b>Loi de viscosité</b> $\eta = K \cdot \dot{\gamma}^{m-1}$	98500	0.38	121000	0.45	92600	0.29	93300	0.11
<b>Énergie d'activation, E<sub>a</sub></b>	-		42 kJ/mol		49.9 kJ/mol		-	
<b>Loi de glissement</b> $V_s = A\sigma^b$ with $V_s$ (mm/s) and $\sigma$ (MPa)	A	b	A	b	A	b	A	b
	33500	4.47	69800	6.44	2.8.10 <sup>12</sup>	30.05	-	-

Tableau 3.16 – Lois de viscosité et glissement pour les produits caoutchoucs à 100°C.

À 100°C, le BR A et le SBR A subissent un glissement à des taux de cisaillement et des contraintes de cisaillement relativement faibles. Ces fluides peuvent être utilisés pour effectuer des observations de glissement à la paroi. Au contraire, le SBR B subit un glissement à des taux de cisaillement plus élevés. Cela en fait un choix idéal pour les observations d'écoulements. Le SBR C ne présente aucun glissement à la paroi à des taux de cisaillement élevés qui peut être attribué à sa nature adhésive. Il peut être utilisé avec le SBR B pour démontrer la différence du comportement d'écoulement due à un comportement adhésif accru.



## Chapter 4

# Transparent flow observations

### Contents

---

4.1. Transparent flat die observations .....	114
4.2. Flow observations in the Monocuve mixer .....	117
4.2.1. Flow observations with round rotor .....	117
4.2.2. Flow observations with cam rotor .....	118
4.2.3. Symmetry of the flow outlines in Monocuve mixer .....	124
4.3. Flow observations in MaCROS mixer .....	126
4.3.1. Evaluation of the prototype and identification of model fluid .....	129
4.3.2. Types of flow observations .....	129
4.3.2.1. Counter-rotation condition .....	129
4.3.2.2. Co-rotation condition .....	131
4.4. Steady state flow observations at a small fill factor .....	133
4.4.1. Silicone fluid observations .....	133
4.4.2. Effect of surface properties on stabilization velocities .....	139
4.4.3. Symmetry of the flow outlines in MaCROS mixer .....	141
4.4.4. Flow observations of rubber products .....	142
Conclusions .....	146

---

Three transparent tools were used during this PhD work. Two of these transparent tools, the flat die and the MaCROS mixer, were developed during the course of this work. The flow observations with the flat die and the Monocuve mixer are presented in this chapter. The different types of flow observations which can be observed with the MaCROS mixer are outlined. Stabilization experiments were conducted at small fill factors with the silicone fluid. Finally, the symmetry of the free surfaces were characterized.

### 4.1. Transparent flat die observations

Flow observations were carried out on the rubber products with the help of the transparent flat die at 100°C, the reference temperature of the rheological characterization. The fluid is fed into the transparent flat die by the injection piston of the RhéoART™. The maximum descending speed of the injection piston of the RhéoART™ is 5 mm/s which can provide shear rates up to 75 s<sup>-1</sup> across the transparent flat die (Equation 2.18).

From the rheological characterization of the rubber products in Chapter 3.2, we know that BR A and SBR A will undergo wall slip in these conditions. Thus, SBR A and BR A can be used to estimate the wall slip velocities. SBR C, due to its complete lack of transparency, is not fit for flow observations. However, SBR B and SBR C are suited for conducting steady state flow observations with the transparent flat die. Thus, preliminary flow observations were carried out with SBR B at 100°C.

An example of the transparent flat die flow observations with SBR B at 100°C is presented in Figure 4.1. From Figure 4.1, we can observe the presence of bubbles in the flow stream. These bubbles are formed in the connecting channel of the transparent flat die (180° divergent). The change in geometry of the flow channel results in the encapsulation of air bubbles in the fluid. Some of these bubbles exit the flow channel without breaking while others break under the pressure in the Poiseuille flow. Subsequent cycles of purging were required to eliminate the trapped air bubbles in the flow channel.

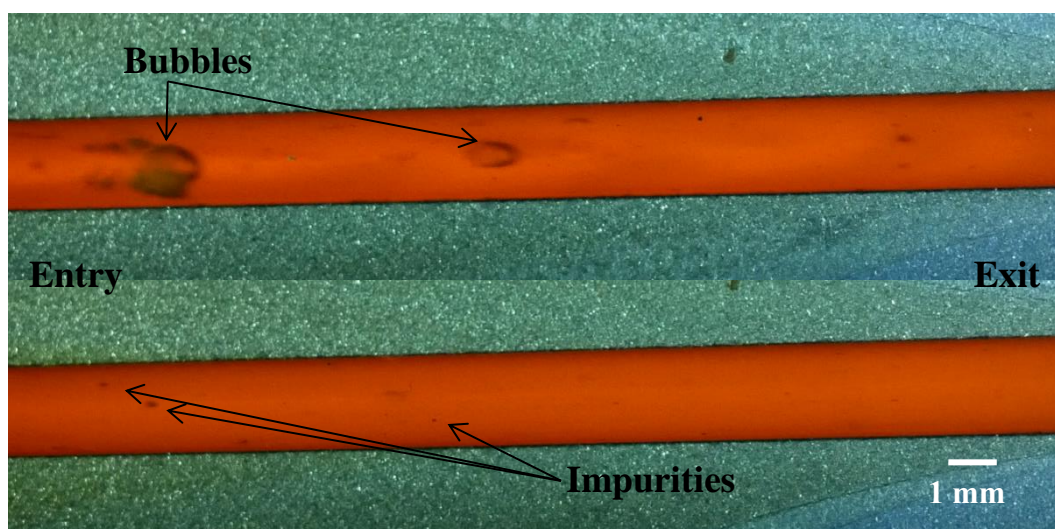


**Figure 4.1** – Flow observations with transparent flat die and SBR B at 100°C.

The motion of tracer particles in the flow channel can be used to estimate the flow field. The choice of tracer particles, particle size and quantity of particles added to the fluid is crucial. It is essential that the tracers exhibit a different reflectivity to the fluid to observe its movement. The size of the tracer particles is crucial as large particles tend to obstruct the flow locally and break during flow. An excess of tracers in the flow channel pollutes the observation zone making effective estimates of the flow field difficult. The trapped air bubbles in the fluid can also serve as tracers. However, the amount and size of the bubbles in the fluid cannot be controlled. Furthermore, large air bubbles can impact the local flow field and thus are not suitable tracers. The pure rubber products do not provide complete transparencies. However, their comparable transparencies permit the observation of the tracer particles along the thickness of the flow channel (30 mm).

Traces of impurities, characterized by their opaqueness or difference in transparency, were visible in the flow channel. These impurities can be used as tracers and help estimate the flow field. If the amount of impurities in the flow channel was not sufficient to predict the flow rate at different points of the flow channel, additional tracer particles can be added to the fluid. The velocities of the tracer particles can be identified with the help of any image processing software such as ImageJ. The position of the tracer particles was recorded at equal intervals of time.

The movement of three tracer particles across the transparent flat die with SBR B at 100°C is presented in Figure 4.2. The position of the tracer particles can be determined accurately on the x and y axes but not along the z-axis. The lack of complete transparency of the rubber products does not permit us to determine if the tracer particles are on the same z-axis. The opaqueness of the tracer particle indicates the proximity of the tracer particle to the plane of observation. However, no accurate estimations can be made on the position of the tracer particle along the z-axis.

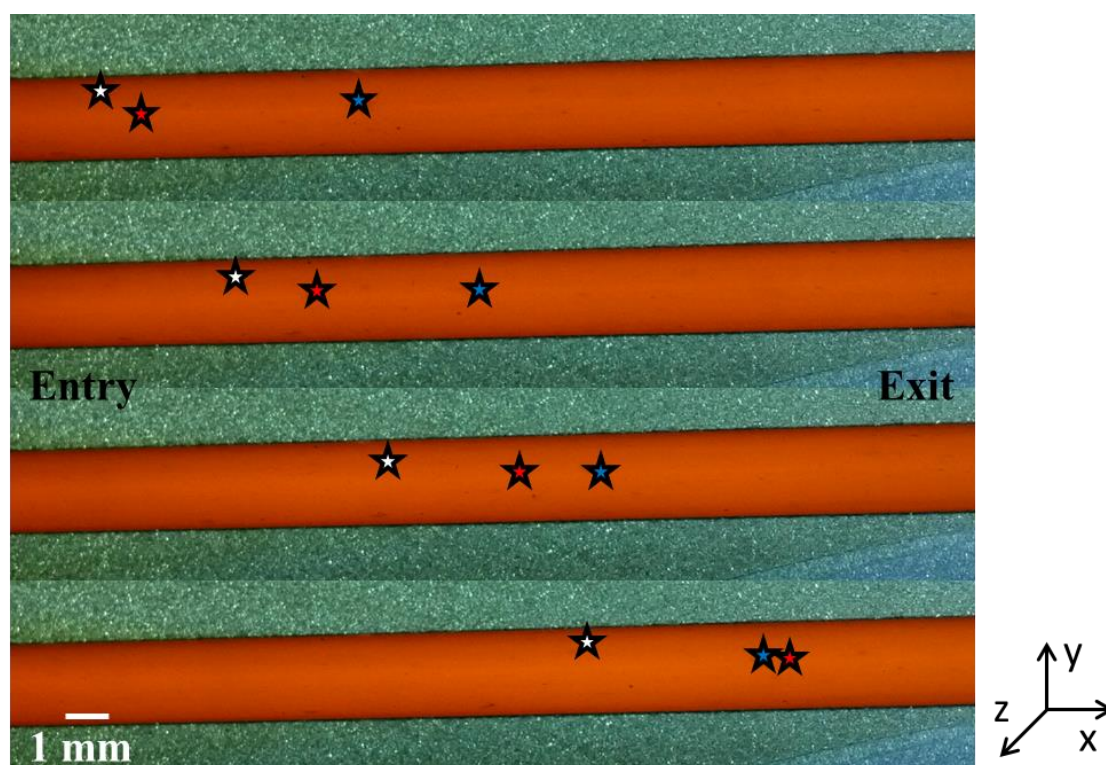


**Figure 4.2** – Observations of the motion of three tracer particles across the transparent flat die with SBR B at  $15\text{s}^{-1}$  and at  $100^\circ\text{C}$ .

Figure 4.2 shows the movement of a few particles along the x axis with time at a constant apparent shear rate. We observe the red tracer particle overtaking the blue tracer particle. This should not be possible if the particles were on the same depth. This type of flow is uncharacteristic of a 2D Poiseuille flow between two infinitely parallel plates. This indicates that the flow across the transparent flat die is 3D in nature with a Poiseuille flow observed along the x and z axes. The blue tracer particle exhibits an inferior velocity to the red tracer particle due to its proximity to the transparent walls. It is difficult to focus at a z-position with the camera even with a small field depth setting. Thus, extensive studies are required to obtain an accurate estimation of the 3D flow field of the transparent flat die with visual observations. Sophisticated methods like laser Doppler velocimetry, similar to the work of Robert [Robert *et al.*, 2004], are better suited to obtain accurate estimations of the flow field for the transparent flat die. However, such methods are extremely time consuming and could not be carried out during the course of this PhD work.

The pressure drop evolutions of SBR B across the transparent flat die at  $100^\circ\text{C}$  and at 35 and  $70\text{s}^{-1}$  are presented in Figure 4.3. An overshoot of pressure is observed during the flow across the transparent flat die and the pressure drop drops towards a steady state value. Stationary flow could not be obtained

due to the short length of the transparent flat die and short duration of the experiments. Due to the small volume of the injection chamber (9 cm<sup>3</sup>) of the RhéoART™, the fluid in the injection chamber (and subsequently, the transparent flat die) is purged quickly, providing short observation times. Without steady state values, the pressure measurements cannot be used for the rheological characterization. Steady state flow could be achieved with a longer flow channel. Thus, the transparent flat die with its current design is not suited for transparent flow observations and rheological characterization.

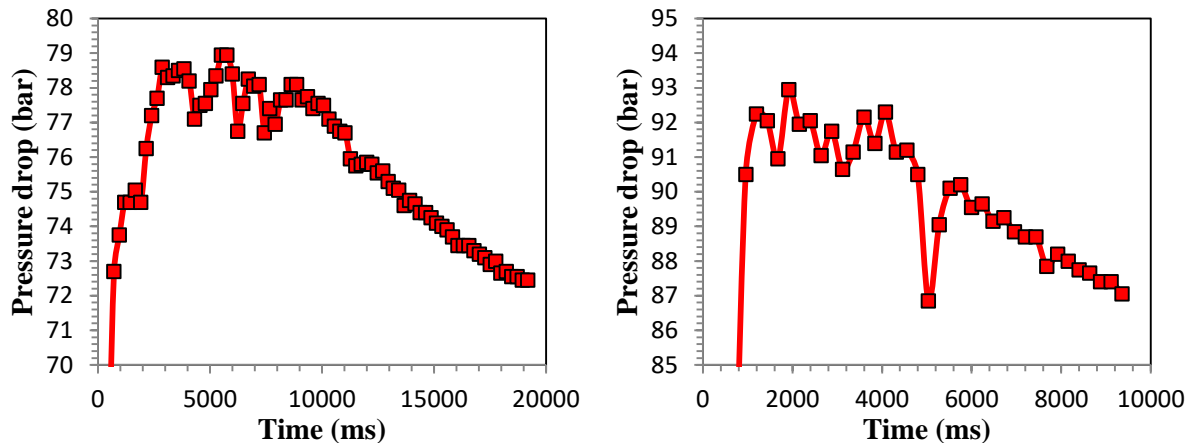


**Figure 4.3** – Pressure drop evolutions of SBR B across the transparent flat die at 100°C and at 35 s<sup>-1</sup> (left) and 70 s<sup>-1</sup> (right).

### Stick-slip flow

Trials were also performed on the SBR A. Stick-slip flow behavior was observed while working at shear rates above 10 s<sup>-1</sup> with SBR A. On examining the flow extrudates (Figure 4.4) a change in the aspect of the flow extrudates was observed, indicating a change in flow regime. At low shear rates (< 10 s<sup>-1</sup>), striations were observed in the flow extrudates characteristic of sharkskin surface defect. These striations were created due to the die swell as the polymer melt flows across the exit of the transparent flat die. At higher shear rates (> 10 s<sup>-1</sup>), these striations were replaced by oscillations along the flow extrudates.

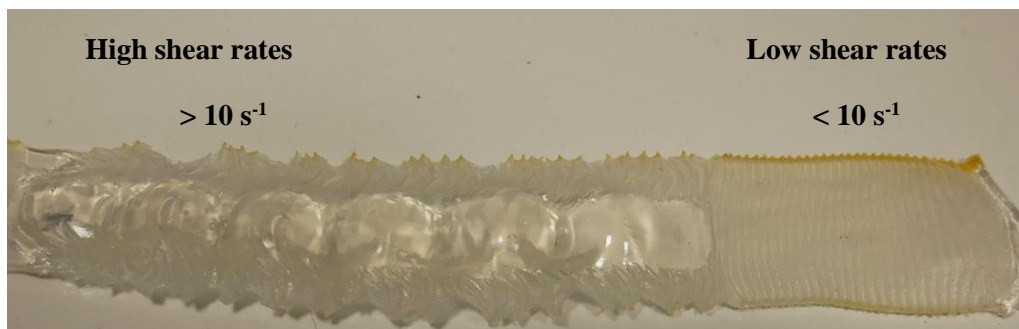


**Figure 4.4** – Flow extrudates of SBR A across the transparent flat die at 100°C.

These oscillations are typical of the stick-slip flow instabilities observed in flat dies [Robert, 2000]. During the flow observations, the stick-slip instability was found to originate at the walls of the flat die at the exit. Such observations can be used to estimate the flow field during the slip flow behavior to obtain direct estimations of the wall slip velocities.

### Design improvements

This preliminary work shows that it is possible to observe the different flow regimes and detect transitions in flow regimes. The major disadvantages of the transparent flat die are:

- the length of the flat die is insufficient for steady state flow,
- no rheological measurements could be carried out due to the lack of a steady state flow,
- it is difficult to discern the position of the tracer particles along the z-axis, which limits the estimation of the flow field.

Further observations could not be carried out with the transparent flat die due to the mechanical failure of the transparent flat die. In addition, the lack of a proper sealed flow channel resulted in the rubber permeating into the small gaps between the glass walls and the metallic walls of the transparent flat die. This rubber contracts at the end of the test, providing supplementary stress to the glass walls which resulted in the repeated breakage of the glass walls.

Due to the poor mechanical and corrosive properties of 42CrMo4 steel, the walls of the transparent flat die were corroded and the threading of the die entry endured mechanical failure. As a result, the transparent flat die could not be mounted on the exit of the RhéoART<sup>TM</sup>. Due to time constraints, a new transparent flat die could not be developed during the course of the PhD work. Moreover, the design of the transparent flat die was found to be inadequate for the estimation of wall slip velocities and a new design was required. The design of the transparent flat die can be improved by:

- 1) choosing a material with better mechanical and corrosive properties for the walls of the transparent flat die to prevent its mechanical failure and corrosion.
- 2) ensuring a completely sealed flow channel to prevent the permeation of rubber and in turn, the repeated breakage of the glass walls.
- 3) increasing the length of the transparent flat die to provide a larger zone of observation and sufficient length to obtain steady state flow observations.
- 4) using an industrial extruder instead of a capillary rheometer to obtain higher shear rates than those provided by a capillary rheometer. The large reservoir of an industrial extruder takes longer to purge which provides us with longer observation times.
- 5) using three or more pressure transducers in the flow channel of the transparent flat die to obtain a more precise measurement of the pressure drop across the flow channel. This was not possible with this transparent flat die due to the small dimensions ( $h = 2$  mm) of the flow channel. Thus, the thickness of the flow channel should be adapted for the use of multiple pressure transducers in the flow channel.

## 4.2. Flow observations in the Monocuve mixer

### 4.2.1. Flow observations with round rotor

The Monocuve mixer can be equipped with the round or the cam rotor. Preliminary observations on the rubber products resulted in a simple 2D flow behavior i.e. the position of the fluid/gas interface does not seem to vary along the thickness of the internal mixer (Figure 4.5). Thus, the Monocuve mixer provides a simpler 2D flow observation of the internal mixer with its simplified geometry in comparison to previous observations reported in the literature [Freakley and Wan Idris, 1979; Asai *et al.*, 1982; Sato *et al.*, 1981; Min and White, 1985, 1987 and Min, 1987a]. For reference purposes, the position of the free surface (fluid/gas interface) will be called the flow outline. Figure 4.5 shows the flow observations of SBR A with the Monocuve mixer at 60% volume fill factor, 100°C and at 10 rpm (Left) and 30 rpm (Right). For the sake of clarity, the fluid phase is represented in red while the rotor and the mixing chamber surface are colored in grey.

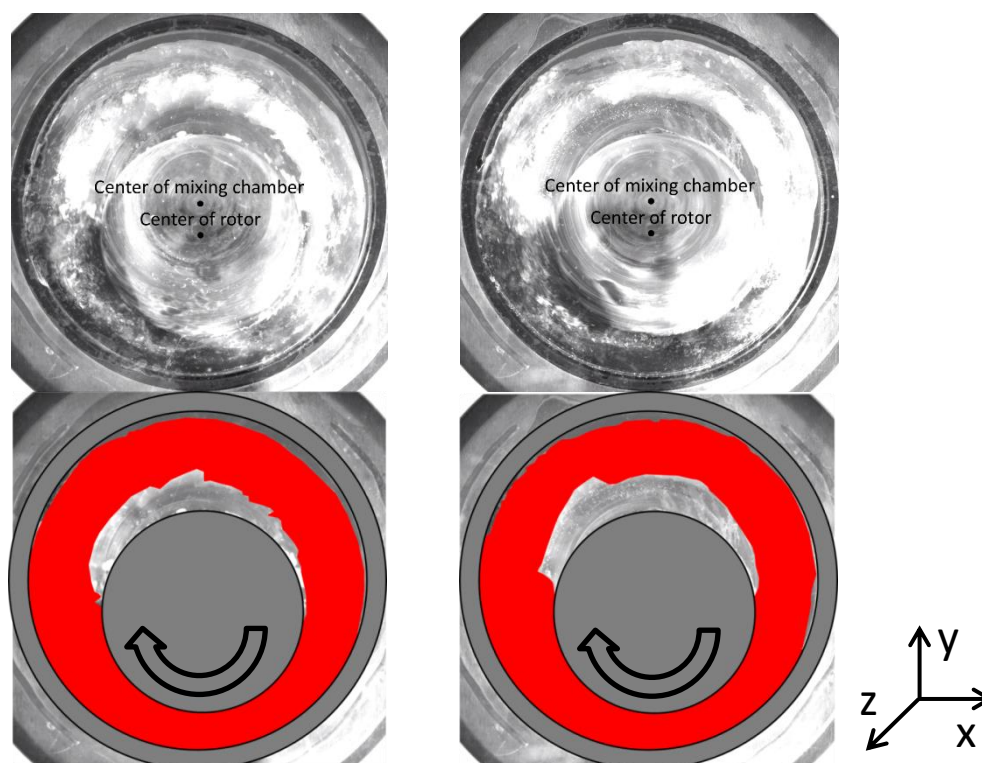


**Figure 4.5** – Flow observations of SBR A with the Monocuve mixer and the round rotor at 60% volume fill factor, 100°C and 10 rpm (Left) and 30 rpm (Right).

In the Monocuve mixer, the fluid is introduced in the mixing chamber through the hopper in the form of small cubes. After a few cycles of rotation, the fluid transitions from a solid like behavior to a fluid like behavior (softening of the elastomer). This transition corresponds to the first stage of mixing, (viscosity reduction), and is characterized by the first peak on the torque curve during the mixing cycle [Kent, 2018]. The fluid is displaced around the mixer as the rotor rotates around the mixing chamber.

After softening of the elastomer, we observe that the flow outline of the fluid/gas interface with respect to the rotor hardly evolves with time. The flow outline of the fluid with respect to the rotor is in steady state but not with respect to the walls of the mixing chamber. This flow can be considered as a quasi-steady state flow. It is clear that the shearing efficiency of the round rotor is quite low due to the large thin flow gap (10 mm in a mixing chamber of 100 mm diameter). Due to the lack of efficient shearing with the round rotor, we observe an irregular 2D flow outline (Figure 4.5). Thus, the flow behavior at the metal-fluid interface cannot be effectively studied. The irregular flow outline of the fluid can be prevented by increasing the volume fill factor or by a change of rotor geometry.

At higher fill factors ( $> 60\%$ ), the flow outline of the fluid at the rotor interface becomes harder to study due to the lack of free volume in the internal mixer. Thus, the cam rotor (with a smaller thin flow gap and a more pronounced converging zone at the thin flow gap) is better suited for the quasi-steady state observations of the fluid outline during mixing. Subsequent flow observations with the Monocuve mixer were carried out with the cam rotor.

#### 4.2.2. Flow observations with cam rotor

Figure 4.6 illustrates the initial mixing behavior of SBR A with the Monocuve mixer and the cam rotor at 30% volume fill factor, 5 rpm and ambient temperature. The cam rotor provides a sharper converging flow in front of the thin flow gap. This flow geometry leads to a pressure maximum during the contraction and forces the flow of the material through the thin flow gap.

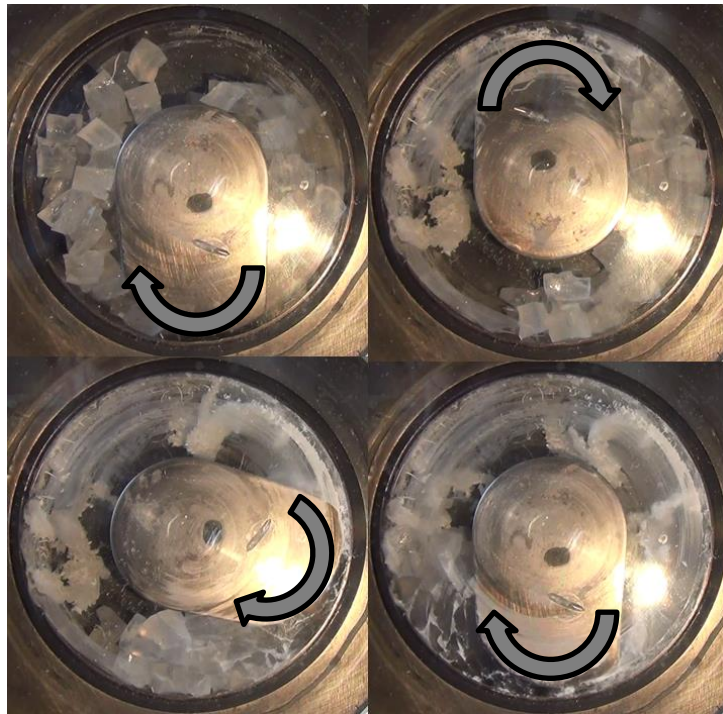


**Figure 4.6** – Initial mixing behavior of SBR A at 30% volume fill factor, 5 rpm and ambient temperature with the transparent Monocuve mixer and the cam rotor.

The mixing cycle begins with the introduction of the fluid in the shape of cubes through the hopper (Figure 4.6 – Top left). The rotor was set to rotation after the hopper is closed and the cubes were sheared as the rotor rotates in the mixer (Figure 4.6 – Top right). The fluid passes through the thin flow gap and most of the fluid was sheared by the walls of the rotor and the mixing chamber. Some of the solid cubes slipped between these surfaces. As the rotor continues its rotation, more solid cubes stop slipping and were sheared by the rotor (Figure 4.6 – Bottom left). This continues till most of the fluid was sheared by subsequent passes of the rotor (Figure 4.6 – Bottom right).

At the end of this step, the fluid no longer behaves like a solid and exhibits pure fluid like behavior. The flow behavior of the fluid during the transition from solid to liquid like behavior is difficult to describe. This stage is often neglected during the numerical simulation of the mixing process. This can be achieved after several rotor rotations (ranging from a couple to 20 in some cases). As a visual aid, the rotor and the mixing chamber surface are colored in grey while the fluid outline is highlighted in red.

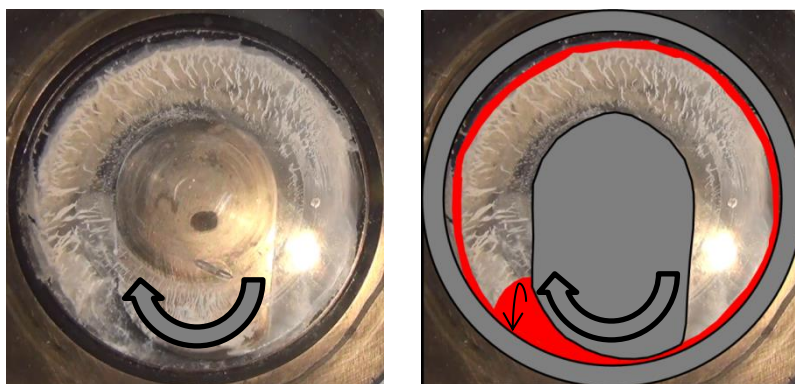


**Figure 4.7** – Quasi-steady state flow observations of SBR A at 5 rpm and 100°C with the transparent Monocuve mixer.

The lack of a second mixing chamber eliminates the continual transfer of fluid between chambers and the creation of stagnation zones in the mixer, as in White's experiments [White, 1986]. Once the initial

softening cycle is complete, quasi-steady state flow observations are obtained. As the rotor moves around the mixing chamber, the fluid was forced to pass through the thin flow gap creating a uniform layer of fluid around the mixing chamber wall. The thickness of this layer corresponds to the thickness of the thin flow gap. The rest of the fluid was recirculated between the rotor and the uniform fluid layer of the fluid as the rotor moves around the mixing chamber. The recirculating volume forms a partial ellipsoid outline. These two components of the flow outline will be called as the ellipsoid flow outline and the continuous flow outline (Figure 4.8).



**Figure 4.8** – Ellipsoid and continuous flow outline of SBR A at 5 rpm and 100°C with the transparent Monocuve mixer.

Once the continuous flow outline is created around the mixing chamber wall, the rotor was unable to displace the fluid in this layer. Thus, most of the fluid in this volume is largely undisturbed during mixing. Sometimes, this layer was completely in contact with the mixing chamber surface (Figure 4.10), while sometimes it was not (Figure 4.7). This depends on factors such as the elasticity of the fluid, pressure exerted by the fluid, the rotation speed of the rotor and the adhesion energy of adhesion of the fluid. However, the thickness of the layer remains uniform irrespective of the state of contact with the walls of the mixing chamber. This thickness only varies in case of irregular flow rate in this section. i.e. wall slip.

In addition to the flow outline of the fluid marked in red in Figure 4.8, we also observe thin fluid filaments (striations) deposited on the transparent wall. These striations were caused by the fluid sheared between the minute gap between the rotor and the transparent wall. A minute gap was provided between the rotor and the transparent wall to limit the friction between these surfaces. As the rotor moves, some fluid of the ellipsoid flow outline enters in this gap and was sheared forming filaments which were deposited on the transparent wall. These striations were subsequently absorbed by the ellipsoid flow outline as the rotor moves and this process continues viciously. However, at high rotation speeds or after long observation times, a large amount of the fluid in the ellipsoid flow outline was lost in the form of striations (Figure 4.9) resulting in a difficulty of observation.



**Figure 4.9** – Striations of SBR B (at 25% fill factor and 80°C) on the transparent wall of the Monocuve mixer at 10 rpm (Left); 50 rpm (Middle) and 100 rpm (Right).

### Effect of different parameters

The primary factors affecting the flow behavior in the Monocuve mixer (equipped with the cam rotor) are the fluid used, the rotation speed, the volume fill factor and the temperature. Due to the geometry of the Monocuve mixer, the influence of velocity on the flow outline can be negated (assuming no slip). An increase in the wall pressure and torque is observed at high velocities. However, the overall flow outline remains unchanged at high velocities.

Figure 4.10 represents the quasi-steady state flow observations (observed at fixed position of the rotor for sake of clarity) of SBR B at increasing fill factors. A change in the fill factor does not seem to impact the continuous flow outline. However, the ellipsoid flow outline occupies a larger volume at higher fill factors. The shape of the ellipsoid flow outline is such that the apsis of the flow outline is approximately in the middle of the local gap. The apparent contact angle of the ellipsoid flow outline with the rotor surface does not change significantly with the volume fill factor. A quantitative analysis of the contact angle and the apsis of the flow outline could not be performed as the flow observations are not completely steady state in nature. To better compare the flow outline between two experiments, screenshots were taken when the rotor is at the same position in the mixer (Figure 4.10).



**Figure 4.10** – Flow observations of SBR B in the Monocuve mixer at 20 rpm, 100°C and at 20% (Left), 25% (Middle) and 35% (Right) volume fill factors.

The influence of the flow outline with an increase in temperature was studied with SBR C. Due to its designed formulation, the fluid should exhibit a larger variation in adhesive energy with temperature in comparison to other rubber products. A change in temperature will impact the adhesive behavior of the fluid enabling us to also study the effect on the flow outlines. Figure 4.11 (page 122) shows the flow observations for SBR C at 25% volume fill factor, 2 rpm and at 40, 70 and 100°C.

As we work at temperatures above the Zosel temperature of the fluid ( $T_{Zosel} = 28^{\circ}\text{C}$  for SBR C), the adhesion energy of the fluid decreases with a rise in temperature (Chapter 5.1.1). However, the observation of the flow outlines at different temperatures does not show any significant change in its shape. The ellipsoid flow outline of the fluid appears symmetrical which would tend to indicate no difference of adhesion with the rotor surface (adhesive contact) or the continuous flow outline surface (cohesive contact). The variation of temperature results in a change of adhesive and cohesive behavior of the fluid. However, the ellipsoid flow outline remains symmetrical indicating that a change in adhesion energy and the temperature does not significantly impact the flow outline of the fluid in the Monocuve mixer.

The nature of the contact of the ellipsoid flow outline is adhesive on one surface and cohesive in the other (Figure 4.11). At small volume fill factors, no continuous flow outline can be formed around the mixing chamber wall and a transient flow was obtained. Figure 4.12 (page 122) shows transient flow observations of a small fluid volume being sheared by the rotor in the Monocuve mixer. As the rotor moves, the fluid was sheared by the rotor and driven through the thin flow gap in the downstream direction (opposite to the direction of rotation of the rotor). The use of counter-rotating rotors can

result in the stabilization of small volumes of fluid, permitting the observations of two free surfaces with adhesive contact on either end of the free surface.

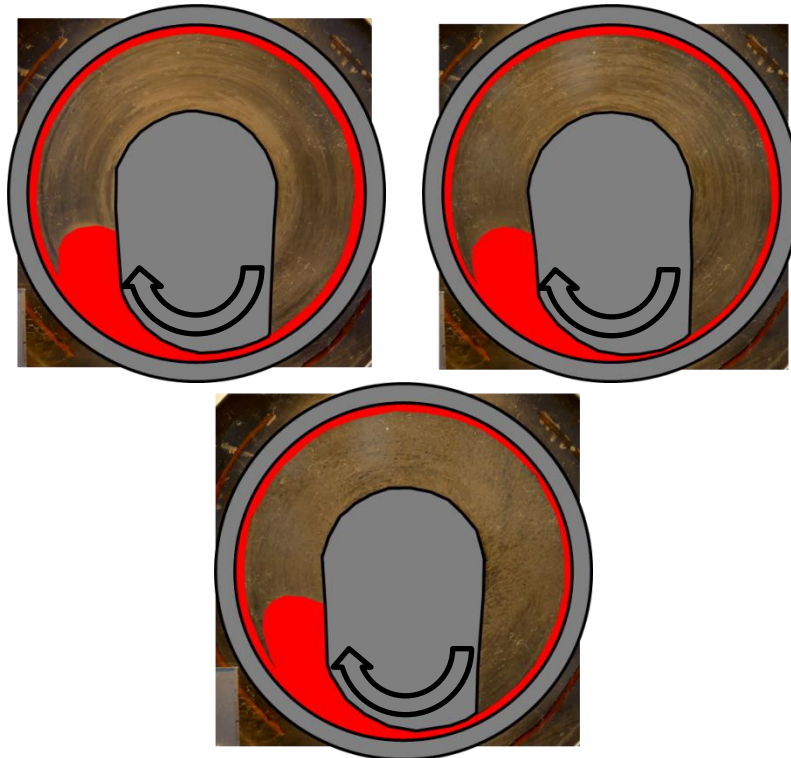


**Figure 4.11** – Flow observations of the SBR C at 25% volume fill factor, 2 rpm and at 40°C (Top left), 70°C (Top right) and 100°C (Bottom) with the Monocuve mixer.

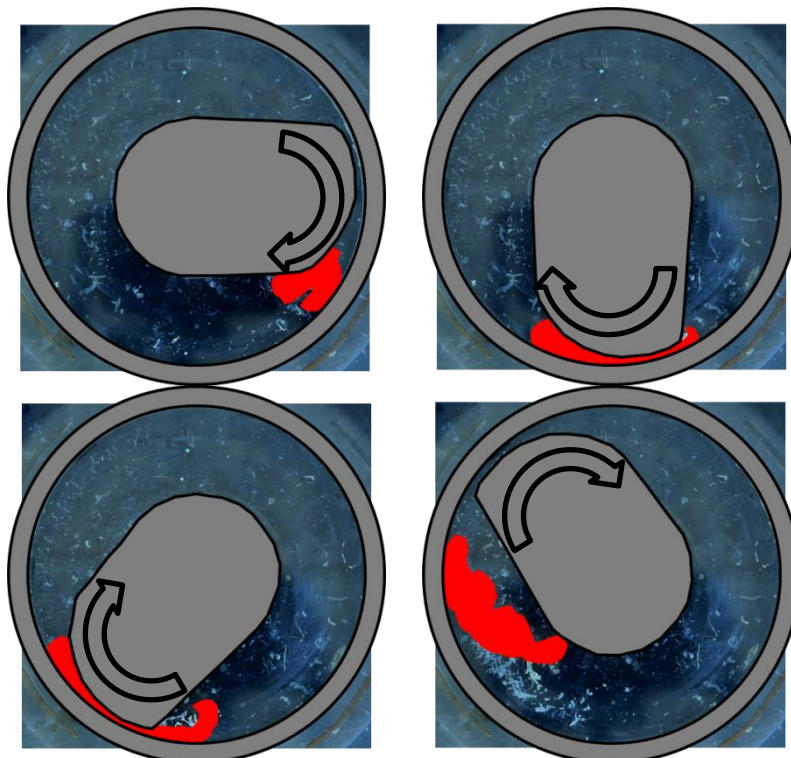


**Figure 4.12** – Flow behavior of SBR B at 5% volume fill factor and 2 rpm with the Monocuve mixer at 100°C (clockwise).

Comparison of fluids

The flow outlines of the different rubber products are compared in Figure 4.13 at 2 rpm, 25% volume fill factor and 100°C.

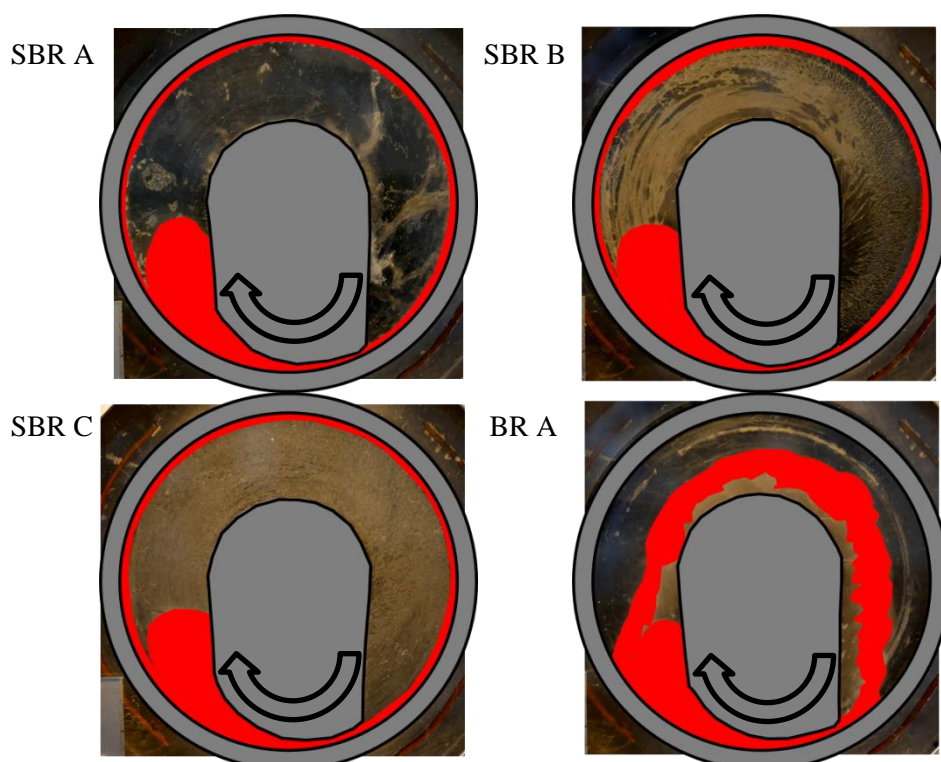


**Figure 4.13** – Flow observations of SBR A, SBR B, SBR C and BR A at 2 rpm, 25% volume fill factor and 100°C.

Under these conditions, the shear rate at the thin flow gap is around  $5 \text{ s}^{-1}$ . BR A undergoes stick-slip flow at the walls of the mixing chamber. As the fluid undergoes stick-slip behavior, the flow rate in the downstream condition is irregular. This results in the deposit of a layer having an irregular thickness along the mixing chamber wall. The wall slip also results in the non-adherence of the fluid on the mixing chamber wall. This is surprising as the rheological characterization in chapter 3.2.2 indicates that BR A undergoes wall slip at higher shear rates. The other rubber products were found to exhibit simple 2D flow with apparent symmetric flow outlines.

In addition to the rubber products, the flow behavior of the silicone fluid was investigated at ambient temperature (Figure 4.14). At ambient temperature, the silicone fluid exhibits a lower viscosity (by a factor of around 10) than the rubber products at 100°C. Despite this difference, the silicone fluid also exhibits a simple 2D flow outline with apparent symmetric flow outlines. Striations were also observed on the transparent wall while working with the silicone fluid. Due to the similarity in flow behavior between the silicone fluid and the rubber products (except BR A), the silicone fluid appears to be a good model fluid.

The Monocuve mixer provides simpler flow observations in comparison to other transparent lab-scale internal mixers. The interfacial flow behavior (wall slip behavior, flow outlines) can be observed and the quasi-steady state observations permit the analysis of the free surfaces. These flow observations enable us to better understand the mixing behavior of the fluids and has been used as a comparison tool for numerical simulations. However, for effective analysis of the flow outlines, steady state flow observations are required. To circumvent the limitations of the Monocuve flow observations, two design improvements were used:

- 1) counter-rotation cylinders to stabilize the fluid and conduct steady state observations,

- 2) O-rings to limit the amount of fluid passing through the minute gap between the rotor and the transparent walls to limit the loss of fluid during the experiment and facilitate the observations.



Figure 4.14 – Flow observations of the silicone fluid in the Monocuve mixer at 25% volume fill factor, 2 rpm and at ambient temperature.

#### 4.2.3. Symmetry of the flow outlines in Monocuve mixer

The free surfaces of the fluid during mixing can be impacted by various factors such as the pressure distribution, adhesion energy of the fluid among others. To characterize the symmetry of the free surfaces, visual observation is not sufficient and a quantitative analysis is required. Screenshots of the flow observations permit us to record the ellipsoid flow outlines during shear flow. These screenshots were used to measure the peak angles ( $\theta_{Peak}$ ) of the ellipsoid flow outlines.

Figure 4.15 shows how the peak angles of the ellipsoid flow outlines are measured. In this study, we assume that the flow outlines are impacted uniquely by the adhesion energy of the fluid. If the adhesion energy of the fluid does not impact the flow outlines, the fluid must exhibit symmetrical flow outlines. Symmetrical flow outlines can be defined as flow outlines where its apsis (point of inflection of the free surface) is tilted towards neither the rotor nor the continuous flow outline surface. To quantify the tilt of each ellipsoid flow outline, we measure the angle between the imaginary line joining the intercepts of the free surface (B and C) and the line joining the apsis (A) and the midpoint of the previous line (D).

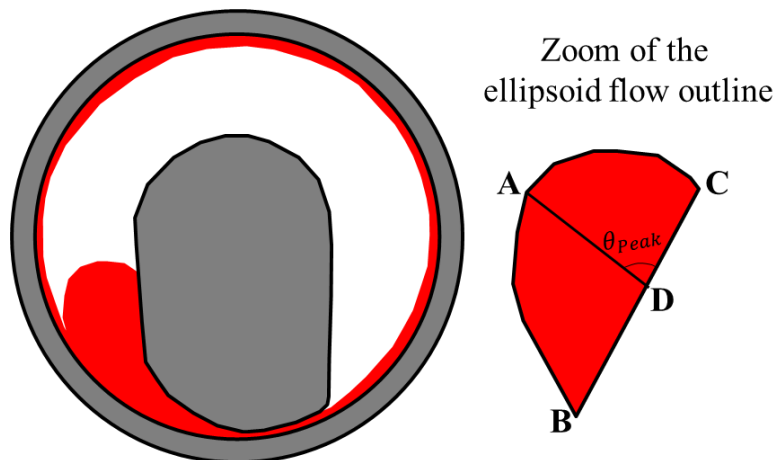


Figure 4.15 – Example of the estimation of the peak angle on the recorded flow outlines.

## Chapter 4: Transparent flow observations

For this study, we assume that the free surface is influenced only by adhesion energy. Thus, a peak angle of close to  $90^\circ$  indicates that the ellipsoid flow outline is tilted to neither the rotor nor the continuous flow outline surface i.e. no influence of adhesion on the free surface. This gives us:

$\theta_{Peak} \approx 90^\circ \rightarrow$  Symmetric flow outline

$\theta_{Peak} < 90^\circ \rightarrow$  Preference of adhesion to rotor surface

$\theta_{Peak} > 90^\circ \rightarrow$  Preference of adhesion to continuous flow outline surface

During the course of this study, the peak angles will be measured for three cases: i) Monocuve observations, ii) MaCROS observations and iii) finite element simulations of the free surface. The free surfaces obtained in all the three cases are different and hence the interpretation of the peak angles must also vary. In the case of the Monocuve observations, the intercept C has an adhesive contact with the rotor surface whereas the intercept B has a cohesive contact with the continuous flow outline. Thus, the peak angles indicate if the free surface is influenced by either the adhesive or the cohesive contact.

In the case of MaCROS observations (Chapter 4.4.3), the stabilized fluid has two free surfaces. These free surfaces have an adhesive contact with the cylinder surfaces. However, these free surfaces are 3D in nature and the recorded free surfaces are but a 2D projection of them. As is the nature with 3D shapes, the 2D projection is not an accurate representation of the 3D free surfaces. Thus, the measured peak angles of the MaCROS observations indicate the degree of symmetry of the 2D projection of the free surfaces and not the actual free surfaces.

Finally, the free surfaces of the finite element simulations (Chapter 5.3) are 2D free surfaces with adhesive contact with the inner and outer cylinders. In these cases, the peak angles do indicate the presence (or absence) of a preference in adhesion to either surface.

### Peak angles of the Monocuve observations

One of the assumptions of the Monocuve mixer was that the flow outline of the fluid with respect to the rotor is in steady state. This can be verified by measuring the peak angles during mixing at different positions of the rotor. The flow outline of the fluid was recorded at 4 different positions of the rotor for the SBR A at 2 rpm, 25% volume fill factor and  $100^\circ\text{C}$ . The measured peak angles at these 4 different positions are presented in Table 4.1.

Position of the rotor, ( $^\circ$ )	Peak angles, $\theta_{Peak}$ , ( $^\circ$ )
0	75.7
90	76.2
180	78.3
270	72.8

**Table 4.1** – Peak angles of the ellipsoid flow outlines determined for different positions of the rotor (SBR A at 2 rpm, 25% volume fill factor and  $100^\circ\text{C}$ ).

The peak angles in Table 4.1 were found to be quite close to each other. This indicates that the flow outline does not vary significantly as the rotor moves around the mixer. A slight preference of adhesion to the rotor surface was observed ( $\theta_{Peak} \approx 75^\circ$ ). Similarly, the influence of the fill factor, temperature on the flow outlines was investigated with the symmetry factor (Table 4.2 and 4.3). No influence of the temperature on the peak angles was found. The fill factor at 35% provides more symmetric free surfaces than at 20 or 25%. This is expected, as at higher fill rates, the ellipsoid flow outline is less elongated (rounder) making it difficult for the free surface to tilt towards either the rotor or the continuous flow outline surface.

Fill factor, (%)	Peak angles, $\theta_{Peak}$ (°)
20	70.4
25	72.4
35	98.8

**Table 4.2** – Peak angles of the ellipsoid flow outlines at different fill factors (SBR A at 2 rpm and 100°C).

Temperature, (°C)	Peak angles, $\theta_{Peak}$ (°)
40	80.1
70	78.7
100	81.6

**Table 4.3** – Peak angles of the ellipsoid flow outlines at different temperatures (SBR C at 2 rpm, 25% volume fill factor).

Finally, the flow outlines of the rubber products (100°C) and the silicone fluid (ambient temperature) are recorded at 2 rpm and 25% volume fill factor. The measured peak angles for the different fluids are presented in Table 4.4. The flow outlines of the silicone fluid, BR A and SBR A were found to be symmetric while that of SBR B and SBR C indicate a preference of adhesion to the rotor surface. This might indicate that the adhesive contact influences the free surfaces of SBR B and SBR C more than the cohesive contact.

Temperature, (°C)	Fluid	Peak angles, $\theta_{Peak}$ (°)
Ambient temperature	Silicone fluid	91.5
100	BR A	94.9
100	SBR A	89.7
100	SBR B	78.3
100	SBR C	81.6

**Table 4.4** – Peak angles of the ellipsoid flow outlines of the different fluids at 2 rpm and 25% volume fill factor.

### 4.3. Flow observations in MaCROS mixer

After the assembly of the MaCROS mixer, the new prototype was first tested and calibrated to determine its functionality. Preliminary observations were carried out at ambient temperature without activating the heating system of the mixer. Various fluids were tested to conduct steady state observations, with the mixer at ambient temperature. The identification of the silicone fluid enabled us to identify the properties required for a fluid to conduct steady state observations with the MaCROS mixer at ambient temperature. The different types of flow observations which can be carried out with the MaCROS mixer are presented.

#### 4.3.1. Evaluation of the prototype and identification of model fluid

Preliminary tests were performed to calibrate, evaluate the limits of the MaCROS mixer and also to define the fluid characteristics necessary to perform counter-rotation experiments with a small fill factor.

#### Rotation speeds

The rotation velocities of the inner and outer cylinders are controlled with the help of a joystick. Slight fluctuations were noticed in the rotation velocities of the cylinders while imposing a constant value. These fluctuations are due to fluctuations of the current supplied to each motor. At higher rotation velocities, these fluctuations become more significant. The maximum rotation velocities of the

cylinders were limited to  $\pm 3.2$  rpm and  $\pm 16$  rpm for the outer and inner cylinders respectively to obtain precise control of the rotation velocities of the cylinders. While imposing rotation velocities below these limits, fluctuations are limited to small error values of  $\pm 0.51\%$  and  $\pm 0.25\%$  for the inner and outer cylinders respectively. At these rotation velocities and a thin flow gap of 3 mm, the cylinders can provide shear rates up to 25 and 35  $\text{s}^{-1}$  in the co-rotation and counter-rotation conditions respectively.

### Introduction of fluid

The fluid is introduced by dismantling the front transparent wall. Figure 4.16 shows an example of flow behavior of the silicone fluid with the MaCROS mixer. During the flow observations, we find that some fluid stagnates in different locations of the mixer. These stagnation zones are located at the intersection of either two moving parts or a moving part and a fixed one. The stagnation zones are shown in Figure 4.16.

These stagnation zones occur at the:

- i) minute gap between the front transparent wall and the rotor,
- ii) gap between the back transparent wall and the rotor,
- iii) intersection between the rotor and the fixed bridle,
- iv) intersection between the back transparent wall and the rotor.

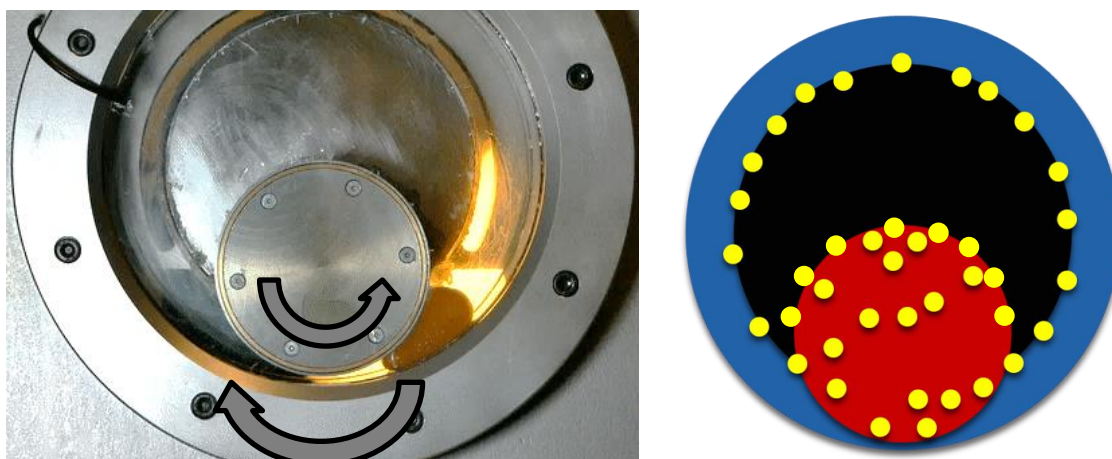


**Figure 4.16** – Example of *in-situ* observation during flow in the MaCROS mixer (Left). Stagnation zones in the chamber (Right). The inner cylinder is depicted in red, the bridle in black, the back transparent wall in blue and the stagnation zones in yellow.

O-rings (mounted on springs) were fitted on either side of the inner cylinder to prevent the fluid entering the gaps between the transparent walls and the inner cylinder. The O-rings can limit the amount of fluid entering this gap but they are not able to completely prevent the fluid penetration. Most of the fluid in the stagnation zones remains stuck during the course of the experiment. However, part of the trapped fluid can also be released from time to time. This leads to a difference between the initial volume introduced into the mixer and the volume being sheared by the mixer.

The gap between the back transparent wall and the inner cylinder is larger than the equivalent front gap. This is due to the presence of the rotor shaft, the bridle and the back transparent wall. A larger gap is required to limit friction between these parts. This leads to a large fluid volume being trapped in this gap. A consequence of the fluid trapped in these gaps is that the energy required to shear the fluid across such small gaps can be significant. It can be comparable to that required to shear the fluid in the flow channel. Thus, the torques measured by sensors on both motor axes are not reliable as they measure the two contributions.

At the end of the experiment, the front transparent wall is dismantled and the flow channel is cleaned with ethanol. During the clean-up, a negligible amount of fluid remains in the stagnation zones of the mixer. The complete elimination of the residual fluid would require a complete disassembly of the machine. The complete disassembly of the machine is undesirable as it is time consuming (few days). It was preferable to clean the flow channel as much as possible without disassembly of the machine between two fluid introductions.

### Loss of transparency

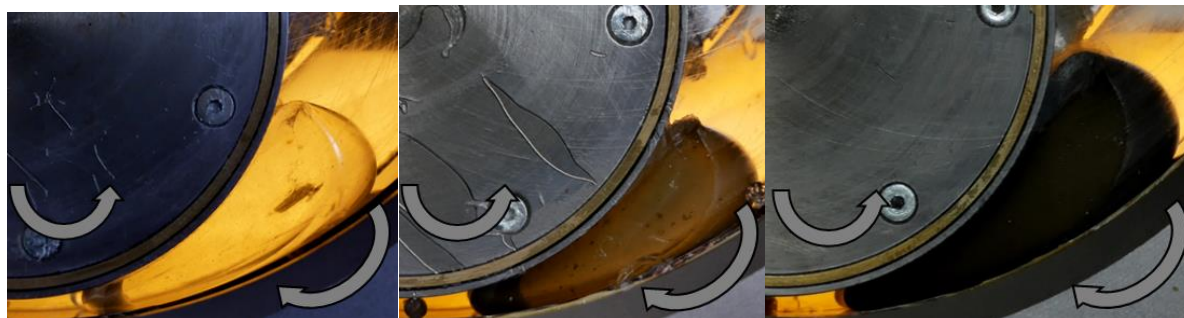


**Figure 4.17** – Gradual loss of transparency during mixing with MaCROS mixer.

Figure 4.17 (above) shows the gradual loss of transparency of the silicone fluid. During the course of these experiments, after long observation times, part of the trapped fluid in the stagnation zones can be released and re-enter the flow channel. It was verified that the loss of transparency of the fluid does not modify the rheology of the fluid. Rheological measurements were carried out with the pure and used silicone fluid (Figure 3.4).

### Viscosity threshold

During the identification phase of the model fluid, we found that the rotor of the inner cylinder is unable to shear fluids above a certain viscosity threshold. Shearing highly viscous fluids can generate very high shear stresses which can displace the rotation axis of the rotor. Subsequently, the bridle and the back transparent wall will be dislodged, eventually leading to the damage of the back transparent wall. Through trial and error, the upper viscosity threshold of the fluid was identified to be  $5.10^4$  Pa.s. This has to be taken into account while working with the rubber products or other highly viscous fluids.

### Temperature control

The heating system of the mixer was tested. The heating of the system is assured by the circulation of heat transfer fluid. This ensures a uniform thermal regulation of the the inner cylinder surface in static and dynamic conditions. The cylinder surfaces can be heated to up to  $100^{\circ}\text{C}$ . At higher temperatures, the outer cylinder surface undergoes substantial thermal expansion leading to mechanical failure. On the other hand, a uniform heating of the outer cylinder surface cannot be achieved in dynamic conditions. A uniform heating of the inner cylinder can be achieved due to the comparatively small size of the inner cylinder. The rotation of the large outer cylinder surface creates a discontinuous flow of the calorific fluid in the heating canals of the outer cylinder surface. Due to this discontinuous flow, air bubbles are created in the heating canals which result in an irregular heating of the surfaces.

Moreover, it was found that there is a difference between the temperature indicated by the thermocouples and the actual temperature on the cylinder surfaces. The position of the temperature sensors in the heating canals was found to be misplaced. However, the rotation of the cylinder surfaces makes it difficult to place temperature sensors on the cylinder surfaces. Thus, the heating system was calibrated by using external temperature sensors when the cylinders were in static condition. An precise control of the heating of the outer cylinder could not be achieved with the MaCROS mixer.

### Drag due to rotating transparent windows

The motion of the transparent windows provides a considerable drag on the fluid which deforms the fluid and influences the flow field in the fluid. A 3D flow profile is attained due to the lateral movement of the transparent windows.

### Suitable fluid characteristics

Preliminary experiments were conducted to define the suitable fluid characteristics in order to be able to stabilize a small volume of fluid in the converging zone between the cylinders in the counter-rotation mode. The required fluid properties for stabilization experiments are:

- Incompressibility:  
The stabilization conditions are not reproducible while working with compressible fluids.
- Viscoelastic character of the fluid:  
An elastic component is required from the fluid so that the fluid can maintain a stable form while being sheared between the inner and outer cylinders.
- Non-thixotropic properties:  
The rheological behavior of thixotropic fluids varies with time. This leads to the evolution of the stabilization conditions making steady state observations difficult. Care must be taken to avoid any potential changes to the properties of the fluid over time such as the presence of bubbles (which will break over time) or products sensible to evaporation.
- Low degree of crosslinking:  
During shear flow, the crosslinked bonds of gels and other highly crosslinked fluids can break irreversibly.
- Lower limit of viscosity:  
To avoid an influence of gravity during the flow, the fluid must exhibit a sufficiently high viscosity ( $\eta > 10^3$  Pa.s).
- Upper limit of viscosity:  
Above a certain viscosity threshold ( $\eta > 5 \cdot 10^4$  Pa.s), the torque generated by the inner rotor is insufficient to shear the fluid.
- Non-dominance of wall slip:  
When fluids exhibit slip during the counter-rotation of the cylinders, the fluid experiences no shear (hence, no shear flow) till contact with the walls is reestablished.
- Wetting domination:  
Fluids must not have a strong preference of wetting one surface over the other, which can result in the fluid experiencing more drag from one surface than the other.

### 4.3.2. Types of flow observations

On varying the volume fill factor, direction of rotation and rotation velocities, four different types of observations can be carried out with the MaCROS mixer. Among these observations, three types of observations are in steady state conditions while one type of observation is transient in nature. The different types of flow observations and the conditions under which they are achieved will be explained in detail below. *In-situ* flow observations were carried out at ambient temperature with the silicone fluid.

#### 4.3.2.1. Counter-rotation condition

##### Large fill factor

In these cases, the flow outlines are similar to those obtained with the Monocuve mixer. Large fill factor observations are carried out when the fill factor is larger than 8.7% of the free volume of the mixer. This fill factor threshold corresponds to the volume of the continuous flow outline in the MaCROS mixer. At these fill factors, a uniform layer of fluid is deposited on the outer cylinder

surface (Figure 4.18a). The rest of the fluid is stabilized in the upstream direction of the inner cylinder surface in the form of a partial ellipsoid, similar to the observations with the Monocuve mixer (Figure 4.8). The continuous flow outline of the fluid is displaced by the outer cylinder, while the ellipsoid flow outline is recirculated between the inner cylinder and the continuous flow outline. This provides a flow outline similar to the one represented on the schema of Figure 2.32a.

Steady state observations, similar to Figure 4.18a, can be obtained under ideal conditions of rotations speeds. For a given outer cylinder rotation velocity ( $V_1$ ), steady state observations can be observed if the inner cylinder rotates in the opposite direction at rotation velocities ranging from  $V_2 = 0$  to  $V_{limit}$ .

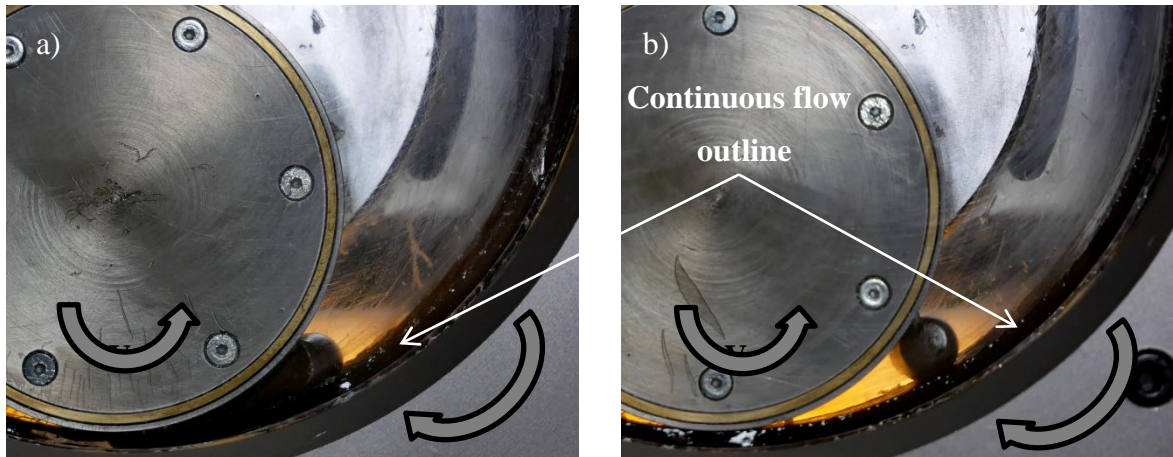


**Figure 4.18** – Flow observations under counter-rotation condition at large fill factors. a) Steady state flow observations and b) Transient flow observations due to excess inner cylinder velocities.

At higher inner cylinder rotation velocities ( $V_2 > V_{limit}$ ), the flow exerted by the inner cylinder dominates the flow provided by the outer cylinder and the rest of the fluid is displaced in the upstream direction (Figure 4.18b). The form of the fluid changes from a partial ellipsoid to a cylinder. It is then moved in the upstream direction till it loses contact with the continuous flow outline. At these velocities, the flow is transient in nature.

### Small fill factor

In this case, the volume is too small to form a continuous flow outline. The contact between the fluid and the cylinder surfaces (metal-fluid) is adhesive in nature. Figure 4.19 represents an example of the steady state flow observation of the silicone fluid at a small fill factor and counter-rotation conditions. This gives us the observation of two free surfaces: the advancing and receding contact lines.

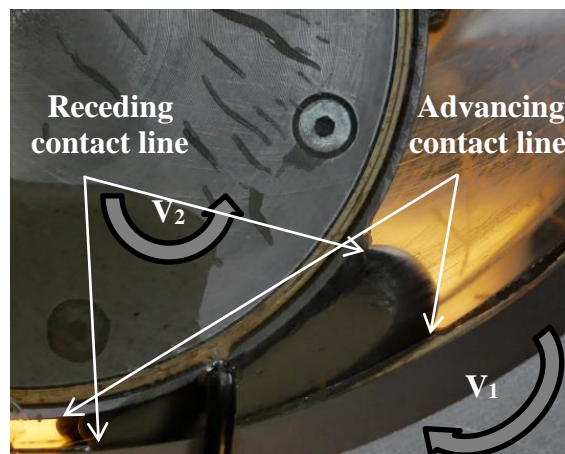


**Figure 4.19** – Steady state flow observations of silicone fluid at a small volume fill factor and counter-rotation condition.

The flow outline of the fluid is dominated by the local gap at larger fill factors. At larger fill factors, the flow channel diverges significantly. Thus, these flow observations are carried out at volume fill factors below 4.5% of the free volume of the mixer. There is also a lower critical limit of the volume fill factor below which the fluid cannot be stabilized. This lower critical fill factor depends on the fluid properties (cohesion, adhesion, rheology, etc) and varies from one fluid to another.

The steady state observation can be achieved only at optimal conditions of velocities. For a given outer cylinder rotation velocity ( $V_1$ ), the fluid was found to stabilize at a certain range of inner cylinder velocities ( $V_2 = V_{\min}$  to  $V_{\max}$ ). The steady state regime allows long durations (30 – 60 minutes). The stabilization conditions and the dimensions of the fluid during stabilization will be discussed in Chapter 4.4.1.

When ( $V_2 < V_{2\min}$ ), the inner cylinder velocity is not sufficient to stabilize the fluid. Thus, the fluid is displaced in the direction of rotation of the outer cylinder until it is split into two blocks at the thin flow gap (Figure 4.20a). As the experiment continues, one block is stabilized in the converging zone and the detached one is dragged by the outer cylinder back to the stabilized volume. These two volumes merge and split again at the thin flow gap, resulting in a vicious cycle. This process continues repeatedly and no steady state observation is obtained. At excessive inner cylinder velocities ( $V_2 > V_{2\max}$ ), the flow is dominated by the rotation of the inner cylinder (Figure 4.20b). In this case, the fluid is dragged in the direction of rotation of the inner cylinder till it loses contact with the outer cylinder.

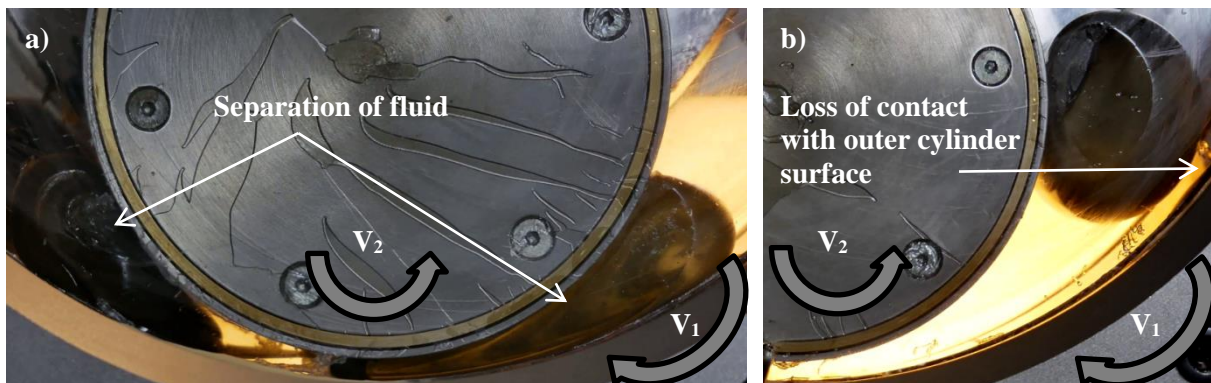


**Figure 4.20** – Flow observations under counter-rotation condition at small fill factors. a) Insufficient inner cylinder velocities and b) excess inner cylinder velocities.

### 4.3.2.2. Co-rotation condition

#### Large fill factor

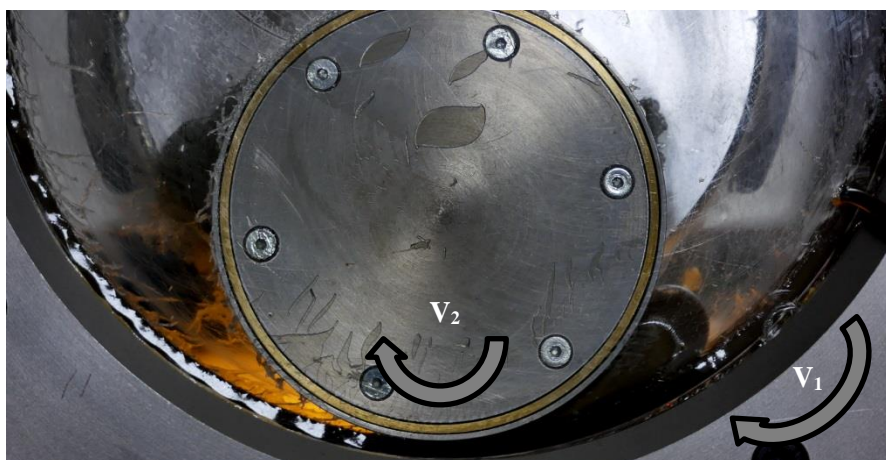


**Figure 4.21** – Steady state flow observations in co-rotation condition at large fill factors.

Figure 4.21 (page 131) presents the steady state flow observations in co-rotation condition at large fill factors. This type of observation is similar to the counter-rotation condition at large fill factor. Similar to the counter-rotation condition, the flow observations are carried out at fill factors larger than 8.7% of the free volume of the mixer. In this case, both cylinders displace the fluid in the same direction. The geometry of the flow channel limits the passage of some of the fluid through the thin flow gap which forms the ellipsoid flow outline, similar to Figure 4.18a. The fluid in the ellipsoid flow outline recirculates between the inner cylinder and the continuous flow outline. A steady state flow observation is obtained irrespective of the cylinder rotation velocities (Figure 4.21).

### Small fill factor

In this case, no steady state conditions can be obtained. Both cylinders displace the fluid in the same direction. Contrary to the previous case, all the volume passes through the thin flow gap. As the fluid passes through the thin flow gap, it forms a partial continuous flow outline (Figure 4.22). This type of flow observation occurs at fill factors inferior to 8.7% of the free volume of the mixer. The flow outlines of the three types of steady state observations obtained with the MaCROS mixer are compared in Figure 4.23.



**Figure 4.22** – Flow observations in co-rotation condition at small fill factors a) before passing through the thin flow gap and b) after passing through the thin flow gap.

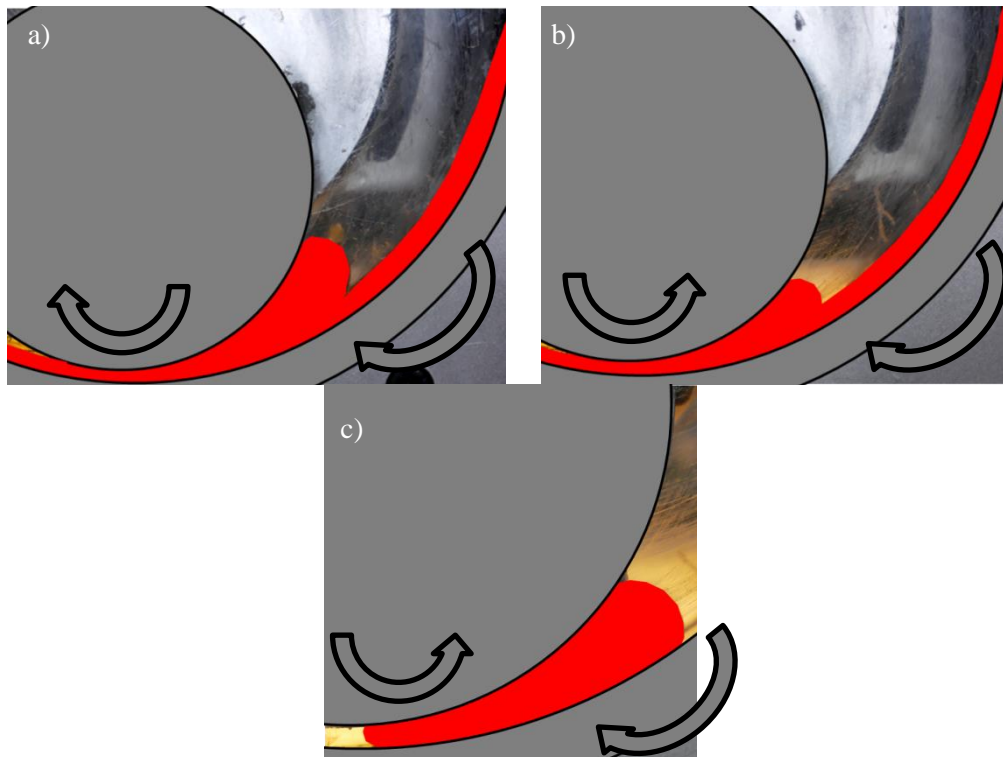


**Figure 4.23** – Steady state observations with the MaCROS mixer under a) co-rotation at large fill factors, b) counter-rotation at a large fill factors and c) counter-rotation at small fill factors.

Among the steady state observations, the flow observations under counter-rotation condition at small fill factor is more interesting than the other two for four reasons:

- i) a better observation of the free surfaces of the fluid,
- ii) the stabilization of the fluid is achieved due to the rheological response of the fluid and not due to the flow geometry,
- iii) the fluid is in contact with both cylinder surfaces and the nature of contact is purely adhesive,
- iv) the observation of four contact lines, two advancing and two receding lines.

From here onwards, the stabilization experiments with the MaCROS mixer indicates stabilization experiments under counter-rotation at small fill factors.

### 4.4. Steady state flow observations at a small fill factor

Stabilization experiments were conducted with the silicone fluid at ambient temperature. The stabilization velocities of the inner and outer cylinders were measured for different volume fill factors. To study the influence of the adhesion energy on the stabilization velocities, a model adhesive fluid would be required. However, a suitable model adhesive fluid could not be identified for the small fill factor observations in counter-rotation conditions. Thus, the surface properties of the cylinder walls (nature of surface and surface roughness) were modified to alter the adhesion energy exhibited by the fluid during the stabilization experiments. The stabilization velocities were compared for the different cases of surface properties. Finally, stabilization experiments were carried out on the rubber products to compare their flow behavior with that of the silicone fluid. For reference, rotation velocities in the anti-clockwise direction are considered as negative while those in the clockwise direction are considered as positive.

#### 4.4.1. Silicone fluid observations

Steady state flow observations could be obtained with the improved design of the MaCROS mixer. However, these observations are more complex (3D shape) in nature. The observation of the shear flow of the fluid through the transparent walls provides a 2D projection of the stabilized volume. This is observed by a difference in contrast of the 2D projection. The fluid in contact with the transparent front window is marked by a sharper contrast (Figure 4.24a). To represent this contact, the fluid in contact with the front transparent window is colored in red while the rest of the fluid is highlighted in blue (Figure 4.24b).

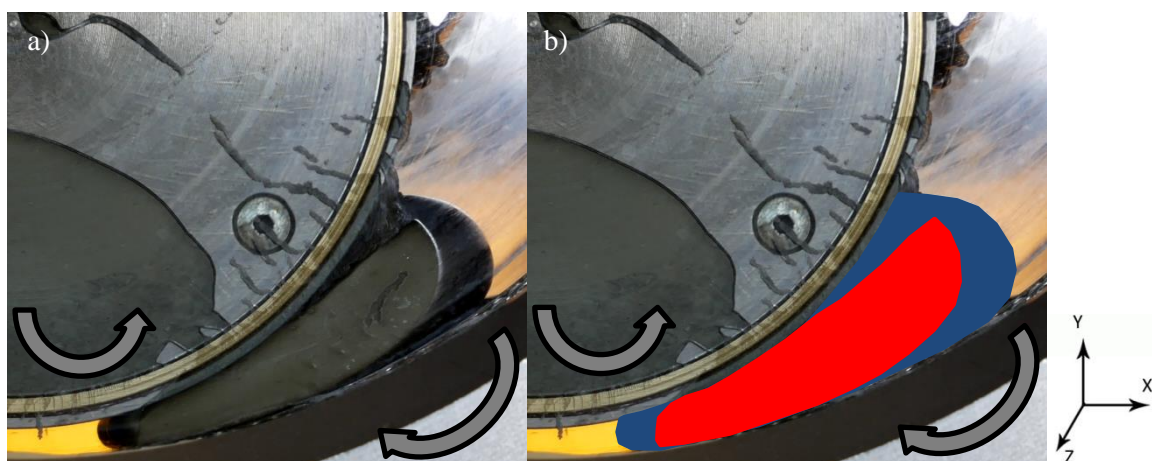


**Figure 4.24** – a) Small fill factor flow observations with the MaCROS mixer, b) Flow outline of stabilized silicone fluid (blue) and the fluid in contact with the front transparent window (red).

The stabilized volume takes up a 3D shape due to the additional drag provided by the rotating transparent windows. To better observe the 3D shape, the rotation of the cylinders was stopped and the fluid was taken out of the mixer. The extracted volume is shown in Figure 4.25. The fluid is distorted

as it is removed from the mixer. However, we observe that the free surface outline in the upstream direction takes the form of a curve with its apsis around the mid-point of the thickness of the flow channel (15 mm). On the other hand, in the downstream direction, the free surface outline takes the form of a ‘fish tail’ with its periapsis around the mid-point of the thickness of the flow channel (15 mm).

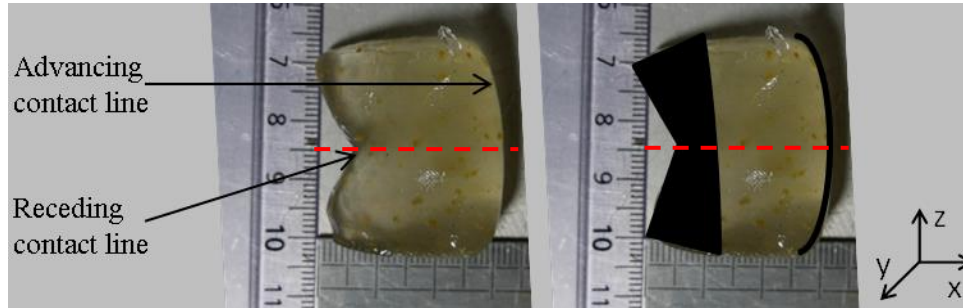


**Figure 4.25** – Top view of the 3D shape of the stabilized volume after extraction of the mixer. The form of the fluid is slightly distorted after extraction from the MaCROS mixer.

Figure 4.26 shows how the 3D shape of the fluid can be explained by the influence of the rotating transparent windows on the fluid. Considering stationary windows, the fluid would take a parallelepiped form as shown in Figure 4.26a. In our case, the transparent walls rotate at the same rotational velocity as the outer cylinder. This rotation causes the fluid near the transparent windows to experience a drag force in the direction of rotation of the transparent windows (Figure 4.26b) at the extremities of the stabilized volume. This drag force results in the distortion of the fluid at these extremities (Figure 4.26c) resulting in the attainment of a 3D form (Figure 4.26d) similar to Figure 4.24. Due to the plane of observation ( $xy$ ), the 3D shape of the fluid volume cannot be characterised.

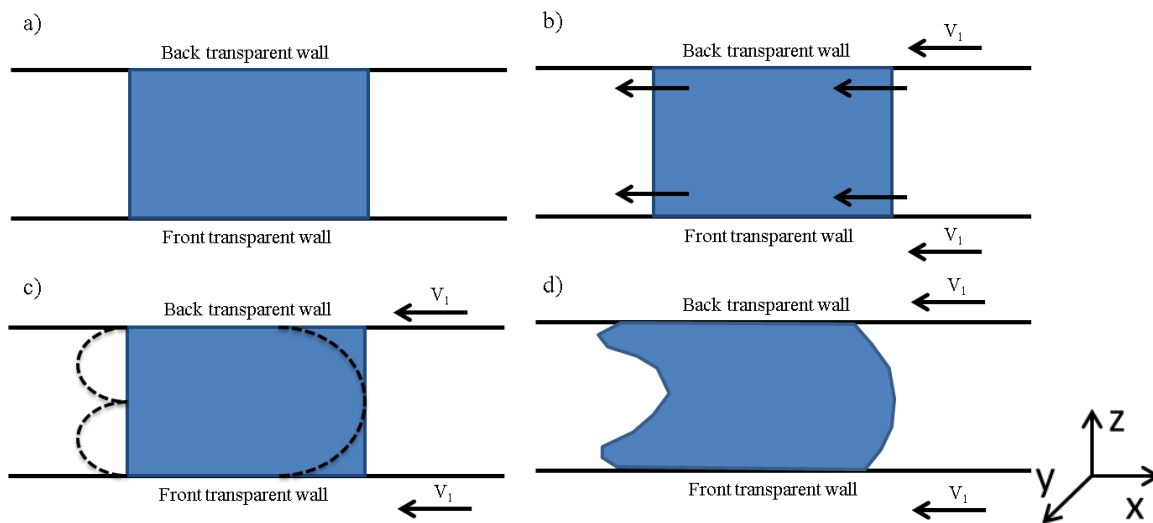


**Figure 4.26** – Influence of the transparent windows on the form of the stabilized fluid.

The 2D projection of the stabilized fluid does not represent the actual shape of the stabilized fluid but rather the visible sections of the stabilized fluid (Figure 4.27). The 2D projection of the fluid is recorded and reproduced on an Excel sheet. These projections will be used for flow analysis in Chapter 5.2. The 2D projection can help identify the:

- 1) points of loss of contact with the cylinder surfaces,
- 2) free surfaces of the stabilized fluid,
- 3) contact areas with the cylinder surfaces and the transparent walls.

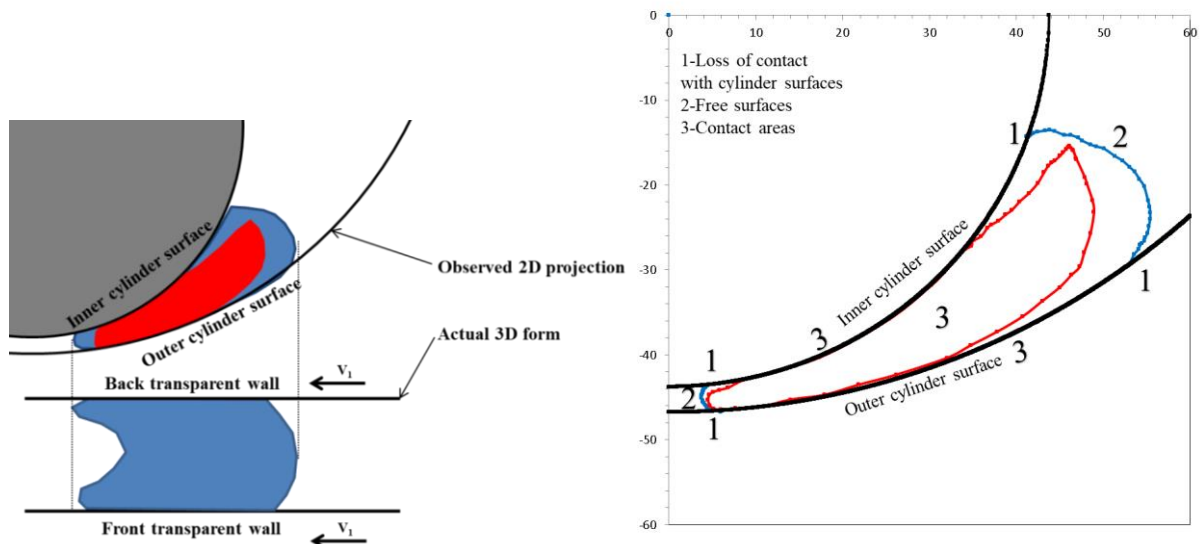


Figure 4.27 – (Left) Observed 2D projection and actual 3D form of the fluid. (Right) Information obtained from the 2D projection of the fluid.

The silicone fluid gradually loses its transparency during the experiment. Impurities in the fluid can serve as tracers. The accumulation of impurities with time results in the observation of streamlines across the volume of the stabilized fluid (Figure 4.28). A 3D flow field is observed where the fluid is recycled from the front to the back of the fluid (Figure 4.28b). Similar to the observations with the transparent flat die, the position of the particles along the thickness of the flow channel ( $z$ -axis) could not be ascertained. Thus, an effective estimation of the 3D flow field could be time-consuming.

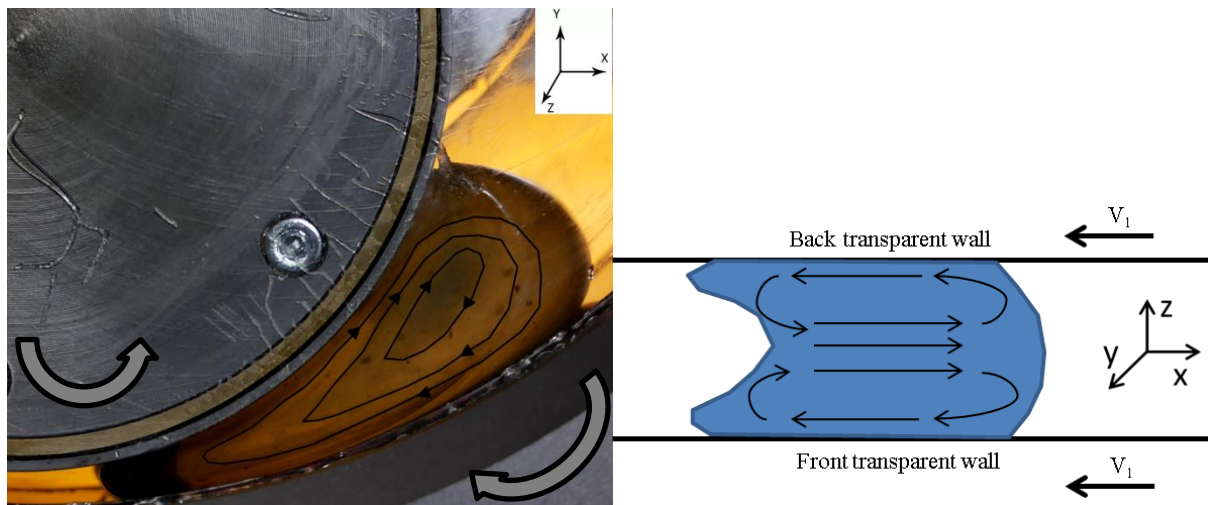


Figure 4.28 – Illustration of the flow field of silicone fluid during the stabilization experiments.

### Evidence of unilateral contact

The silicone fluid was found to exhibit unilateral contact with the cylinder surfaces. Similar to the Monocuve flow observations, the free surfaces of the stabilized fluid exhibit a symmetrical shape between the cylinder surfaces indicating no preference of adhesion with either cylinder surface. Thus, the fluid must exhibit a unilateral contact with both cylinder surfaces. In such a case, the energy cost to detach the fluid from either cylinder surface must be negligible. This can manifest by a lack of distortion of the fluid as it loses the contact with the cylinder surface.

To put this theory at test, the fluid was stabilized between the cylinder surfaces (Figure 4.29a). The rotation of the cylinder surfaces was stopped momentarily. The outer cylinder surface was rotated in

the opposite direction (Figure 4.29b) causing the fluid to lose contact with the inner cylinder surface. As the fluid loses contact, the 2D projection of the fluid remains unchanged indicating that it costs no energy to detach from the surface.



Figure 4.29 – Dewetting of the inner cylinder surface indicating unilateral contact of the fluid with the cylinder surfaces.

### Stabilization conditions

Besides the visual observations, the measured output from the stabilization experiments is the stabilization velocities of both cylinders. The stabilization velocities were measured at different volume fill factors. However, as the volume introduced is not the volume of the fluid stabilized. We represent the volume fill factors in grams rather than in % of volume to not mislead the reader. 8g is the minimum amount of fluid required to carry out steady state stabilization experiments with the MaCROS mixer. The maximum fill factor was limited to 20g after which the flow channel becomes significantly more divergent.

As mentioned earlier, for a given outer cylinder rotation velocity ( $V_1$ ), the fluid can be stabilized at a certain range of inner cylinder velocities [ $V_{2min}$ ,  $V_{2max}$ ]. The minimum inner cylinder velocity required to stabilize the fluid is recorded as the inner cylinder velocity and noted as  $V_2$  in the following. The experiments were carried out with similar surface roughness and nature of surface i.e. both cylinders were made of 42CrMo4 steel. The cylinder surfaces were polished with 320 emery sheets to provide similar surface roughness. The minimum inner cylinder velocity to stabilize the fluid is plotted as a function of the outer cylinder velocity in Figure 4.30.

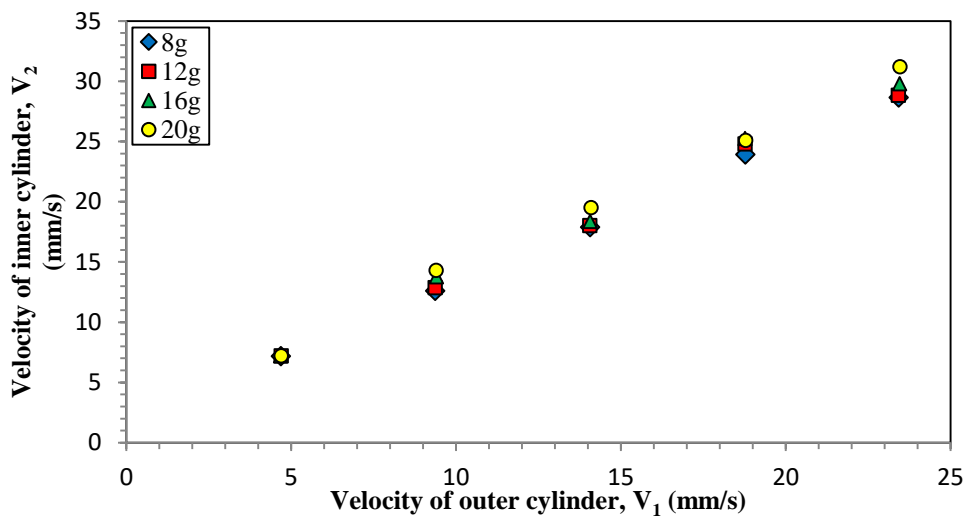


Figure 4.30 – Minimum inner cylinder velocity to stabilize the fluid as a function of the outer cylinder velocity with 42CrMo4 steel cylinders and similar surface roughness.

A linear dependence between the inner and outer cylinder velocities can be observed. A small dependence in volume fill factor can be observed with larger fill factors requiring slightly larger inner cylinder velocities to stabilize the fluid. However, the difference in inner cylinder velocities is too small and within the margin of error. The influence of volume fill factor can be considered to be negligible. To better understand the stabilization conditions, we define the stabilization ratio ( $V^*$ ). The stabilization ratio is given by:

$$\text{Stabilization ratio, } V^* = \frac{V_2}{V_1} \quad \text{Equation 4.1}$$

where  $V_2$  and  $V_1$  are the linear velocities (mm/s) of the inner and outer cylinders respectively.

Figure 4.31 shows the stabilization ratio plotted as a function of the imposed outer cylinder velocity for the stabilization experiments with 42CrMo4 steel cylinders and similar surface roughness. The optimal conditions of stabilizations were found to occur at stabilization ratios between 1.2 and 1.6 for the silicone fluid.

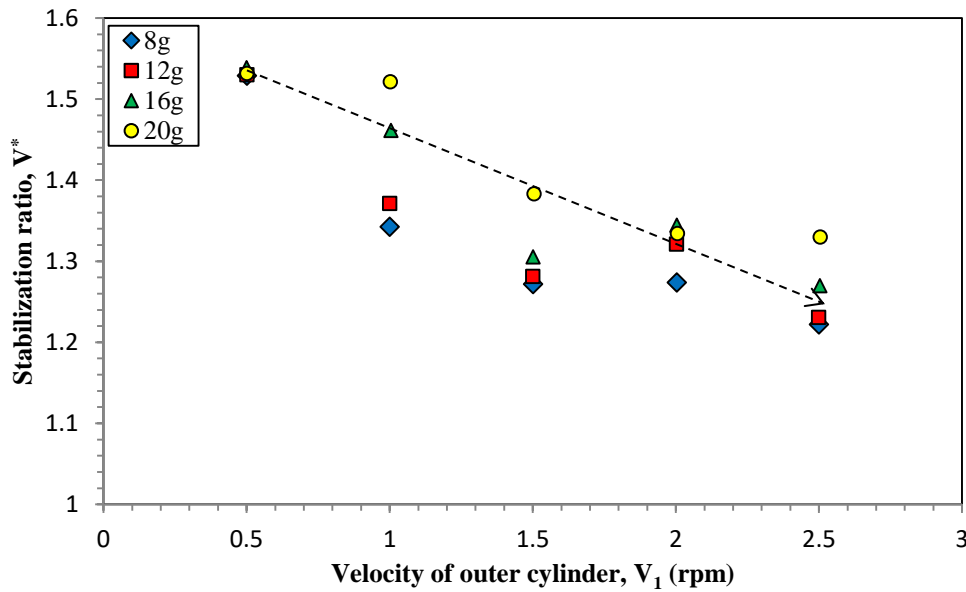


**Figure 4.31** – Stabilization ratio in function of the outer cylinder velocity with 42CrMo4 steel cylinder and similar surface roughness.

From Figure 4.31, we find that the stabilization ratios are above 1 irrespective of the volume fill factor and the outer cylinder velocities. Without the rotation of the transparent windows, a stabilization at  $|V_1| = |V_2|$  (linear velocities) would be expected. However, the inner cylinder has to provide a higher velocity than the outer cylinder to stabilize the fluid to overcome the drag provided by the outer cylinder and the transparent walls. The stabilization ratio decreases with an increase in the outer cylinder velocity. An increase in outer cylinder velocity reduces the contact time of the fluid with the transparent windows. This diminishes the amount of drag provided by the transparent windows. The diminishing effect of the drag force with the rise of outer cylinder velocity is evident in Figure 4.32.

At low outer cylinder velocities (Figure 4.32a), we observe that the fluid presents a small crown like protrusion (depicted in red). This protrusion disappears at larger outer cylinder velocities (Figure 4.32b). The protrusion is only visible for a few millimeters near both transparent walls. The protrusion occurs due to the increased impact of the drag force of the transparent walls at low outer cylinder velocities. At  $V_1 = -1$  rpm, the protrusion diminishes and disappears completely at velocities above  $V_1 = -1.5$  rpm (Figure 4.32b).

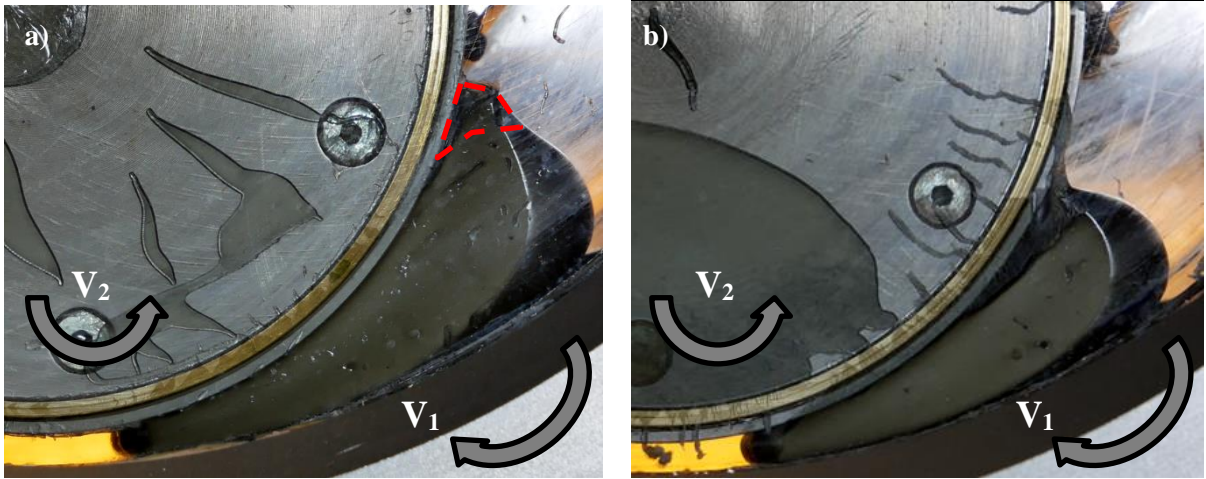


**Figure 4.32** – 2D projection of the stabilized fluid at a)  $V_1 = -0.5$  rpm and b)  $V_1 = -1.5$  rpm with 42CrMo4 steel cylinders and similar surface roughness.

Once the optimal cylinder velocities are provided, the fluid can be stabilized at different positions in the flow channel. Figure 4.33 illustrates two extreme stabilization positions obtained on the same fluid volume for the same conditions of cylinder velocities. The mean shear rate experienced by the fluid and the shape of the stabilized volume are dependent on the local geometry of the flow channel. Thus, the forms of the free surfaces are dependent on the position of the fluid (local geometry of the flow channel). This poses a problem in the analysis of the shape and dimensions of the stabilized volume. As multiple positions can be obtained for a given stabilization condition, the dimensions of the stabilized fluid are not a function of the cylinder velocities.

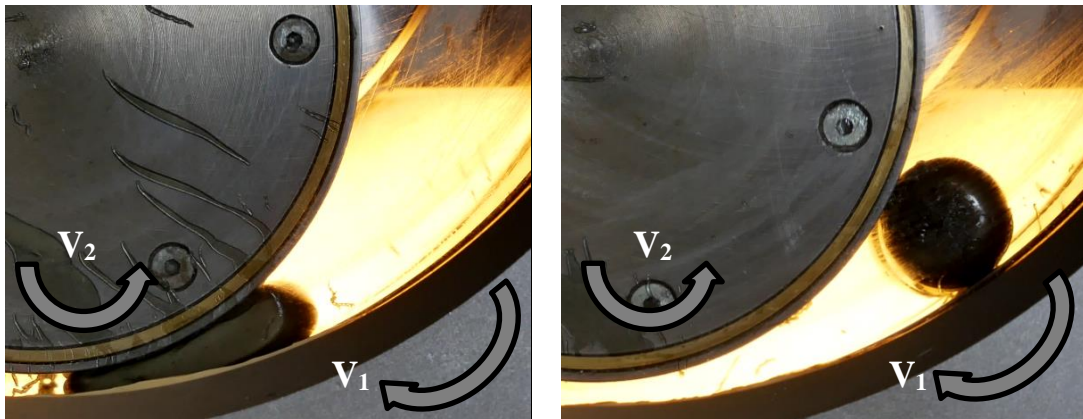


**Figure 4.33** – Different positions of stabilization at  $V_1 = -2$  rpm,  $V_2 = 4.7$  rpm with 42CrMo4 steel cylinders and similar surface roughness.

For simplicity purposes, the 2D projection of the stabilized volume can be represented by the local flow gap ( $h(\theta)$ ) and the contact lengths ( $l_1$  and  $l_2$ ) of the fluid/metal interface (Figure 4.34). These dimensions are mainly imposed by the stabilization location in the flow channel and the fluid volume. On analysis, the contact surfaces of the fluid ( $S_1$  and  $S_2$ ) are comparable, which implies that the contact lengths of the fluid ( $l_1$  and  $l_2$ ) are also comparable. For analysis purposes, the fluid is stabilized as close as possible to the thin flow gap and the contact length with the outer cylinder ( $l_2$ ) is considered as the length of the fluid.

The variation of the contact length ( $l$ ), the local flow gap ( $h(\theta)$ ) and the mean shear rate ( $\dot{\gamma}_m$ ) with the position of the fluid ( $\theta$ ) is given by:

$$l_2 = 2\pi R_2 \left( \frac{\theta_{sup} - \theta_{inf}}{360} \right) \quad \text{Equation 4.2}$$

$$h(\theta) = R_1 - \left[ e * \cos(\theta) + R_2 * \left( 1 - \frac{e * \sin(\theta)}{2R_2} \right)^{0.5} \right] \quad \text{Equation 4.3}$$

$$\dot{\gamma}_m = \frac{V_2 - V_1}{h_m} \quad \text{Equation 4.4}$$

where  $e$  is the eccentricity between the two rotation centers of the cylinders,  $h_m$  is the mean local flow gap,  $R_i$  the cylinders radius and  $l_2$  corresponds to the contact length at the inner cylinder.

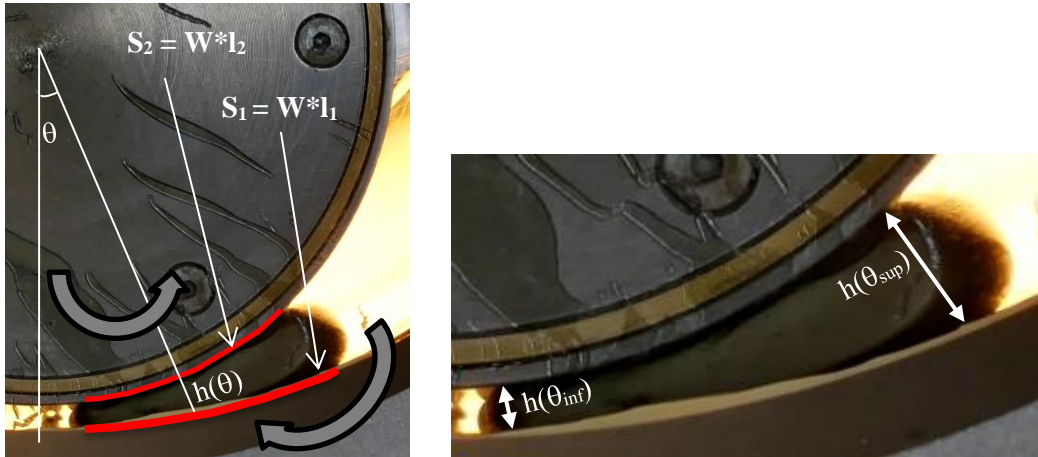


Figure 4.34 – Representation of the 2D projection of the stabilized fluid in terms of the local thin flow gap and the contact lengths.

The mean local flow gap ( $h_m$ ) is given by:

$$h_m = \frac{h(\theta_{inf}) + h(\theta_{sup})}{2} \quad \text{Equation 4.5}$$

#### 4.4.2. Effect of surface properties on stabilization velocities

A change in the surface properties of the cylinder surfaces could induce a change in the adhesive behavior of the fluid. The surface properties were varied via a modification of the surface roughness and via modification of surface energy by changing the material of the surface. The inner cylinder surface was polished with 1200 grade emery sheets to provide a smoother surface than the outer cylinder surface (polished with 320 grade emery sheets). Moreover, the steel surface of the inner cylinder was replaced with brass surface. Brass surfaces exhibit lower surface energies than steel surfaces [Aspenes *et al.*, 2008]. The surface properties of the cylinders of the three different surface conditions are presented in Table 4.5.

Surface condition	Material of surface		Surface roughness (Grade of emery sheet)	
	Inner cylinder	Outer cylinder	Inner cylinder	Outer cylinder
Steel 320-320	Steel	Steel	320	320
Steel 1200-320	Steel	Steel	1200	320
Brass-Steel	Brass	Steel	-	320

Table 4.5 – Three different conditions of surface properties of the cylinders for the stabilization experiments with the silicone fluid.

The objective was to introduce an asymmetrical surface condition to create a difference in the adhesive behavior of the fluid between the cylinder surfaces. The improved adhesive behavior of the fluid could

induce a difference in the stabilization velocities of the fluid or in the shape of the free surfaces. Figure 4.35 and 4.36 present the stabilization velocities under the asymmetrical surface conditions of Steel 1200-320 and Brass-Steel respectively.

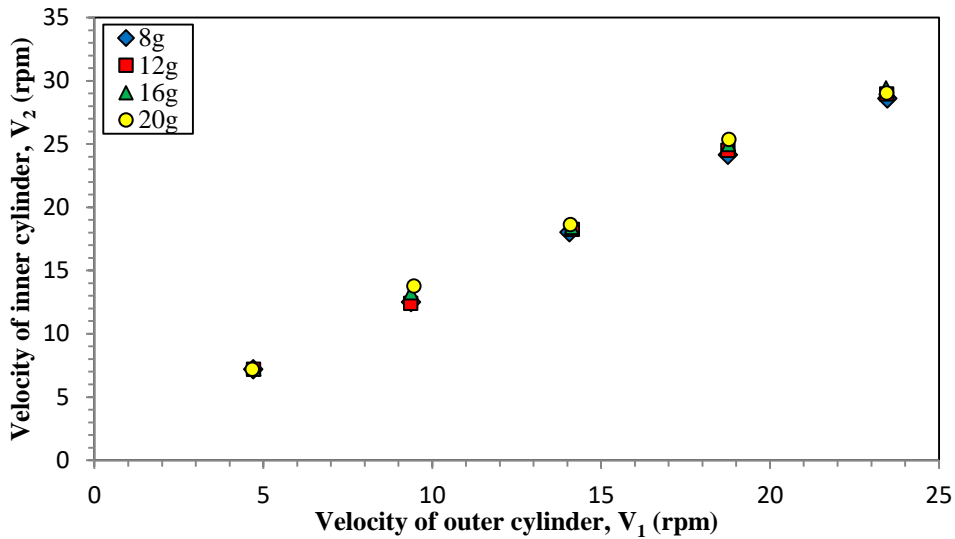


Figure 4.35 – Stabilization velocities under the Steel 1200-320 surface condition.

It was found that on changing the surface conditions, the stabilization velocities showed a similar trend to the symmetrical surface condition of Steel 320-320 (Figure 4.30). No significant changes in the 2D projection of the stabilized volume were observed with imposing the asymmetrical condition in surface roughness. The change in surface properties induced no discernable changes in the stabilization velocities.

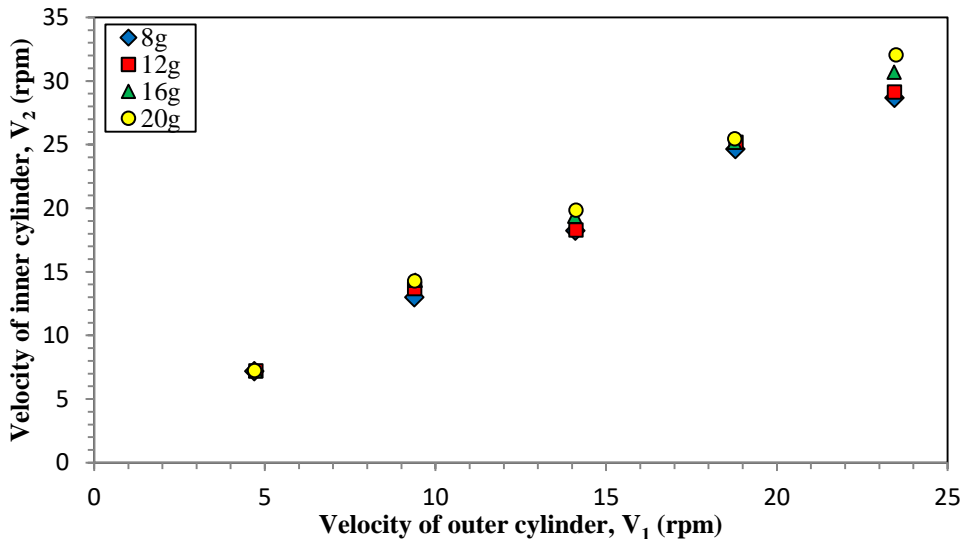


Figure 4.36 – Stabilization velocities under the Brass-Steel surface condition.

The stabilization velocities at different conditions of cylinder velocities, volume and surface conditions are presented in Appendix XII. To compare the change in stabilization velocities, the stabilization ratios of the three conditions at a fixed volume fill factor are reported in Table 4.6. The stabilization velocities under the Steel 320-320 surface condition are considered as reference. The comparison provides a mean error on the stabilization ratio of 1.59% for the Steel 1200-320 condition and 1.96% for the Brass-Steel condition. These errors are very small and are within the range of the error of the machine i.e. fluctuations in velocity control. Hence, the surface properties appear to have no effect on the stabilization velocities of the silicone fluid.

Mass (g)	Outer cylinder velocity (rpm)	Stabilization ratios ( $V^*$ )		
		Steel 320-320	Steel 1200-320	Brass-Steel
8	0.5	1.53	1.53	1.53
8	1	1.34	1.33	1.38
8	1.5	1.27	1.28	1.29
8	2	1.27	1.29	1.31
8	2.5	1.22	1.22	1.22

**Table 4.6** – Stabilization velocities at a fixed volume fill factor (8g) under different surface conditions.

#### 4.4.3. Symmetry of the flow outlines in MaCROS mixer

To investigate the effect of surface properties on the shape of the flow outlines, the peak angles ( $\theta_{Peak}$ ) were measured on the free surfaces of the stabilized fluid. The two free surfaces were called the converging and diverging free surfaces (Figure 4.37).

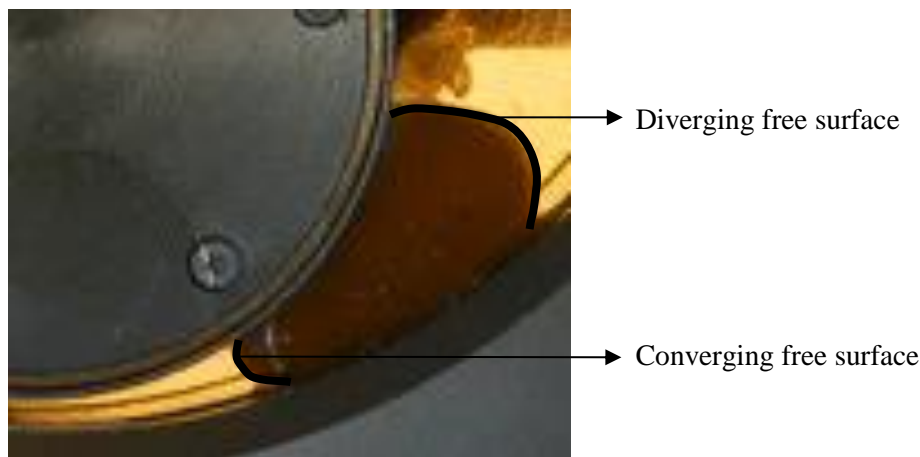


**Figure 4.37** – Converging and diverging free surfaces of the flow outline of the stabilized fluid.

The average peak angles of the converging and diverging free surfaces under different conditions of nature and surface roughness of the cylinder surfaces are summarized in Figures 4.38 and 4.39 respectively. The peak angles during the stabilization experiments were measured at different conditions of cylinder velocities, volume and surface conditions are presented in Appendix XII.

On analyzing the peak angles under the different conditions, no clear relation between the fill factor, cylinder velocity and the surface condition could be identified. In general, the converging and diverging free surfaces were found to show peak angles close to  $90^\circ$ , indicating symmetric free surfaces. The average peak angles of the converging and diverging free surfaces for the different surface conditions are compared in Table 4.7. As mentioned before, the peak angles measurements were carried out on the 2D projection of the 3D free surface. From Table 4.7, we can comment that the 2D projections are quite symmetric with a significant data dispersion. However, we refrain from suggesting that the 3D free surfaces are symmetric considering the fact that we are unable to carry out peak angle measurements of the 3D free surfaces. The dispersion in measured peak angles was found to be more pronounced for the converging free surface. This might be due to:

- the constricting flow channel,
- difficulty in discerning the 2D projection of the flow outline due to the visibility of the two polymer melt fronts (Figure 4.26).

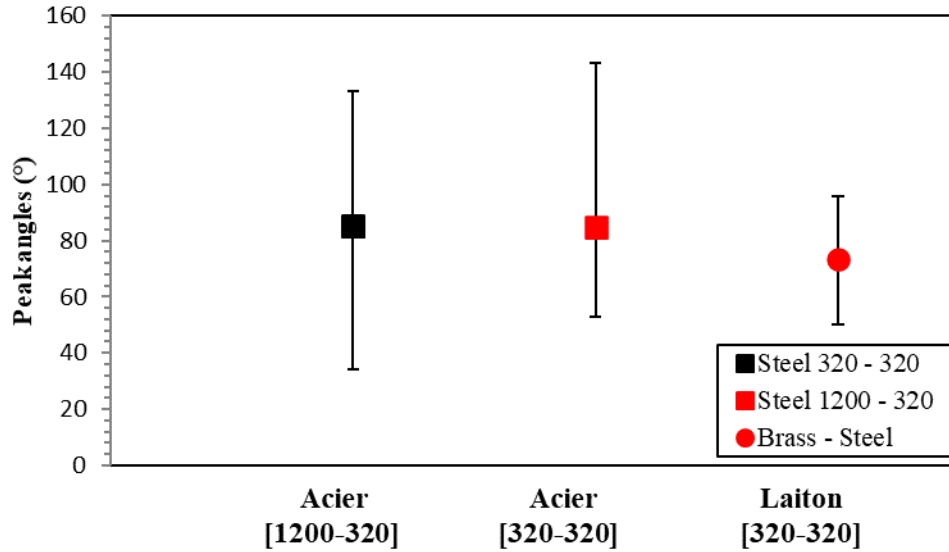


Figure 4.38 – Peak angles of the converging free surfaces for different fill factors, cylinder velocities and surface conditions.

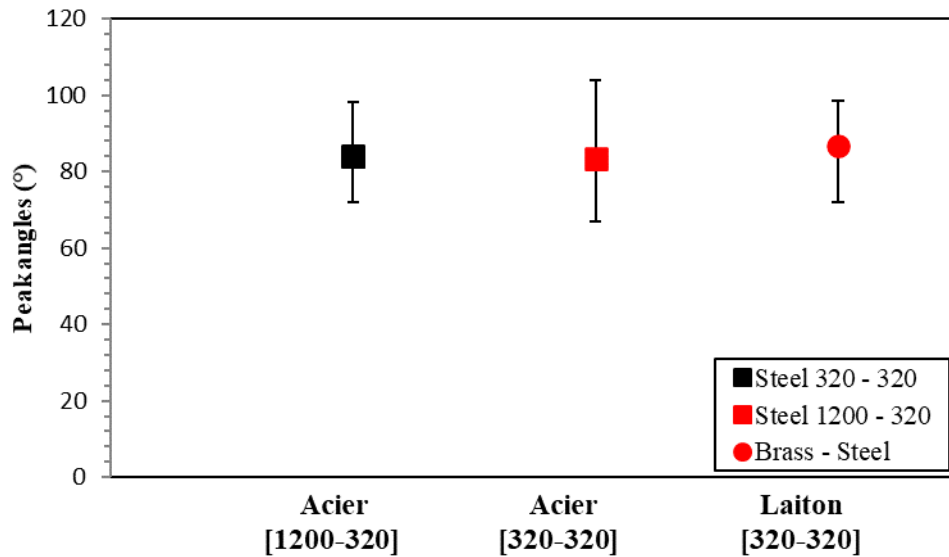


Figure 4.39 – Peak angles of the diverging free surfaces for different fill factors, cylinder velocities and surface conditions.

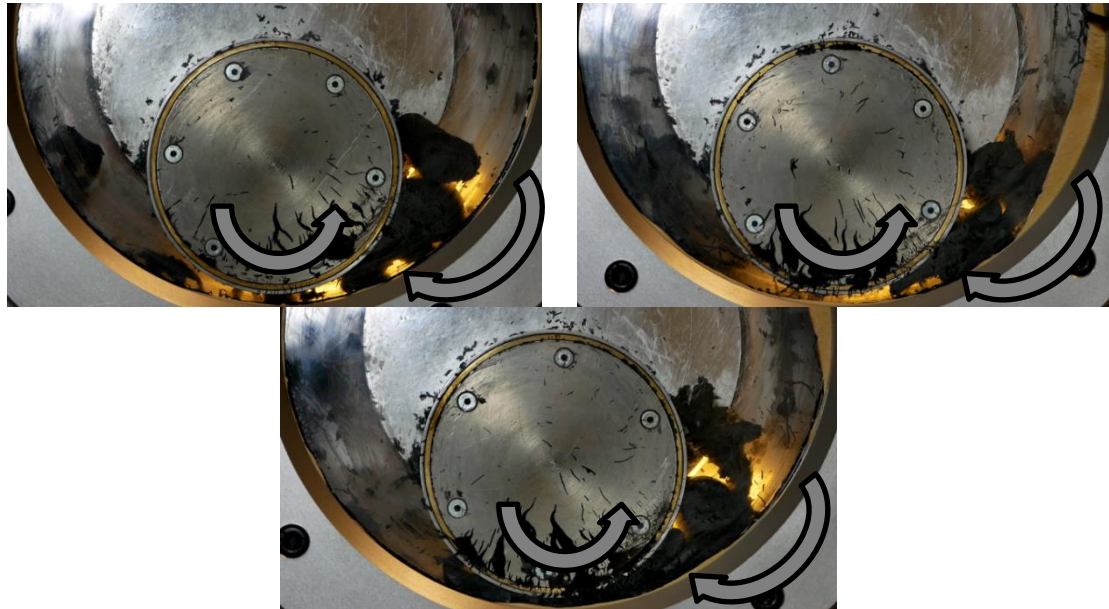
Surface condition	Average peak angles ( $\theta_{Peak}$ )	
	Converging free surface	Diverging free surface
Steel 320-320	85°	84°
Steel 1200-320	85°	84°
Brass-Steel	73°	87°

Table 4.7 – Average peak angles of the converging and diverging free surfaces for the different surface conditions.

#### 4.4.4. Rubber products observations

Due to the upper limit of viscosity of the machine ( $\eta > 5.10^4$  Pa.s), the rubber products cannot be sheared by the cylinders at ambient temperature. The cylinder surfaces were heated to 100°C in static conditions. Stabilization experiments were attempted on the rubber products. However, it was not possible to obtain homogenous flow with SBR C and BR A despite long mixing times. The elastomers

tend to break into smaller blocks and were unable to merge to form a homogenous volume (Figure 4.40). Observations show that these products have not undergone the first stage of mixing (softening phase). This can be due to several factors such as the small fill factor, lack of sufficient shear, the geometry of the flow channel, etc. The most important factors are the complex formulation of SBR C and the wall slip behavior of BR A.



**Figure 4.40** – Absence of stabilized flow behavior with SBR C under the conditions of small fill factor in the counter-rotation mode.

The working conditions of the MaCROS mixer are far from the mixing conditions in an industrial mixer, leading to difficulty in shearing the rubber products. The transition from solid to fluid like behavior could be observed for SBR C and BR A by increasing the fill factor. Large fill factor stabilization experiments could be conducted with SBR C and BR A (Figure 4.41) but they were unsuitable for small fill factor experiments.



**Figure 4.41** – Large fill factor stabilization experiments with SBR C.

SBR A and SBR B can form a homogenous block during mixing in the counter-rotation condition. Contrary to SBR C and BR A, separated blocks of SBR A could merge to form a homogeneous flow. SBR A was found to exhibit wall slip at 100°C (imposed temperature in static conditions). Wall slip was found to occur at shear rates lower than those encountered from the capillary characterization ( $< 8 \text{ s}^{-1}$ ). This is likely due to the bad temperature control of the outer cylinder surface. During the experiment, SBR A was found to undergo slip between two stable positions in the flow channel: 1) at the thin flow gap where it undergoes a separation of fluid, 2) upstream in the flow channel where the

separated blocks of fluid merge again. Figure 4.42 shows SBR A slipping between two stable positions. This transitive behavior is presented in Appendix XIII.

As the fluid moves downstream, it undergoes wall slip near the thin flow gap. The fluid slips in the downstream direction where it separates into two unequal blocks of fluid at the thin flow gap (Figure 4.20a). These blocks move in opposite directions. The part of the fluid in the upstream direction moves to another position where it remains stable for a few seconds (Figure 4.42b). Meanwhile, the fluid in the downstream direction moves with the outer cylinder. As the outer cylinder completes a rotation, the two blocks of fluid are brought in contact and merge to form a single homogenous volume. The fluid then moves into a stable position near the thin flow gap (Figure 4.42a). The flow remains stable for a few seconds in this position before the fluid undergoes wall slip and the cycle repeats itself.

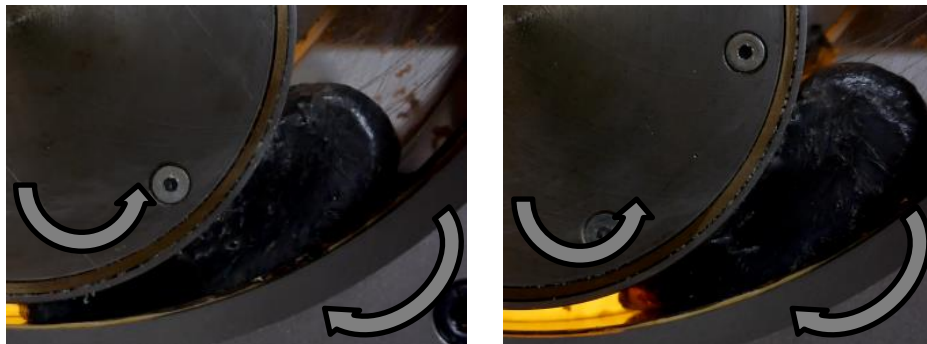


**Figure 4.42** – SBR A slipping between two stable positions during the stabilization experiments.

Steady state observations could be obtained with SBR B. Contrary to the silicone fluid, the 2D projection of SBR B is completely opaque (Figure 4.43) from the beginning of the mixing cycle. The extraction of the stabilized fluid shows that SBR B presents a 3D shape similar to the silicone fluid as depicted in Figure 4.25. The 2D projection of the volume shows similar flow behavior to the silicone fluid despite their differences in rheology and operating temperature.

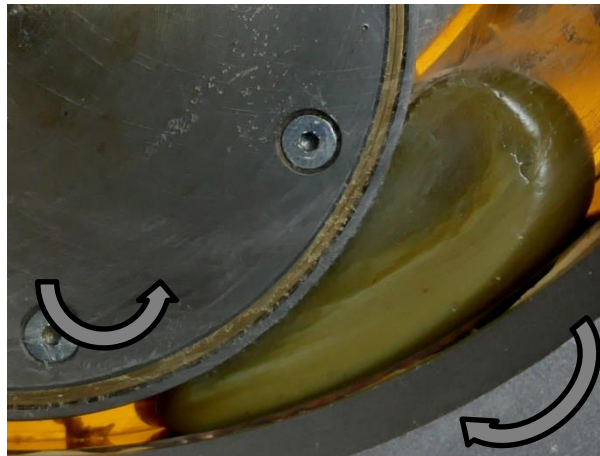


**Figure 4.43** – Small fill factor steady state observations with SBR B.

The stabilization velocities of SBR B are presented in Figure 4.44. The stabilization velocities show a similar trend to the silicone fluid (Figure 4.30). However, it is to be taken into account that the temperature, and hence the rheology (viscosity level), at the outer cylinder surface is uncertain. Hence, the stabilization velocities are not used for flow analysis.

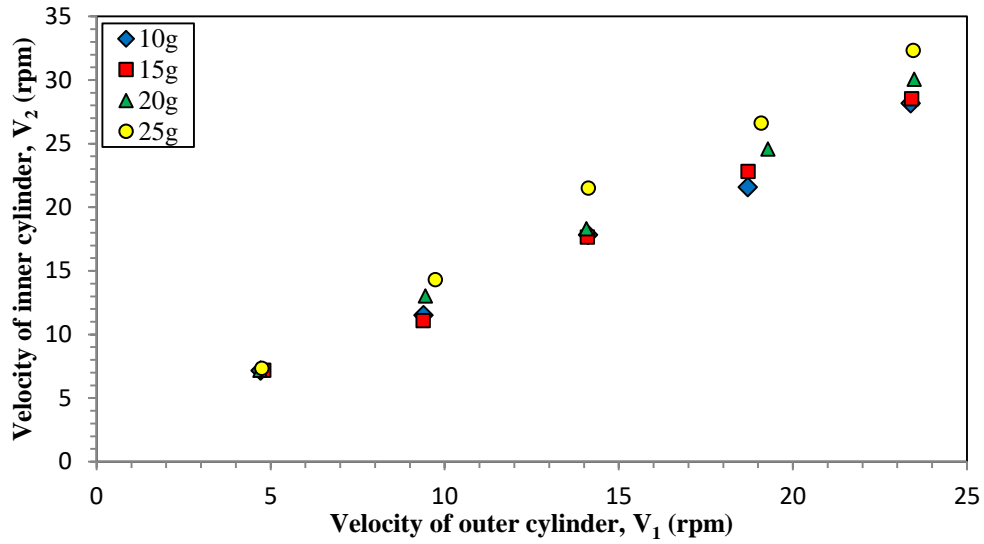


Figure 4.44 – Stabilization velocities of SBR B at 100°C (Outer cylinder temperature was uncertain).

### Conclusions

*In-situ* flow observations were carried out with three transparent flow geometries: 1) transparent flat die, 2) Monocuve mixer and 3) MaCROS mixer. The objective was to highlight the interfacial flow behavior of highly viscous fluids. Steady state flow observations could not be obtained with the transparent flat die. Wall slip could be observed with SBR A, yet wall slip velocities could not be estimated due to mechanical failure of the transparent flat die. Due to the limitations of the design and the time constraints of the PhD, further studies with the transparent flat die were abandoned.

The simple geometry of the Monocuve mixer provides simpler flow observations in comparison to observations conducted with other transparent internal mixers. A simple 2D flow could be obtained. Moreover, a quasi-steady state observation was attained where the form of the fluid remains quite stable with reference to the rotor. The flow behavior of the rubber products was compared at a given condition. Wall slip behavior was encountered with SBR A. The flow behavior of the silicone fluid was found to be similar to the other rubber products which do not undergo wall slip. Thus, the silicone fluid is a suitable fluid to mimic the flow behavior of the rubber products at ambient temperature.

The 2D flow outlines of the elastomers were recorded. A peak angle ( $\theta_{Peak}$ ) was defined to quantify the degree of symmetry of the flow outlines. The silicone fluid, BR A and SBR A showed symmetric free surfaces during mixing. On the other hand, the free surfaces of SBR B and SBR C were inclined towards the rotor surface indicating that the fluid prefers adhering to the rotor surface more than the continuous flow outline surface. Further studies are required to quantify the role of adhesion in the attainment of asymmetric free surfaces under dissimilar surface contact condition.

The MaCROS mixer was tested and calibrated to determine its functionality. The heating control of the outer cylinder surface was not accurate. Hence, a model fluid was identified to conduct flow observations at ambient temperature. On varying the direction of rotation and the volume fill factor, four different types of flow observations can be obtained of which three are steady state in nature. Among these observations, the observations in counter-rotation mode at small fill factors are interesting as they provide the observation of two free surfaces under similar adhesive contact condition. Consequently, steady state experiments were conducted with the silicone fluid in this condition.

The silicone fluid demonstrates that during viscous flow, the fluid has a unilateral contact with the metallic surfaces. Steady state observations at small fill factor show a significant distortion of the volume due to the rotation of the transparent windows. This leads to a complex 3D shape of the stabilized fluid which cannot be accurately ascertained by visual observation through the transparent walls. On analyzing the stabilization velocities of the cylinders, it was found that the inner cylinder rotates at higher velocities to counteract the drag provided by the rotating transparent windows.

The surface roughness and the nature of the inner cylinder surface were modified to investigate the role of adhesion on the stabilization velocities. Despite the change in surface properties, no significant difference was observed in the stabilization velocities or the form of the free surfaces. Thus, adhesion plays a negligible role in the interfacial flow behavior of the silicone fluid. Peak angle measurements of the free surfaces during stabilization experiments in the MaCROS mixer shows that in general, the free surfaces are symmetric but the data was found to be quite disperse.

Flow observations in the counter-rotation mode at a small fill factor were conducted with SBR A and SBR B at 100°C. Wall slip was observed while working with SBR A. Stabilized steady state flow observations conditions could be performed with SBR B. SBR B exhibits a similar flow behavior to the silicone fluid. The MaCROS mixer, due to the geometry of its flow channel, appears to be more adapted for large fill factor steady state flow observations of the rubber products. However, flow analysis could not be conducted due to the uncertainty of the fluid's rheology as a product of bad temperature control of the outer cylinder surface.

### Résumé en français

Des observations d'écoulement *in-situ* ont été effectuées avec trois géométries d'écoulement transparentes : 1) filière plate transparente, 2) mélangeur Monocuve et 3) mélangeur MaCROS. L'objectif était de mettre en évidence le comportement d'écoulement interfacial des fluides très visqueux. Les observations d'écoulement en régime permanent n'ont pas pu être obtenues avec la filière plate transparente. Du glissement à la paroi a été observé avec le SBR A. Pourtant la rupture mécanique de la filière plate a empêché la détermination des vitesses de glissement. Du fait de cette casse et des contraintes de temps de la thèse, les études avec la filière plate transparente ont été abandonnées.

La géométrie simple du mélangeur Monocuve fournit des observations avec un écoulement simple par rapport aux observations effectuées sur d'autres mélangeurs internes transparents. Un comportement d'écoulement 2D du fluide a été obtenu. De plus, une observation quasi-stationnaire a été atteinte où la forme des surfaces libres reste assez stable par rapport à la position du rotor. Le comportement d'écoulement des fluides a été comparé à une condition donnée montrant un comportement d'écoulement similaire pour les fluides sauf BR A qui montre un glissement de stick-slip. De ce fait, le fluide silicone peut être considéré comme un bon fluide modèle qui est représentatif du comportement des caoutchoucs à température ambiante. Les surfaces libres du fluide pendant l'écoulement ont été enregistrées en régime stationnaire. Un angle de sommet ( $\theta_{Peak}$ ) a été défini pour quantifier le degré de symétrie de ces surfaces libres. Le fluide silicone, le BR A et le SBR A présentaient des surfaces libres symétriques pendant l'écoulement. D'autre part, les surfaces libres du SBR B et du SBR C étaient inclinées vers la surface du rotor. Ceci indique que le fluide préfère adhérer à la surface du rotor plus que l'autre surface. D'autres études sont nécessaires pour quantifier le rôle de l'adhésion dans l'obtention de surfaces libres asymétriques

Le mélangeur MaCROS a été testé et étalonné pour déterminer sa fonctionnalité. Le contrôle de la température de la surface du cylindre externe s'est avéré peu précise en rotation. Par conséquent, le fluide silicone a été utilisé pour conduire des observations d'écoulement à température ambiante. En variant le sens de rotation et le facteur de remplissage, quatre types d'observations d'écoulement peuvent être obtenus dont trois en régime permanent et un en régime transitoire. Parmi ces observations, les observations du type contre-rotation aux faibles taux de remplissage sont intéressantes car elles présentent deux surfaces libres avec un contact adhésif aux deux extrémités de la surface libre. Un contact unilatéral a été observé avec le fluide silicone. Les observations en régime permanent aux faibles taux de remplissage montrent une distorsion significative du volume cisailé due à la rotation des fenêtres transparentes. Cela conduit à une forme du fluide complexe et 3D. Cette forme ne peut pas être déterminée avec précision par une observation visuelle à travers les parois transparentes. En analysant les conditions de stabilisation, on constate que le cylindre interne tourne à des vitesses plus élevées que celle du cylindre externe pour compenser l'entraînement dû aux fenêtres transparentes.

La rugosité et la nature de la surface du cylindre interne ont été modifiées pour induire un meilleur comportement adhésif. Malgré ces modifications, aucune différence significative n'a été observée sur les vitesses de stabilisation ou la forme des surfaces libres. Ces observations indiquent que l'adhésion joue un rôle négligeable sur l'écoulement interfacial du fluide silicone. Les mesures d'angle de sommet des surfaces libres pendant les expériences de stabilisation dans le mélangeur MaCROS montrent qu'en général, les surfaces libres sont symétriques mais les données se sont avérées assez dispersées. Les observations avec les produits en caoutchouc à 100°C montrent que le mélangeur MaCROS est plus adapté pour des observations à grands taux de remplissage. Un glissement à la paroi a été observé avec le SBR A à faible taux de remplissage. Les vitesses de stabilisation ont été déterminées avec le SBR B. On trouve un comportement d'écoulement du SBR B similaire à celui du fluide silicone. Une analyse des vitesses de stabilisation n'a pas pu être effectuée à cause de l'incertitude sur la rhéologie du fluide en raison du mauvais contrôle de la température.



## Chapter 5

# Influence of adhesion energy on free surfaces during shear flow

### Contents

---

5.1. Probe tests .....	150
5.1.1. Rubber products .....	150
5.1.2. Silicone fluid .....	154
5.2. Modelling the steady state flow observations .....	157
5.2.1. Adhesion model .....	157
5.2.2. Drag model .....	161
5.2.3. Drag model: Prediction of stabilization conditions .....	163
5.3. Finite element simulation of free surface profiles .....	166
5.3.1. Cimlib simulation: Newtonian case .....	166
5.3.2. Cimlib simulation: Non-Newtonian case .....	169
Conclusions .....	172

---

In the previous chapter, the MaCROS mixer was used to conduct steady state observations of the free surfaces of viscous fluids under shear flow. These observations showed no influence of the adhesion energy on the free surfaces. Perhaps, adhesion energies of large magnitudes could significantly influence the free surfaces of the fluid under shear flow. However, we were unable to test this hypothesis experimentally within the framework of this PhD. Numerical models can be used to simulate these steady state flow observations. The adhesion energy of the fluid can be varied numerically to study the influence of adhesion energy on shear flow.

In this chapter, probe tests were carried out on the silicone fluid and the rubber products. These tests were conducted to determine the order of magnitude of the adhesion energy exhibited by these fluids. An adhesion model was proposed to model the steady state flow in the MaCROS mixer and estimate the adhesion energy exhibited by the fluids. A drag model was used to take into account the drag caused by the lateral movement of the transparent windows. This model provides corrections to the adhesion model and can be used to predict the stabilization velocities. Finally, a finite element analysis was carried out on the steady state observations with the MaCROS mixer using the Cimlib software. This was used to estimate the energy required to generate a loss of contact with the cylinder surfaces during shear flow. The adhesion energy of the fluid was varied to investigate its role during shear flow.

### 5.1. Probe tests

#### 5.1.1. Rubber products

##### Instron apparatus: sphere-plane geometry

The adhesion energies of the rubber products were characterized at 40, 60 and 80°C using the sphere-plane geometry. A compression force of 50 N was imposed on the samples for a contact time of 2.5s. At the end of the compression cycle, a tensile speed of 5 mm/s was imposed and the tensile response was measured. The tensile response of BR A at 80°C with the plane-plane geometry using Instron apparatus is presented in Figure 5.1.

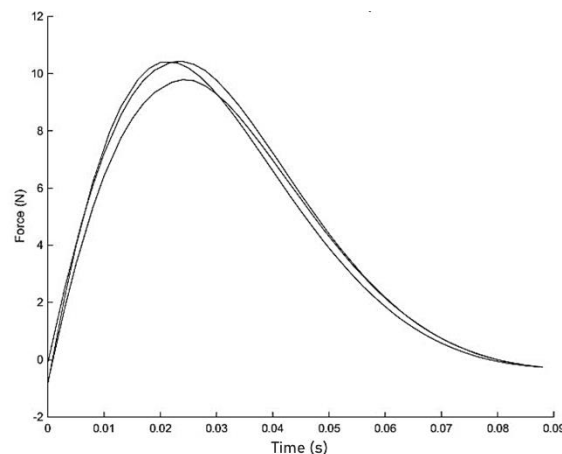


**Figure 5.1** – Tensile response of BR A at 80°C with the sphere-plane geometry using Instron apparatus.

From Figure 5.1, a typical normal distribution (bell curve) is observed indicating adhesive failure [Abbott, 2015]. Similar to BR A, adhesive failure was also observed with the other rubber products at 40, 60 and 80°C. The area under the Force vs Time curve gives us the adhesion energies (Equation 2.14). To ensure the consistency of the tack results, the tack experiments were replicated four times. The average adhesion energies of the rubber products at 40, 60 and 80°C are presented in Table 5.1.

Fluid	Temperature (°C)	Tensile force (N)	Adhesion energy (J/m <sup>2</sup> )	Standard deviation (J/m <sup>2</sup> )
BR A	40	11	82	35
	60	10	41	16
	80	10	44	15
SBR A	40	31	81	6
	60	29	63	4
	80	28	118	17
SBR B	40	28	185	28
	60	26	244	35
	80	24	198	25
SBR C	40	59	656	137
	60	32	478	65
	80	23	222	5

**Table 5.1** – Adhesion energy of the rubber products at various temperatures obtained with sphere-plane geometry using Instron apparatus.

The adhesion energies of the pure rubber products with the plane-plane geometry at different temperatures are generally ranked in the decreasing order of molecular weights. In order to estimate the adhesion energy of the rubber products at 100°C, we use the prediction technique described in Chapter 1.5.2. The adhesion energies of BR A, SBR A, SBR B and SBR C with the plane-plane geometry (100°C) and the sphere-plane geometry (40°C, 60°C and 80°C) are plotted in Figure 5.2, 5.3, 5.4 and 5.5.

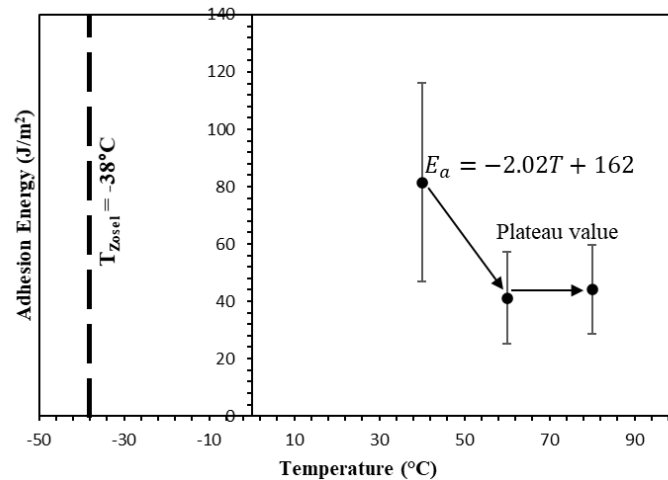


**Figure 5.2** – Adhesion energies of BR A obtained with sphere-plane using Instron apparatus.

From Figure 5.2, two different trends were observed: i) a linear trend where the adhesion energy decreases from 40 to 60°C and ii) a plateau like trend where the adhesion energy is almost constant from 60 to 80°C. We can assume that up to temperatures of 60°C, BR A exhibits Zone 3 behavior and that above 60°C, it exhibits Zone 4 behavior. The Zone 3 behavior can be fitted with a linear thermodependent law:

$$E_a = -2.02T + 162 \quad \text{Equation 5.1}$$

where  $E_a$  is the adhesion energy and  $T$  is the temperature of the experiment.

As for the terminal zone (Zone 4), the adhesion energy at 100°C must correspond to a plateau value. This value is obtained by the average of the adhesion energy at 60 and 80°C, which provides us with an adhesion energy of 42.7 J/m<sup>2</sup> for BR A at 100°C.

Strangely, the adhesion energies of SBR A at 40 and 60°C are lower than those at 80°C. This can only be explained by SBR A exhibiting a Zone 4 behavior at these temperatures as no clear dependence in temperature (similar to Zone 3) can be observed here. The data from 40 to 80°C can be assumed to be on either side of a plateau value (Figure 5.3). Thus, the average of the adhesion energies at 40, 60, 80 and 100°C gives us the plateau value. This provides us with an adhesion energy of 87.5 J/m<sup>2</sup> for SBR A at 100°C.

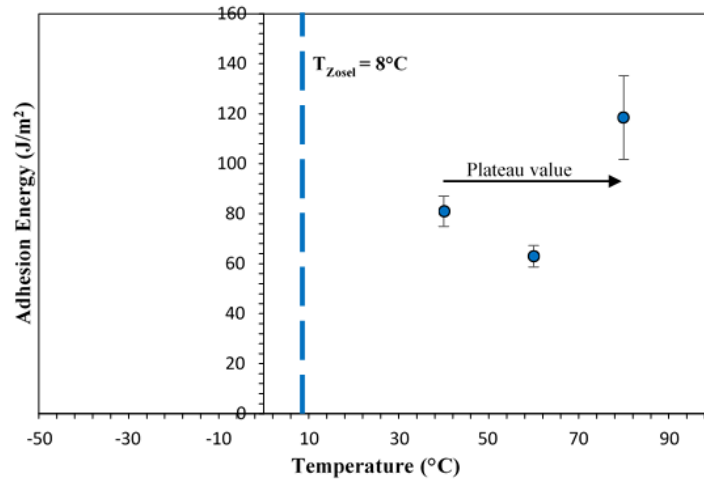


Figure 5.3 – Adhesion energies of SBR A obtained with sphere-plane using Instron apparatus.

Figure 5.4 shows that SBR B exhibits a Zone 4 behavior from 40 to 100°C. The pure rubber products are all found to exhibit Zone 4 behavior as they are far from their Zosel temperature at 100°C. This trend is quite doubtful for SBR B as the fluid exhibits a plateau like behavior at 40°C when the Zosel temperature is 22°C. Nevertheless, the plateau gives us an adhesion energy of 209.2 J/m<sup>2</sup> for SBR B at 100°C.

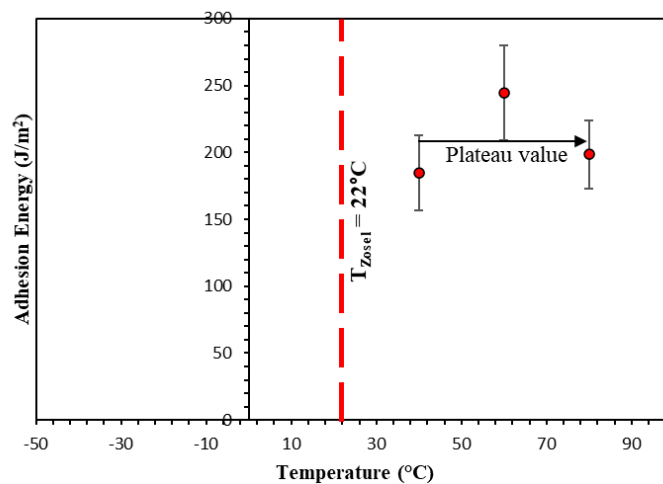


Figure 5.4 – Adhesion energies of SBR B obtained with sphere-plane using Instron apparatus.

SBR C exhibits Zone 3 behavior from 40 to 80°C (Figure 5.5). A sharp decline in adhesion energy is observed from 40 to 80°C. This strong dependence with temperature explains why SBR C exhibits a lower adhesion energy than SBR B at 100°C (Table 5.1). The Zone 3 behavior of SBR C can be fitted with a linear thermodependent law (Equation 5.2). This thermodependent law gives us an adhesion energy of 18 J/m<sup>2</sup> for SBR C at 100°C. This magnitude seems to be uncharacteristically small for SBR C. This might be due to its stark thermodependent behavior above the Zosel temperature.

$$E_a = -10.86T + 1104 \quad \text{Equation 5.2}$$

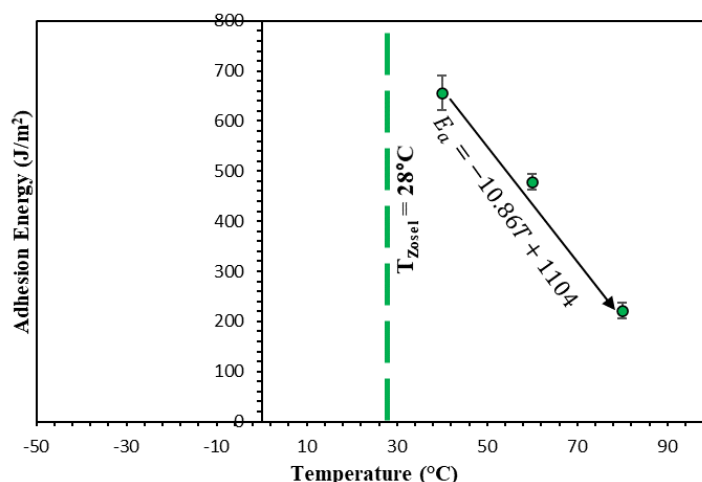


Figure 5.5 – Adhesion energies of SBR C obtained with sphere-plane using Instron apparatus.

Instron apparatus: plane-plane geometry.

Tack tests were carried out on the rubber products at 100°C, the reference temperature of the rheological characterization, using the Instron apparatus. The tack experiments with the sphere-plane geometry were conducted under similar conditions as the experiments with the plane-plane geometry (Compression force = 50 N, Contact time = 5s and Tensile speed = 5 mm/s). Similar to the experiments with the sphere-plane geometry, adhesive failure was observed with the different rubber products at the different temperatures. The average adhesion energy determined for the rubber products at 100°C, and their standard deviation, are presented in Table 5.2.

Fluid	Tensile Force (N)	Adhesion Energy (J/m <sup>2</sup> )	Standard deviation (J/m <sup>2</sup> )
BR A	21	29	7
SBR A	66	107	31
SBR B	60	204	56
SBR C	28	179	46

Table 5.2 – Adhesion energy of the rubber products at 100°C with the plane-plane geometry using Instron apparatus.

The rubber products were found to exhibit relatively low adhesion energies at 100°C ( $\leq 200$  J/m<sup>2</sup>). Among the pure rubber products, SBR B exhibits the highest adhesion energy followed by SBR A and finally by BR A. Similar to previous works [Akram *et al.*, 2013; Galliano *et al.*, 2003; Jenkins *et al.*, 2013], the adhesion energies of the pure rubber products were found to be ranked in the order of decreasing molecular weights. The rubber compound, SBR C, exhibits lower adhesion energy than SBR B. This was surprising as the formulation of SBR C was tailored to provide high adhesion energies at high temperatures. Table 5.3 compares the adhesion energies obtained for the rubber products at 100°C with the plane-plane geometry and sphere-plane geometry.

Fluid	Adhesion energy at 100°C (J/m <sup>2</sup> )	
	Sphere-plane geometry	Plane-plane geometry
BR A	43	29
SBR A	87	107
SBR B	209	204
SBR C	18	179

Table 5.3 – Adhesion energy of the rubber products at 100°C obtained with the sphere-plane and plane-plane geometry.

The adhesion energy values obtained from both methods were found to be comparable except for SBR C. The low adhesion energy of SBR C obtained with the sphere-plane geometry can be explained by

SBR C exhibiting a Zone 4 like behavior above 80°C. As a result, the extrapolation technique used for the sphere-plane geometry could not accurately predict its adhesion energy at 100°C.

This method of predicting adhesion energies is not classical. To obtain accurate results, it is better to carry out direct experiments at the desired temperature. However, the objective of this exercise is not to accurately quantify the adhesion energy of the rubber products but rather to estimate their order of magnitude without the use of a backing layer. In an internal mixer, the temperature of the rubber products can easily rise above 100°C. At these temperatures, the rubber products are often in the terminal section of the Zosel curve and thus exhibit typically low adhesion energies. From Table 5.3, we can expect the rubber products to exhibit adhesion energies of the order of less than a few hundreds of J/m<sup>2</sup> at these temperatures. Thus, we consider the adhesion energies characterized by the plane-plane geometry as the actual adhesion energy values of the rubber products.

### 5.1.2. Silicone fluid

The adhesion energy of the silicone fluid was characterized with the help of the Zwick apparatus at ambient temperature. Tack tests were conducted for different contact times, compression speeds, contact substrates and tensile speeds to study their influence on the adhesion energy of the fluid. During the steady state observations with the MaCROS mixer, the fluid experiences high local speeds of the order of 4 to 32 mm/s at the metal-fluid interfaces. High tensile speed experiments (5 – 15 mm/s) were conducted to work at similar speeds. Low tensile speed experiments (0.05 – 0.25 mm/s) were conducted to encourage cohesive contact failure with the substrate. The force response of the silicone fluid at low and high tensile speeds is presented in Figure 5.6.

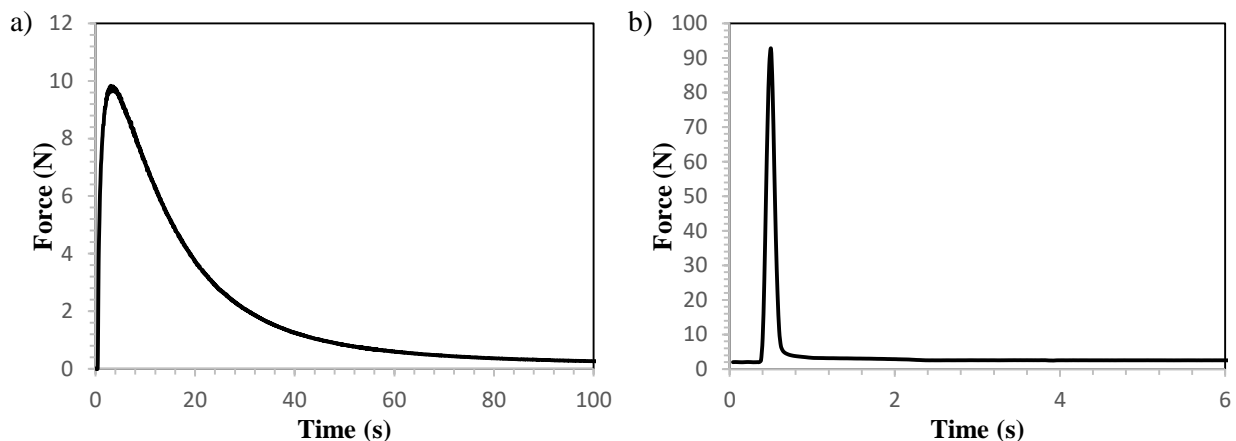


**Figure 5.6** – Force response of the silicone fluid at a) low (5 mm/min or 0.08 mm/s) and b) high tensile speeds (300 mm/min or 5 mm/s).

The force response of the silicone fluid at high tensile speeds (Figure 5.6b) is typical of a brittle or adhesive contact failure, characterized by a sharp maximum at low strains/times [Shull and Creton, 2004; Zosel, 1989a; Zosel 1989b; Lakrout *et al.*, 1999]. This was confirmed by the fluid separating from the substrate without leaving any visual residue. On the other hand, at low tensile speeds (Figure 5.6a), a cohesive fracture occurs within the adhesive layer and the debonding process is dominated by viscous flow [Poivet *et al.*, 1999]. At these speeds, the presence of fibrils and residues on the substrate after rupture confirms cohesive failure. Thus, two types of contact failure could be obtained with the silicone fluid by varying the tensile speeds.

The influence of the parameters on the adhesion energy of the fluid was studied at low tensile speeds (Figure 5.7). The silicone fluid was found to exhibit low adhesion energies (< 30 J/m<sup>2</sup>) under cohesive failure conditions. It was found that the parameters did not influence the adhesion energy significantly. With the Zwick apparatus, short contact times (< 60 s) could not be achieved and the experiments were conducted at contact times of 60 and 120 s (Figure 5.7a). At such long contact times, the influence of adhesion saturates [Lai and Meng, 2017]. The substrate surface (Figure 5.7b) and

compression speed (Figure 5.7c) did not have a marked influence on the adhesion energy. This can be attributed to the weak adherence exhibited by the fluid which is insignificant to study the influence of these parameters.

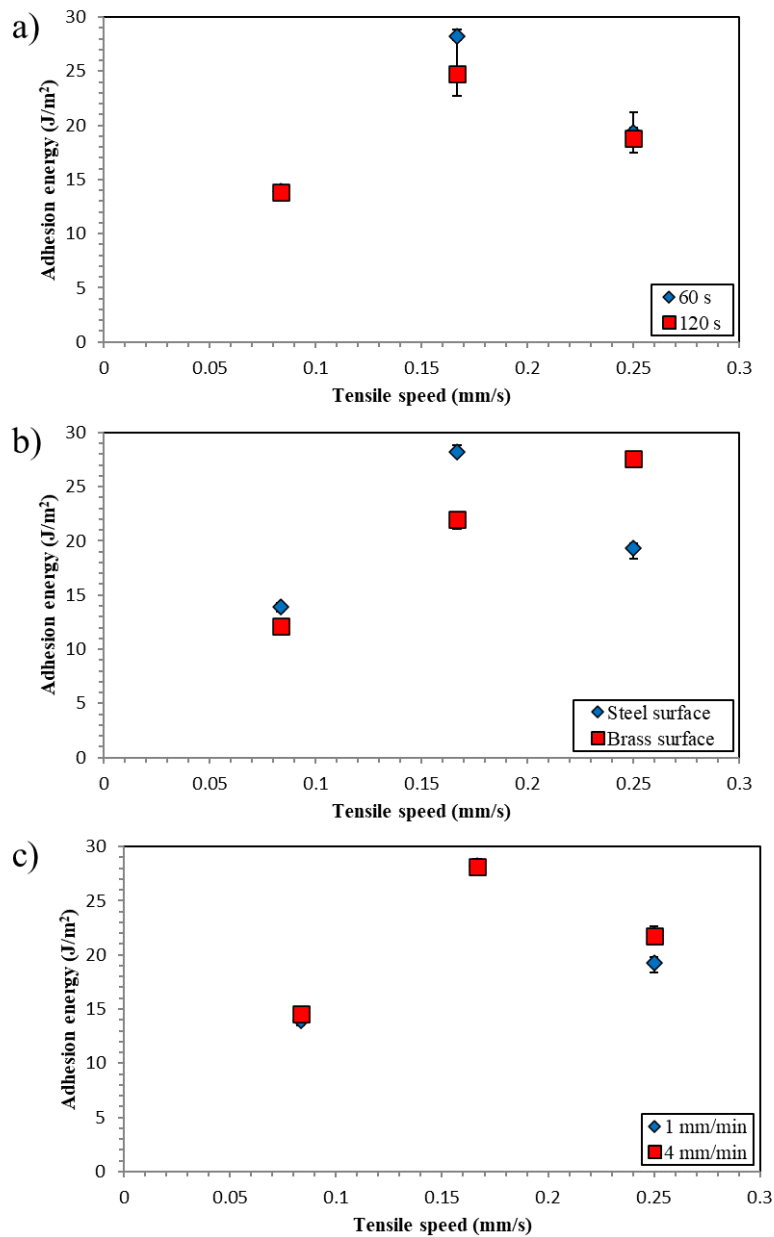


**Figure 5.7** – Adhesion energy of the silicone fluid at low tensile speeds and ambient temperature for different a) contact times, b) contact substrates and c) compression speeds.

At high tensile speeds (Figure 5.8), the silicone fluid exhibits slightly higher adhesion energies of the order of 30 – 50 J/m<sup>2</sup>. In Table 5.4, the adhesion energies of the fluids at their service temperature are compared with their corresponding peak angles ( $\theta_{\text{peak}}$ ) from the Monocuve flow observations (Table 4.4). The average adhesion energy of the silicone fluid at high tensile speeds (43 J/m<sup>2</sup>) was used for this comparison. We find that the fluids with inferior adhesion energies such as silicone fluid, BR A and SBR A exhibit symmetric free surfaces ( $\theta_{\text{peak}} \approx 90^\circ$ ). On the other hand, SBR B and SBR C exhibit asymmetric free surfaces ( $\theta_{\text{peak}} \approx 80^\circ$ ) and this can be attributed to their superior adhesion energies. Thus, an increase of 100-150 J/m<sup>2</sup> in adhesion energy can influence the free surfaces of the rubber products in conditions of dissimilar surface contact (adhesive contact on one end and cohesive contact on the other).

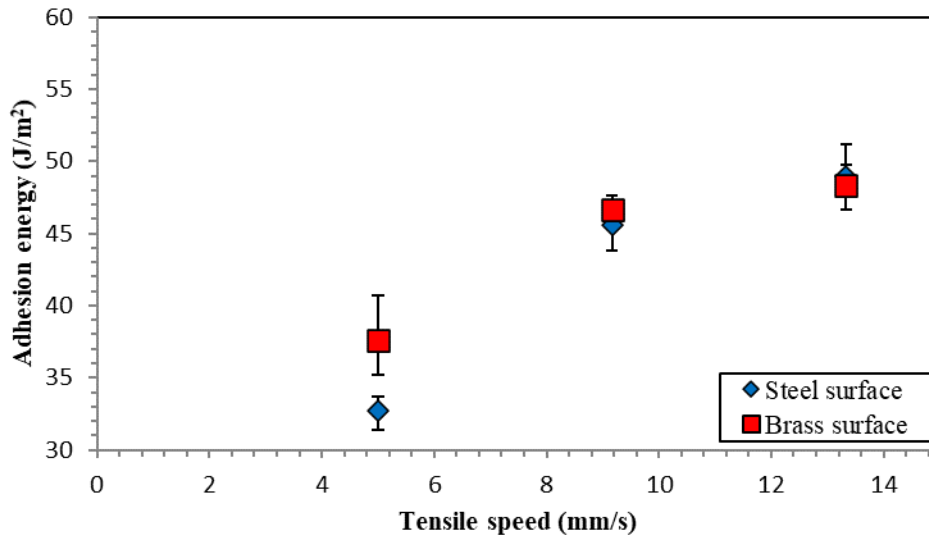


Figure 5.8 – Adhesion energy of the silicone fluid at ambient temperature and at high tensile speeds.

Fluid	Service temperature	Adhesion energy (J/m <sup>2</sup> )	Peak angle, $\theta_{peak}$ , (°)
Silicone fluid	Ambient temperature	43	91.5
BR A	100°C	29	94.9
SBR A	100°C	107	89.7
SBR B	100°C	204	78.2
SBR C	100°C	200	81.6

Table 5.4 – Adhesion energy of fluids and their corresponding peak angles measured during Monocuve flow observations.

The asymmetry of the free surfaces during mixing under dissimilar surface contact conditions cannot be simply related to the adhesion energy. Other factors, notably the pressure distribution can also play a role in the form of the free surfaces. Let us consider the peak angles measured for SBR C at different temperatures during Monocuve mixer observations (Table 4.3). These peak angles are compared with their corresponding adhesion energies (Table 5.5). Previously, we found that a superior adhesion energy of 100 – 150 J/m<sup>2</sup> was sufficient to influence the form of the free surface, yet in Table 5.5, we find that an increase in adhesion energy of 400 J/m<sup>2</sup> has no impact on the form of the free surfaces. Hence, further studies are required to investigate the role of adhesion during mixing under dissimilar surface contact condition.

Temperature, (°C)	Adhesion energy (J/m <sup>2</sup> )	Peak angles, $\theta_{peak}$ , (°)
40	656	80.1
70	478	78.7
100	222	81.6

Table 5.5 – Peak angles of SBR C compared with its corresponding adhesion energy at different temperatures in the Monocuve mixer (2 rpm, 25% volume fill factor).

Though Table 5.4 shows that adhesion energy can influence the contact lines, their influence on the shear flow of viscous fluids is insignificant. The adhesive and rheological behavior of the fluids can be used to make a rough estimate of this influence. This is achieved by calculating the theoretical displacement caused by the adhesion energy on the fluid. The theoretical displacement of the fluid caused by their adhesion energy at a shear rate of 15 s<sup>-1</sup> is presented in Table 5.6. This displacement is insignificant and of the order of a few microns. Thus, the role of adhesion energy during viscous flow is often neglected.

Fluid	Adhesion energy at service temperature (J/m <sup>2</sup> )	Theoretical displacement (μm) at 15 s <sup>-1</sup>
Silicone fluid	43	49
BR A	29	6
SBR A	107	16
SBR B	204	60
SBR C	179	85

Table 5.6 – Theoretical displacement caused by the adhesion energy of the fluids at 15 s<sup>-1</sup>.

## 5.2. Modelling the steady state flow observations

During the stabilization experiments with the MaCROS mixer, the fluid is stabilized due to the rotation of the cylinders and the transparent windows. Under these conditions, the flow rate can be considered to be close to zero. However, in our study, the net force provided by the rotation of the cylinders and the windows on the fluid is non-zero. We can assume that this difference in energy is due to the adhesion energy exhibited by the fluid which balances the forces, resulting in stabilization of the fluid. An adhesion model is proposed to obtain a numerical estimation of the adhesion energy exhibited by the fluid during shear flow in the MaCROS mixer. The outputs obtained from the stabilization experiments are the 2D projection of the fluid and the stabilization velocities. The model uses these outputs to estimate the numerical adhesion energy.

### 5.2.1. Adhesion model

Figure 5.9b represents the cylinder surfaces and the 2D projection of the stabilized fluid plotted on a Cartesian coordinate system. The thickness of the flow channel in the vertical direction ( $h$ ) varies with the abscissa  $x$  along the flow channel (Figure 4.34). The thickness of the flow channel ( $h(x)$ ) can be represented as a function of its position along the outer cylinder surface. Equation 4.3 gives us the variation of thickness with the local position  $\theta$  (Figure 4.34). The thickness,  $h(x)$  can be expressed as the difference between the ordinates of each corresponding point on circles  $C_1$  (outer cylinder) and  $C_2$  (inner cylinder).

$$C_1: y = R_1 - (R_1^2 - x^2)^{0.5} \quad \text{Equation 5.3}$$

$$C_2: y = (h_0 + R_2) - (R_2^2 - x^2)^{0.5} \quad \text{Equation 5.4}$$

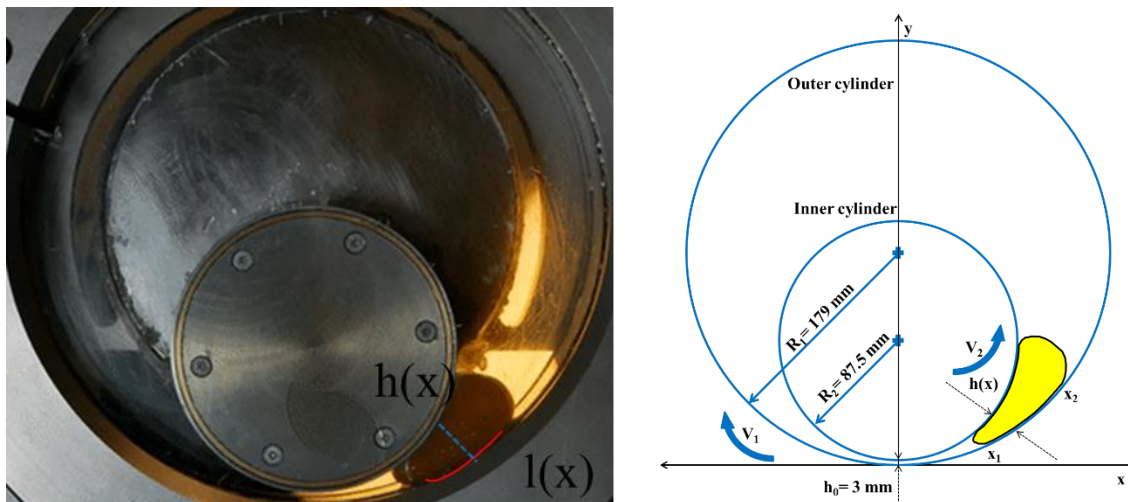


Figure 5.9 – a) Steady state observations of the silicone fluid under shear flow, b) 2D representation of the fluid under shear flow with the outer cylinder surface at the thin flow gap as the point of reference.

Thus,

$$h(x) = h_0 + R_2 \left( 1 - \sqrt{1 - \left(\frac{x}{R_2}\right)^2} \right) - R_1 \left( 1 - \sqrt{1 - \left(\frac{x}{R_1}\right)^2} \right) \quad \text{Equation 5.5}$$

Assuming that  $\frac{x}{R_i} \ll 1$ , Equation 5.5 can be linearized to get:

$$h(x) = h_0 + \frac{1}{2} \left( \frac{1}{R_2} - \frac{1}{R_1} \right) x^2 \quad \text{Equation 5.6}$$

The term  $\frac{h_0}{2} \left( \frac{1}{R_2} - \frac{1}{R_1} \right)$  is significantly small (typically  $1.7 \cdot 10^{-2}$ ) and can be replaced by  $\varepsilon^2$  which can be represented as:

$$\varepsilon^2 = \frac{h_0}{2} \left( \frac{1}{R_2} - \frac{1}{R_1} \right) \ll 1 \quad \text{Equation 5.7}$$

and finally:

$$h(x) = h_0 \left( 1 + \left( \frac{\varepsilon x}{h_0} \right)^2 \right) \quad \text{Equation 5.8}$$

In the following, we will consider that  $h(x) = h_0$ .

When using the Hele-Shaw equation, the flow rate due to the pressure driven flow ( $Q_P$ ) for a Newtonian fluid of viscosity  $\eta$  is given by:

$$Q_P = -\frac{Wh_0^3}{12\eta} \nabla P \quad \text{Equation 5.9}$$

where  $W$  is the width of the flow channel,  $\eta$  is the viscosity of the fluid and  $\nabla P = \frac{\partial P}{\partial x}$ . Equation 5.9 comes from the integration on  $y$  of the momentum equation projected on to  $x$ :

$$\frac{\partial}{\partial y} \left( \eta \frac{\partial u}{\partial y} \right) = \nabla P \quad \text{Equation 5.10}$$

The displacement provided by the rotating cylinders contributes to the total flow rate and the shear rate, which modifies the viscosity for power-law fluids. The flow rate due to the rotating cylinder surfaces ( $Q_D$ ) is given by:

$$Q_D = \frac{WV_a h_0}{2} \quad \text{Equation 5.11}$$

where  $V_a$  is the net advancing velocity of the fluid. The advancing velocity of the fluid,  $V_a$ , can be presented as:

$$V_a = \frac{(V_1 + V_2)}{2} \quad \text{Equation 5.12}$$

Let us notice that this value ( $V_a$ ) is zero when both cylinders rotate at the same velocity in opposite directions. Equally, we can also define the global shear rate ( $\dot{\gamma}_0$ ) as:

$$\dot{\gamma}_0 = \frac{(V_2 - V_1)}{h_0} \quad \text{Equation 5.13}$$

When the pressure gradient is zero, the velocity field is a simple shear flow that can be approximated at the leading order by a flow between ordinates 0 and  $h_0$ :

$$u_0(y) = V_2 \frac{y}{h_0} - V_1 \frac{y - h_0}{h_0} \quad \text{Equation 5.14}$$

The flow induced by the pressure gradient is assumed to be small compared to  $u_0$  so that a small perturbation  $u_1$ , vanishing at the walls, can be added to the total velocity field  $u$ :

$$u(y) = u_0(y) + u_1(y) \quad \text{Equation 5.15}$$

Linearizing equation 5.10 and taking a power-law model leads to:

$$\frac{\partial}{\partial y} \left( K \left( \frac{\partial u}{\partial y} \right)^m \right) = \frac{\partial}{\partial y} \left( K \left( \dot{\gamma}_0 + \frac{\partial u_1}{\partial y} \right)^m \right) \quad \text{Equation 5.16}$$

$$\frac{\partial}{\partial y} \left( K \left( \frac{\partial u}{\partial y} \right)^m \right) = \frac{\partial}{\partial y} \left( K \dot{\gamma}_0^m \left( 1 + \frac{1}{\dot{\gamma}_0} \frac{\partial u_1}{\partial y} \right)^m \right) \quad \text{Equation 5.17}$$

$$\frac{\partial}{\partial y} \left( K \left( \frac{\partial u}{\partial y} \right)^m \right) = K \dot{\gamma}_0^m \frac{\partial}{\partial y} \left( 1 + \frac{m}{\dot{\gamma}_0} \frac{\partial u_1}{\partial y} \right) \quad \text{Equation 5.18}$$

$$\frac{\partial}{\partial y} \left( K \left( \frac{\partial u}{\partial y} \right)^m \right) = m K \dot{\gamma}_0^{m-1} \frac{\partial^2 u_1}{\partial y^2} \quad \text{Equation 5.19}$$

$$\frac{\partial}{\partial y} \left( K \left( \frac{\partial u}{\partial y} \right)^m \right) = \nabla P \quad \text{Equation 5.20}$$

which gives, after integration, the flow rate induced by the pressure drop:

$$Q_{P1} = - \frac{W h_0^3}{12 m K \dot{\gamma}_0^{m-1}} \nabla P \quad \text{Equation 5.21}$$

As the experiments are conducted in steady state conditions, the net flow rate must be equal to zero.

$$Q = Q_D + Q_{P1} = 0 \quad \text{Equation 5.22}$$

$$Q = \frac{W V_a h_0}{2} - \frac{W h_0^3}{12 m K \dot{\gamma}_0^{m-1}} \nabla P = 0 \quad \text{Equation 5.23}$$

which can be simplified as:

$$h_0^2 \nabla P = 6 m \eta_0 V_a \quad \text{Equation 5.24}$$

where  $\eta_0 = K \dot{\gamma}_0^{m-1}$ . The dewetting of the fluid at the cylinder surfaces induces a traction on the fluid sample, modelled as a negative pressure across the thickness of the flow channel. We will later assume that this negative pressure imposes a pressure driven flow on the fluid. The pressure across the thickness of the flow channel is given, at each end of the flow sample, by:

$$P_i = \frac{-E_i}{h_0} \quad \text{Equation 5.25}$$

where  $E_i$  is the adhesion energy of the fluid on the corresponding cylinder ( $i=1$ : rotor,  $i=2$ : cuve). Defining the sample length as  $l_0 = x_2 - x_1$ , the pressure gradient can then be approximated by:

$$\nabla P = \frac{E_2 - E_1}{h_0 l_0} \quad \text{Equation 5.26}$$

Finally, substituting Equation 5.25 in Equation 5.24, one gets:

$$E_2 - E_1 = 6m\eta_0 \frac{l_0}{h_0} V_a \quad \text{Equation 5.27}$$

Equation 5.27 gives us the difference of the adhesion energy between the two cylinder surfaces exhibited by the fluid during the steady state shear flow. The length of the fluid under shear flow  $l_0$  and the thickness of the fluid  $h_m$  are obtained from the experimental observations. As shown in Figure 5.9, the length of the fluid under shear flow is measured by measuring the length of contact of the fluid with the outer cylinder surface. As for the thickness of the fluid under shear flow, taking  $h_0$  provides superior values of the difference of adhesion energies. However, the experimental thickness is calculated from the median position of the stabilized fluid, which on average, varies from  $h_0$  by a factor of 2.8, which shows the limit of our approximation. Using these values ( $h_m$ ), the difference in adhesion energy between the surfaces is calculated for the silicone fluid under different conditions of nature and surface roughness of the cylinders.

The difference in adhesion energy between the cylinder surfaces ( $\Delta E$ ) for different conditions of cylinder velocities, volume and surface conditions are presented in Appendix XIV. Figure 5.10 presents the difference in adhesion energy between the cylinders surfaces for different surface conditions. On comparing the average difference in adhesion energy values, we find that a change in surface roughness or nature of surface has no impact within the limit of the tested conditions. Also, the obtained  $\Delta E$  values were found to be too disperse to draw out any conclusions. The magnitude of the  $\Delta E$  values was found to be significantly higher than the adhesion energy of the silicone fluid. Clearly, the stabilization velocities are dependent on another factor such as the viscous dissipation in the bulk volume. This factor can also be the lateral displacement provided by the rotating windows of the MaCROS mixer. Thus, a drag model was defined to take into account the displacement exerted by the windows.

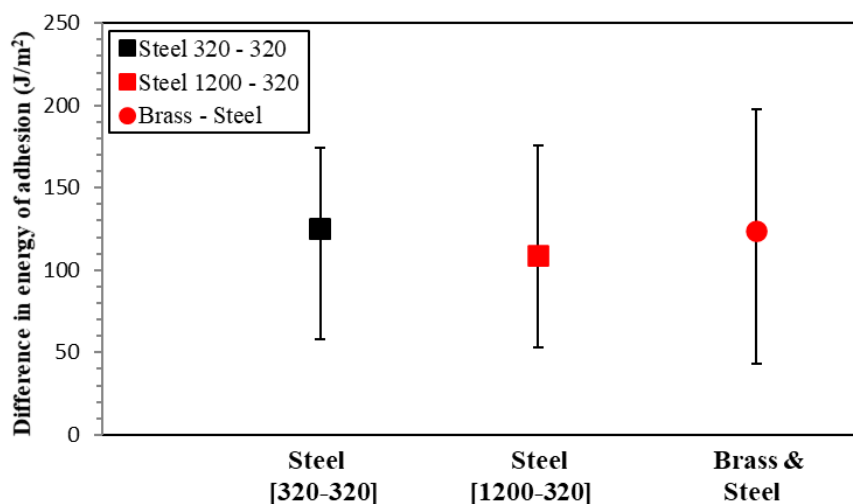
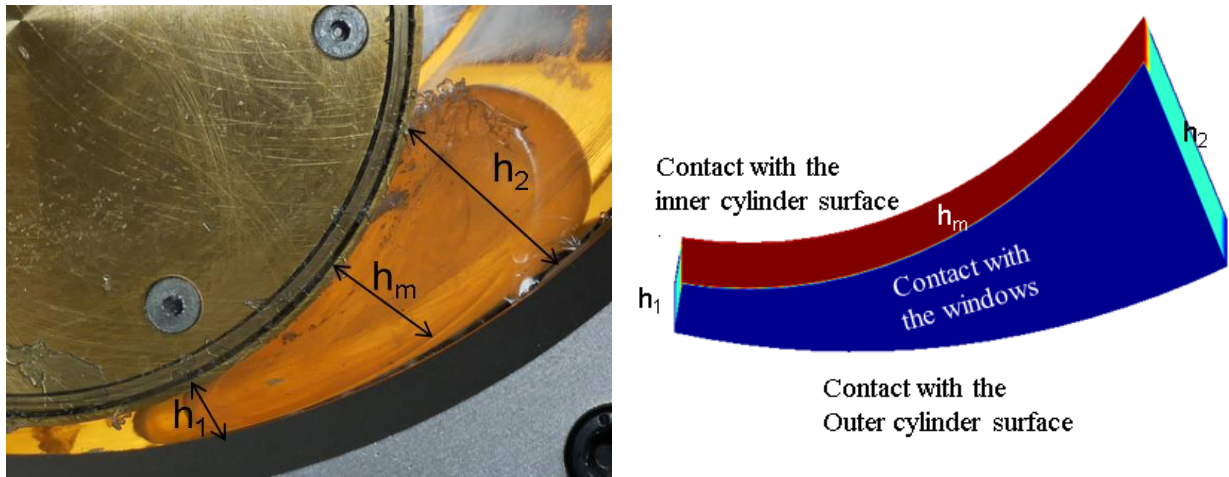


Figure 5.10 – Difference in adhesion energy estimated for the silicone fluid under different conditions of nature and surface roughness of the cylinder surfaces.

### 5.2.2. Drag model

A MATLAB® code was used with a PDE (Partial Differential Equations) solver to investigate the effect of the rotation of the windows of the MaCROS mixer on the flow rate and the  $\Delta E$  values estimated with the adhesion model. The estimation of the net flow rate due to the drag flow and pressure driven flow across flow channels of finite width was tackled by Tadmor and Klein [Tadmor and Klein, 1970]. They were able to estimate constants  $F_D$  and  $F_P$  which calculate the contribution of drag and pressure flow respectively, according to the geometry of the flow channel. Later, efforts were made to fit these laws for Non-Newtonian flow behavior [White and Huang, 1981; Schenkel and Kühnle, 1981].

The fluid under shear flow was represented with a simplified 2D geometry of the fluid as shown in Figure 5.11, where flow direction was assumed to be orthonormal. The 2D projection of the stabilized fluid was used to define the geometry and the curves on either side of the stabilized fluid were neglected. The input variables of the drag model are the rheology of the fluid, the stabilization velocities ( $V_1$ ,  $V_2$ ), the length ( $l_0$ ) and the mean thickness ( $h_m$ ) of the stabilized fluid.



**Figure 5.11** – a) Steady state observations of the silicone fluid under shear flow. b) Geometry of the stabilized fluid as defined in the MATLAB® program.

The boundary conditions were defined so as to respect the conditions of the experiment. The rotational velocity of the inner cylinder ( $V_2$ ) was applied to the edge which corresponds to the surface of the stabilized fluid in contact with the inner cylinder surface. The rotational velocity of the outer cylinder ( $V_1$ ) was applied to the edges corresponding to the surfaces of the stabilized fluid which are in contact with the windows of the mixer and the outer cylinder surface. The viscosity of the silicone fluid was defined with a Carreau-Yasuda law, resulting in a generalized Poisson problem:

$$\frac{\partial}{\partial x} \left( \eta(\dot{\gamma}) \frac{\partial V}{\partial x} \right) = \frac{\partial P}{\partial x} \quad \text{Equation 5.28}$$

where  $V$  is the velocity field to compute,  $\dot{\gamma}$  the associated strain rate and  $\nabla P = \frac{E_2 - E_1}{h_0 l_0}$  as previously defined. The program was solved to obtain the net flow rate of the stabilized fluid across the flow channel.

The difference in surface energies between the cylinders and the windows can induce an adhesion driven flow. This pressure gradient ( $\nabla P_a$ ) is defined as:

$$\nabla P_a = \frac{\frac{E_2 - E_1}{h_m} - \frac{E_w}{W}}{l_0} \quad \text{Equation 5.29}$$

where  $t$  is the thickness of the MaCROS mixer and  $E_i$ ,  $E_o$ ,  $E_w$  are the surface energies of the inner cylinder, outer cylinder and the transparent windows respectively.

An example of the velocity field across the flow channel obtained with the MATLAB® program is presented in Figure 5.12. Due to the opposing direction of rotations of the cylinder surfaces, the flow rate near the inner cylinder surface is at its maximum while the flow rate near the outer cylinder surface is at its minimum. The attainment of a 3D flow profile confirms the influence of the rotating windows of the MaCROS mixer. The 3D flow profile obtained with the drag model confirms the mechanism behind the 3D form of the fluid, as explained in Figure 4.26. Appendix XV presents the flow field obtained with the drag model for different cylinder velocities.

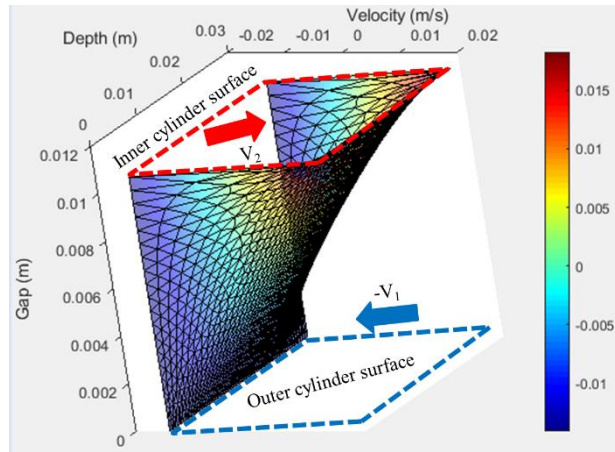


Figure 5.12 – Velocity field across the flow channel obtained with the MATLAB® program for the silicone fluid at  $\omega_2 = 3.9$  rpm and  $\omega_1 = 1.5$  rpm with Steel 320-320 surface condition.

The corrected advancing velocity ( $V_{num}$ ) of the stabilized fluid was obtained by integrating the net flow rate over the flow channel. The numerically obtained advancing velocity ( $V_{num}$ ) is plotted in function of the experimental advancing velocity in Figure 5.13. A linear dependence was found between these velocities. On taking into account the lateral movement of the transparent windows with the drag model, we obtain smaller advancing velocities i.e. advancing velocities closer to zero indicating a perfectly stabilized state. From Figure 5.13, we observe a slope of 0.3 on plotting the numerical and experimental advancing velocities.

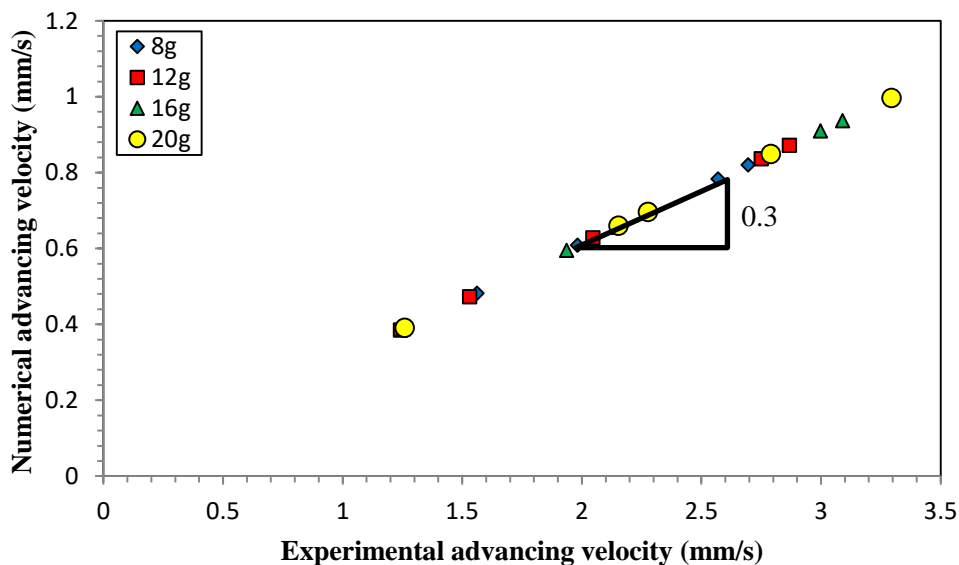
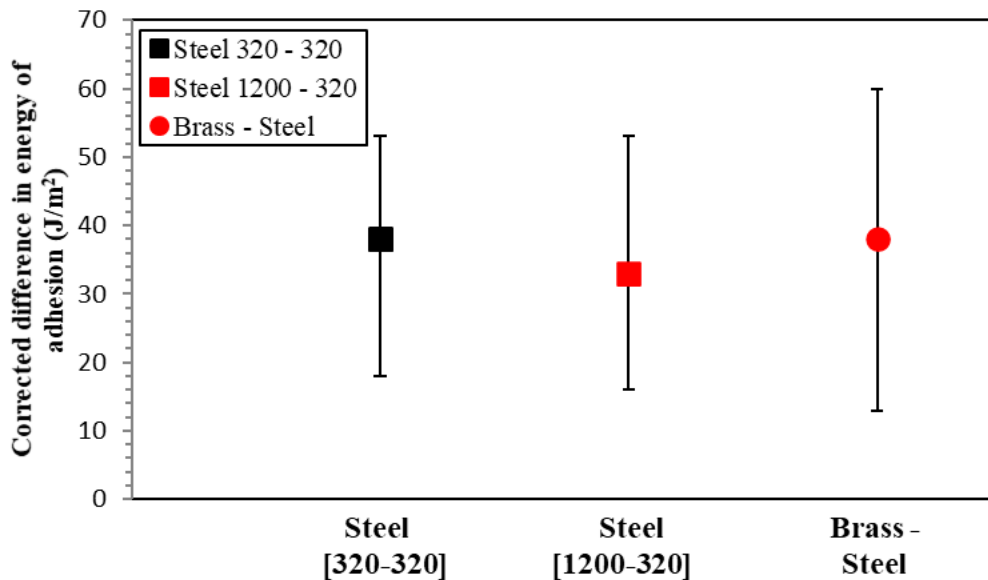


Figure 5.13 – Corrected advancing velocity plotted in function of their corresponding experimental advancing velocities.

The numerical advancing velocities were calculated for different conditions of cylinder velocities, volume and surface conditions. These values were used in Equation 5.27 to obtain the corrected estimations of the  $\Delta E$  values of the adhesion model. The corrected estimations of the  $\Delta E$  values for the silicone fluid for different conditions of cylinder velocities, volume and surface conditions are presented in Appendix XIV. Figure 5.14 presents the difference in adhesion energy under different surface conditions.



**Figure 5.14** – Corrected difference in adhesion energy estimated for the silicone fluid under different conditions of nature and surface roughness of the cylinder surfaces.

On comparing the average  $\Delta E$  values, no significant difference was observed for the different surface conditions. It appears that the surface properties and hence the adhesion of the fluid plays no role on the stabilization velocities of the fluid. The average  $\Delta E$  values for the Steel 320-320, Steel 1200-320 and Brass – Steel surface conditions are 38, 33 and 38 J/m<sup>2</sup>. In addition, a significant dispersion of the  $\Delta E$  values was observed. As a result, we are unable to conclude on the influence of the surface conditions on the estimated  $\Delta E$  values.

The average  $\Delta E$  values obtained at different surface conditions were found to be comparable to the adhesion energy of the silicone fluid obtained through tack experiments ( $\sim 45$  J/m<sup>2</sup> in average). Considering that the fluids undergo extensional flow, we can divide the adhesion energy by a factor of 3 to obtain the adhesion energy under shear ( $\sim 15$  J/m<sup>2</sup>). This shows that the estimated corrected difference in adhesion energy values ( $\Delta E$ ) are superior to the actual adhesion energy of the fluid by a factor of 2. The estimation of  $\Delta E$  values with the corrected adhesion model is not accurate and significantly disperse. Thus, the failure of the model indicates that the pressure driven flow due to adhesion provides a minor contribution to the difference in energy resulting from the rotation of the cylinders and windows. This difference in energy must be due to a stronger factor like the viscous dissipation in the bulk volume.

### 5.2.3. Drag model: Prediction of stabilization conditions

The drag model can also be used to predict the stabilization velocities in the MaCROS mixer. The cylinder velocities ( $V_1$  and  $V_2$ ) can be varied to identify cases where the net flow rate is zero. This can provide the stabilization velocities for new fluids without the need for carrying out the experiments. This prediction can depend on the dimensions of the stabilized fluid (length,  $l_0$  and mean thickness,  $h_m$ ). Their influence is investigated by varying the length and the mean thickness in Figure 5.15 and Figure 5.16 respectively.

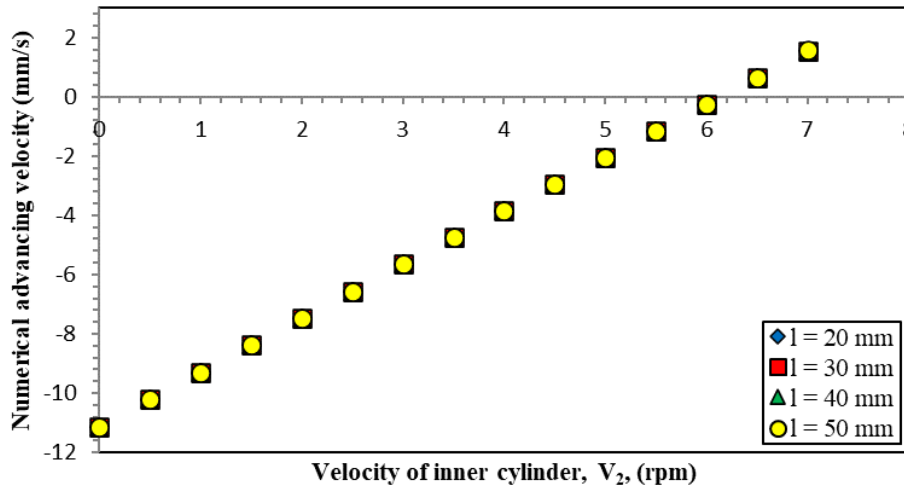


Figure 5.15 – Numerical advancing velocity in function of the velocity of the inner cylinder for different lengths of the stabilized fluid.

The length of the stabilized fluid does not influence the numerical advancing velocity. On the other hand, the thickness plays a more significant role (Figure 5.16). Shorter flow channels are found to provide higher advancing velocities. As the thickness increases, the contact area of the fluid with the windows also increases resulting in the fluid undergoing more drag. Thus, at larger thicknesses, the fluid undergoes more drag in the downstream direction providing smaller (or more negative) advancing velocities. Thus, the length of the stabilized fluid can be maintained as a constant for future estimations.

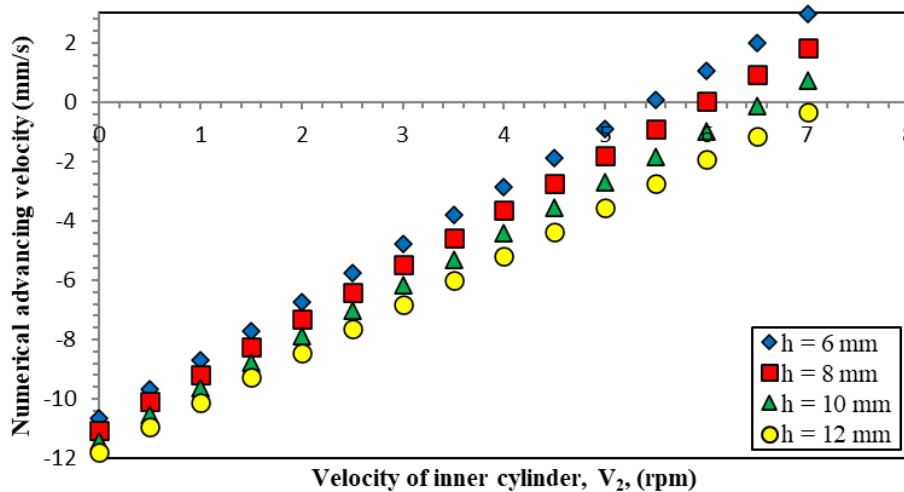


Figure 5.16 – Numerical advancing velocity in function of the velocity of the inner cylinder for different mean thicknesses of the stabilized fluid.

To determine the stabilization conditions, the thickness of the stabilized fluid ( $h_m$ ) is first defined. Then, one cylinder speed is maintained as constant ( $V_1$  in our example), while the other is varied. The numerical advancing velocity is obtained by varying the cylinder velocities and plotting them on a graph as shown Figure 5.17. Trend lines are drawn for each constant cylinder speed ( $V_1$  in our example) and the intercepts with the x-axis gives us the cases where the net flow is zero i.e. stabilized flow.

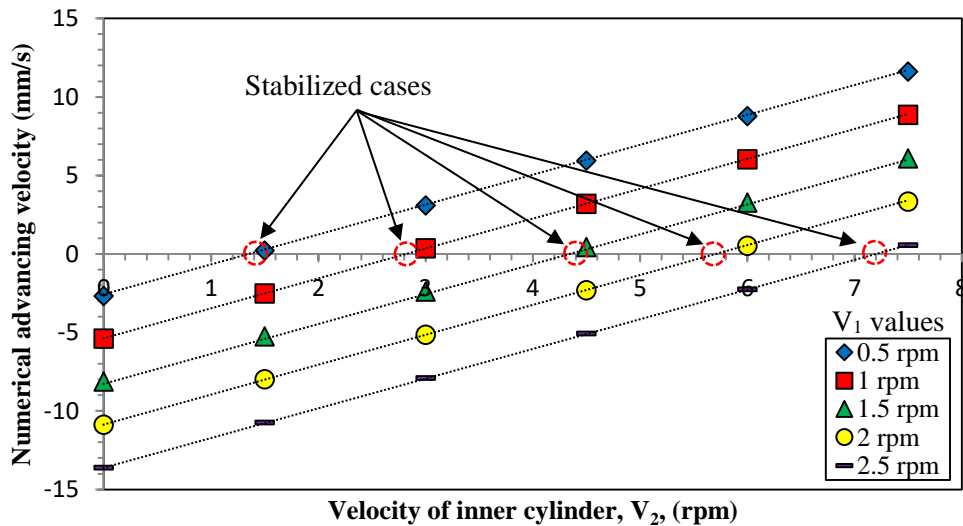


Figure 5.17 – Advancing velocity in function of velocity of inner cylinder for varying outer cylinder velocities.

For a given outer cylinder velocity, the inner cylinder velocity for stabilized cases is estimated using the drag model. The estimated inner cylinder velocities for different thicknesses are presented in Table 5.7.

Outer cylinder velocity, $V_1$ , (rpm)	Estimated inner cylinder velocity for stabilized cases, $V_{2num}$ , (rpm)		
	$h_m = 7$ mm	$h_m = 8.5$ mm	$h_m = 10$ mm
-0.5	1.39	1.48	1.58
-1	2.82	3.01	3.22
-1.5	4.27	4.57	4.88
-2	5.72	6.13	6.56
-2.5	7.19	7.70	8.25

Table 5.7 – Estimated inner cylinder velocities for stabilized cases obtained using the drag model.

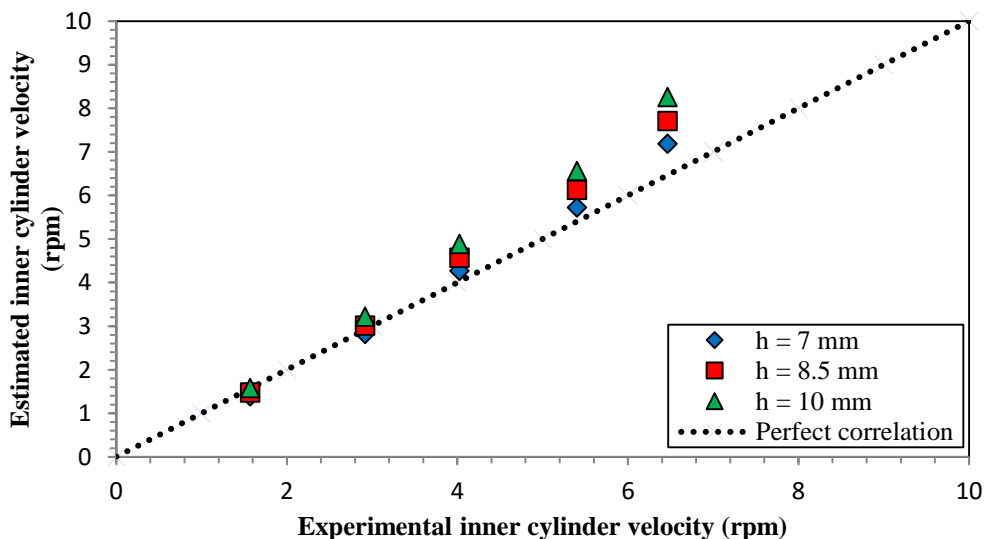


Figure 5.18 – Inner cylinder velocities estimated with the drag model in function of the experimental inner cylinder velocities under stabilized conditions for  $V_1 = -0.5, -1, -1.5, -2$  and  $-2.5$  rpm.

To determine the accuracy of the drag model, the experimental and numerical stabilization velocities were compared. Figure 5.18 plots the numerically estimated and experimental inner cylinder

velocities. The estimated inner cylinder velocities for different outer cylinder velocities ( $V_1 = -0.5, -1, -1.5, -2$  and  $-2.5$  rpm) was used in this comparison. These velocities were compared with the experimental inner cylinder velocities obtained during the Steel 320-320 surface condition experiments (Figure 4.30). The drag model estimations were found to have a fairly good correlation with the experimental data. However, the stabilization velocities are independent of the mean thickness ( $h_m$ ) during the experiments. Better precision was obtained with the drag model at smaller thicknesses where the effect of lateral drag by the windows diminishes. Thus, the drag model can serve as a fairly accurate tool to predict the stabilization conditions in the MaCROS mixer for new fluids.

### 5.3. Finite element simulation of free surface profiles

In the previous section, the adhesion and drag model showed that the attainment of stabilization conditions with the MaCROS mixer is dependent on the bulk rheology and not adhesion. In the MaCROS mixer, the free surfaces have a similar surface contact condition (adhesive contact on both ends of the free surfaces). In this section, the influence of adhesion energy on the free surfaces of the stabilized fluid is studied with the CIMLIB-CFD software. This is achieved by changing the adhesion boundary condition and observing the free surface of the stabilized fluid. A 2D flow was considered for the finite element simulations.

The computational approach was based on the Cimlib solver [Hachem *et al.*, 2016]. This solver is a parallel, finite element library that takes into account the air/fluid free surface as well as the rheological behaviour of the fluid. Gravity and surface tension of the fluid were neglected for all cases. The finite element simulations were carried out using a Variational MultiScale method (VMS). A level set function is a signed distance function from each interface that is advected with the computed velocity. In order to capture the fluid/air interface as a function of time, a level set method, which enables the localization and the capturing of interfaces, has been used.

Velocity and pressure fields are computed using a unified framework (by simply mixing the different fluids properties) where all the fluid occupies a single computational mesh. Smoothed heavyside functions which are built from each level set functions, take into account the discontinuities of viscosity ( $\eta$ ) through the interface. The motion of the solid bodies (inner and outer cylinders) was prescribed by directly assigning velocities to the nodes of the grid boundaries. This general solver has been successfully used in simulations of mixing processes [Valette *et al.*, 2009] or complex rheological tests [Valette *et al.*, 2019].

#### 5.3.1. Cimlib simulation: Newtonian case

To begin with, the simulation was carried out with a Newtonian fluid of 1 Pa.s. The geometry of the simulation is a 2D representation of the inner and outer cylinder. A vertical and horizontal symmetry condition is applied on the center of the inner cylinder. The fluid is introduced through the thin flow gap (Figure 5.19a).

Once the fluid is introduced, it starts to fill up the free volume of the geometry. A Poiseuille flow could be observed. To stop the flow at a certain position, an adhesion boundary condition is applied on the inner cylinder at a point on the inner cylinder, by simply imposing the value of the levelset field close to this point. The adhesion boundary condition imposes the free surface of the fluid to not move past this point on the inner cylinder surface during the simulation (Figure 5.19b). To introduce different volumes of fluid, the filled volume and then adhesion boundary condition can be applied on different points on the inner cylinder. Figures 5.19b and 5.19c show two different volumes imposed in the Cimlib simulation.

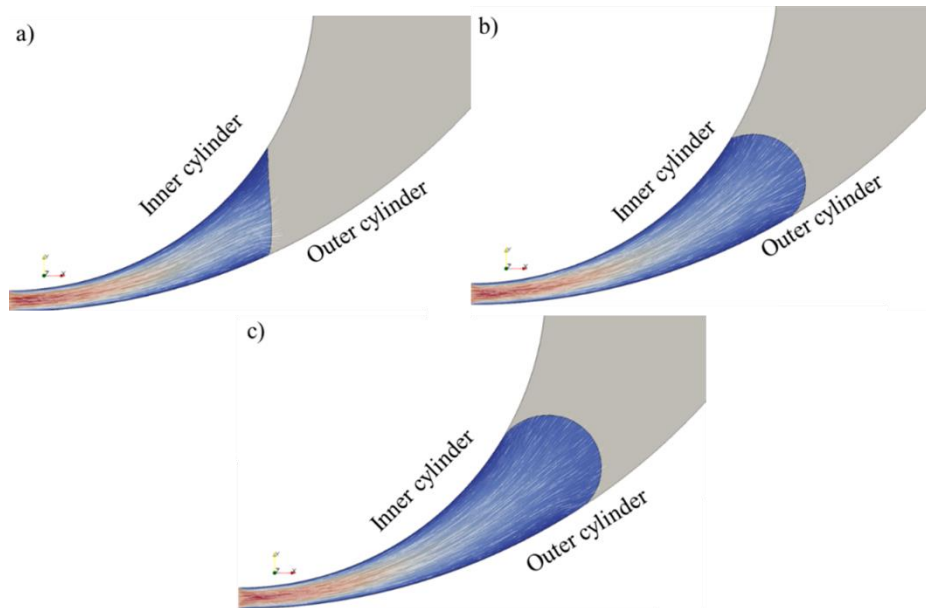


**Figure 5.19** – Cimlib simulation of a) introduction of fluid in the MaCROS mixer, b) and c) different volumes introduced in the MaCROS mixer.

The simulation of the stabilized fluid provides only one free surface of the fluid. Two adhesion boundary conditions are required to obtain a form similar to the 2D projection of the stabilized fluid (Figure 4.27b). However, dynamic simulations with two free surfaces with Cimlib did not provide a stable flow for long durations, which made the (numerical) stabilization procedure too cumbersome. It was then decided to impose simple shear flow as the inlet flow at the left boundary. Figure 5.20 shows the streamlines of the fluid under dynamic conditions. The adhesion boundary condition was set on the inner cylinder surface at a position of  $x = 21.5$  mm. This position is typical of the position of the free surface of the silicone fluid (8g) during the stabilization experiments with the MaCROS mixer. The cylinder velocities were applied and a fountain flow could be observed between the cylinder surfaces.

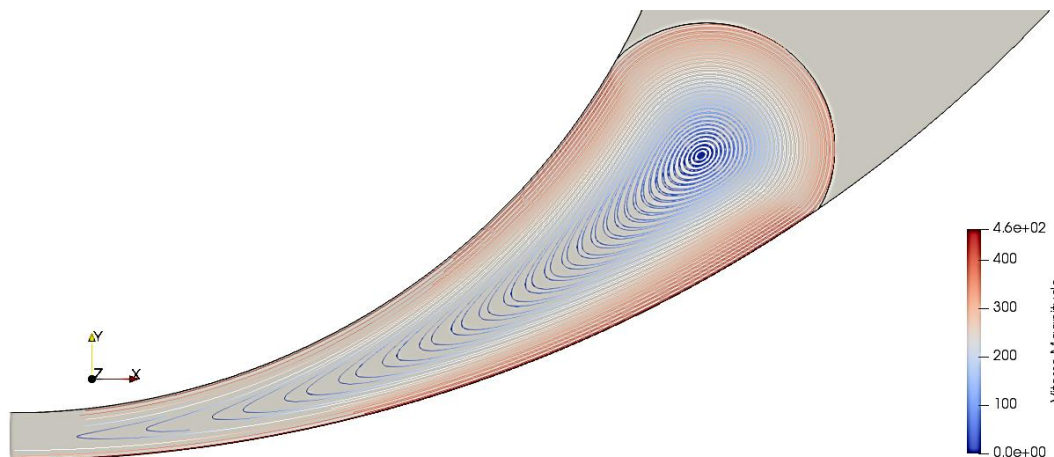


**Figure 5.20** – Streamlines of the stabilized fluid at an adhesion boundary condition at 21.5 mm and cylinder velocities of  $V_1 = -0.504$  rpm and  $V_2 = 1.5725$  rpm.

When the adhesion boundary condition is changed (i.e. moved to a higher upstream position), a bulge is created on the inner cylinder surface. The free surface stabilizes as the bulge moves from the inner cylinder surface towards the outer cylinder surface. As the bulge reaches the outer cylinder surface, the free surface stabilizes to a new steady state position. The transition leading to the new steady state is presented in the Appendix XVI. Every change in the adhesion boundary condition results in the free surface stabilizing to a new steady state position. Figure 5.21 presents the free surfaces for different adhesion boundary conditions.

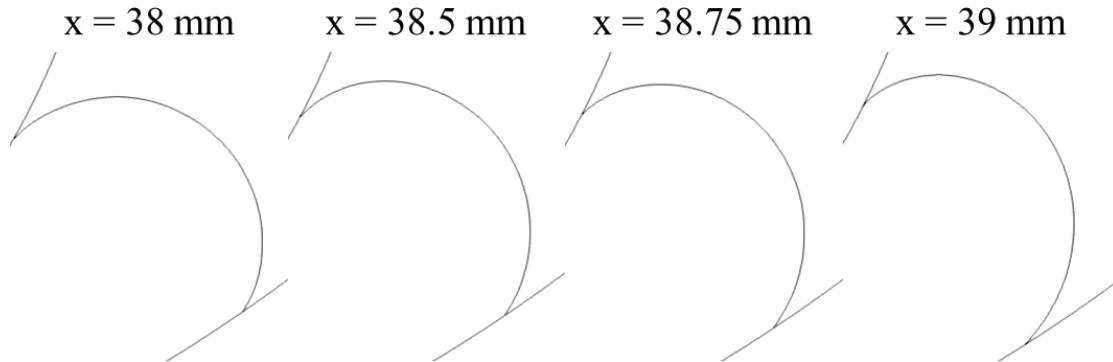


**Figure 5.21** – Free surfaces of stabilized fluid for different adhesion boundary conditions with initial boundary condition:  $x = 38$  mm.

With increasing adhesion boundary condition, the free surface tends to dewet the outer cylinder surface. This leads to the free surface becoming more asymmetric as the adhesion boundary condition is increased. This continues till a critical point after which the free surface loses contact with the outer cylinder surface (Figure 5.22). The transition leading to loss of contact with the outer cylinder surface is shown in Appendix XVII.

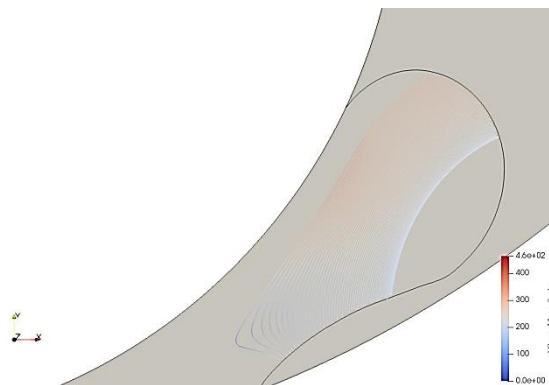


**Figure 5.22** – Fluid loses contact with the outer cylinder surface with an increase in the adhesion boundary condition.

Once the adhesion boundary condition is changed to its critical value, a bulge occurs similar to the previous cases. Once this bulge reaches the outer cylinder surface, the free surface is unable to stabilize to a new steady state resulting in the rupture of contact. In these cases, the energy required for the fluid to lose contact with the outer cylinder surface is lower than that required to undergo shear flow with the asymmetric free surface. At the outer cylinder surface, the fluid reaches a state where it costs less energy to lose contact with the surface than undergo shear flow with the asymmetric free surface.

The inner cylinder normal component of the stress profile of the stabilized fluid is shown in Figure 5.23. From the figure, we can see that the normal stress is localized near the around interface between the inner cylinder and the free surface. Additionally, a stress singularity is observed near the contact line at the inner cylinder surface, similar to the singularity problem explained by Huh and Scriven [Huh and Scriven, 1971]. To quantify the adhesion energy, the stress around the interface is summed up (marked by the red box) and used to calculate the adhesion energy ( $E_R$ ). Neglecting the surface energy implies that the adhesion energy is the normal stress close to the triple line integrated over the sample thickness. This procedure is inspired from peel tests experiments, where adhesion energy is known to be composed of a surface energy and a bulk dissipation energy, which is larger for thicker peeled strips, until a finite value of the thickness. Adhesion energy is then obtained by measuring the peel force per unit width.

In the present case, the stress was integrated in the neighbourhood of the triple point (integration domain is shown as a square on Figure 5.23) and then averaged on the size of the domain in the tangential direction. In this study, the size of the domain was set to 2mm, which is several times larger than the computational mesh size. This quantification neglects the stress at the singularity point (which in theory is integrable, but quite sensitive to the numerical approximation).

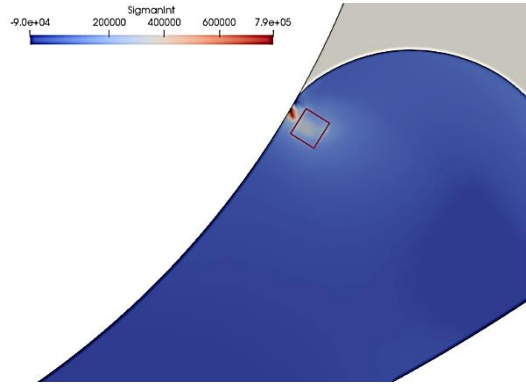


Figure 5.23 – Stress profile (in Pa) of the stabilized fluid in dynamic conditions.

Table 5.8 presents the adhesion energy and the corresponding peak angles ( $\theta_{\text{peak}}$ ) of the free surface for different adhesion boundary conditions. From this table, we find that as the adhesion boundary condition is increased, the adhesion energy also increases. This shows that a fluid with a superior adhesion energy can wet the inner cylinder surface to a greater extent for the same cylinder velocities. Also, an increase in adhesion energy is followed by a decrease in peak angles indicating that an increase of only 0.1 J/m<sup>2</sup> of adhesion energy of this fluid (Newtonian, 1 Pa.s.) can induce a significant asymmetry of the free surfaces.

Adhesion boundary condition (mm)	Adhesion energy, $E_R$ (J/m <sup>2</sup> )	Peak angles, $\theta_{\text{peak}}$ (°)
38	0.13	91
38.5	0.19	83
38.75	0.21	78
39	0.22	69

Table 5.8 – Adhesion energy and their corresponding peak angles for the stabilized fluid (Newtonian, 1 Pa.s.).

The numerical simulations show that an increase in adhesion energy can influence the form of the free surfaces in conditions of similar surface contact condition. Now, the role of adhesion energy on the free surfaces of viscous fluids will be carried out by incorporating the non-Newtonian flow behavior of the silicone fluid. The study will be carried out for the silicone fluid at different conditions of volume and cylinder velocities in the next section.

### 5.3.2. Cimlib simulation: Non-Newtonian case

The non-Newtonian flow behavior of the silicone fluid was introduced in the form of a power law (Equation 3.2). Similar to the Newtonian case, a similar flow field could be achieved with a fountain flow between the cylinder surfaces. The simulation was carried out at two volumes i.e., two different initial boundary conditions ( $x = 21.5$  mm and  $x = 38$  mm). The adhesion energy and their corresponding peak angles for different adhesion boundary conditions are presented in Table 5.9.

As the free surfaces become more asymmetric, the adhesion energy required to cause such a displacement increases. However, the adhesion energy required for the silicone fluid to better wet the inner cylinder surface is several orders of magnitude higher than the required energy of the Newtonian fluid. From Table 5.9, we observe that the silicone fluid must exhibit adhesion energies of the order of a few hundreds of J/m<sup>2</sup> to significantly impact the free surfaces. This is significantly superior to the adhesion energy of the silicone fluid. As the fluid cannot exhibit such high adhesion energy values, the

## Chapter 5: Influence of adhesion energy on shear flow

silicone fluid exhibits symmetric free surfaces during internal mixing or the stabilization experiments with MaCROS. The peak angles measured during the stabilization experiments with the MaCROS mixer (Appendix XII) showed significant asymmetry under certain conditions. However, these results are inconclusive as the observed free surface was the 2D projection of the 3D form of the fluid.

Initial boundary condition (mm)	Adhesion boundary condition (mm)	Adhesion energy, $E_R$ (J/m <sup>2</sup> )	Peak angles, $\theta_{\text{peak}}$ (°)
21.5 (Small volume: Slow)	21.5	228	82
	22	425	77
38 (Large volume: Slow)	38	327	85
	38.5	505	84
	38.75	596	82
	39	693	80
	39.25	786	80

**Table 5.9** – Adhesion energy and their corresponding peak angles of the stabilized silicone fluid for different volumes.

Table 5.9 also shows that an increase of volume in the simulation results in an increase of estimated adhesion energy. This result is a consequence of the diverging flow geometry rather than the volume of the fluid. At larger volumes, the flow geometry becomes more diverging resulting in longer free surfaces which requires more energy to displace the free surface.

Table 5.10 presents the adhesion energy and their corresponding peak angles for different cylinder velocities. These cylinder velocities correspond to the lowest and highest shear rate obtained during the stabilization experiments. The influence of adhesion energy on the free surfaces remains unchanged at higher cylinder velocities. The magnitude of the adhesion energy almost doubles with the increase in cylinder velocities.

Cylinder velocities (rpm)	Adhesion boundary condition (mm)	Adhesion energy, $E_R$ (J/m <sup>2</sup> )	Peak angles, $\theta_{\text{peak}}$ (°)
$V_1 = -0.504$ $V_2 = 1.5725$ (Large volume: Slow)	38	327	85
	38.5	505	84
	38.75	596	82
	39	693	80
	39.25	786	80
$V_1 = -2.506$ $V_2 = 6.998$ (Large volume: Fast)	38	649	90
	38.5	1159	85
	38.75	1200	81
	39	1438	75
	39.25	1681	73

**Table 5.10** – Adhesion energy and their corresponding peak angles of the stabilized silicone fluid for different cylinder velocities.

Figure 5.24 shows the adhesion energy required for each change in adhesion boundary condition for different cases of volume and cylinder speeds. We find that in order to influence the peak angle of the free surface by a few degrees (°), an enormous amount of adhesion energy is required. These adhesion energies are unrealistically superior to the adhesion energy of the silicone fluid. Thus, an increase of adhesion energy of the order of a few hundreds of J/m<sup>2</sup> can influence the free surface but only by a few mm.

From Figure 5.24, we can observe that the adhesion energy required to influence the free surface is dependent on the cylinder velocities, rheological behavior and the local geometry. Under the conditions of the MaCROS mixer, an adhesion energy of 0.1 and 200 J/m<sup>2</sup> is required to influence the free surface form for the Newtonian and silicone fluid respectively.

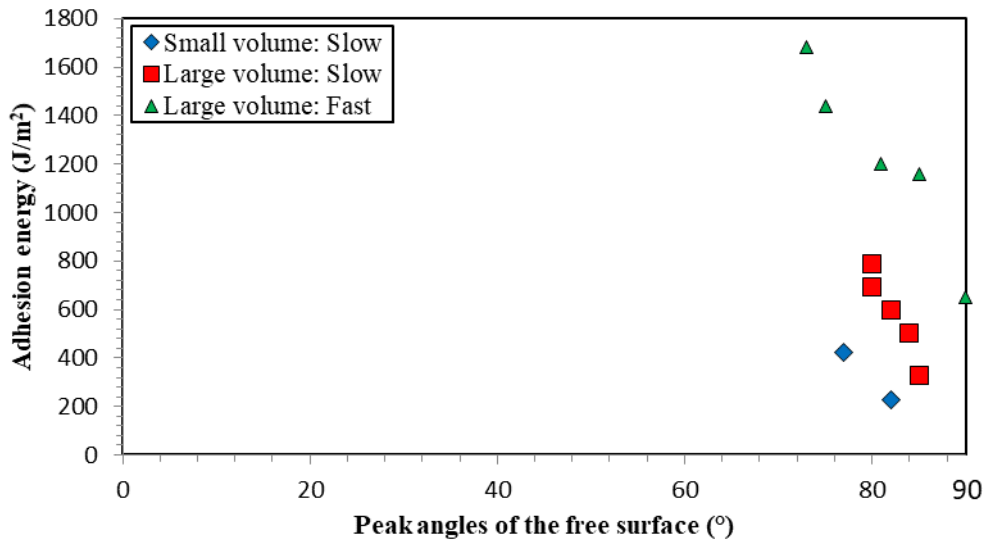


Figure 5.24 – Adhesion energy required for each change in adhesion boundary condition for different cases of volume and cylinder speeds.

In an industrial internal mixer, the geometry of the flow channel is much more divergent. The fluids used in internal mixer often have viscosities which are 10 times superior to that of the silicone fluid. Additionally, we also encounter higher shear rates in internal mixers than in the MaCROS mixer. Considering these facts, we can conclude that the adhesion energy required ( $> 10^5 \text{ J/m}^2$ ) to influence the free surfaces during mixing is too substantial. Table 5.11 summarizes the adhesion energy required to influence the free surfaces during shear flow for different cases. Such adhesion energies cannot be provided by the rubber compounds used during internal mixing. Therefore, we can assume that the adhesion plays no role in the movement of free surfaces during internal mixing.

Type of fluid	Consistance, K (Pa.s.)	Adhesion energy required to influence free surfaces (J/m <sup>2</sup> )
Newtonian (1 Pa.s.)	1	$>0.1$
Silicone fluid	15000	$>300$
Rubber products	100000	$>10^5$

Table 5.11 – Required adhesion energy to influence the free surfaces during shear flow.

## Conclusions

The adhesion energy of the fluids used in this study were characterized with the help of probe tests. Estimation techniques, based on the work of Zosel, were required to estimate the adhesion energy of the rubber products at 100°C. This technique predicts that the rubber products exhibit low adhesion energies of the order of 30 to 200 J/m<sup>2</sup> at 100°C. The silicone fluid exhibits adhesion energies of the order of 35 to 50 J/m<sup>2</sup>. The rheological behavior of the fluids implies that the adhesion energy would not significantly influence the shear flow. However, the Monocuve observations point that an increase in adhesion energy can result in the asymmetry of the free surfaces in cases of dissimilar surface contact condition.

An adhesion model was proposed to determine the difference in adhesion energy between the cylinder surfaces during the stabilization experiments with the MaCROS mixer. This model proposes that the flow rate during the stabilization experiments must be zero. The difference in flow rate due to the rotation of the inner and outer cylinders must be due to another factor. We assume that this difference in flow rate is due to the pressure driven flow caused by the adhesive behavior exhibited by the fluid on the walls. However, the difference in adhesion energy values predicted by the model were significantly superior to the characterized adhesion energy.

The adhesion model was improved by the drag model which takes into account the lateral movement of the transparent windows. This was achieved with MATLAB<sup>®</sup> and a PDE solver. The drag model provided a 3D flow profile. The form of the fluid during the stabilization experiments indicates a 3D flow profile in the fluid. This flow profile was confirmed by the form of the fluid during the stabilization experiments. The mean velocity from the flow field was used in the adhesion model to obtain the corrected adhesion energy. The corrected adhesion energy from the drag model was again found to be superior to the characterized adhesion energy by a factor of 2 or more. This indicates that the pressure driven flow due to adhesion is negligible in comparison to the viscous dissipation in the bulk volume.

The drag model can also be used to estimate the stabilization velocities in the MaCROS mixer. The velocity field could be predicted for different cylinder velocities. When the numerical advancing velocity of the flow field is zero, the flow is considered to be under stabilized conditions. The predicted stabilization conditions were found to be close to the experimentally determined stabilization conditions. This prediction was found to improve at smaller thicknesses ( $h_m$ ). At larger thicknesses, the prediction of stabilization conditions was found to diverge. This is attributed to the increased effect of the lateral drag of the windows at larger thicknesses.

The stabilization experiments with the MaCROS mixer were analyzed with the help of the Cimlib software. An adhesion boundary condition was imposed on the inner cylinder surface to set the position of the free surface of the fluid. Initially, the simulation was carried out with a Newtonian fluid. As the fluid is introduced into the geometry, a fountain flow could be observed between the cylinder surfaces. The adhesive behavior of the fluid was varied by allowing the fluid to wet the surface more i.e., increasing the adhesion boundary condition.

As the adhesion boundary condition is changed, the free surface stabilizes to a new steady state. This results in the free surface becoming more asymmetric with an increase of adhesion boundary condition. This continues till the fluid ruptures contact with the outer cylinder surface. The stress profile of the stabilized fluid was used to quantify the energy required to cause a rupture of contact. In the case of the silicone fluid, an increase of adhesion energy of the order of a few hundreds of J/m<sup>2</sup> was found to influence the form of the free surface. However, this energy is several times superior to the actual adhesion energy exhibited by the fluid (15 J/m<sup>2</sup> in shear). The adhesion energy required to influence the free surface of the viscous fluid (by a few °) is often superior to its actual adhesion energy. Thus, the role of adhesion in the movement of free surfaces during mixing can be considered as negligible.

### Résumé en français

L'énergie d'adhésion des fluides a été caractérisée avec des tests de tack en traction. On trouve de faibles énergies de l'ordre de 30 à 200 J/m<sup>2</sup> à 100°C. Le fluide silicone présente des énergies d'adhésion de l'ordre de 35 à 50 J/m<sup>2</sup> à température ambiante. Le comportement rhéologique des fluides implique que l'énergie d'adhésion aura une influence négligeable sur l'écoulement de cisaillement. Cependant, les observations de Monocuve indiquent qu'une augmentation de l'énergie d'adhésion peut entraîner une asymétrie des surfaces libres (dans le cas de contact adhésif d'un côté et cohésif de l'autre).

Un modèle d'adhésion a été proposé pour déterminer la différence d'énergie d'adhésion entre les surfaces des cylindres lors des expériences de stabilisation avec le mélangeur MaCROS. Ce modèle propose que le débit en écoulement stabilisé est nul. La différence de débit due à la rotation des cylindres interne et externe doit être liée à un autre facteur. Nous supposons que cette différence de débit est due à la pression négative provoquée par le comportement adhésif du fluide. Cependant, la différence d'énergie d'adhésion prédite par le modèle était significativement supérieure à l'énergie d'adhésion caractérisée.

Le modèle d'adhésion a été amélioré par un modèle d'entraînement qui prend en compte le mouvement latéral des fenêtres transparentes. Le modèle d'entraînement fournit un profil d'écoulement 3D ce qui est confirmé par la forme du fluide lors des expériences de stabilisation. La vitesse moyenne du champ d'écoulement a été utilisée dans le modèle d'adhésion pour obtenir l'énergie d'adhésion corrigée. Cette énergie corrigée est supérieure à l'énergie d'adhésion caractérisée d'un facteur d'au moins 2. Cela indique que l'adhérence est négligeable par rapport à la dissipation visqueuse du fluide.

Le modèle d'entraînement peut également être utilisé pour estimer les vitesses de stabilisation dans le mélangeur MaCROS. La vitesse numérique d'avancement peut être prédite pour différentes vitesses de cylindre. Lorsque cette vitesse moyenne est nulle, l'écoulement est considéré comme étant dans des conditions stabilisées. En comparant les vitesses de stabilisation numériques et expérimentales, on trouve une corrélation qui est assez proche. La prédiction des vitesses de stabilisation est meilleure à faible entrefer ( $h_m$ ). Ceci est attribué à l'effet important de l'entraînement latéral des entrefers plus importants.

Les expériences de stabilisation avec le mélangeur MaCROS ont été analysées par la méthode d'éléments finis. Une condition aux limites d'adhérence a été imposée sur la surface du cylindre interne pour définir la position de la surface libre du fluide. Initialement, la simulation a été réalisée avec un fluide newtonien. Dans des conditions dynamiques, un écoulement fontaine est observé entre les cylindres. Le comportement adhésif du fluide a été modifié en permettant au fluide de mouiller davantage la surface, c'est-à-dire en augmentant la condition aux limites d'adhésion.

Lorsque la condition aux limites d'adhérence est modifiée, la surface libre se stabilise à un nouveau régime stationnaire. Ceci se traduit par rendre la surface libre plus asymétrique. Cela continue jusqu'à ce que le fluide rompe le contact avec la surface du cylindre externe. L'énergie nécessaire pour provoquer cette rupture de contact a été quantifiée. Dans le cas du fluide silicone, une augmentation de l'énergie d'adhésion de l'ordre de quelques centaines de J/m<sup>2</sup> s'est avérée influencer la forme de la surface libre. Cependant, cette énergie est plusieurs fois supérieure à l'énergie d'adhésion réelle présentée par le fluide (15 J/m<sup>2</sup> en cisaillement). L'énergie d'adhésion nécessaire pour influencer la surface libre du fluide visqueux (de quelques degrés) est souvent supérieure à son énergie d'adhésion réelle. Ainsi, le rôle de l'adhérence dans le mouvement des surfaces libres lors du mélange peut être considéré comme négligeable.



## Chapter 6

# Discussion and conclusion

### Contents

---

6.1. General conclusions .....	176
6.2. Suggestions for future studies .....	178

---

## 6.1. General conclusions

This work aims at investigating the interfacial phenomena during shear flow of rubber compounds in conditions close to an internal mixer. The characterization of the wall slip behavior, free surface movement and the adhesive behavior of these compounds can help improve the numerical simulation of the internal mixing process. These investigations were carried out through the development of transparent flow geometries, experimental techniques and numerical simulation. The results of this work will be summarized in three main themes: wall slip, free surface movement and adhesion.

### Wall slip

Initially, a transparent flat die was developed to conduct direct observations of the flow field and determine wall slip velocities. The transparent flat die was mounted at the end of the RhéoART™ capillary rheometer. The flow observations showed that SBR A undergoes wall slip across the transparent flat die. The primary drawback of the transparent flat die was the inability to attain steady state flow (under no-wall slip condition). Due to time constraints of this PhD and the mechanical failure of the transparent flat die, further studies with the die were abandoned. Consequently, wall slip characterization was carried out through indirect rheological methods.

The rheological behavior of the rubber products was characterized with the help of oscillatory and capillary rheometers. The ideal properties required for steady state flow observations with the MaCROS mixer were identified. It was found that the rheological behavior of the rubber compounds obtained through these methods were quite close to each other. Their different flow regimes, flow instabilities and wall slip behavior were characterized with the capillary rheometer.

The rheological behavior of the rubber products was compared at 100°C. BR A and SBR A were found to undergo stick-slip behavior at comparatively low shear rates. BR A and SBR A were used for transparent flow observations of the wall slip behavior. SBR B undergoes wall slip at comparatively high shear rates. SBR C exhibits no wall slip probably due to its improved adhesive behavior. Transparent flow observations were conducted with SBR B. SBR C was used to demonstrate the flow behavior of an adhesive rubber compound.

Wall slip velocities were estimated with the Shear Rate Difference method. The influence of temperature on the wall slip velocities of SBR A and SBR B was studied. A general trend of increasing wall slip velocities with increasing temperature was observed. Nevertheless, the wall slip velocity curves of different die diameters were found to cross each other. Thus, an accurate relation between the wall slip velocities and the temperature could not be obtained from this data.

### Free surface movement

Transparent mixers have been used to observe the flow behavior of rubber compounds in internal mixers. The complex geometry of these mixers results in the attainment of a 3D flow behavior. The simple geometry of Michelin's Monocuve mixer can be used to carry out transient 2D flow observations of the flow behavior. To conduct steady state flow observations of the free surfaces of viscous fluids during shear, the MaCROS mixer was designed and developed during the course of this work. Its geometry is best described as a counter-rotating Couette cell.

The flow observations of the rubber compounds with the Monocuve mixer provided simpler 2D flow observations in comparison to classic transparent internal mixers. Stick-slip flow was observed with BR A. The observations with the silicone fluid, SBR A, SBR B and SBR C showed a quasi-steady state behavior i.e. the free surfaces maintained their form more or less while being constantly displaced in the mixer. As the silicone fluid exhibits a similar flow behavior to SBR A, SBR B and SBR C, we can consider that it is a viable choice as a model fluid to conduct steady state flow observations with the MaCROS mixer.

The free surfaces of the fluids during mixing with the Monocuve mixer were recorded to analyze their degree of symmetry. It is to note that the free surfaces during mixing with the Monocuve mixer have an adhesive contact with the rotor on one end and a cohesive contact on the other. To characterize the symmetry of the free surfaces, a peak angle was defined. Peak angles were measured for different positions, temperature and fill factors. Only the fill factor was found to influence the peak angles. On comparing the peak angles of the free surfaces of the rubber products at a given condition, it was found that SBR B and SBR C showed more asymmetric free surfaces in comparison to BR A and SBR A.

The prototype MaCROS mixer was tested and calibrated to determine its functionality. The MaCROS mixer provides good velocity control at low cylinder velocities ( $V_1 = \pm 3.2$  rpm and  $V_2 = \pm 7$  rpm). A viscosity limit was identified with the fluids above which the cylinders were unable to shear the fluid without damaging the transparent windows. Due to this limit, the rubber products were required to be sheared at high temperatures (100°C or above). However, the heating control was found to be inaccurate. Flow observations could be conducted with SBR A and SBR B.

By the variation of the direction of rotation and the volume fill factor, four different types of flow observations can be obtained (of which three provide steady state observations). In this work, the steady state observations of the free surfaces were conducted in the counter-rotation condition at small fill factors. Under this condition, we obtain two free surfaces with adhesive contact (cylinder surfaces) on both ends. The movement of the transparent windows during the experiments resulted in a significant distortion of the volume. This led to a complex 3D shape of the sheared volume under stabilized conditions. The visual observation of the stabilized fluid through the transparent windows could provide a 2D projection of the 3D form of the stabilized fluid.

The analysis of the stabilization velocities of the silicone fluid showed that the inner cylinder needs to rotate at higher velocities than the outer cylinder to overcome the drag provided by the rotating transparent windows. The stabilization velocities were compared at different surface conditions (roughness and surface nature). No significant difference was observed with the stabilization velocities for the different surface conditions. The silicone fluid demonstrates a unilateral contact with the metallic surfaces during shear flow. These results point to the fact that adhesion plays a negligible role in the interfacial flow behavior of viscous fluids.

The peak angles of the free surfaces were also measured during the stabilization experiments with the silicone fluid. The peak angles were found to be quite disperse and it was difficult to comment on the nature of these free surfaces. This difficulty can be attributed to the fact that the observed free surfaces of the stabilized silicone fluid were a 2D projection of its 3D free surface. Thus, it is better to not draw out conclusions based on the measured peak angles. Flow observations with the rubber products showed that SBR A undergoes wall slip at 100°C. Steady state flow observations conditions could be performed at a small fill factor with SBR B. However, the stabilization velocities were not analyzed due to the uncertainty of the outer cylinder temperature and thus the rheology of the fluid during stabilization.

### Adhesion

The adhesion energy of the silicone fluid and the rubber products were determined at their respective service temperatures. Despite its formulation, SBR C exhibits lower adhesion energy than SBR B at 100°C. This is a result of its stark thermodependence above its Zosel temperature. A simple calculation points out that the role of adhesion in shear flow of viscous fluids is negligible. The results from the Monocuve mixer show that an adhesion energy of few hundreds of J/m<sup>2</sup> can influence the free surfaces of the fluid. However, a detailed study is required to see if this behavior is a result of adhesion energy or another factor.

Subsequently, the role of adhesion on the free surfaces was investigated. An adhesion model, which uses the stabilization velocities of the MaCROS mixer, was defined. It is based on the hypothesis that

the difference in flow rates due to the rotation of the inner and outer cylinders was attributed to the pressure driven flow caused by the adhesion. The difference in adhesion energy between the cylinders was predicted by the adhesion model. However, these values were found to be disperse and inaccurate. In our study, we find that the bulk rheology of the fluid dominates over the adhesion energy of the fluid during stabilization experiments with the MaCROS mixer.

Finite element analysis was carried out on the stabilization experiments with the MaCROS mixer. Adhesion boundary conditions were used to fix the position of the free surface of the fluid. Initially, the simulation was carried out with a Newtonian fluid. The adhesion boundary condition was changed to allow the fluid to wet the surface more. With the change in adhesion boundary condition, the free surface stabilizes to a new state where it becomes gradually more asymmetric. The stress profile of the fluid during mixing was used to determine the adhesion energy of the fluid for each adhesion boundary condition. It was found that the energy required to influence the form of the free surfaces during mixing is significantly higher than the adhesion energy of the fluids. Thus, we can conclude that the role of adhesion can be neglected during numerical simulations and that the unilateral contact is a good hypothesis for viscous fluids during simulation.

### Synthesis of general conclusions

This work was carried out within the framework of the OSUM project. The objective was to incorporate the interfacial flow phenomena into a numerical simulation of the internal mixing process/ With this perspective, the essential takeaway points can be summarised as:

- Wall slip velocity laws were obtained for the rubber products via the classical methods and can be used as boundary conditions during simulation.
- An accurate thermodependent wall slip velocity law could not be obtained by capillary rheometer with these rubber products.
- The role of adhesion on the movement of free surfaces during viscous flow can be neglected.
- Unilateral contact of the fluid with the metallic surfaces during mixing is a good hypothesis.
- In case of adhesive contact on both ends of the free surfaces, the free surface can be considered as symmetric. The adhesion energy required to influence the form of the free surface in this case is too high.
- The free surfaces of the fluid can be influenced in cases of dissimilar surface contact (adhesive and cohesive contact on the extremities of the free surfaces). Detailed studies are required to characterize the role of adhesion in these cases.

### 6.2. Suggestions for future studies

In this section, a non-comprehensive list of improvements and areas of interest for future studies are presented. Some of these improvements could not be carried out during this study due to constraints of available resources and time.

#### Materials:

Flow visualization experiments are easier to carry out at lower shear rates. For direct estimations of the wall slip velocity, fluids which undergo pure wall slip at low shear rates are desired. BR A and SBR A undergo stick-slip flow at low shear rates. This behavior is not adequate as the analysis of stick-slip flow is more complicated than pure slip flow. Fluids which undergo pure slip behavior at low shear rates can help provide better estimations of wall slip velocities.

Through numerical simulation, we were able to conclude that the role of adhesion during shear flow and free surface movement is negligible. To verify this experimentally, viscous fluids with an

improved adhesive behavior ( $> 10^3 \text{ J/m}^2$ ) are required. Flow visualizations with such fluids in the Monocuve or MaCROS mixer investigate the role of adhesion in the movement of free surfaces.

### **Transparent flat die:**

As mentioned in Chapter 4.1, the design of the transparent flat die could be improved to provide better flow observations. To avoid mechanical failure, a better choice of material must be used. Surface treatments can be used to avoid corrosion. The design of the die must ensure a sealed flow. The use of an extruder rather than a capillary rheometer is encouraged: i) to obtain higher shear rates and ii) to obtain continuous flow. A longer flat die provides a larger zone of observation and the attainment of steady state flow under non-slip conditions. The use of three or more pressure transducers in the flow channel is necessary to provide a more precise measurement of the pressure drop across the flow channel. The use of multiple heating elements in the flow channel can be used to provide uniform heating of the flow channel.

### **Wall slip velocities:**

Wall slip velocities have been determined with the indirect method since the early 1930's. These methods provide adequate results. However, direct flow observations of the flow field or laser velocimetry is necessary to obtain accurate measurements of the wall slip velocities.

### **Monocuve mixer:**

Flow observations must be carried out at conditions of dissimilar surface contact (adhesive and cohesive contact on the extremities of the free surfaces) to investigate the role of adhesion on the form of the free surfaces. The Monocuve mixer provides simple, yet transient observations of the fluid's free surfaces during mixing. A detailed study is required to investigate the evolution of peak angles in function of the rheology of the fluid, adhesion energy of the fluid, fill factor, rotation speeds and temperature. This study can confirm if the free surface is influenced by the adhesion energy or not.

### **MaCROS mixer:**

Steady state flow observations can be carried out with the MaCROS mixer at large factors. These observations provide a dissimilar surface contact and can be used to carry out the study mentioned in the previous paragraph.

To obtain steady state 2D flow behavior in the MaCROS mixer, a solution must be found to rotate the outer cylinder without rotating the transparent windows. High temperature experiments can be effectively carried out by improving the heating system of the outer cylinder surface to provide a steady temperature under dynamic conditions. The inner cylinder must be equipped with a stronger motor to shear more viscous fluids ( $> 10^4 \text{ Pa.s.}$ ) at elevated temperatures.

Another prototype mixer with the geometry of a Couette cell can be used to obtain quasi-steady state flow observations of the free surfaces. For this study, the ratio of inner to outer cylinder diameter must be close to 0.8 or 0.9. With a small amount of fluid, we can observe the fluid being displaced around the Couette cell in a non-diverging flow channel. Such observations will be 2D in nature and will permit the observation of two free surfaces with adhesive contact on either end.

### **Free surface movement:**

The movement of free surfaces of the fluid is an active area of research. The finite element analysis of the shear flow can be used to study this movement for other applications such as coating, inkjet printing, etc.



## **Bibliographic references**

## Bibliographic references

---

- S. Abbott. Adhesion Science: Principles and Practice. Lancaster, USA: DEStech Publications, pp. 328 (2015).
- J. F. Agassant, P. Avenas, J-P. Sergent, B. Vergnes and M. Vincent. Mise en forme des polymères. Paris, France : Lavoisier, pp. 844 (2014).
- I. Ahmed, H. Poudyal and A. Chandy. Fill factor effects in highly-viscous non-isothermal rubber mixing simulations. International Polymer Processing. 34, pp. 182-194 (2019).
- N. Akram, R. S. Gurney, M. Zuber, M. Ishaq and J. L. Keddie. Influence of polyol molecular weight and type on the tack and peel properties of waterborne polyurethane Pressure Sensitive Adhesives. Macromolecular Reaction Engineering 7 (10), pp. 493-503 (2013).
- E. H. Andrews and A. J. Kinloch. Mechanics of adhesive failure. I. Proceedings of the Royal Society of London A, 332, 1590, pp. 385-399 (1973).
- ANSYS, Inc. ANSYS Polystat User's Guide. Release 18.2. Canonsburg, USA: ANSYS Inc, pp. 778 (2017).
- Arlanxeo. Technical data sheet – Buna® SBR 2300 [online]. Available on: < <http://tsr.arlanxeo.com/en/products/product-search/bunar-sbr-2300/> > (Accessed on 09/03/2020).
- T. Asai, T. Fukui, K. Inoue and M. Kuriyama. Paper III-4 presented at International Rubber Conference, Paris (1982).
- G. Aspenes, S. Høiland, T. Barth, K. M. Askvik, R. Kini and R. Larsen. Petroleum hydrate deposition mechanisms: the influence of pipeline wettability. Proceedings of the 6<sup>th</sup> International Conference on Gas Hydrates (2008).
- B. T. Atwood and W. R. Schowalter. Measurement of slip at the wall during flow of high-density polyethylene through a rectangular conduit. Rheologica Acta 28, pp. 134-136 (1989).
- P. Avenas, A. Leveque, J. F. Agassant and H. Prus. Une presse à injecter prototype, le Rhéoplast. Revue Générale des Caoutchoucs et Plastiques, 52, 9 (1975)
- E. B. Bagley. End corrections in the capillary flow of polyethylene. Journal of Applied Physics, 28, pp. 193-209 (1957).
- F. H. Banbury. Machine for treating rubber and other heavy plastic material. Patent US1200070A (Published on 03/10/1916).
- F. H. Banbury. Rubber-mixing machine. Patent US1689990A (Published on 30/10/1928).
- J. L. Barden and S. Crudden. Improvement in rotary churns. Patent US166181A (Published on 03/08/1875).
- O. Bäumchen, R. Fetzer, M. Klos, M. Lessel L. Marquant, H. Hähl and K. Jacobs. Slippage and nanorheology of thin liquid polymer films. Journal of Physics: Condensed Matter 24, 325102 (2012).
- J. J. Bikerman and C-R. Huang. Polyethylene Adhesive Joints. Transactions of the Society of Rheology 3, 5 (1959).
- W. R. Bolen and R. E. Colwell. Intensive mixing. Society of Plastics Engineering 14 (8), pp. 24-28 (1958).

## Bibliographic references

---

- D. Bonn, J. Eggers, J. Indekeu, J. Meunier and E. Rolley. Wetting and spreading. *Reviews of modern physics* 81, 739 (2009).
- B. B. Boonstra and A. I. Medalia. Effect of carbon black dispersion on the mechanical properties of rubber vulcanizates. *Rubber Chemistry and Technology*, 36 (1), pp. 115-142 (1963).
- I. J. Boudimbou. Mécanismes élémentaires de dispersion de charges de silice dans une matrice élastomère. PhD Thesis, Ecole Nationale Supérieure des Mines de Paris, France (2011).
- F. Brochard-Wyart and P. G. de Gennes. Dynamics of partial wetting. *Advances in colloid and interface science* 39, pp. 1-11 (1992).
- P. Carreau. Rheological equation from molecular network theories. PhD Thesis, University of Wisconsin, France (1968).
- E. Chaffee. Making Rubber Fabrics. Patent US16A (Published on 31/08/1836).
- T. Chen, Y. Hao, X. Chen, H. Zhao, J. Sha, Y. Ma and L. Xie. Mixing ability examination of three different rotor cross sections and rotor geometry quantification with pressurization coefficient. *Journal of Applied Polymer Science* 135, 37 (2017).
- J. J. Cheng and I. Manas-Zloczower. Hydrodynamic analysis of a Babury mixer. *Polymer Engineering and Science* 29 (11), pp. 701-708 (1989).
- N. P. Cheremisinoff. Condensed encyclopedia of polymer engineering terms. Wobur, USA : Butterworth-Heinemann, pp. 362 (2001).
- R. Collier. The river that God forgot. Dalton, USA : Collins, pp. 288 (1968).
- W. P. Cox and E. H. Merz. Correlation of dynamic and steady flow viscosities. *Journal of Polymer Science* 28, pp. 619-622 (1958)
- C. Creton. Pressure-Sensitive-Adhesives: an introductory course. *MRS Bulletin* 28 (6), pp. 434-439 (2003).
- C. Creton and M. Ciccotti. Fracture and adhesion of soft materials: A review. *Reports on progress in physics* 79, 046601 (2016).
- A. Crié. Caractérisation et lois rhéologiques d'élastomères chargés à basse température pour la simulation du procédé d'extrusion. PhD Thesis, Ecole Nationale Supérieure des Mines de Paris, France (2014).
- J. Curchod. Synthèse, propriétés et technologie des élastomères. Paris, France : IFOCA (1984).
- C. A. Dahlquist. Adhesion Fundamentals and Practice. New York, USA: Gordon and Breach Science Publishers, pp. 143 (1969).
- S. Das. Investigation of design and operating parameters in partially-filled rubber mixing simulations. Master of Science Thesis. Akron, USA: University of Akron, pp. 134 (2016).
- P. G. de Gennes. Fracture d'un adhésif faiblement réticulé. *Comptes Rendus de l'Académie des Sciences de Paris, Série II*, 307, 1949-1953 (1988).
- P. G. de Gennes. Soft Adhesives. *Langmuir*, 12, 4497-4500 (1996).

## Bibliographic references

---

- K. H. de Haas, D. van den Ende, C. Blom, E. G. Altena, G. J. Beukema, and J. Mellema. A counter-rotating Couette apparatus to study deformation of a sub-millimeter sized particle in shear flow. *Review of Scientific Instruments* 69, 1391 (1998).
- J. Delay and D. Plazek. Time-Temperature superposition – A Users Guide. *Rheology Bulletin*, 78, 2, pp. 16-31 (2009).
- J. L. den Otter. Mechanisms of melt fracture. *Plast. Polym*, 38 (135), pp. 155-168 (1970).
- J. L. den Otter. Some investigations of melt fracture. *Rheol Acta* 10, pp. 200–207 (1971).
- M. M. Denn. Extrusion instabilities and wall slip. *Annual Review of Fluid Mechanics*, 33, pp. 265-287 (2001).
- P. Dhakal, S. Das, H. Poudyal and A. Chandy. Numerical simulations of partially-filled rubber mixing in a 2-wing rotor-equipped chamber. *Journal of Applied Polymer Science*. 134 (2016).
- F. Dimier, B. Vergnes and M. Vincent. Le glissement à la paroi d'un mélange de caoutchouc naturel. *Rhéologie* 1, pp. 35-39 (2002).
- E. S. Dizon and L. A. Papazian. The processing of filler-reinforced rubber. *Rubber Chemistry and Technology* 50 (4), pp. 765-779 (1977).
- H. L. Dryden, F. D. Murnaghan and H. Bateman. *Hydrodynamics*. National Research Council (U.S.): Dover, USA, pp. 163 (1956).
- C. Dubois, F. Thibault, P. Tanguy and A. Ait-Kadi. Characterization of viscous mixing in a twin intermeshing conical helical mixer. *ICHEME Symposium Series* 140, pp. 249-258 (1996).
- B. C. Duncan and L. A. Lay. An intercomparison of tack measurements. NPL Report No CMMT(A) 176 (1999).
- A. Dupré. *Théorie mécanique de la chaleur*. Paris, France : Gauthier-Villars, pp. 368 (1869).
- E. B. Dussan V. On the spreading of liquids on solid surfaces: static and dynamic contact lines. *Annual Review of Fluid Mechanics* 11, pp. 371-400 (1979).
- N. El Kissi and J. M. Piau. The different capillary flow regimes of entangled polydimethylsiloxane polymers: macroscopic slip at the wall, hysteresis and cork flow. *Journal of Non-Newtonian Fluid Mechanics*, 37, pp. 55–94 (1990).
- D. D. Eley. *Adhesion*. London, UK: Oxford University Press, pp. 290 (1961).
- M. S. Evans. Tyre Compounding for Improved Performance. *Rapra Review Reports* 12, pp. 1-132 (2002).
- J. D. Ferry. *Viscoelastic Properties of Polymers*. USA: John Wiley & Sons, pp. 672 (1980)
- T. G. Fox. *Bulletin of the American Physical Society* 1, 123 (1956).
- L. Fradette, H-Z. Li, L. Choplin and P. Tanguy. Gas/liquid dispersions with a SMX static mixer in the laminar regime. *Chemical Engineering Science* 61, 11, pp. 3506-3518 (2006).
- I. Franta. *Elastomers and Rubber Compounding Materials: Manufacture, Properties and Applications*. New York, USA: Elsevier, pp. 607 (1989).

## Bibliographic references

---

- P. K. Freakley and W. Y. Wan Idris. Visualization of flow during the processing of rubber in an internal mixer. *Rubber Chemistry Technology* 52, pp. 134-145 (1979).
- T. French. *Tyre technology*. New York, USA : IOP Publishing Ltd, pp. 170 (1989).
- J. F. Funt. *Mixing of rubber*. Shrewsbury, UK: Smithers Rapra Technology Limited, pp. 186 (1977).
- A. Galliano, S. Bistac and J Schultz. Adhesion and friction of PDMS networks: molecular weight effects. *Journal of colloid and interface science* 265 (2), pp. 372-379 (2003).
- M. Garside. Natural and synthetic rubber - global consumption 1990-2019 [online]. Available on: < <https://www.statista.com/statistics/275399/world-consumption-of-natural-and-synthetic-caoutchouc/> > (Accessed on 08/02/2021).
- K. Geiger. Rheologische Charakterisierung von EPDM-Kautschukmischungen mittels Kapillarrheometer-Systemen. *Kautschuk Gummi Kunst* 42 (4), pp. 273-283 (1989).
- M. H. R. Ghoreishy. A transient finite element model of mixing of rubber compounds in a Banbury Mixer. *Iranian Polymer*, 5 (1) pp. 30-41 (1996).
- M. Gierlowski, C. Peiti and B. Vergnes, Flow instabilities of pure SBR and SBR compounds. *Proceedings European Congress on Rheology*, Erlangen (2002).
- Gomu Rubbers / Elastomers and Future Transportation. *Japan Rubber Technology Forum*, pp. 69 (2010).
- C. Goodyear. Improvement in India-Rubber fabrics. Patent US3633A (Published on 15/06/1844).
- P. J. Gramann, J. C. Mätzig and T. A. Osswald. Boundary Element Simulation of the Mixing Process of Polymer Blends. *International Polymer Processing VII*, pp. 117-134 (1992).
- A. A. Griffith. The phenomena of rupture and flow in solids. *Philosophical Transactions of the Royal Society of London, series A: Mathematical and Physical Sciences*, A221, pp. 163-198 (1920).
- A. Griffith. The theory of rupture. *Proceedings of the first international congress on applied mechanics*, pp. 54-63 (1924).
- W. I. Griffith. The accelerated characterization of viscoelastic composite materials. PhD Thesis, Virginia Polytechnic Institute and State University, USA (1980).
- R. M. Griffith, R. Kannabiran and G. S. Tomlinson. Rubber flow in an internal mixer. *Rubber Chemistry and Technol* 60 (1), pp. 111-124 (1987).
- R. F. Grossman. *The mixing of rubber*. Dordrecht, Netherlands : Springer, pp. 242 (1997).
- R. M. Guedes. Analysis of temperature and aging effects on biomedical ultrahigh molecular weight polyethylene's grades using a viscoelastic model. *Polymer Testing*, 30, 6, pp. 641-650 (2011).
- E. Hachem, M. Khalloufi, J. Bruchon, R. Valette and Y. Mesri. Unified adaptive Variational MultiScale method for two phase compressible-incompressible flows. *Computer Methods in Applied Mechanics and Engineering* 308, pp. 238-255 (2016).
- C. D. Han. Rheology in Polymer Processing. *Journal of polymer science: Polymer Letters Edition* 14, 11, pp. 697-698 (1976).

## Bibliographic references

---

- T. Hancock. Personal narrative of the origin and process of the caoutchouc or India-Rubber manufacture in England. London, UK: Spottiswoode & Co., (1857).
- S. Hatzikiriakos. Appropriate boundary conditions in the flow of molten polymers. *International Polymer Processing Journal of the Polymer Processing Society* 25 (01): 55 (2010).
- S. Hatzikiriakos and J. M. Dealy. Wall slip of molten high density polyethylene. I. sliding plate rheometer studies. *Journal of Rheology*, 35, pp. 497 (1991).
- M. Hénot, M. Grzelka, J. Zhang, S. Mariot, I. Antoniuk, E. Drockenmuller, L. Léger, and Frédéric Restagno. Temperature-Controlled Slip of Polymer Melts on Ideal Substrates. *Physical Review Letters* 121, 177802 (2018).
- H. Hervet and L. Léger. Flow with slip at the wall: from simple to complex fluids. *Comptes Rendus Physique* 4, 2, pp. 241-249 (2003).
- F. Hofmann and C. Coutelle. Process for the production of caoutchouc substances. Patent US11136300A (Published on 03/10/1911).
- C. Huh and L. E. Scriven. Hydrodynamic model of steady movement of a solid/liquid/fluid contact line. *Journal of Colloid and Interface Science* 35, pp. 85–101 (1971).
- B. C. Hutchinson, A. C. Rios and T. A. Osswald. Modeling the distributive mixing in an internal mixer. *International Polymer Processing* 14, 315 (1999).
- C. E. Inglis. Stresses in a plate due to the presence of cracks and sharp corners. *Trans. Inst. Naval Archit.*, 55, 219 (1913).
- G. R. Irwin. Analysis of stresses and strains near the end of a crack traversing a plate. *J. Appl. Mech.*, 24, 361 (1957).
- Y. Ishikawa. Systematic review of tyre technology. *National Museum of Nature and Science* 16, 2011.
- N. A. Isitman, M. Pompei and G. M. V. Thielen. Pneumatic Tire. Patent US20170037225A1 (Published on 09/02/2017).
- C. C. Jacoby, L. F. Munoz Mejia and N.A. Isitman. Pneumatic Tire. Patent US20160159157A1 (Published on 09/06/2016).
- C. L. Jenkins, H. J. Meredith and J. J. Wilker. Molecular weight effects upon the adhesive bonding of a mussel mimetic polymer. *ACS Applied Materials Interfaces* 5, 11, pp. 5091-5096 (2013).
- J. Jin, J. W. M. Noordermeer, W. K. Dierkes and A. Blume. The effect of silanization temperature and time on the machining modulus of silica-filled tire tread compounds. *Polymers* 12, 209 (2020).
- P. S. Johnson. *Elastomerics* 115 (1), 9 (1982).
- H. C. Jones and E. G. Snyder. Banbury mixing of zinc oxide. *Industrial and Engineering Chemistry* 43, 11, pp. 2602-2607 (1951).
- M. Jugo Viloría. Analysis and comprehension of flow instabilities of elastomer compounds. PhD Thesis, MINES ParisTech, Sophia-Antipolis, France (2017).
- D. H. Kaelble. Peel adhesion: influence of surface energies and adhesive rheology. *Journal of Adhesion*, 1, pp. 102-123 (1969).

## Bibliographic references

---

- D. S. Kalika and M. M. Denn. Wall slip and extrudate distortion in linear low-density polyethylene. *Journal of Rheology*, 31, pp. 815-834 (1987).
- S. Karam, Modélisation de l'injection des élastomères chargés : approche expérimentale et théorique, PhD Thesis, ENSMP, Sophia-Antipolis, France (1995).
- S. Karam, M. Vincent and Y. de Zelicourt. Injection Moulding of Rubber Compounds: Experimental and Theoretical study. *International Polymer Processing* 13, 2 (1998).
- S. Kasolang, M. A. Ahmad, R-D Joyce and C. F. M. Tai. Preliminary study of pressure profile in hydrodynamic lubrication journal bearing. *Procedia Engineering* 41, pp. 1743-1749 (2012).
- R. Kent. Energy management in plastics processing: Strategies, targets, techniques, and tools. Cambridge, USA : Elsevier, pp. 1356 (2018).
- D. H. Killeffer. Banbury : The Master Mixer. Palmerton, USA : Palmerton Publishing Co., Inc pp. 165 (1962).
- J. Kim and J. L. White. *Nihon Rheorogi Gakkaishi* 17, 203 (1989).
- J. K. Kim, J. L. White, K. Min and W. Szydlowski. Simulation of flow and mixing in an internal mixer *Intern Polymer processing* 4 (1) (1989).
- Kobelco Stewart Bolling Incorporated. Rubber Machinery | Kobelco | Kobe Steel Group | KSBI | Kobelco Steel Group Inc. | Rubber Mixer [online]. Available on: < [https://www.ksbiusa.com/machinery\\_mixers.htm](https://www.ksbiusa.com/machinery_mixers.htm) > (Accessed on 07/02/2021).
- T. Lai and Y. Meng. Logarithmic contact time dependence of adhesion force and its dominant role among the effects of AFM experimental parameters under low humidity. *Applied Surface Science* 419, pp. 294-304 (2017).
- H. Lakrout, P. Sergot and C. Creton. Direct observation of cavitation and fibrillation in a probe tack experiment on model acrylic pressure-sensitive-adhesives. *Journal of Adhesion*, 69, pp. 307-359 (1999).
- H. H. Le, S. Ilisch, B. Jakob and H. J. Radsch. Online characterization of the effect of mixing parameters on carbon black dispersion in rubber compounds using electrical conductivity. *Rubber chemistry and technology* 76, pp. 147-160 (2003).
- J. L. Leblanc. *Rhéologie des élastomères et mise en oeuvre des polymères*. Namur, pp. 375 (1996).
- S. D. Lee, J. L. White, N. Nakajima and R. Brzoskowski. *Kautschuk Gummi Kunststoffe* 4, 992 (1989).
- L. Léger, H. Hervet, Y. Marciano, M. Deruelle and G. Massey. Role of surface-anchored polymer chains in adhesion and slippage. *Israel Journal of Chemistry*, 35 (1), pp. 65-74 (1994).
- L. Léger and H. Hervet. Friction à l'interface entre un fluide polymère et un solide. *Physique et Statique*, 9, 37-43 (2006).
- A. Limper. *Mixing of Rubber Compounds*. Munich, Germany: Hanser Publications, pp. 239 (2012).
- J. Liu, F. Li, L. Zhang, Y. Liqun and H. Yang. Numerical simulation of flow of rubber compounds in partially filled internal mixer. *Journal of Applied Polymer Science* 132, 42496 (2015).

## Bibliographic references

---

- T. Lundgren and P. Koumoutsakos. On the generation of vorticity at a free surface. *Journal of fluid mechanics* 382, pp. 351-366 (1999).
- J. C. Majesté and F. Vincent. A kinetic model for silica-filled rubber reinforcement. *Journal of Rheology* 59 (2), pp.405-427 (2015).
- A. Y. Malkin, A. V. Baranov and O. K. Dakhin. Non-isothermal dispersive flow of a rubber mixture inside an internal rotor mixer. *International Polymer Processing* 10, pp. 99-104 (1995).
- I. Manas-Zloczower. *Mixing and compounding of polymers*. Munich, Germany : Hanser Publications, Munich, pp. 1188 (2009).
- S. J. Marshall, S. C. Bayne, R. Baier, A. P. Tomsia and G. W. Marshall. A review of adhesion science. *Dental materials* 26 (2), pp. 11-16 (2010).
- W. C. Mathews and G. S. Haslam. Some factors involving the Banbury mixing of zinc oxide in rubber stocks. *Rubber Age* 32, 206 (1932).
- Maxxis Tires. How a tyre is made | Tyre technology | Maxxis Tyres UK [online]. Available on: < <https://www.maxxis.co.uk/technology/how-a-tyre-is-made> > (Accessed on 07/02/2021).
- E.S. Mickaily-Huber, F. Bertrand, P. Tanguy, T. Meyer. A. Renken, F.S. Rys and M. Wehrli. Numerical simulations of mixing in an SMRX static mixer. *The Chemical Engineering Journal and the Biochemical Engineering Journal* 63 (2) pp. 117-126 (1996).
- K. Min and J. L. White. Flow visualization of the motions of elastomers and molten plastics in internal mixer. *Rubber Chem. Technol.* 58, pp. 1024-37 (1985).
- K. Min and J. L. White. Flow visualisation investigations of the addition of carbon black and oil to elastomers in an internal mixer. *Rubber Chem. Technol.* 60, 3, pp. 61-80 (1987).
- K. Min. Flow visualization parallel and perpendicular to the rotor axes for elastomers and molten plastics in an internal mixer: The Influence of Rotor Design. *Int. Poly. Proc.* 1, 179 (1987a).
- K. Min. *Adv. Poly. Tech.* 7, 243 (1987b).
- M. A. Minuto. Method of making bouncing silicone putty-like compositions. Patent US4371493 (Published on 01/02/1983).
- S. Mirshahidi. 6 wing banbury rotor [online]. Available on : < <https://grabcad.com/library/6-wing-banbury-rotor> > (Accessed on 09/03/2020).
- A. Mongruel and M. Cartault, Nonlinear rheology of styrene-butadiene rubber filled with carbon-black or silica particles, *J. Rheol.* 50, pp. 115-135 (2006)
- S. E. Moon, A. Chiche, A. M. Forster, W. Zhang, and C. M. Stafford. Evaluation of temperature-dependent adhesive performance via combinatorial probe tack measurements. *Review of Scientific Instruments* 76 (6) (2005).
- M. Mooney. Explicit formulas for slip and fluidity. *Journal of Rheology* 2, pp. 210-222 (1931).
- T. Moribe. Advanced intermeshing mixers for energy saving and reduction of environmental impact. *Mitsubishi Heavy Industries Technical Review* 49, 4 (2012).
- A. Morikawa, K. Min and J. L. White. Flow visualization of the rubber compounding cycle in an internal mixer based on elastomer blends. *International Polymer Processing* 4 (1) (1989).

## Bibliographic references

---

- P. Mourniac, J. F. Agassant and B. Vergnes, Determination of wall slip velocity in the flow of rubber compounds, *Rheol. Acta*, 31, pp. 565-574 (1992).
- MREPC. MREPC Rubber Industry – Overview [online]. Available on: < [http://www.mrepc.com/industry/world\\_production.php](http://www.mrepc.com/industry/world_production.php) > (Accessed on 09/03/2020).
- J. Narongthong, P. Sae-Oui and C. Sirisinha. Effects of mixing parameters and their interactions on properties of carbon black filled styrene-butadiene rubber. *Rubber Chemistry and Technology* 91 (3), pp. 521-536 (2018).
- V. Nassehi and P.K. Freakley. Spreader blade analogy of flow past an internal mixer rotor: Two dimensional steady state model. *International Polymer Processing* 6 (2) (1991).
- V. Nassehi and M. H. R. Ghoreishy. Finite element analysis of mixing in partially filled twin blade internal mixers. *International Polymer Processing* 12 (3), 231 (1997).
- H. Palmgren, Processing Conditions in the Batch-Operated Internal Mixer, *Rubber Chemistry and Technology* 48 (3), pp. 462–494 (1975).
- H. Parola, F. Barbotin, P. Kiener, B. Anselme and F. Martinet. Method for the continuous preparation of a catalytic system that is used to polymerise a conjugated diene and installation for implementing same. Patent W/2007/045417 (Published on 26/04/2007).
- P. Pfleiderer. Kneading and mixing machine. Patent US254042A (Published on 21/02/1882).
- J. M. Piau, N. El Kissi and B. Tremblay. Influence of upstream instabilities and wall slip on melt fracture and sharkskin phenomena during silicones extrusion through orifice dies. *Journal of Non-Newtonian Fluid Mechanics*, 34, pp.145–180 (1990).
- S. Poivet, F. Nallet, C. Gay and P. Fabre. Cavitation-induced force transition in confined viscous liquids under traction. *Europhysics Letters*, 62, pp. 244-250 (2003).
- B. D. Porrit and H. Rogers. *Indian Rubber Journal*, 68, 265 (1924).
- W. Prager and J. K. Talbot, in (ed. E. C. Bernhardt). *Processing of thermoplastic materials*. Reinhold: New York, USA, pp. 437 (1959)
- B. Rabinowitsch. Über die viskosität und elastizität von solen. *Zeitschrift für Physikalische Chemie* 145A (1)Z Phys 630Chem A 145, pp. 1–26 (1929).
- A. V. Ramamurthy. Wall slip in viscous fluids and influence of materials of construction. *Journal of Rheology*, 30, pp.337 (1986).
- L. F. Ramos De Valle and F. Aramburo. Rheological characterization of Guayule rubber. I. *Journal of Rheology* 25, pp. 379-403 (1981).
- M. L. Rathod and J. L. Kokini. Effect of mixer geometry and operating conditions on mixing efficiency of a non-Newtonian fluid in a twin screw mixer. *Journal of Food Engineering* 118 (3), pp. 256-265 (2013).
- O. Reynolds. *Philosophical Transactions of the Royal Society of London* 177A, 157 (1886).
- J. R. Rice. *Mathematical analysis in the mechanics of fracture. Fracture: an advanced treatise* 2, pp. 191-311 (1968).

## Bibliographic references

---

- H. Ritchie and M. Roser. CO<sub>2</sub> and Greenhouse Gas Emissions [online]. Available on: < <https://ourworldindata.org/co2-and-other-greenhouse-gas-emissions> > (Accessed on 5/10/2020).
- L. Robert, Y. Demay and B. Vergnes. Stick-slip flow of high density polyethylene in a transparent slit die investigated by laser doppler velocimetry. *Rheologica Acta* 43, pp. 89–98 (2004).
- L. Robert, B. Vergnes and Y. Demay. Complex transients in the capillary flow of linear polyethylene. *Journal of Rheology* 44, pp. 1183–1187 (2000).
- S. A. Salahudeen, R. H. Elleithya, O. Y. Alothman and S. M. Al Zahrani. Comparative study of internal batch mixer such as cam, banbury and roller: Numerical simulation and experimental verification. *Chemical Engineering Science* 66, (12), pp. 2502-2511 (2011).
- N. Sato, M. Miyaoka, S. Yamasaki, K. Inoue, A. Kuriyama, T. Fukui and T., Asai. Mixing and kneading machine. Patent US4300838A (Published on 17/11/1981).
- F. Saulnier. Quelques processus dynamiques aux interfaces polymères. PhD Thesis, Université Paris 6, France (2003).
- G. P. M. Schenkel and H. Kühnle. Zur Extrusion von Kunststoffen aus reschteck Kanalen. *Kunststoffe* 71, pp. 479–484 (1981).
- P. Schidrowitz and T. R. Dawson. History of the Rubber Industry. Cambridge, UK : Heffer and Sons, pp. 406 (1952).
- A. M. Schwartz, C. A. Rader and E. Huey. Resistance to flow in capillary systems of positive contact angle. Contact Angles, Wettability and Adhesion, American Chemical Society, New York, USA 250-267 (1964).
- D. K. Setsua and J. L. White. *Kautschuk Gummi Kunststoffe* 44, 542 (1991).
- K. R. Shull and C. Creton. Deformation behavior of thin, compliant layers under tensile loading conditions. *Journal of Polymer Science Part B Polymer Physics* 42 (22), pp. 4023 – 4043 (2004).
- V. P. Sierra, N. Müller, C. Sá, T. Thorsten, C. Vatterott and A. Stark. Rubber compound and vehicle tires. Patent DE102015210423A1 (Published on 08/12/2016).
- J. Silva, A. C. Santos and S. V. Canevarolo. In-line monitoring flow in an extruder die by rheo-optics. *Polymer Testing* 41, pp. 63-72 (2015).
- F. Snijkers and D. Vlassopoulos. Appraisal of the Cox-Merz rule for well-characterized entangled linear and branched polymers. *Rheologica Acta*. 53, pp. 935-946 (2014).
- TA Instruments. Understanding the rheological characteristics of thermoplastic polymers [online]. Available on: < <https://www.azom.com/article.aspx?ArticleID=12100> > (Accessed on 11/09/2018).
- Z. Tadmor and I. Klein. Engineering Principles of Plasticating Extrusion. Van Nostrand Reinhold, New York, USA (1970).
- M. Tassieri, M. Laurati, D. J. Curtis, D.W. Auhl, S. Coppola, A. Scalfati, K. Hawkins, P. R. Williams and J.M. Cooper. i-Rheo: Measuring the materials' linear viscoelastic properties “in a step”. *Journal of Rheology* 60, 649 (2016).
- A. V. Tobolsky and R. D. Andrews. Systems manifesting superposed elastic and viscous behavior. *Journal of Chemical Physics* 13, pp. 3-27 (1945).

## Bibliographic references

---

- N. Tokita and J. L. White. Milling behavior of gum elastomers: Experiment and theory. *Journal of Applied Polymer Science* 10 (7), pp. 1011-1026 (1966).
- E. S. Tompkins. *The history of the pneumatic tire*. Sudbury, UK : Eastland Press, pp. 122 (1981).
- Total. Technical Data Sheet Wingtack® STS [online]. Available on: < <http://www.crayvalley.com/docs/TDS/wingtack-sts.pdf> > (Accessed on 09/03/2020).
- Trinseo. Trinseo SPRINTAN™ SLR 3402-SCHKOPAU Solution-Styrene Butadiene Rubber (S-SBR) [online]. Available on: < <http://www.matweb.com/search/DataSheet.aspx?MatGUID=e681911d702a480e82a8c9531e8cc630&ckck=1> > (Accessed on 09/03/2020).
- D. M. Turner and M. D. Moore. The contribution of wall slip in the flow of rubber. *Plastics and Rubber Processing* 5, pp. 81-84 (1980).
- R. Valette, T. Coupez, C. David and B. Vergnes. A direct 3D numerical simulation code for extrusion and mixing processes. *International Polymer Processing*, 24, pp. 141-147 (2009).
- R. Valette, E. Hachem, M. Khalloufi, A. S. Pereira, M. R. Mackley and S. A. Butler. The effect of viscosity, yield stress, and surface tension on the deformation and breakup profiles of fluid filaments stretched at very high velocities. *Journal of Non-Newtonian Fluid Mechanics*, 263, pp. 130-139 (2019).
- A. Vananroye, P. Leen, P. Van Puyvelde, C. Clasen. TTS in LAOS: validation of time temperature superposition under large amplitude oscillatory shear. *Rheologica Acta* 50, 9–10, pp. 795–807 (2011).
- B. Vergnes. Extrusion defect and flow instabilities of molten polymers. *International Polymer Processing* 30, pp. 3-28 (2015).
- J. P. Villemaire, B. Vergnes and J. F. Agassant. The rheoplast: a preshearing rheometer for studying the influence of thermomechanical treatments on the rheological behavior. 61<sup>st</sup> annual meeting of the Society of Rheology, Montreal, Canada (1989)
- J. P. Villemaire, B. Vergnes and J. F. Agassant. Rheoplast: an automated rheometer with pre-shearing. 10th Annual Meeting of the Polymer Processing Society, Akron, USA (1994)
- VTT Technical Research Center of Finland. One-third of car fuel consumption is due to friction loss [online]. Available on: <[www.sciencedaily.com/releases/2012/01/120112095853.html](http://www.sciencedaily.com/releases/2012/01/120112095853.html)> (Accessed on 5/10/2020).
- K. V. Vyakaranam, B. K. Ashokan and J. L. Kokini. Evaluation of effect of paddle element stagger angle on the local velocity profiles in a twin-screw continuous mixer with viscous flow using Finite Element Method simulations. *Journal of Food Engineering* 108, 4, pp. 585-599 (2012).
- Q. J. Wang and Y-W. Chung. *Encyclopedia of Tribology*. Boston, USA : Springer, pp. 4139 (2013).
- M-J. Wang, Y. Kutsovsky, P. Zhang, L. J. Murphy, S. Laube and K. Mahmud. Carbon—Silica Dual Phase Filler, a new Generation Reinforcing Agent for Rubber: Part IX. Application to Truck Tire Tread Compound. *Rubber Chemistry Technology* 74, 741 (2001).
- G. D. West. On the resistance to the motion of a thread of mercury in a glass tube. *Proceedings of the Royal Society A* 86, 20 (1911).
- J. L. White. *Rubber Processing*. Cincinnati, USA : Hanser Gardner Publications, pp. 586 (1995).

## Bibliographic references

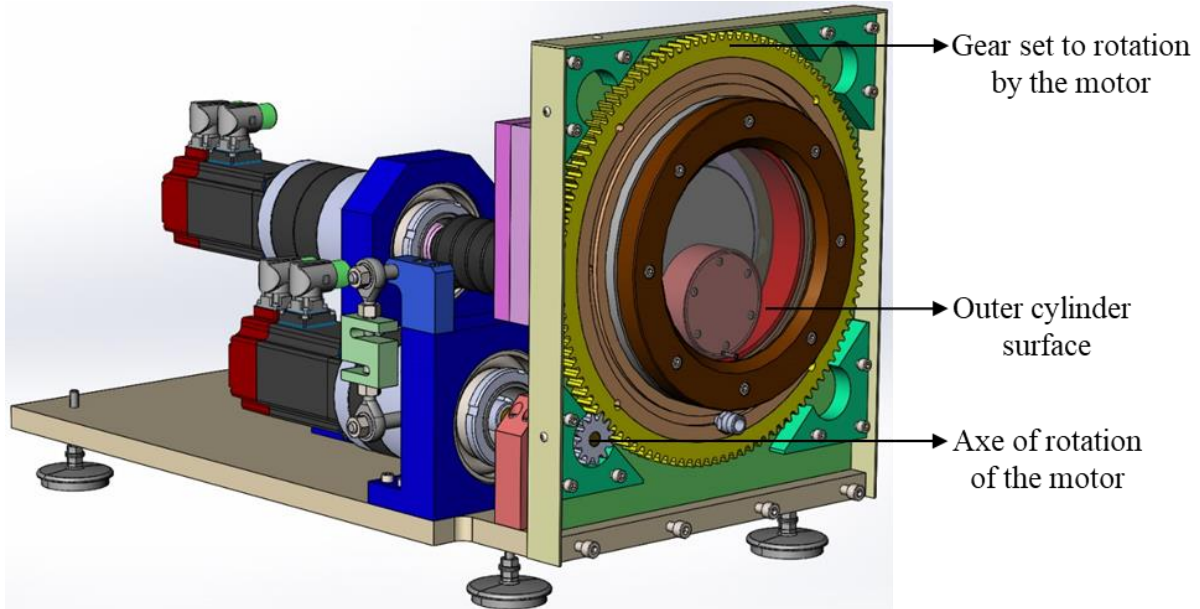
---

- J. L. White and D. Huang. Extrudate swell and extrusion pressure loss of polymer melts flowing through rectangular and trapezoidal dies. *Polymer Engineering* 21, pp. 1101-1107 (1981).
- J. L. White, K. Min, C. Y. Ma and R. Brzoskowski. Basic studies of flow visualization of processing of elastomers and their compounds: internal mixer and extrusion. *Journal of Polymer Engineering* 6, pp. 79-93 (1986).
- J. L. White and N. Tokita. Instability and failure phenomena in polymer processing with application to elastomer mill behavior. *Journal of Applied Polymer Science* 12, 7, pp. 1589-1600 (1968).
- S. Wiegrefe. Untersuchungen zum Wandgleitverhalten von EPDM und SBR. *Kautschuk und Gummi, Kunststoffe*, 44, pp. 216-221 (1991).
- S. Wu. *Polymer Interface and Adhesion*. Boca Raton, USA : CRC Press pp. 630 (1982).
- K. Yagii and K. Kawanishi. Flow analysis in an internal mixer Part I: Application of finite element analysis. *International Polymer Processing* 5 (3), 164 (1990).
- H. H. Yang and I. Manas-Zloczower. Analysis of mixing performance in a VIC mixer. *International Polymer Processing* 9 (4), pp. 291-302 (1994).
- C. H. Yao and I. Manas-Zloczower. Influence of design on mixing efficiency in a variable intermeshing clearance mixer. *International Polymer Processing* 12, 92 (1997).
- C. H. Yao, I. Manas-Zloczower, R. Regalia and L. Pomini. Distributive mixing in variable intermeshing clearance mixers: Simulation and experiments. *Rubber chemistry and technology* 71 (4), pp. 690-707 (1998).
- G. D. Yarnold. The motion of a mercury index in a capillary tube. *Proceedings of the Physical Society*, 50, 540 (1938).
- K. Yasuda. Investigation of the analogies between viscometric and linear viscoelastic properties of polystyrene. Ph.D. thesis, MIT, Cambridge (1979).
- T. Young. An essay on the cohesion of fluids. *Philosophical transactions of the Royal Society of London*, 95, pp. 65-87 (1805).
- O. A. Zakharkin, V. B. Golkin, D. P. Emelyanov, V. G. Epshtein, A. K. Yueva and Y. S. Kuz'min. Polyak, M. A., *Soviet Rubber Tech.* 25, 15 (1966).
- Z. Zhang and W. Rena. Simulation of moving contact lines in two-phase polymeric fluids. *Computers and Mathematics with Applications* 72, 4, pp. 1002-1012 (2016).
- X. Z. Zhu, T. S. Wang and G. Wang. Evaluations of flow and mixing efficiency in the kneading disks of a novel tri-screw extruder. *Journal of Applied Fluid Mechanics* 9 (1), pp. 51-60 (2016).
- A. Zosel. Adhesion and tack of polymers: Influence of mechanical properties and surface tensions. *Colloid & Polymer Sci* 263, pp. 541-553 (1985).
- A. Zosel. Adhesive failure and deformation behaviour of polymers. *Journal of Adhesion*, 30, 135-149 (1989a).
- A. Zosel, *Adhesives Age*, pp. 42-47 (1989b).
- A. Zosel. Effect of Cross-Linking on Tack and Peel Strength of Polymers, *The Journal of Adhesion*, 34:1-4, pp. 201-209 (1991).

# Appendix

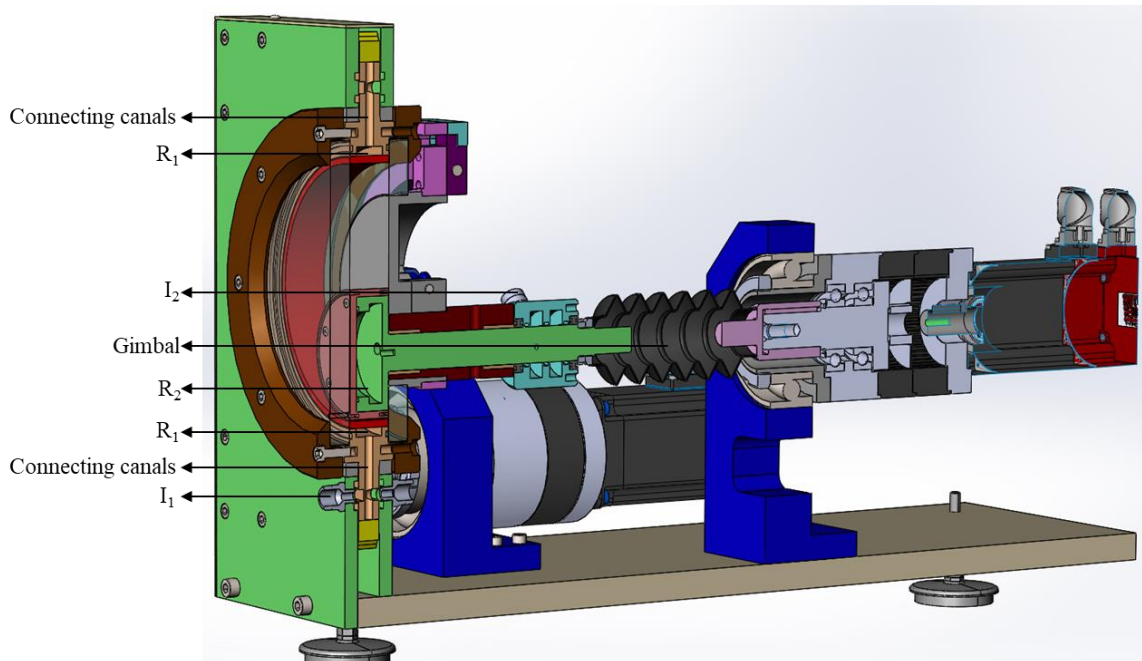
**Appendix I:** Additional views of the CAD design of the MaCROS mixer

Figure I shows the outer cylinder surface which is welded onto a large gear. The rotation of the outer cylinder surface is achieved by the MdP rotor (100 Nm). The MdP rotor rotates the small gear on its axis which in turn rotates the large gear (yellow).



**Figure I** – View of the CAD design of the MaCROS mixer without the front metallic wall.

Figure II shows the inlets and reservoirs for the heat transfer fluid in the MaCROS mixer. The outlets are hidden by the cross-section. The heat transfer fluid in the reservoirs is used to heat the cylinder surfaces (inner and outer) through heat conduction. The heat transfer fluid in the reservoirs is continually recirculated by the thermal baths via the inlets and outlets.



**Figure II** – Transverse cut view of the CAD design of the MaCROS mixer.

Legend for Figure II

$R_1$  is the reservoir of heat transfer fluid to heat the outer cylinder.

$R_2$  is the reservoir of heat transfer fluid to heat the inner cylinder.

$I_1$  is the inlet of heat transfer fluid to heat the outer cylinder.

$I_2$  is the inlet of heat transfer fluid to heat the inner cylinder.

In Figure 3, the metallic support (magenta) holds the bridle (grey). The gimbal links the axe of the MdP rotor (50 Nm) and the inner cylinder. The bridle holds the gimbal on one end and the back transparent window on the other end.

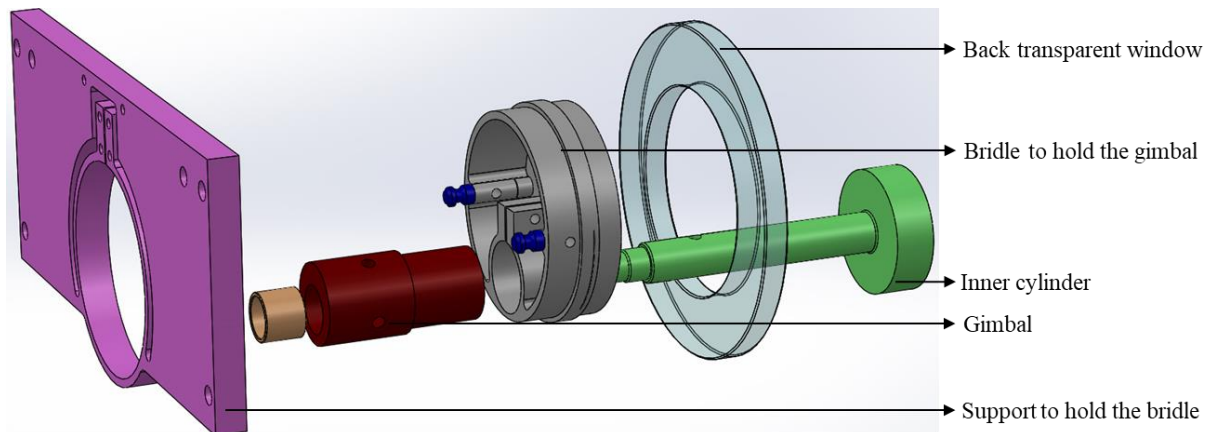


**Figure III** – Exploded view of the movable inner cylinder axis of the MaCROS mixer.

**Appendix II:** Comparison of viscosity laws of the fluids at their service temperature obtained by oscillatory and capillary rheometry

In the context of this PhD work, the service temperature of the silicone fluid is ambient temperature while that of the rubber products (BR A, SBR A, SBR B and SBR C) is 100°C.

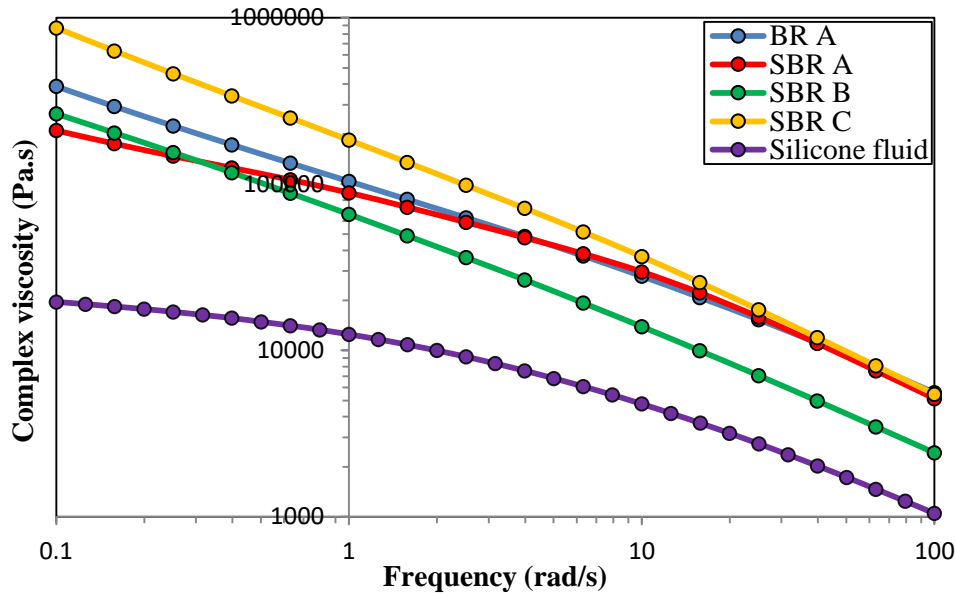


**Figure IV** – Comparison of the viscosities of the fluids obtained by oscillatory rheometry at their service temperatures.

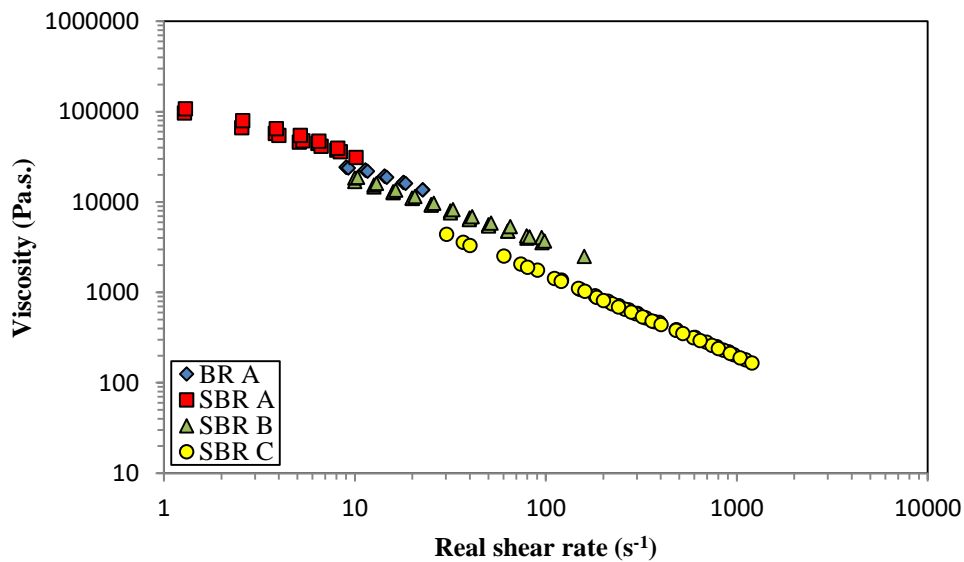


**Figure V** – Comparison of viscosities of the rubber products obtained by capillary rheometry at 100°C.

Appendix III: Pressure drop evolutions of BR A for different L/D ratios at 100°C

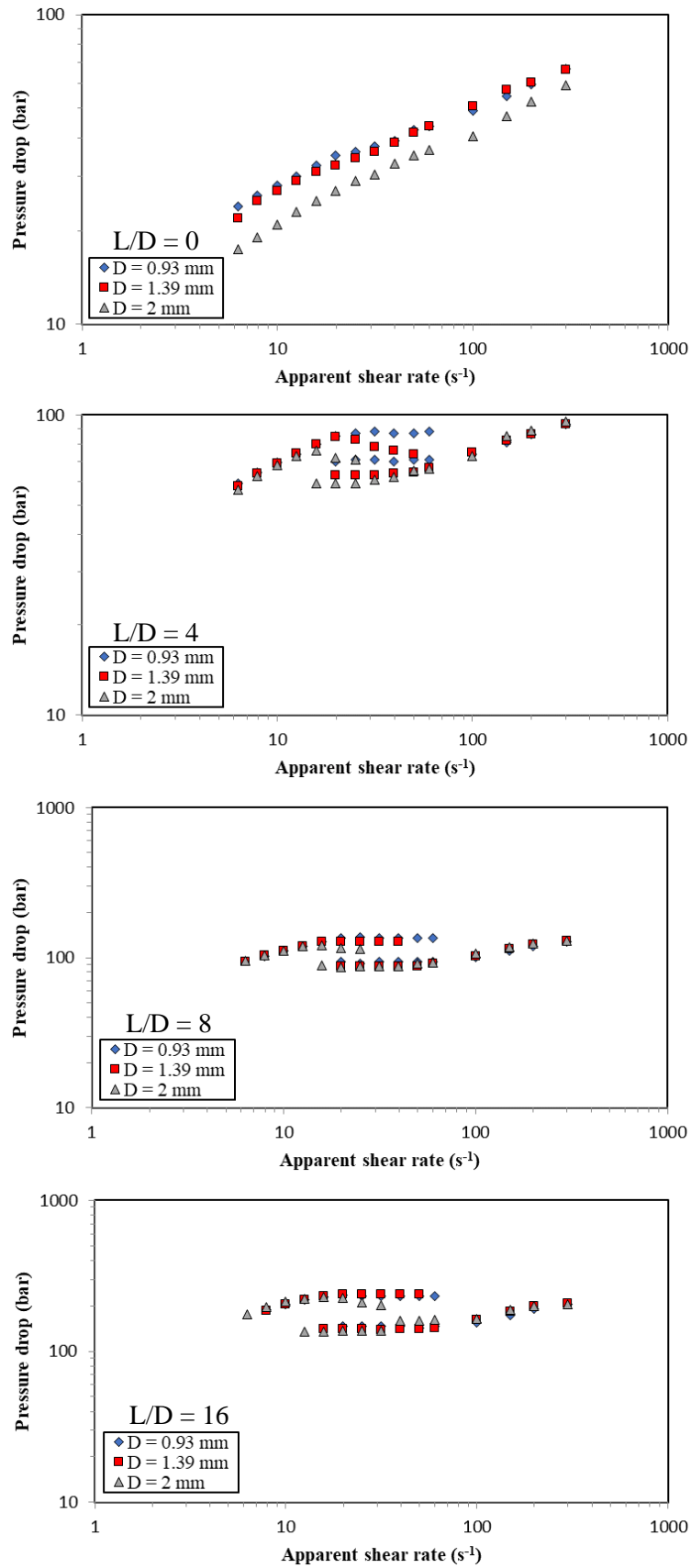


Figure VI – Pressure drop evolutions of BR A at 100°C for different L/D ratios (0, 4, 8, 16).

Appendix IV: Pressure drop evolutions of SBR A for different L/D ratios at 100°C

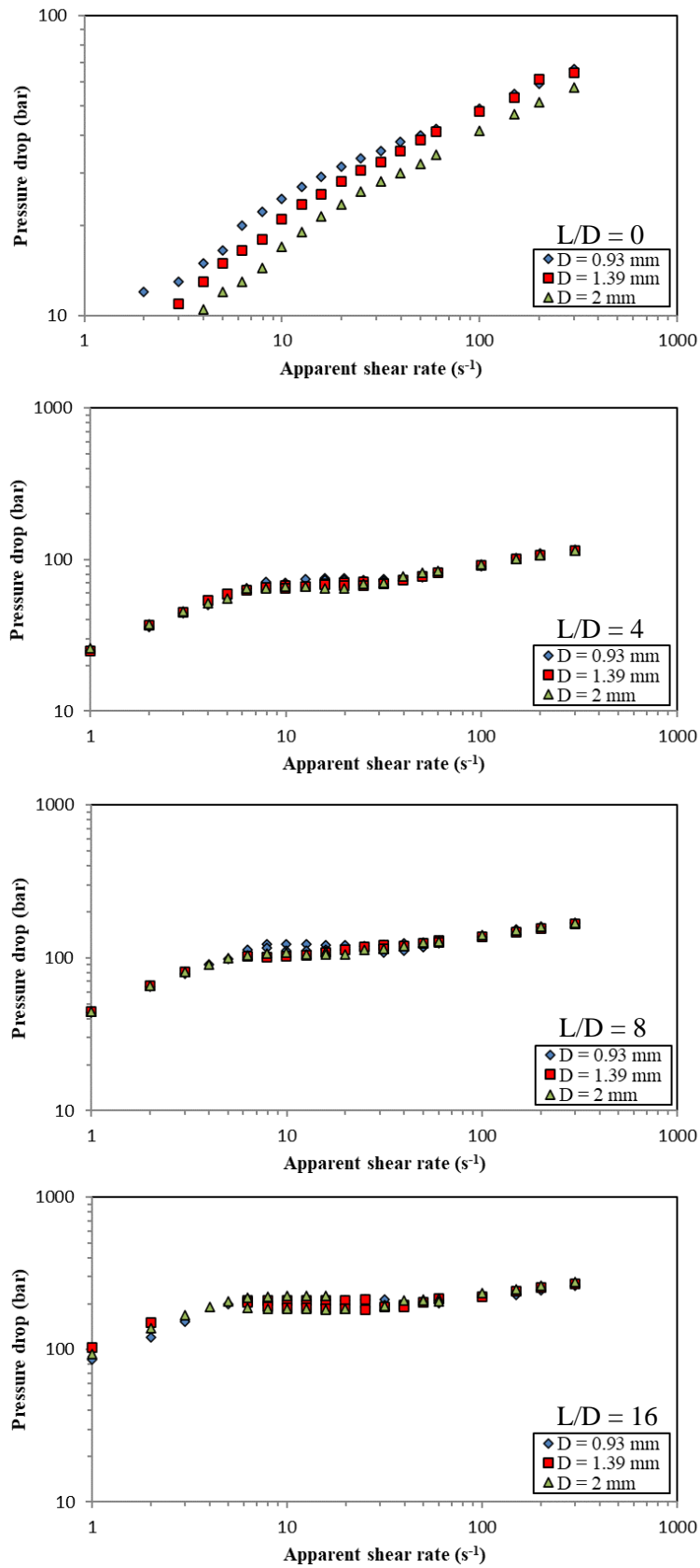


Figure VII – Pressure drop evolutions of SBR A at 100°C for different L/D ratios (0, 4, 8, 16).

Appendix V: Pressure drop evolutions of SBR A at 120°C

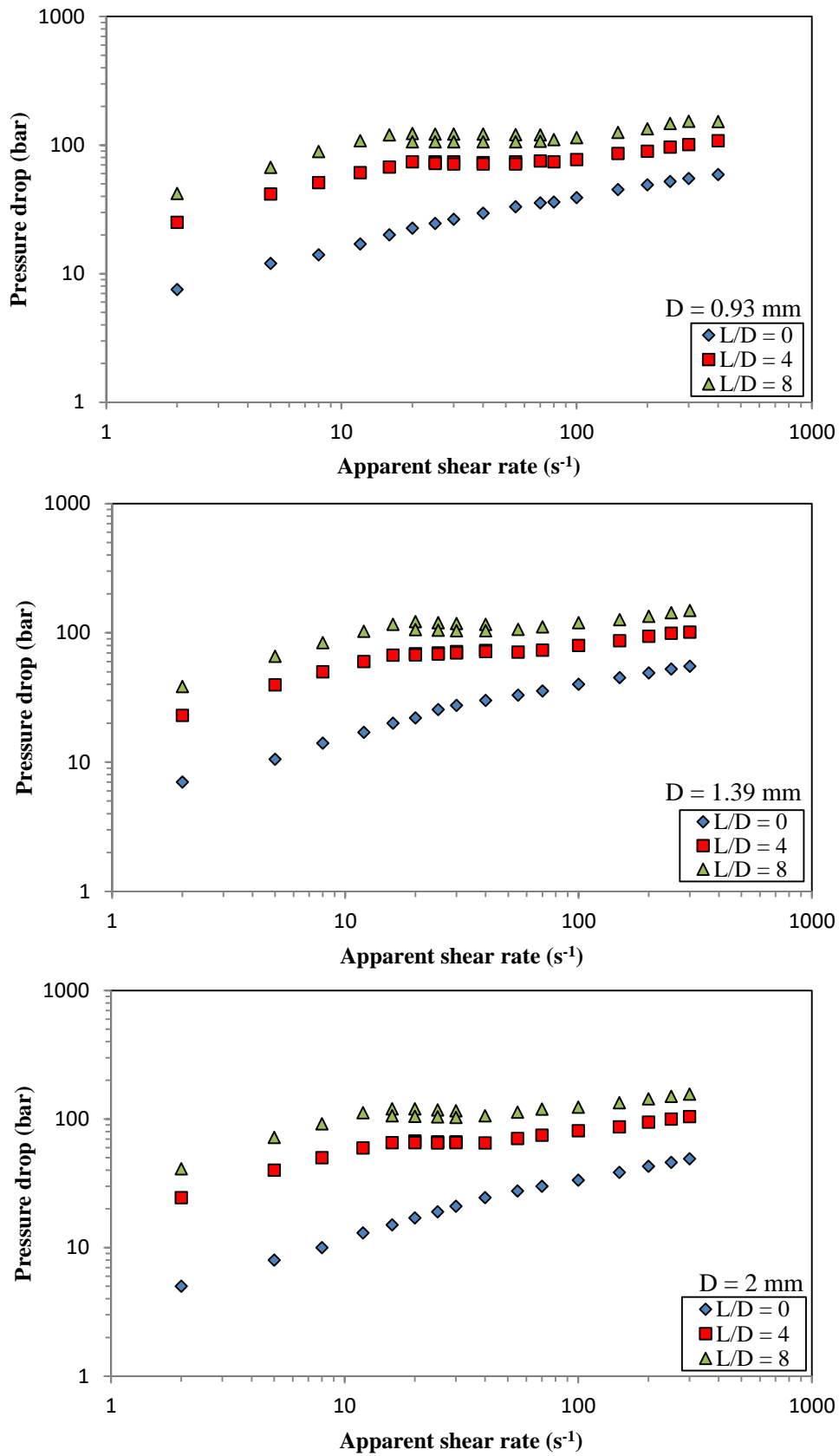


Figure VIII – Pressure drop evolutions in function of apparent shear rates of SBR A at 120°C with different capillary die diameters (D = 0.93, 1.39 and 2 mm) and L/D ratios (0, 4 and 8).

Appendix VI: Pressure drop evolutions of SBR A at 140°C

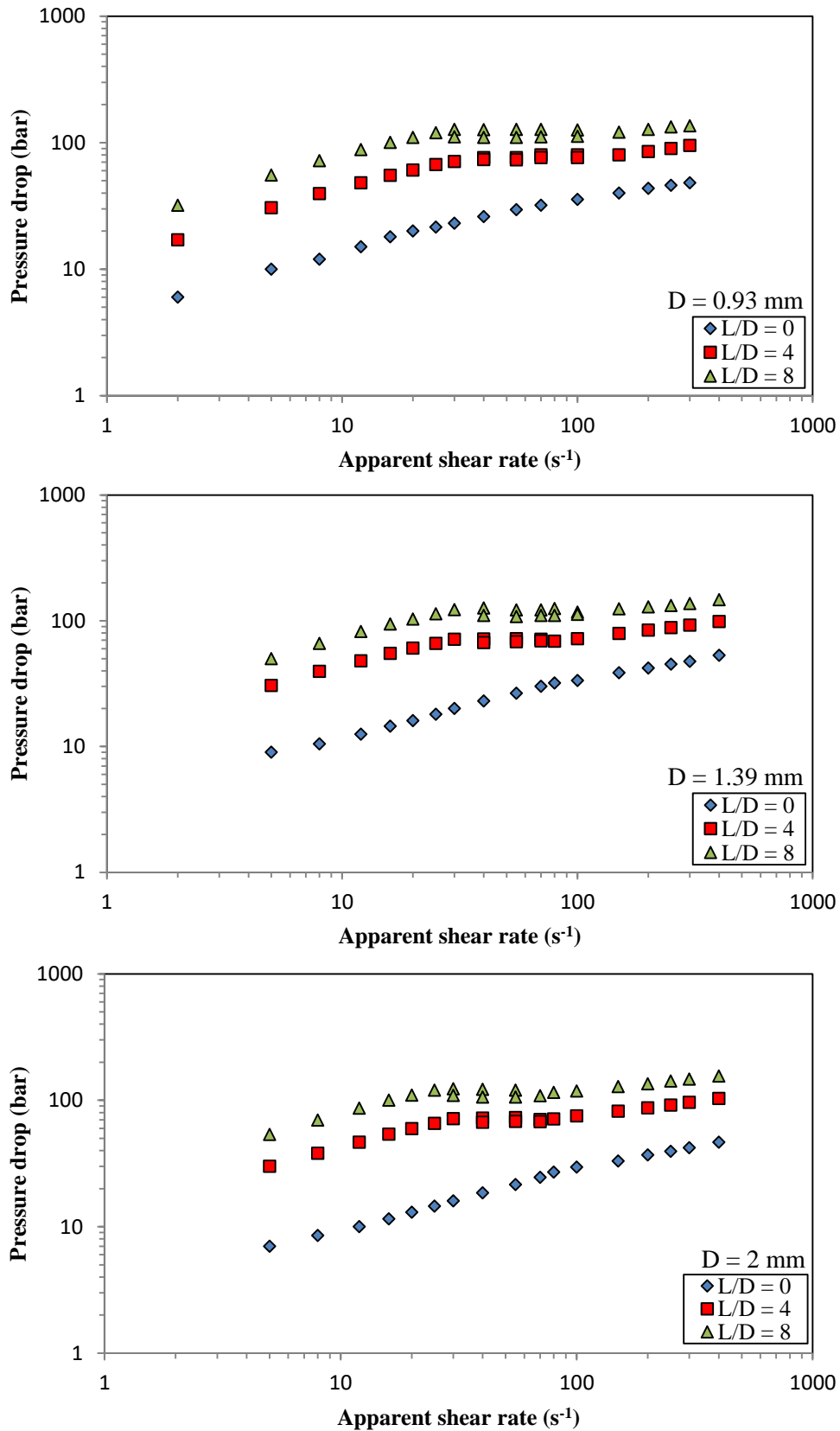


Figure IX – Pressure drop evolutions in function of apparent shear rates of SBR A at 140°C with different capillary die diameters ( $D = 0.93, 1.39$  and  $2$  mm) and  $L/D$  ratios (0, 4 and 8).

Appendix VII: Master viscosity curve of SBR A and SBR B (capillary data)

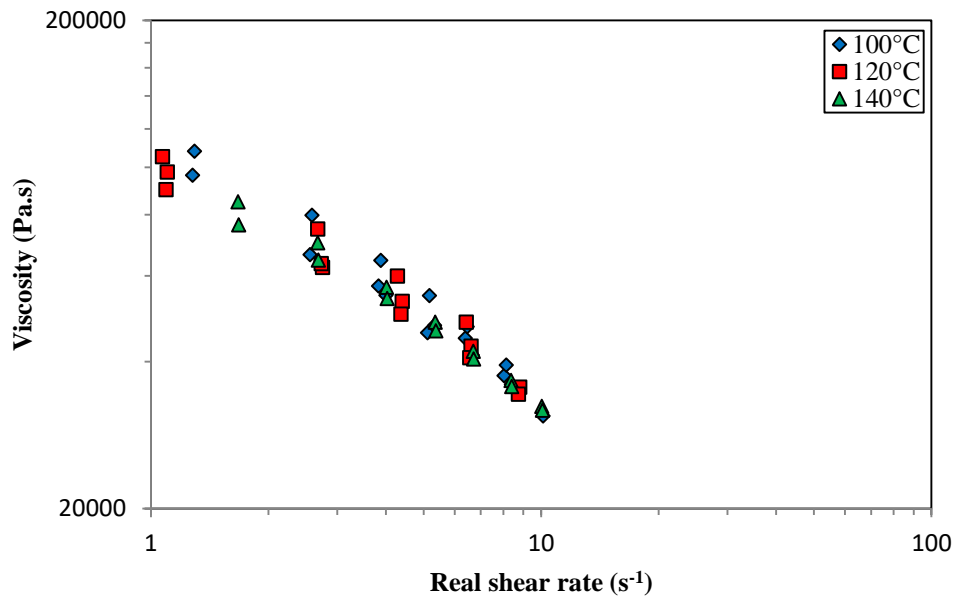


Figure X – Master viscosity curve of SBR A (capillary data).

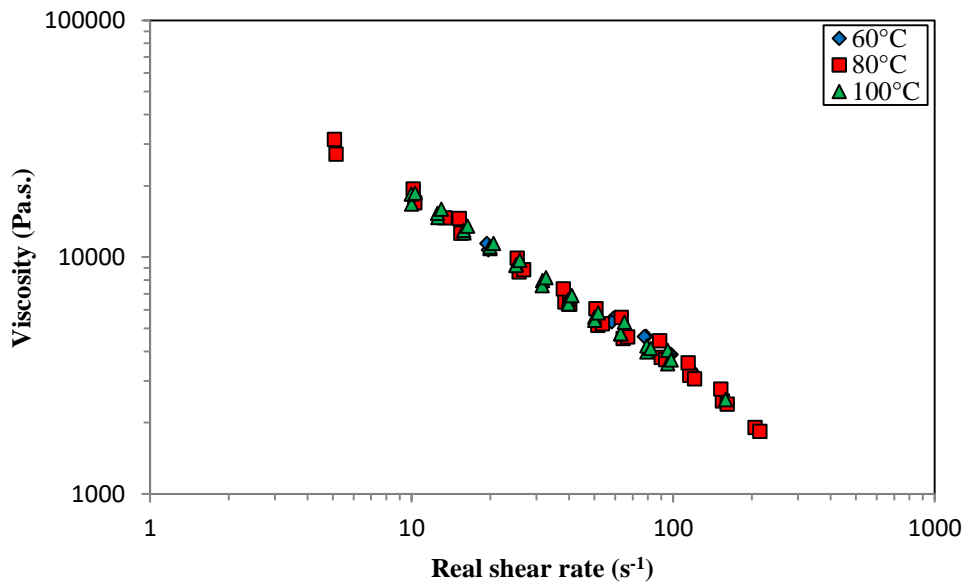


Figure XI – Master viscosity curve of SBR B (capillary data).

Appendix VIII: Pressure drop evolutions of SBR B for different L/D ratios at 100°C

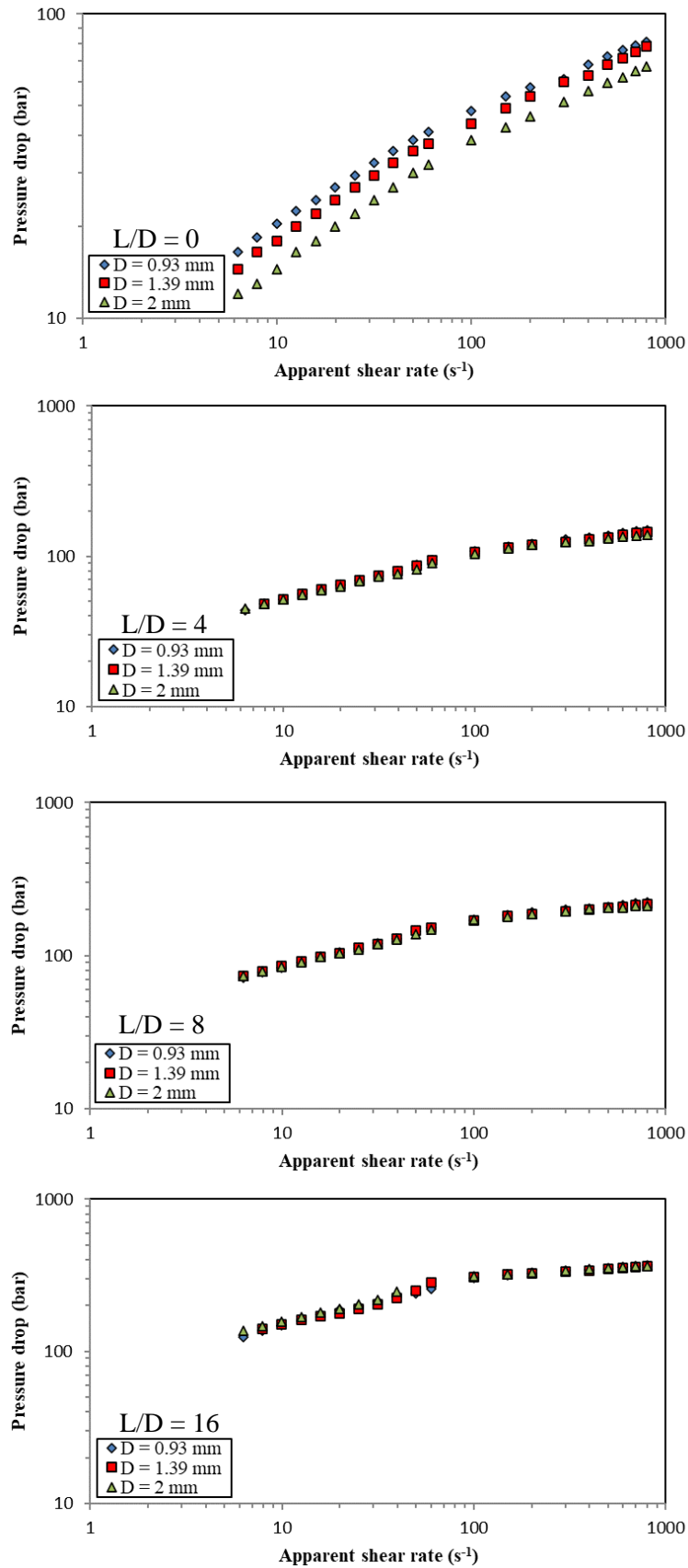


Figure XII – Pressure drop evolutions of SBR B at 100°C for different L/D ratios (0, 4, 8, 16).

Appendix IX: Pressure drop evolutions of SBR B at 60°C

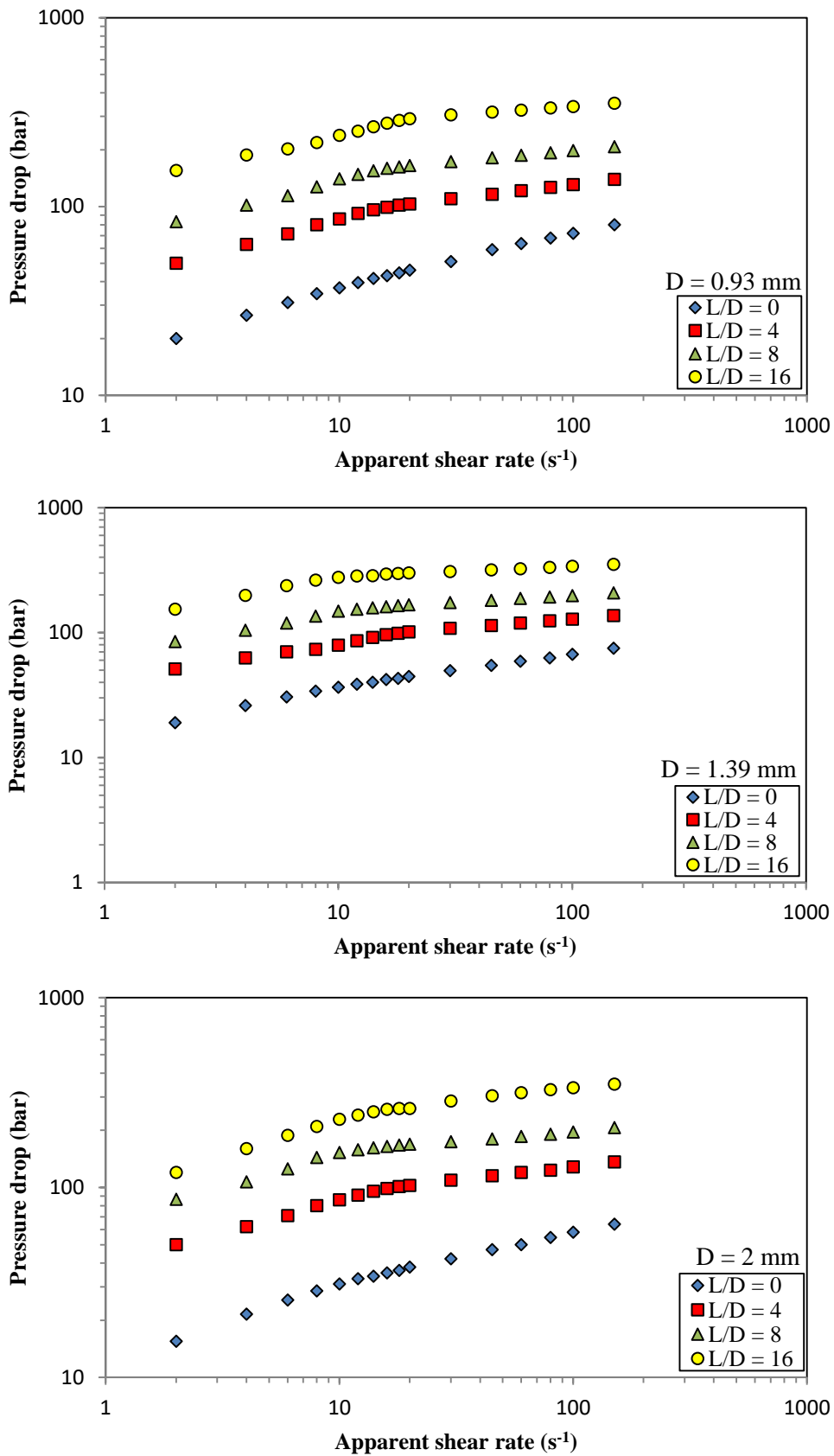


Figure XIII – Pressure drop evolutions in function of apparent shear rates of SBR B at 60°C with different capillary die diameters (D = 0.93, 1.39 and 2 mm) and L/D ratios (0, 4, 8 and 16).

Appendix X: Pressure drop evolutions of SBR B at 80°C

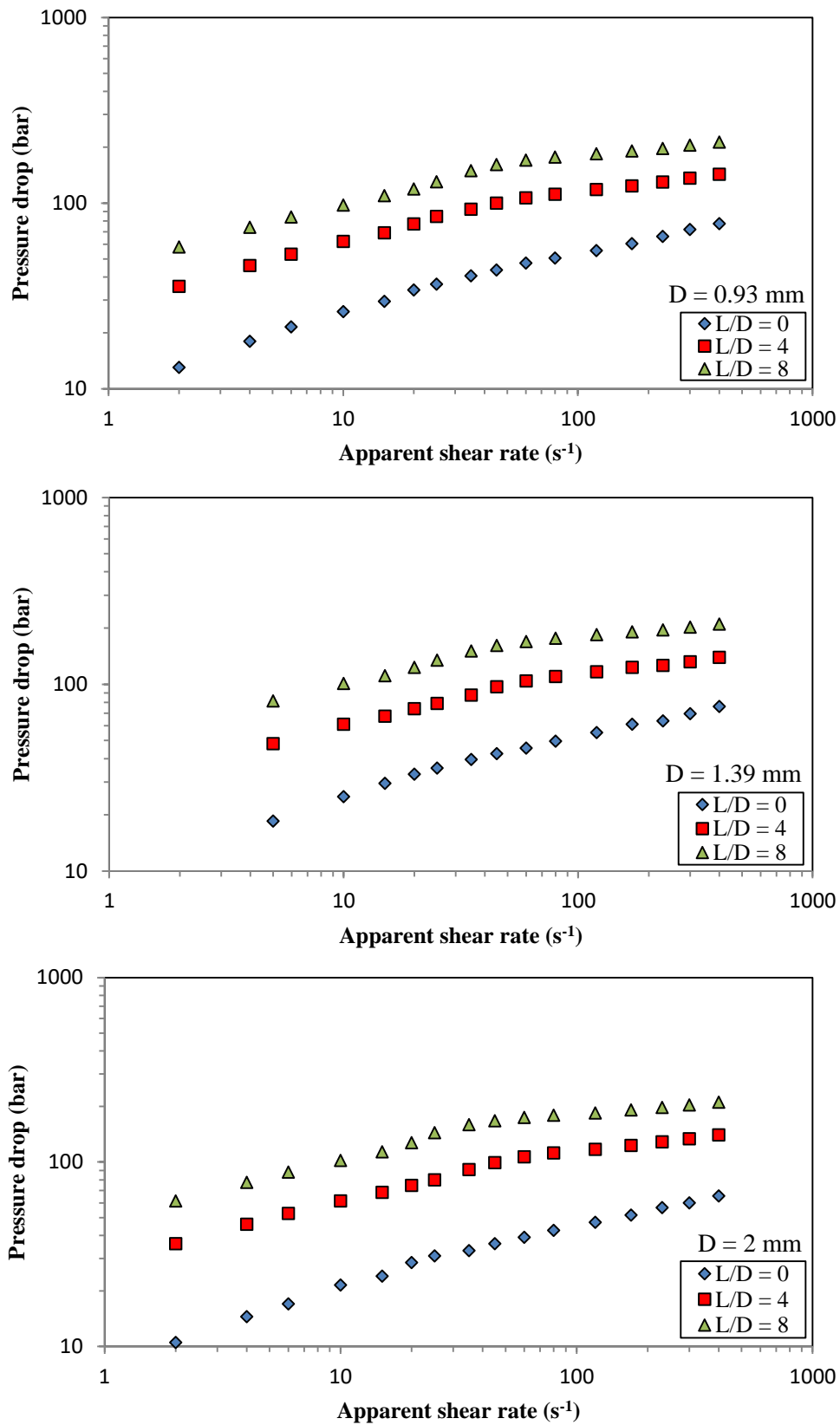


Figure XIV – Pressure drop evolutions in function of apparent shear rates of SBR B at 80°C with different capillary die diameters ( $D = 0.93, 1.39$  and  $2$  mm) and  $L/D$  ratios ( $0, 4$  and  $8$ ).

Appendix XI: Pressure drop evolutions of SBR C for different L/D ratios at 100°C

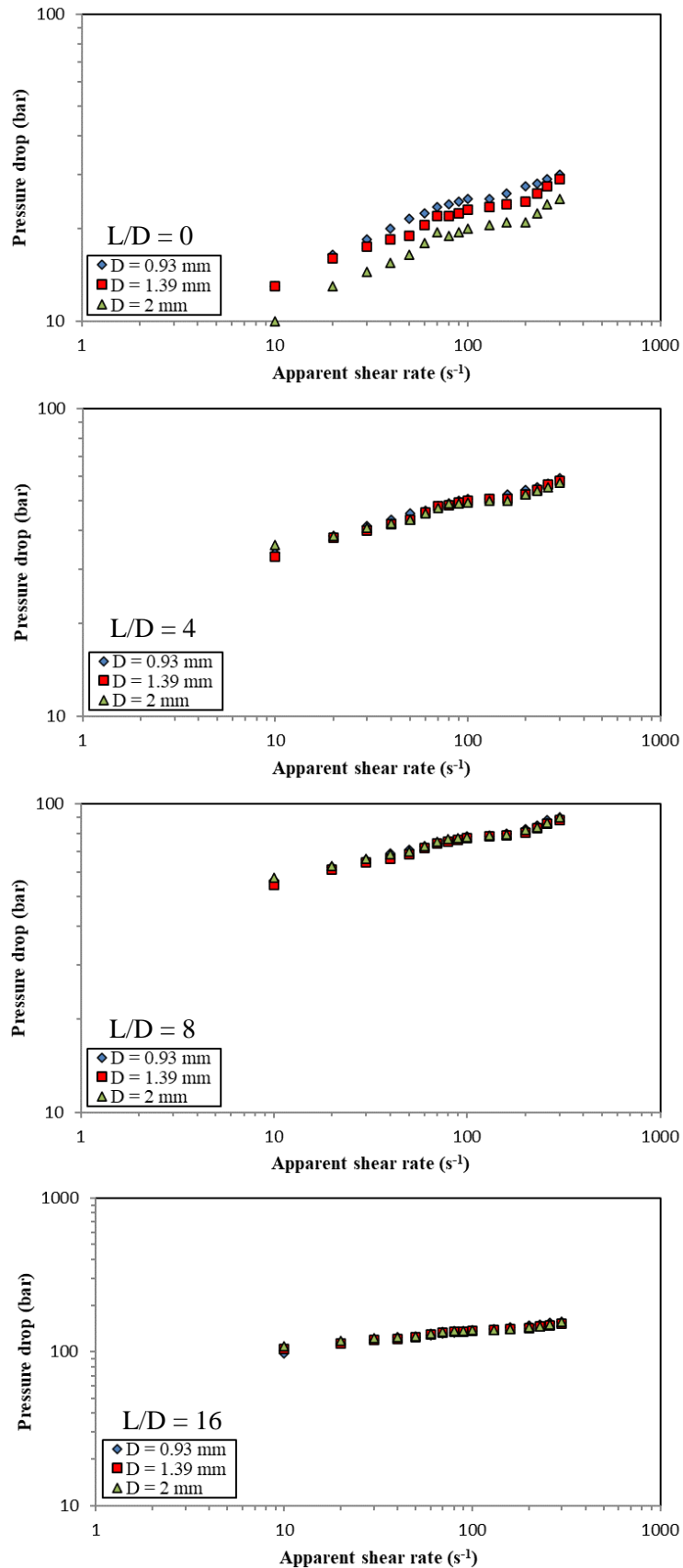


Figure XV – Pressure drop evolutions of SBR C at 100°C for different L/D ratios (0, 4, 8 and 16).

**Appendix**

**Appendix XII:** Peak angles of the converging and diverging free surface for silicone fluid during the stabilization experiments in the MaCROS mixer

Surface condition	Mass (g)	Rotation speeds (rpm)		Converging free surface	Diverging free surface
		V <sub>1</sub>	V <sub>2</sub>	$\theta_{Peak}$ (°)	$\theta_{Peak}$ (°)
Steel 320 – 320	8	-0.5005	1.5655	62.6	84.9
	8	-1	2.7465	69.5	76.4
	8	-1.501	3.905	82.1	90.1
	8	-2.0035	5.22	77.2	76.3
	8	-2.4995	6.249	98.0	86.7
	12	-0.5015	1.57	34.1	90.4
	12	-0.9995	2.804	69.9	74.0
	12	-1.5	3.932	67.7	81.5
	12	-2.0025	5.412	86.9	92.2
	12	-2.499	6.291	73.8	81.5
	16	-0.4995	1.5725	45.2	90.9
	16	-1.004	3.0015	130.0	72.1
	16	-1.501	4.0085	124.8	88.9
	16	-2.003	5.509	82.0	83.5
	16	-2.503	6.5015	94.3	76.6
	20	-0.501	1.57	84.3	91.5
	20	-1.0025	3.12	133.2	72.6
	20	-1.5045	4.257	91.4	93.3
	20	-2.005	5.4725	79.5	78.2
	20	-2.504	6.8115	89.0	98.3

**Table I** – Peak angles of the stabilized silicone fluid during the stabilization experiments in the MaCROS mixer with Steel 320 – 320 surface condition.

**Appendix**

Surface condition	Mass (g)	Rotation speeds (rpm)		Converging free surface	Diverging free surface
		$V_1$	$V_2$	$\theta_{Peak}$ (°)	$\theta_{Peak}$ (°)
<b>Steel 1200 – 320</b>	8	-0.501	1.568	63.8	81.0
	8	-1	2.727	71.5	86.2
	8	-1.5005	3.9345	70.0	74.8
	8	-2	5.268	65.8	67.3
	8	-2.504	6.244	116.1	67.5
	12	-0.502	1.569	74.1	83.2
	12	-0.998	2.7095	102.4	67.4
	12	-1.5095	3.981	124.1	82.1
	12	-2.001	5.3455	57.5	96.0
	12	-2.5015	6.3175	75.5	90.5
	16	-0.503	1.5755	53.4	100.1
	16	-1	2.891	66.5	67.1
	16	-1.507	4.0175	143.3	92.5
	16	-2.0025	5.445	100.3	75.2
	16	-2.5	6.423	70.6	74.4
	20	-0.4985	1.5695	112.6	80.0
	20	-1.009	3.004	107.0	94.4
	20	-1.503	4.0685	74.4	103.8
	20	-2.0035	5.537	52.7	87.2
	20	-2.5015	6.3355	97.4	99.9

**Table II** – Peak angles of the stabilized silicone fluid during the stabilization experiments in the MaCROS mixer with Steel 1200 – 320 surface condition.

**Appendix**

Surface condition	Mass (g)	Rotation speeds (rpm)		Converging free surface	Diverging free surface
		V <sub>1</sub>	V <sub>2</sub>	$\theta_{Peak}$ (°)	$\theta_{Peak}$ (°)
<b>Brass – Steel</b>	8	-0.5	1.5705	63.6	81.0
	8	-1.001	2.836	84.5	81.2
	8	-1.504	3.9805	90.8	90.2
	8	-2.004	5.383	95.7	94.3
	8	-2.501	6.259	72.9	89.4
	12	-0.505	1.575	50.1	79.6
	12	-1.002	2.9885	66.8	88.6
	12	-1.506	3.9905	83.7	96.6
	12	-2.0065	5.4955	72.4	80.9
	12	-2.501	6.3585	65.4	98.4
	16	-0.504	1.5725	78.2	90.6
	16	-1.004	3.1315	59.8	98.7
	16	-1.5015	4.226	85.6	78.1
	16	-2.001	5.498	73.8	79.9
	16	-2.5	6.7005	70.0	93.6
	20	-0.5015	1.58	58.9	87.0
	20	-1.002	3.1165	86.2	71.9
	20	-1.5055	4.3305	71.3	84.5
	20	-2.002	5.556	87.3	92.7
	20	-2.506	6.998	53.6	82.1

**Table III** – Peak angles of the stabilized silicone fluid during the stabilization experiments in the MaCROS mixer with Brass – Steel surface condition.

**Appendix XIII:** Screenshots of wall slip with SBR A in MaCROS mixer

The transition of wall slip with SBR A in the MaCROS mixer can be subdivided into four stages:

- i) SBR A undergoes wall slip at one position (Image 1),
- ii) SBR A moving downstream to another position (Image 4) where it splits into two blocks,
- iii) SBR A moving back upstream to its previous position (Image 7),
- iv) the separated block of SBR A joins the stabilized block to form one single block of fluid before undergoing wall slip again.

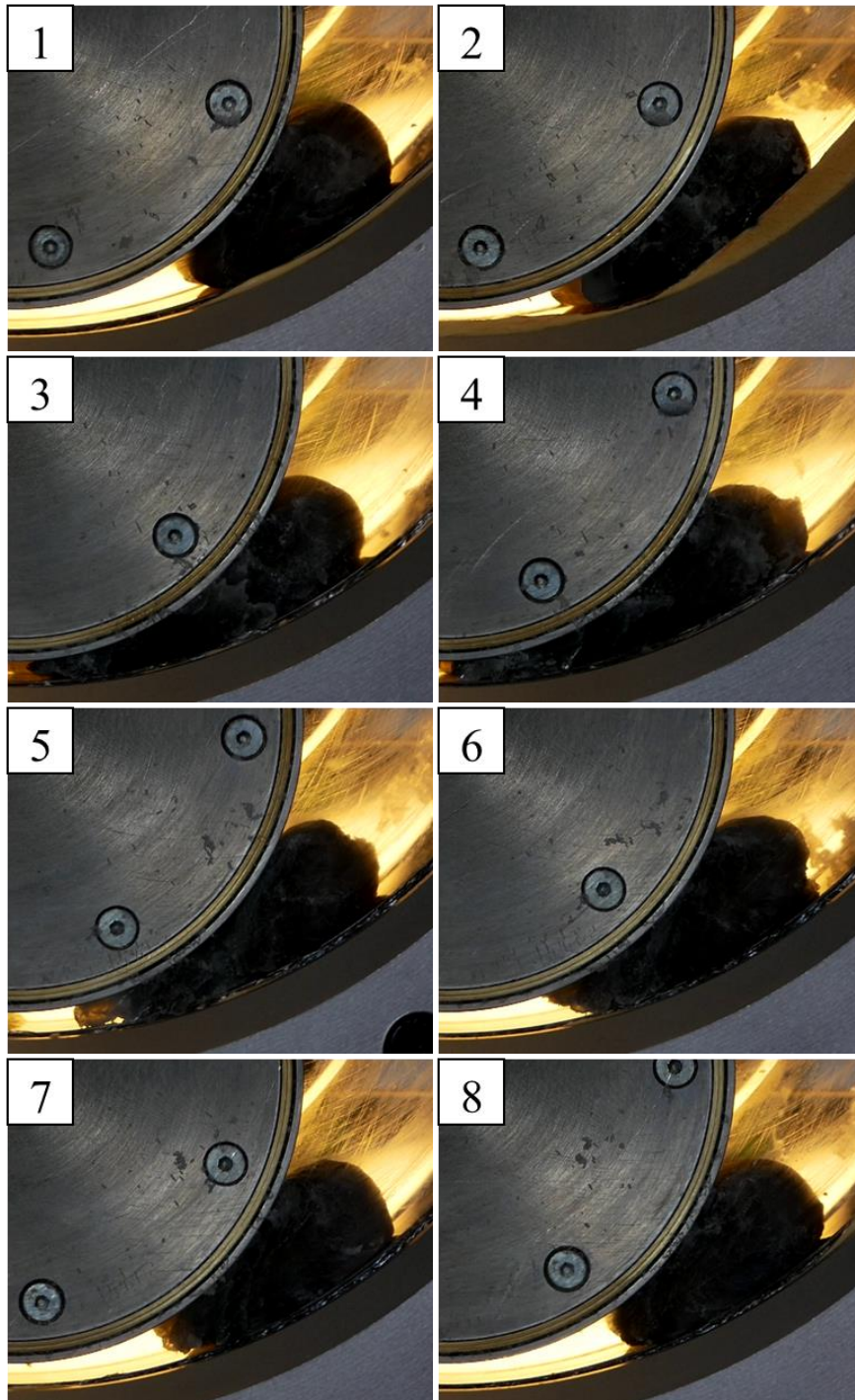


**Figure XVI** – Transition of images showing SBR A undergoing wall slip at  $\dot{\gamma} = 10\text{s}^{-1}$  and  $100^\circ\text{C}$ .

## Appendix

### Appendix XIV: Difference in adhesion energy estimated for silicone fluid during the stabilization experiments in the MaCROS mixer (before and after corrections)

$V_{exp}$  and  $\Delta E_{exp}$  are the advancing velocity and difference in adhesion energy estimated with the experimental values.  $V_{num}$  and  $\Delta E_{num}$  are numerically estimated values after corrections with the drag model.

Surface condition	Mass (g)	Rotation speeds (rpm)		Dimensions of the stabilized fluid (mm)		Advancing velocity (mm/s)		Difference in adhesion energy (J/m <sup>2</sup> )	
		V <sub>1</sub>	V <sub>2</sub>	l <sub>0</sub>	h <sub>m</sub>	V <sub>exp</sub>	V <sub>num</sub>	$\Delta E_{exp}$	$\Delta E_{num}$
Steel 320 – 320	8	-0.5005	1.5655	24.45	9.25	1.24	0.09	236	17
	8	-1	2.7465	25.57	6.28	1.56	0.00	266	1
	8	-1.501	3.905	17.7	8.20	1.98	-1.03	168	87
	8	-2.0035	5.22	20.49	6.51	2.70	-0.63	251	58
	8	-2.4995	6.249	24.44	5.68	2.57	-1.03	273	109
	12	-0.5015	1.57	25.09	9.10	1.24	0.10	244	20
	12	-0.9995	2.804	31.53	6.63	1.53	-0.10	314	20
	12	-1.5	3.932	35.56	7.55	2.05	-0.77	360	135
	12	-2.0025	5.412	26.18	6.55	2.87	-0.50	339	59
	12	-2.499	6.291	29.63	7.32	2.75	-1.84	315	210
	16	-0.4995	1.5725	24.05	10.79	1.25	-0.09	218	15
	16	-1.004	3.0015	42.03	7.65	1.94	0.00	486	0
	16	-1.501	4.0085	36.73	7.73	2.14	-0.75	384	135
	16	-2.003	5.509	40.59	7.61	3.09	-0.83	525	140
	16	-2.503	6.5015	34.41	7.92	3.00	-1.98	383	253
	20	-0.501	1.57	31.84	11.01	1.26	-0.10	288	22
	20	-1.0025	3.12	41.85	8.57	2.15	-0.06	504	14
	20	-1.5045	4.257	36.63	8.29	2.28	-0.83	393	143
	20	-2.005	5.4725	30.46	9.87	3.30	-1.73	371	195
	20	-2.504	6.8115	32.6	6.73	2.79	-1.46	365	191
<b>Average <math>\Delta E</math></b>								<b>334</b>	<b>91</b>

**Table IV** – Estimated difference in adhesion energy of stabilized silicone fluid during the stabilization experiments in the MaCROS mixer with Steel 320 – 320 surface condition.

**Appendix**

Surface condition	Mass (g)	Rotation speeds (rpm)		Dimensions of the stabilized fluid (mm)		Advancing velocity (mm/s)		Difference in adhesion energy (J/m <sup>2</sup> )	
		V <sub>1</sub>	V <sub>2</sub>	l <sub>0</sub>	h <sub>m</sub>	V <sub>exp</sub>	V <sub>num</sub>	ΔE <sub>exp</sub>	ΔE <sub>num</sub>
<b>Steel 1200 – 320</b>	8	-0.501	1.568	32.52	7.315	1.24	0.31	349	88
	8	-1	2.727	31.17	6.37	1.61	0.02	330	4
	8	-1.5005	3.9345	25.33	6.915	1.91	-0.65	251	85
	8	-2	5.268	27.73	6.565	2.57	-0.76	323	96
	8	-2.504	6.244	23.57	7.065	2.60	-1.81	242	168
	12	-0.502	1.569	30.44	8.34	1.25	0.19	309	48
	12	-0.998	2.7095	35.79	7	1.74	-0.01	391	3
	12	-1.5095	3.981	31.79	7.875	1.98	-0.92	307	143
	12	-2.001	5.3455	37.11	6.915	3.01	-0.56	490	91
	12	-2.5015	6.3175	32.4	7.62	2.70	-2.05	332	252
	16	-0.503	1.5755	28.18	12.595	1.26	-0.28	240	53
	16	-1	2.891	45.73	8.42	2.17	0.00	560	0
	16	-1.507	4.0175	41.86	8.095	2.15	-0.86	430	172
	16	-2.0025	5.445	32.85	10.115	3.23	-1.89	389	228
	16	-2.5	6.423	38.13	8.205	3.16	-2.03	438	281
	20	-0.4985	1.5695	47.41	10.42	1.25	-0.04	435	15
	20	-1.009	3.004	44.65	10.09	2.45	-0.18	561	41
	20	-1.503	4.0685	42.66	9.335	2.70	-0.86	507	162
	20	-2.0035	5.537	45.75	9.6	3.14	-1.73	540	297
	20	-2.5015	6.3355	41.29	9.39	3.87	-2.18	538	303
<b>Average ΔE</b>								<b>398</b>	<b>126</b>

**Table V** – Estimated difference in adhesion energy of stabilized silicone fluid during the stabilization experiments in the MaCROS mixer with Steel 1200 – 320 surface condition.

**Appendix**

Surface condition	Mass (g)	Rotation speeds (rpm)		Dimensions of the stabilized fluid (mm)		Advancing velocity (mm/s)		Difference in adhesion energy (J/m <sup>2</sup> )	
		V <sub>1</sub>	V <sub>2</sub>	l <sub>0</sub>	h <sub>m</sub>	V <sub>exp</sub>	V <sub>num</sub>	ΔE <sub>exp</sub>	ΔE <sub>num</sub>
<b>Brass – Steel</b>	8	-0.5	1.5705	26.70	8.86	1.25	0.14	265	30
	8	-1.001	2.836	31.64	6.99	1.81	0.04	358	8
	8	-1.504	3.9805	25.93	7.83	2.07	-0.84	261	106
	8	-2.004	5.383	30.80	6.82	2.94	-0.58	400	79
	8	-2.501	6.259	25.72	7.28	2.62	-1.93	261	192
	12	-0.505	1.575	19.75	11.86	1.24	-0.22	170	31
	12	-1.002	2.9885	39.14	7.47	2.15	0.21	503	50
	12	-1.506	3.9905	39.92	7.51	2.08	-0.72	412	142
	12	-2.0065	5.4955	28.59	9.41	3.19	-1.61	345	175
	12	-2.501	6.3585	36.81	7.78	2.85	-2.03	393	280
	16	-0.504	1.5725	38.31	10.02	1.24	-0.01	355	3
	16	-1.004	3.1315	25.70	11.84	2.47	-0.58	302	71
	16	-1.5015	4.226	42.61	9.10	2.64	-0.82	503	156
	16	-2.001	5.498	35.30	9.98	3.22	-1.84	419	239
	16	-2.5	6.7005	48.10	8.42	3.63	-1.78	622	304
	20	-0.5015	1.58	31.65	13.05	1.27	-0.33	266	69
	20	-1.002	3.1165	53.23	10.02	2.44	-0.17	670	45
	20	-1.5055	4.3305	52.89	9.75	2.86	-0.89	650	201
	20	-2.002	5.556	45.76	10.46	3.35	-1.97	551	324
20	-2.506	6.998	32.11	9.90	4.29	-2.17	449	227	
<b>Average ΔE</b>								<b>408</b>	<b>137</b>

**Table VI** – Estimated difference in adhesion energy of stabilized silicone fluid during the stabilization experiments in the MaCROS mixer with Brass – Steel surface condition.

**Appendix XV:** Prediction of flow rate across the flow channel with the drag model

The flow field obtained for different velocities of inner and outer cylinder are presented in Figure XVII and XVIII. Table VII presents the numerically estimated advancing velocity (mean velocity of the velocity field) at these conditions. All estimations were carried out at  $h = 8 \text{ mm}$  and  $l = 30 \text{ mm}$ .

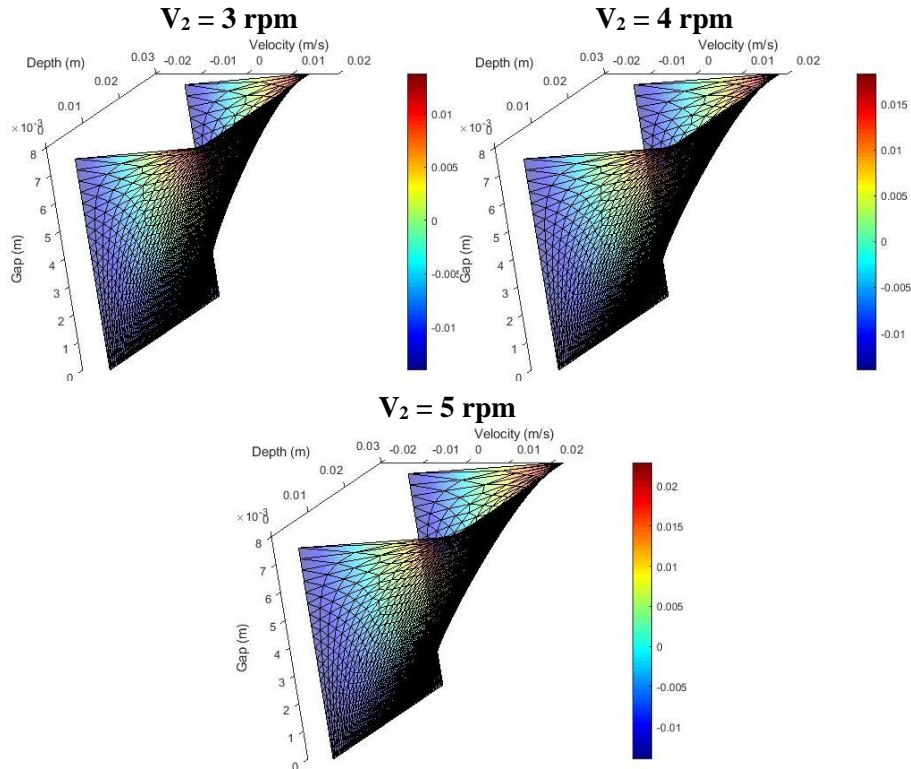


**Figure XVII** – Estimated flow field with the drag model at  $V_1 = -1.5 \text{ rpm}$ .

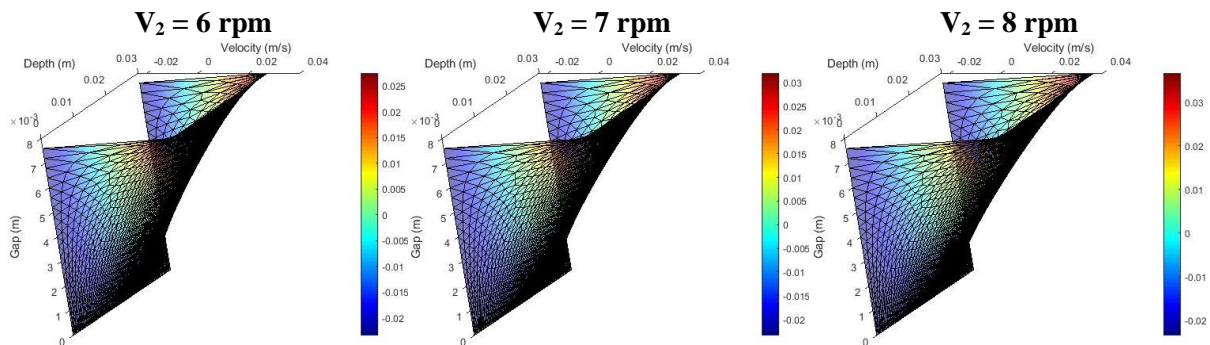


**Figure XVIII** – Estimated flow field with the drag model at  $V_1 = -2.5 \text{ rpm}$ .

Outer cylinder velocity, $V_1$ (rpm)	Inner cylinder velocity, $V_2$ (rpm)	Numerical advancing velocity, $V_{num}$ (mm/s)
-1.5	3	-2.68
	4	-0.84
	5	0.99
-2.5	6	-2.80
	7	-0.98
	8	0.84

**Table VII** – Numerical advancing velocity for different inner and outer cylinder velocities.

**Appendix XVI: Stabilization of free surface when the adhesion boundary condition is changed during the Cimlib simulation**

Figure XIX shows the transition of free surface of the fluid stabilizing after the adhesion boundary condition of the inner cylinder surface is changed. Figure XIX shows the: 1) change in adhesion boundary condition of the inner cylinder, 2 – 4) free surface transitioning to a new steady state and 5) new position of the stabilized free surface.

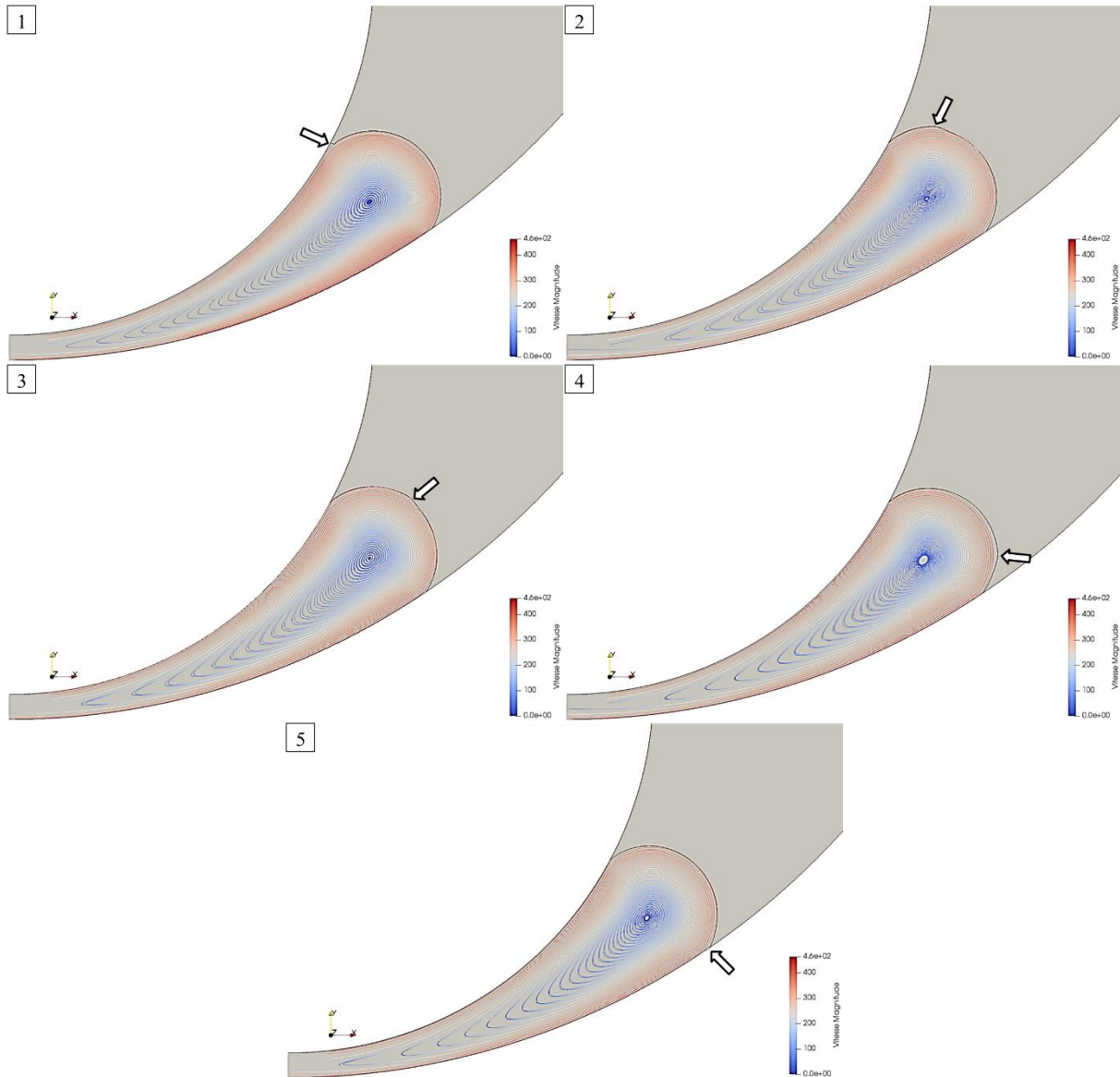


**Figure XIX** – Transition of images showing the stabilization of the free surface after a change in the adhesion boundary condition during the Cimlib simulation.

**Appendix XVII:** Loss of contact with the outer cylinder surface when the adhesion boundary condition is changed during the Cimlib simulation

Figure XX shows the transition of the fluid losing contact with the outer cylinder surface as the adhesion boundary condition of the inner cylinder surface is changed. The images show the: 1) change in adhesion boundary condition, 2) free surface transitioning to a new state, 3) crack initiation as the bulge reaches the outer cylinder surface, 4) crack propagation and 5) complete loss of contact with outer cylinder surface

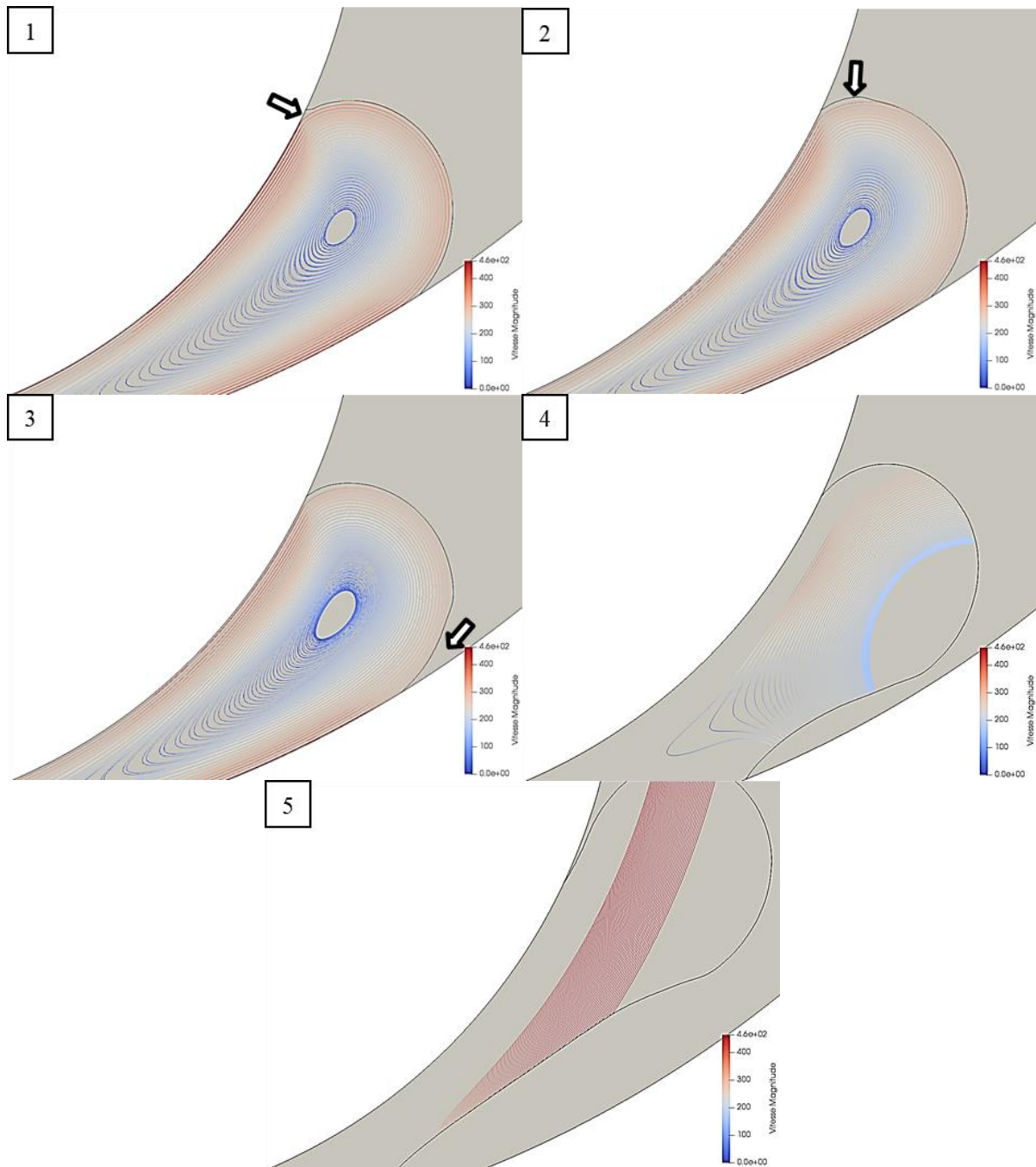


**Figure XX** – Transition of images showing loss of contact with the outer cylinder surface when the adhesion boundary condition is changed during the Cimlib simulation.



**MINES ParisTech**  
**Centre de Mise en Forme des Matériaux (CEMEF)**  
CNRS UMR 7635  
1 rue Claude Daunesse, CS 10207, 06904 Sophia Antipolis Cedex, France  
<http://cemef.mines-paristech.fr>

## RÉSUMÉ

---

Le procédé de mélange interne est crucial pour la fabrication de mélanges de caoutchouc car il détermine les propriétés finales du produit. La compréhension des phénomènes interfaciaux lors du mélange est cruciale pour l'évaluation du procédé, la détermination des paramètres du procédé et la simulation numérique du procédé. Ces phénomènes comprennent le glissement à la paroi, l'adhésion et le mouvement des surfaces libres. L'évolution des vitesses de glissement a été caractérisée indirectement avec des méthodes rhéologiques classiques. Un prototype a été conçu et développée pendant cette thèse afin d'observer les surfaces libres des fluides visqueux sous cisaillement en régime permanent. Un petit volume d'un fluide silicone visqueux permet l'observation des surfaces libres en contre-rotation. Les vitesses de stabilisation ont été étudiées pour différentes conditions de vitesse des cylindres, de volume de fluide, de rugosité de surface et de nature des surfaces de cylindre. La contribution de l'énergie d'adhésion semble négligeable. Enfin, l'influence du cisaillement sur le mouvement et la forme des surfaces libres a été explorée par la méthode des éléments finis. L'énergie d'adhésion a été intégrée dans les simulations numériques qui montrent un effet clair de l'énergie d'adhésion sur la forme et le mouvement de la surface libre. Par contre, le niveau d'énergie d'adhésion nécessaire dans le cas des fluides visqueux est beaucoup trop élevé pour être observé expérimentalement.

## MOTS CLÉS

---

Mélange interne, Caoutchouc, Glissement à la paroi, Mouvement des surfaces libres, Adhésion.

## ABSTRACT

---

The internal mixing process is crucial to the manufacturing of rubber compounds as it is instrumental to the final properties of the product. Understanding the interfacial phenomena during mixing is crucial to the evaluation of the process, determination of process parameters and numerical prediction of the same. These phenomena include wall slip, adhesion and movement of free surfaces. The evolution of wall slip velocities was characterized with classical indirect rheological techniques. An eccentric counter-rotating Couette cell was designed and developed during this PhD to observe the free surfaces of viscous fluids under shear flow in steady-state conditions. A small volume of silicone fluid was used to study the flow behavior and observe the free surfaces in counter-rotating conditions. Steady state conditions were investigated for different conditions of cylinder velocities, volumes of fluid, surface roughness and nature of cylinder surfaces. The contribution of the adhesion energy to the stabilization velocities appears to be negligible. Finally, the influence of shear flow on the movement and shape of free surfaces was explored with the help of finite element method. Numerical simulations with the integration of an adhesion boundary condition show a clear effect of the adhesion energy on the free surface shape and movement. But the level of adhesion energy necessary in the case of viscous fluids was found to be far too high to be observed experimentally.

## KEYWORDS

---

Internal mixing, Rubber, Wall slip, Movement of free surfaces, Adhesion.